Nano-photonics on luminescent molecular systems and metal particles in optical sub-wavelength microresonators

Spectral and temporal control in the weak and strong coupling regime

Dissertation

der Mathematisch-Naturwissenschaftlichen Fakulät
der Eberhard Karls Universität Tübingen
zur Erlangung des Grades eines
Doktors der Naturwissenschaften
(Dr. rer. nat.)

vorgelegt von
Herr Alexander Konrad
aus Memmingen

Tübingen
2016

Gedruckt mit Genehmigung der Mathematisch-Naturwissenschaftlichen Fakultät der Eberhard Karls Universität Tübingen.

Tag der mündlichen Prüfung:	11.12.2015
Dekan:	Prof. Dr. Wolfgang Rosenstiel
1. Berichterstatter:	Prof. Dr. Alfred J. Meixner
2. Berichterstatter:	PD Dr. Marc Brecht
3. Berichterstatter:	Prof. Dr. Thomas Huser

for my family

Wann immer wir nämlich glauben, die Lösung eines Problems gefunden zu haben sollten wir unsere Lösung nicht verteidigen, sondern mit allen Mitteln versuchen sie selbst umzustoßen.
Ein empirisch-wissenschaftliches System muß an der Erfahrung scheitern können.
Karl Popper, Logik der Forschung, 1934.

When you have eliminated all which is impossible, then whatever remains, however improbable, must be the truth.
Arthur Conan Doyle, The Adventure of the Beryl Coronet / Sherlock Holmes, 1892

Entia non sunt multiplicanda praeter necessitatem.
(Entitäten dürfen nicht über das Notwendige hinaus vermehrt werden)
-Ockhams Rassiermesser- nach Johannes Clauberg, 1654

There is a theory which states that if ever anyone discovers exactly what the Universe is for and why it is here, it will instantly disappear and be replaced by something even more bizarre and inexplicable. - There is another theory which states that this has already happened.
Douglas Adams, The Restaurant at the End of the Universe, 1980

Table of contents

Abstract

Micro-resonators, especially those designed for light within the optical regime are powerful tools to interfere the light-matter interaction and are thus often used devices for sensing and tailoring spectral and temporal properties of nanoscopic objects. In this thesis the luminescence of organic dye molecules, energy transfer coupled model systems, photosynthetic complexes and metal nanoparticles is examined and controlled by altering directly the photonic and phononic environment. The experimental observations were gained by confocal microscopy in combination with spectroscopy and time correlated single-photon counting. The photonic impact was achieved by a tunable Fabry-Pérot micro-resonator and the phononic impact by a helium-bath cryostat permitting experiments at temperatures down to 1.6 K.

This thesis is structured in the following way:

The **first chapter** presents a short introduction sketching the general context in which the specific results of the later chapters are embedded. In the **second chapter** the relevant mechanisms of the interaction between matter and light are described for each examined type of matter i.e. the luminescence of molecules, a certain energy transfer mechanism between two coupled molecules, the class of natural light-to-energy converters namely the photosynthetic complexes, metal nanoparticles and a specific class of devices for constraining photons. The **third chapter** concerns the other point of view, how the phenomena resulting from these mechanisms can be experimentally observed, controlled and analyzed, including the presentation of the Fabry-Pérot-resonators used in this study. The second and third chapter are thus the basic framework in order to understand the experimental results, which are further demonstrated each by a scientific publication and amended by an introducing paragraph. The **fourth chapter** presents a new microscope setup allowing to transfer samples into a cryogenic chamber and to optically examine these samples at temperatures down to 1.6 K on the single-molecule level with a high sensitivity. In **chapter five**, an approach is shown which extends the presented microscope in order to enhance its resolution by immersing the objective lens at low temperatures. In **chapter six**, the impact of a $\lambda/2$ Fabry-Pérot micro-resonator on a certain fluorescent molecule working as a model system is demonstrated. The analysis of the recorded fluorescence in time and spectral domain shows the opportunity to determine and control the

spectral and temporal properties of quantum emitters at ambient conditions and at the ensemble level in a precise manner. In **chapter seven**, the impact of such a resonator on the protein DsRed, which contains chromophores performing the prominent energy transfer FRET, is shown. It is demonstrated how the resonator is able to alter the efficiency of this transfer depending on the resonator deposition. **Chapter eight** presents results concerning the issue of how the resonator is able to affect the energy transfer dynamics between two FRET coupled molecules in the time domain in order to directly sense and describe the energy transfer dynamics. In **chapter nine**, **ten**, **eleven** and **twelve** the photosynthetic complexes Photosystem I and II are examined representing a prominent class of natural energy converters. First the optical properties of Photosystem II at cryogenic temperatures are examined to provide insights capable of explaining the energy transfer dynamics of this prominent protein. For Photosystem I the optical properties of two fluorescent contributions are examined in regard of the orientation of the respective emitters that are regarded as the final traps for the excitation energy. Then the possibility to alter the energy transfer dynamics within Photosystem I by a micro-resonator at cryogenic temperatures is demonstrated. **Chapter thirteen** addresses the optical properties of nanoscopic metal particles and how especially their luminescence at different temperatures gives insight into the underlying processes of this phenomenon. In **chapter fourteen** it is shown and analyzed how such particles are able to interact with a micro-resonator whereas the spectral observations of this combined system show strong coupling behavior in contrast to the weak coupling effects between such resonators and the previously described quantum emitters.

Zusammenfassung

Mikroresonatoren, die für Licht im optischen Bereich entworfen sind, stellen nützliche Werkzeuge dar, um in die Licht-Materie-Wechselwirkung einzugreifen und sind deshalb oft verwendete Instrumente, um die spektralen und zeitlichen Eigenschaften nanoskopischer Objekte zu überwachen und zu beeinflussen. In dieser Arbeit wird die Lumineszenz von organischen Farbstoffmolekülen, energietransfergekoppelten Modellsystemen, photosynthetischen Komplexen und Metallnanopartikeln untersucht und durch den direkten Einfluss der photonischen und phononischen Umgebung kontrolliert. Die experimentellen Beobachtungen wurden durch konfokale Mikroskopie, in Kombination mit Spektroskopie und zeitkorrelliertem Einzelphotonenzählen, erzielt. Der photonische Einfluss wurde durch einen stimmbaren Fabry-Pérot Mikroresonator erreicht und der phononische Einfluss durch einen Helium-Bad-Kryostaten der das Experimentieren bei Temperaturen bis zu 1.6 K ermöglicht. Die Arbeit ist follgendermßen strukturiert:
Das **erste Kapitel** präsentiert eine kurze Einleitung, die den allgemeinen Kontext skizziert in welchem die spezifischen Resultate der späteren Kapitel eingebettet sind. Im **zweiten Kapitel** sind die relevanten Mechanismen der Interaktion zwischen Licht und Materie für jede Sorte von untersuchten Objekten dargelegt. Dabei handelt es sich um die Lumineszenz von Molekülen, einen Energietransfermechanismus zwischen zwei gekoppelten Molekülen, der Klasse der natürlichen Licht-Energie-Umwandler namentlich der photosynthetischen Komplexe, Metallnanopartikel und eine spezielle Sorte von Instrumenten um Photonen einzuschließen, die Fabry-Pérot-Mikroresonatoren. Das **dritte Kapitel** thematisiert den anderen Blickpunkt, wie diese Phäenomene, die aus den beschriebenen Mechanismen folgen, experimentell beobachtet, kontrolliert und analysiert werden können, inklusive der Präsentation der benutzten Fabry-Pérot-Resonatoren. Das zweite und dritte Kapitel stellen deshalb den grundlegenden Rahmen dar, um die experimentellen Resultate verstehen zu können, welche in Form von wissenschaftlichen Publikationen mit einem einleitendem Paragraphen dargelegt werden. Das **vierte Kapitel** stellt ein neues Mikroskop vor, welches uns erlaubt, Proben in eine kryogene Kammer zu transferieren, um diese Proben bei Temperaturen bis zu 1.6 K auf Einzelmölekülniveau mit hoher Sensitivität optisch zu untersuchen. In **Kapitel fünf** wird eine Methode präsentiert, welche das bereits vorgestellte Mikroskop erweitert um dessen Auflösung durch Immersion des

Objektives bei tiefen Temperaturen zu erhöhen. In **Kapitel sechs** wird der Einfluss eines $\lambda/2$ Fabry-Pérot Mikroresonators auf ein bestimmtes fluoreszierendes Molekül, welches ein Modellsystem darstellt, aufgezeigt. Die Analyse der aufgenommenen Fluoreszenz im Zeit- und Spektralbereich demonstriert die Möglichkeit, um die spektralen und zeitlichen Eigenschaften von Quantenemittern bei Raumtemperatur und auf dem Ensemble-Niveau in präziser Art und Weise zu bestimmen und zu kontrollieren. In **Kapitel sieben** wird der Einfluss eines solchen Resonators auf das Protein DsRed, welches aus Chromophoren zusammengesetzt ist, die den prominenten Energietransfer FRET durchführen, gezeigt. Es wird gezeigt, wie der Resonator in der Lage ist, die Effizienz des Energietransfers in Abhängigkeit der Resonatoreigenschaften zu beeinflussen. **Kapitel acht** präsentiert Resultate zu der Frage, wie der Resonator in der Lage ist, die Energietransferdynamik zwischen zwei FRET-gekoppelten Molekülen in der Zeitdomäne zu verändern, um damit direkt die Transferdynamik zu überwachen und zu beschreiben. In **Kapitel neun**, **zehn**, **elf** und **zwölf** werden die photosynthetischen Komplexe Photosystem I und II untersucht, die eine prominente Klasse von natürlichen Energieumwandlern repräsentieren. Zuerst werden die optischen Eigenschaften von Photosystem II bei kryogenen Temperaturen untersucht, welche tiefere Einblicke zur Erklärung der Energietransferdynamik dieses prominenten Proteins ermöglichen. Für Photosystem I werden die optischen Eigenschaften zweier Fluoreszenzbanden im Hinblick auf die räumliche Orientierung der entsprechenden Emitter untersucht, die als letzte Glieder der Energietransferkette gelten. Anschließend wird die Möglichkeit gezeigt, die Energietransferdynamik in Photosystem I durch einen Mikroresonator bei kryogenen Temperaturen zu verändern. **Kapitel dreizehn** beschreibt die optischen Eigenschaften von nanoskopischen Metallpartikeln und wie im Besonderen deren Lumineszenzverhalten bei tiefen Temperaturen Einblicke in die zugrunde liegenden Prozesse dieses Phänomens ermöglicht. In **Kapitel vierzehn** wird gezeigt und analysiert, wie solche plasmonischen Partikel in der Lage sind, mit einem Mikroresonator zu interagieren, wobei die spektralen Beobachtungen dieses kombinierten Systems ein Verhalten von starker Kopplung zeigen im Gegensatz zu beobachtbaren Effekten einer schwachen Kopplung zwischen solchen Resonatoren und den vorher beschriebenen Quantensystemen.

Chapter 1

Introduction

The question how knowledge about the small entities of nature and their associated processes can be gained and utilized is a topic affecting our everyday lives due to the rapid developments in e.g. data communication, energy generation, storage and conversion. More than half a century ago, mankind started to explore space with technologies that today seem to us as old as ancient slide rulers. The digital revolution with its miniaturized computers, sensors, ultra-fast computations and huge varieties of interfaces between human and technology bases on the fundamental developments of micro-, nano-, and quantum optics. Light is the fastest, most efficient and most versatile carrier of information and energy known to us until this day. Sunlight is harvested since millions of years by plants, today by solar cells; sensing objects with our own eyes allows us to obtain information about nature since the first human beings; today, information can be exchanged wireless by radio-waves between countless stand-alone devices. However, light dissipates easily, interacts with almost everything and can not be stored directly compared to fuel or books. Therefore, one major task of todays scientists and engineers in the field of optics, physics and nanotechnology is to efficiently sense and control the interaction between light and the smallest parts of matter, e.g. to observe, enhance or suppress this interplay. Whether the pure urge of understanding or the will to make life easier by new inventions, mastering this interplay is inevitable. Trivially spoken, our modern world with most of its features is unthinkable without the insights scientists accumulated over the last decades about how photons are generated and converted by atoms, molecules or other complex compounds of them. However, the bases of technological revolutions are always preceded by new theories and models explaining empirical facts, from which we can finally deduce practical applications.

The initial quotes of this thesis introducing a main epistemic problem associated with this task indicate also the methods for getting access to the understanding and harnessing the physical world. The micro- and nanoscopic world is not observable directly by us humans, such as ultra-fast processes or particles with few nanometers in size. That

is why any observation directly and indirectly caused by unknown underlying processes have to be examined and conclusions by deduced or stated models have to be drawn explaining the respective phenomenon. However, often more than one explanation fitting both an appropriate theoretic system and the empirical finding can be offered, hampering this whole task. These old problems are inherent in the empirical sciences and can only be sufficiently faced by admitting, that a scientist can never prove any stated theory but disprove it awfully well by observing contradicting phenomena. This study therefore tries to connect both, the theoretical description of the light-matter interaction and the realization and observation of specific phenomena, which may in future contribute to further technical developments.

Making use and controlling the interaction processes between photons and small objects always means interfering in this interaction in order to e.g. quicken, slow down or deactivate certain processes which always requires an external disturbance brought into the system by the scientist. Introducing such disturbances may generate hence complete new systems, which are denoted in this work as hybrid systems or photonic devices. Briefly, the aim of this study is presenting concrete approaches of combining nanoscopic systems such as molecules, molecule-compounds and metal particles, each exhibiting each special features in their interaction with light and optical devices allowing us to precisely control the photonic impact on those nano-objects. Knowing and controlling the impact of hybrid systems or photonic devices thus allows us to deduce statements from new observations and to find and set certain parameters for the disturbance to achieve the desired impact on the perturbed object.

To constrain photons in order to behave in a specific way, one has to design an experimental setup which is able to change either their spatial, energetic or temporal properties, but also to retain them as electromagnetic fields and not convert them into e.g. chemical or kinetic energy. Photons, regarded as the smallest energy portions of e.g. propagating waves, can be encased for a certain time by coupling them into a cavity e.g. consisting of two opposing mirrors with a small separation, called a micro-resonator. Due to the wave nature of light, only specific photons are fitting into such cavities which can lead to a huge impact on e.g. molecules embedded in these cavities. Disturbing matter in such a way requires a concept about the intrinsic properties and processes within the free matter, which can differ extremely between different kinds of objects. As we will see, some observable phenomena are not completely determined by intrinsic properties of matter and can be modified by both the photonic and phononic environment. This means that we are able to modify the behavior of matter by altering e.g. the electromagnetic surrounding or the temperature of the system in which the nanoscopic object is embedded. To sufficiently describe the intrinsic properties of enclosed light and nanoscopic matter in this thesis the

essential existing sets of theories, models and images are discussed and used. Regarding light, several images coexist whereas some of them are more appropriate for explaining specific phenomena. Therefore, the terms energy, frequency, wavelength and k-vector are used meaning more or less only different aspects of the description of light. In this study, matter is considered mainly as a composition of dipoles or just a single (point-) dipole, which approximation has to be justified for each case but facilitates the theoretical analysis of experimental observations.

Finally, the acquired insights and results in this thesis can be mosaic pieces for further applications such as efficient light-to-energy-converters, micro-sensors, ultra-fast computations, versatile information transmitters/receivers or just as a basic research for subsequent scientists.

Chapter 2

Interaction between light and matter

In general, photons can interact with nanoscopic matter[1] by getting scattered or absorbed. These events and the associated properties can be empirically described by the dielectric function of the substance. Understanding such interactions requires knowledge of both, electro-magnetics and the intrinsic and extrinsic dynamics of the nanoscopic subunits of the sample. The quantities, which are necessary for describing the absorption of a photon are the energetic and spatial properties of the incident electromagnetic fields and the induced consequences in the matter. The alternating (electric) fields of light can cause a distinct fluctuation of the charge distribution in the nano-object occurring with a certain frequency if we assume that the regarded matter consists of at least one negative and one positive charge, which is the case for all sorts of substances regarded in this work. Absorbing a photon means in any case that the energy of the electromagnetic field is getting transfered to the object and often converted into kinetic or chemical energy. Nevertheless, for some kind of matter it is necessary to expand the description of the phenomenological optical properties by a quantum mechanical description of the energetic behavior of the respective quantum objects within the matter. Beyond the nanoscopic scale it is hence important to identify the possible conditions of the quantum objects due to their strictly quantified states. Only by understanding the intrinsic arrangement and the associated processes of molecules, atoms or compositions of them, it is possible to describe and finally control the interaction of light and matter in a proper way.

2.1 Fluorescence

A Molecule that can be regarded as a dipole, which functions as an antenna for the incoming electromagnetic field, can absorb a photon, when light with a certain frequency induces a transition dipole moment within the molecule[1], which is transfered from its

[1] Due to the different kinds of examined samples in this thesis, the term nano-object or nanoscopic matter is used meaning in this case: single molecules, compounds of molecules such as protein complexes and metallic nanoparticles, each in size regions smaller than a micrometer

initially occupied ground state to a certain excited state. The amount of absorbed energy and the nature of the distinct states determine the molecule's reaction to this disturbance, which can result e.g. in rotations, vibrations or electronic charge rearrangements. Phenomenologically, the absorbance (or extinction) of a solution with distinct types of molecules can be measured and quantified using the Lambert-Beer law:

$$A(\lambda) = \varepsilon(\lambda)cl, \tag{2.1}$$

whereby $\varepsilon(\lambda)$ is the molar absorptivity (or molar extinction coefficient) depending on the irradiated wavelength λ, c is the concentration and l is the length of the interaction path of light with the sample volume. In the visible regime of light, mainly a single electron within the electronic structure of the specimen changes its energetic and spatial properties if there is a free and accessible target environment, i.e. a molecular orbital of higher energy. In classical theory, such transitions can be described by considering the charge redistribution of the molecule as an oscillating dipole; this concept is often sufficient to understand the optical processes within matter[2]. In this simplified case, the molecule is regarded as a point-dipole of two charges with oscillating distance analogous to spring coupled pendulums or RLC circuits. The concept of oscillating dipoles bases on the presumption that only one (certain) electron is exclusively altering its state with respect to the rigid remaining charge distribution. Such oscillating dipoles exhibit distinct resonances analogously to classical oscillators which can be excited by external driving fields as forces matching the dipoles eigenfrequency. Due to the altered charge distribution with respect to the initial state, the molecule may react to this disordering mainly by getting transfered into an excited vibronic state, which vice versa influences the energetic and spatial properties of the molecular orbitals for the excited electron. One kind of molecules investigated in this work, is the class of organic dyes with comparably large π-electron systems with respect to the size of the molecule. Energetically, the separation of the binding and anti-binding π-orbitals are in the regime of ultraviolet and visible light[1]. Thus, such molecules are ideal candidates for investigations by absorption and fluorescence spectroscopy. One has to keep in mind that the description of a (molecular) orbital by the respective wavefunction of the corresponding state is purely quantum mechanically, however, the transition between such states can be well described classically by the transition dipole moment. Any charge redistribution associated with internal energetic and spatial transitions of the respective charges can be quantified by the transition dipole moment $\mathbf{M}_{12}$. The dipole moment operator $\mathbf{M}$ is given classically by the distances r_i or by the quantum mechanical position operator $\mathbf{r}$ of each electron i with charge e to an arbitrary point in space by:

$$\mathbf{M} = \sum_{i}^{N} e\mathbf{r}_i. \tag{2.2}$$

The empirical absorption coefficient[2] represents for the most simple case the probability of one transition between two states 1 and 2 described by the quantum mechanical wavefunctions Ψ_i of state i, which is given by the Einstein coefficient B_{12}[3]:

$$B_{12} = \frac{2\pi}{3\hbar^2} |\langle \Psi_1 | \mathbf{M} | \Psi_2 \rangle|^2. \tag{2.3}$$

Illustrating transitions including electronic and vibronic states of a molecule can be done by the Frank-Condon-principle, which is schematically explained in Figure 2.1 for a two-atomic molecule behaving as an anharmonic oscillator[4]. The principle is based on the Born-Oppenheimer approximation, which states that during an excitation of an electron from the highest occupied molecule orbital (HOMO) to the lowest unoccupied molecule orbital (LUMO) the nuclei are spatially fixed. Nevertheless, at ambient temperatures and in media the promotion of an electron is most likely accompanied by the generation of phonons. This can be regarded as a reaction of the molecule to the distorted charge distribution. Therefore, higher vibronic levels of the electronic first excited state are more probably excitable from the initial state than the lowest vibronic level is. Relaxations from these intermediate levels to the ground vibronic level of the excited electronic state are very rapid (Kasha's Rule) and responsible for the so-called Stokes shift between absorption and fluorescence spectra, which denotes the (thermal) energy loss between excitation and (radiative) relaxation[5].

The emission of light, which is generally denoted as luminescence, is now one possible relaxation channel for the molecule beside others e.g. internal conversion (IC) or intersystem crossing (ISC). Analogously to absorption, the initial (excited) and target (ground) state determine the properties of the radiated photons. The most simple case of luminescence is denoted as fluorescence. In this case, the molecule relaxes back to the electronically ground state S_0 from the vibronic ground state of the first excited electronic state S_1 by emitting a fluorescence photon and by keeping the electron spin during the complete series of processes. This and other prominent processes are summarized in so-called Jablonsky diagrams like shown in Figure 2.2[4].

The release of energy by fluorescence can be understood by regarding the charge redistribution of the molecule as an oscillating dipole. An electron changes its energetic state and spatial distribution, which can be described analogously to absorption by an oscillation of the charge density. Oscillating dipoles always generate time dependent coupled electric and magnetic fields that are able to propagate through space. If the origin of the electromagnetic wave is far way from the observation point the respective waves can be described as plane waves. However, the electromagnetic fields generated by oscillating dipoles are

[2]The absorption coefficient is here defined as the amount of absorbed energy by a given amount of molecules and must not be confused with the extinction coefficient, which includes also scattering processes

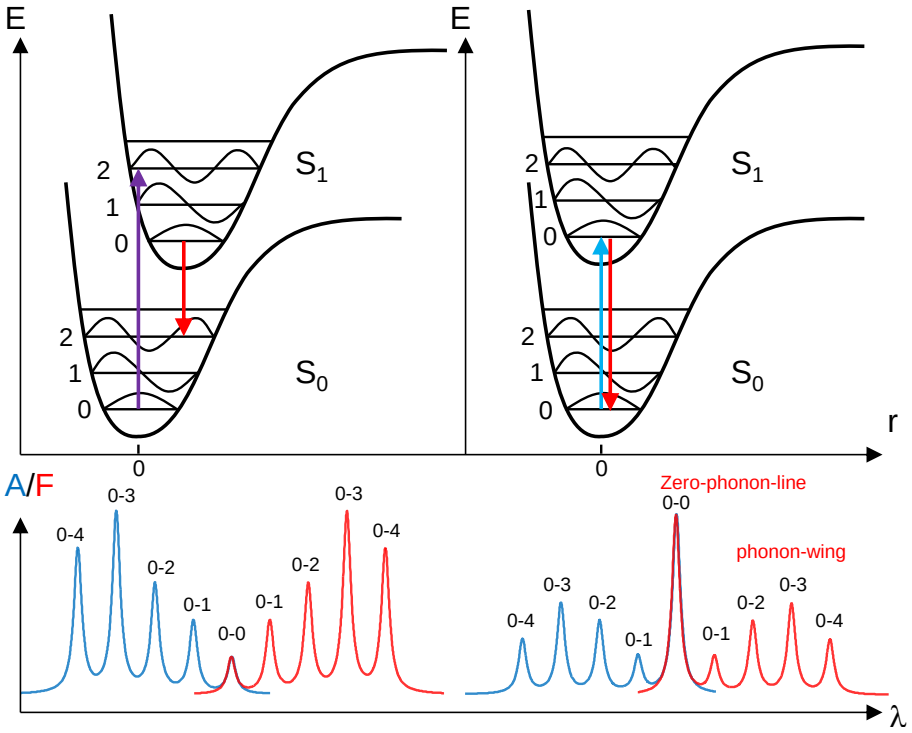

Figure 2.1: *Frank-Condon principle: Diagram of the electronic ground and first excited state of a two-atomic molecule behaving as an anharmonic oscillator. The diagram sketches the classical potential E of anharmonic oscillators as a function of core-core separation r together with the respective quantum mechanical solutions as distinct energy levels. The states of the electron in the HOMO denoted as S_0 and LUMO denoted as S_1 are determined by the vibronic structure of the molecule, which are the energies for a quantum system. An electronic transition (colored arrows) can be accompanied by the excitation of vibrations (left) or not (right) resulting in the observation of different intensities for certain transitions (bottom). For low electron-phonon coupling, the 0-0 transition is pronounced denoted in the spectrum as the zero-phonon-line (ZPL) which is accompanied by the phonon-wing (PW). The respective absorption spectra are indicated by the blue lines, while the emissions are represented by the red lines (dashed lines for broadenend peaks). The transition probability for both processes is given by the Frank-Condon-factor which is the overlap between the wave functions of the initial and target state. Each transition has to obey the Born-Oppenheimer approximation.*

also able to interact with the local environment of the molecule or with the molecule itself before the alternating fields can propagate to the far-field. This can cause a transfer of the field energy to the environment, which can convert this energy e.g. into phonons. A general approach to describe time dependent fields generated by point-sources is given

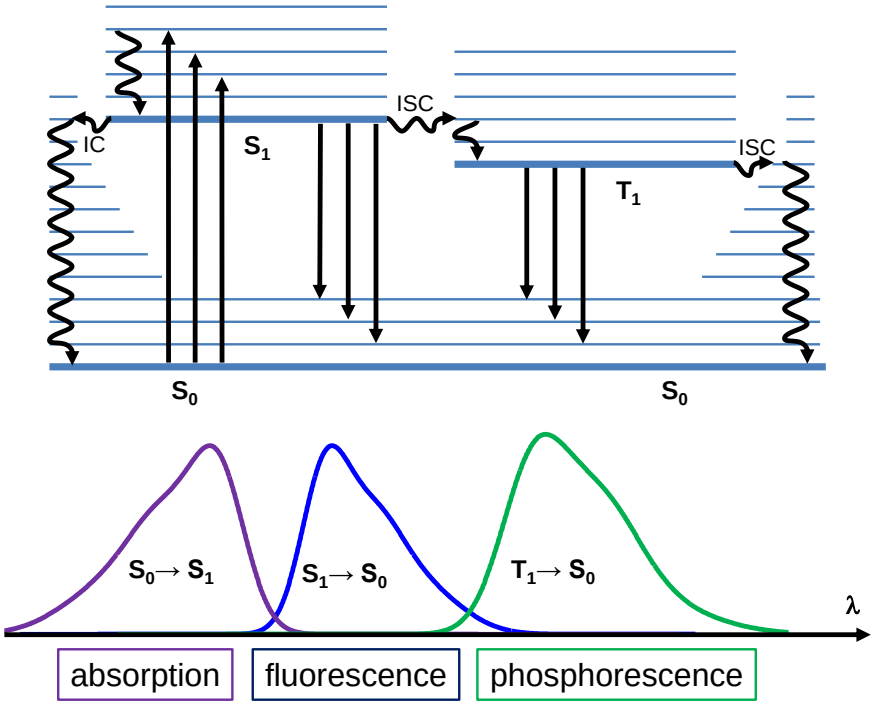

Figure 2.2: *Jablonski diagram: Diagram of possible transitions within e.g. an organic dye molecule with electronic and vibronic states. Radiative transitions are drawn as straight arrows while non-radiative transitions are displayed as curly arrows. The graph below shows the respective spectra for the radiative transitions including inhomogeneous broadening. The terms IC and ISC represent the processes internal conversion and intersystem crossing. The figure is adapted from ref.[1]*

by the formalism of Green's functions, which are solutions of inhomogeneous differential equations and hence can be adapted to the Maxwell equations[6]. In particular, the Green's function $\mathbf{G}$ of a certain problem can be used to describe the vector field of the (electric) fields as a function of dipole location $\mathbf{r}_0$ for each point in space $\mathbf{r}$. A convenient and simple way for describing the electromagnetic fields generated by a point-dipole in homogeneous space at any location either in close spatial proximity or far off can be done e.g. by using the formalism of Hertzian Dipoles[7]. In the following the magnetic parts of the time dependent fields are neglected due to their shift of 90 degree in the near-field of the dipole leading to an amplitude weaker than the electric field amplitude and due to the low magnitudes of the magnetic dipole moment and magnetic permeability of most substances. The electric fields in terms of the Green's function are given by[2]:

$$\mathbf{E}(\mathbf{r}) = \mathbf{E}_0 + i\omega^2 \mathbf{G}(\mathbf{r}, \mathbf{r}_0)\boldsymbol{\mu}, \tag{2.4}$$

whereby ω is the oscillation frequency and $\boldsymbol{\mu}$ is the dipole moment. In free (homogeneous) space and Cartesian coordinates the Green's function can be written as[2]:

$$\mathbf{G}(\mathbf{r},\mathbf{r}_0) = \frac{exp(ikR)}{4\pi R}[(1+\frac{ikR-1}{k^2R^2})\mathbf{I}+\frac{3-3ikR-k^2R^2}{k^2R^2}\frac{\mathbf{RR}}{R^2}], \tag{2.5}$$

with $\mathbf{R} = \mathbf{r} - \mathbf{r}_0$ and whereby $\mathbf{RR}$ is the outer product of $\mathbf{R}$, $\mathbf{I}$ is the unit dyad and k is the magnitude of wavevector $\mathbf{k}$, which can be given in terms of the wavelength ($\lambda = 2\pi/k$). In Figure 2.3 the magnitude of the (real valued) electric field of a radiating y-dipole are displayed as a 3D-slice diagram for the xy, xz and yz-plane. Another commonly

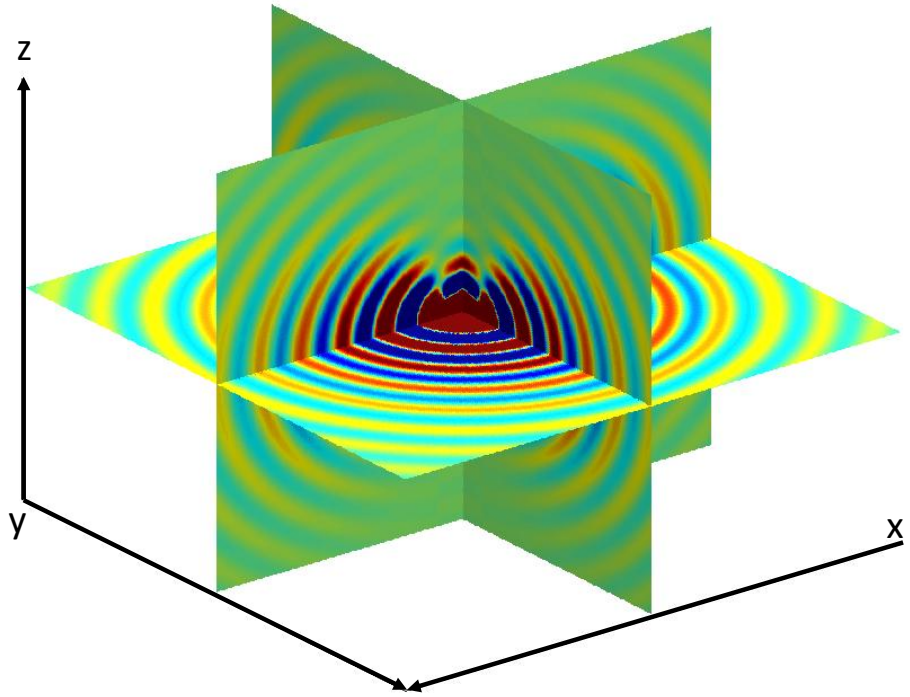

Figure 2.3: *Slice diagram of the radiation pattern of a point-dipole, calculated by Equation* (2.4) *and Equation* (2.5)*. Red color indicates (real valued) positive electric field magnitudes while blue colores represent (real valued) negative field magnitudes. The dipole orientation is set to be parallel to the y-axis.*

used formalism for describing the time dependent electric fields generated by a point-dipole is the Weyl representation[8, 9], which is useful for problems with cylindrical symmetry. The fields in homogeneous space with medium m can be written as the integral (superposition) over all (complex) k-vectors:

$$\mathbf{E}(\mathbf{r}) = \frac{1}{\varepsilon_m}\int \frac{d^3\mathbf{k}}{2\pi^2}[\mathbf{k}^2\boldsymbol{\mu} - \mathbf{k}(\mathbf{k}\cdot\boldsymbol{\mu})]\frac{exp(i\mathbf{k}\cdot\mathbf{R})}{k_m^2 - k^2}. \tag{2.6}$$

In this case, ε_m is the dielectric constant of the medium and $k_m = \sqrt{\varepsilon_m}\omega/c$, where c is the vacuum speed of light.

The Green's function of Equation (2.5) for a dipole contains terms with $(kR)^{-1}$, $(kR)^{-2}$, $(kR)^{-3}$ representing each a characteristic behavior of the electric field depending on the distance to the dipole. For large distances ($R >> \lambda$) to the dipole the -1 term dominates, which corresponds to the solution for a spherical wave. This regime is denoted as the *far-field* and the respective wave can be approximated by a superposition of traveling plane waves whereas geometrical optics can be used for describing their propagation. In the *near-field*[3] ($R < \lambda$) of the dipole, the electric fields are extremely inhomogeneous meaning that high field gradients can occur between closely separated volumes. Also, in the regime of small distances imaginary parts of elements of the electric field vector representing the damping of the amplitude must not be neglected because such fields are still able to transport energy and interact with the environment[2].

In quantum mechanics, fluorescence can be described as a spontaneous emission process of a photon using first order perturbation theory[10]. For a two-level system the emission rate of such a transition can be calculated from Fermi's golden rule[11]:

$$\Gamma_{spE} = \frac{2\pi}{h^2} |\langle \boldsymbol{\mu} \cdot \boldsymbol{E} \rangle|^2 \rho(\omega). \tag{2.7}$$

The term in the brakets denotes the matrix element of the perturbation between final and initial state, induced by the electric field $\boldsymbol{E}$ of e.g. an incident electromagnetic wave and the dipole operator $\boldsymbol{\mu}$. The second term represents the spatially and energetically distributed density of optical states, which means that the probability of emitting a fluorescence photon by a molecule is not determined purely intrinsically. In other words, the local density of optical states (LDOS) corresponds to the number of photonic modes per unit volume and frequency, into which a photon[4] can be emitted during spontaneous decay[2]. Using the wave image, it can be stated that for a low LDOS, the environmental effects cause that electromagnetic waves with certain properties interfere destructive with each other. If the LDOS is high the respective waves interfere constructive such that the LDOS is always a function of propagation direction and frequency of the waves. In other word, the LDOS can be used as a measure for the probability that an oscillating dipole is relaxing to the energy ground state by emitting a photon representing the propagating non-vanished electromagnetic wave to the far-field. This means that the LDOS of a given problem can be evaluated by several methods: by determining the damping of the electric fields via the imaginary parts of the Green's functions, by calculating the Poynting vector ($\vec{S} = \vec{E} \times \vec{B}$) for each propagation angle and wavelength of the electromagnetic fields or

[3] The definition of near- and far-field by the comparison between distance and wavelength is not convenient. Briefly spoken, the terms refer mainly to the two extreme cases of the behavior of the electric fields very close to the origin when the term R^{-3} dominates or very far away from the origin when the term R^{-1} dominates.

[4] A mode can be occupied by an infinite number of photons due to their bosonic nature.

by counting the number of possible modes for a certain geometry (see chapter 2.5). For the most simple case of homogeneous and isotropic space and after averaging over the dipole orientations the LDOS can be given by[2]:

$$\rho_0 = \frac{\omega_0^2}{\pi^2 c^3}. \tag{2.8}$$

According to the model that molecular dipoles can be regarded as damped oscillators, an emission spectrum is expected consisting of several Lorentzian shaped bands as shown in Figure 2.1 each with a full width at half maximum (FWHM) representing the respective homogeneous linewidth (natural broadening) of the transition, which is inversely proportional to the excited state life-time of the damped oscillator in Equation 2.7. However, at ambient conditions the width of a spectral band is additionally enlarged by inhomogeneous broadening[12] which is due to e.g. solvent effects and conformational fluctuations causing the (electronic and vibronic) energy levels to shift energetically in time leading to broadened spectral bands like those shown in Figure 2.2. Additionally, a realistic matrix contains most likely local inhomogeneities leading to an emission angle dependent spectrum. Thus, conventional spectroscopic investigations are not able to resolve the distinct electronic transitions due to the large inhomogeneous broadening, especially for experiments on the ensemble level, where the environment differs between the molecules and also for each molecule itself.

Working at cryogenic temperatures on the other side dramatically reduces the thermal motion of the molecules and their surrounding and can hence reduce line broadening, which is illustrated in the modeled emission spectra sketched in Figure 2.1. This is due to a reduction of coupling between phonons or vibrations and electronic transitions because at lower temperatures the thermal energy is insufficient to achieve a fully occupation of lattice vibration modes by phonons (=energy quanta of lattice vibrations) in the surrounding matrix and the molecule[13]. Thus, conformational changes of the molecule induced by phonons are less probable and occur within longer time scales so that the distinct molecular states can be spectrally observed. In general, the phenomenon of time dependent shifts of the spectral position of emission or absorption lines is denoted as spectral diffusion. The amount of occupied phonon-modes capable of coupling to an electronic transition also determines the ratio between the intensities of the 0-0 transition (zero-phonon line) and the transitions into higher vibronic levels of the ground state (phonon wing). This ratio can be empirically quantified by the Huang-Rhys factor S[14] and can be calculated by the spectral intensities of the zero-phonon line I_{ZPL} (ZPL) and the phonon wing I_{PW} (PW) by:

$$exp(-S) = \frac{I_{ZPL}}{I_{ZPL} + I_{PW}}. \tag{2.9}$$

Before the invention of single-molecule spectroscopy, experimentalists were able to gain spectral information on single molecules by the spectral hole-burning technique beyond inhomogeneous broadening. By narrow laser lines those certain molecules can be removed from an ensemble spectrum that can be promoted by the narrow excitation wavelength into a long-living (or permanent) dark state[15].

For describing the emission of a photon by a single molecule from the lowest vibronic level of the electronically excited state (like shown in Figure 2.2) in the time domain the following rate equation can be given:

$$\frac{dP_1(t)}{dt} = k_{exc}(t)P_0(t) - [\sum_{j=1} k_{rad_j}(\rho_o(\omega_j)) + k_{nrad}(\rho_T)]P_0(t). \tag{2.10}$$

Here, P_1 is the probability that the molecule occupies the ground level of the electronic excited state $n = 1$ whereby the relaxation rate from an intermediate higher vibronic state of the first excited state to the vibronic ground state is neglected due to its fast relaxation rate which is several order of magnitude faster than other relaxation rates[5]. For emitters with more than one radiative transition, the spontaneous emission rate k_{rad} as the complete radiative deactivation rate is described as the sum of the single rate constants k_{rad_j} for each radiative transition j. The total radiative decay rate is usually equal to Γ_{spE} and thus depending on the optical density of states $\rho_o(\omega_i)$. The rate constant for all non-radiative decay channels k_{nrad} accounts mainly to the phononic interactions with the environment depending on the phononic density of states ρ_T. Another simplification concerning the excitation rate $k_{exc}(t)$ is introduced by assuming an infinitesimal narrow excitation pulse in time and the molecule initially in the electronic ground state allowing us to define: $P_1(0) = 1$ and later $P_1(t) = 1 - P_0(t)$. Now, Equation (2.10) can be solved for the excited state population in time yielding a single exponential decay:

$$P_1(t) = exp[-(k_{rad} + k_{nrad}) \cdot t]. \tag{2.11}$$

Most commonly, the decay constant is expressed in terms of the excited state life-time defined as $\tau = 1/(k_{rad} + k_{nrad})$ and can be accessed by time domain measurements. The ratio between the rates of emission of a photon and the sum of all relaxation processes is defined as the fluorescence quantum yield:

$$Q = \frac{k_{rad}}{k_{rad} + k_{nrad}}. \tag{2.12}$$

However, this approach is only valid for simple systems like the one sketched in Figure 2.1. For complex systems Equation (2.10) has to be modified and multi-exponential decay behavior may be observed when relaxation occurs from different excited sub-levels e.g. due to a complex conformational behavior of the molecule or an amorphous surrounding matrix. This problem can be described by introducing the so-called energy landscape

or conformational space replacing the anharmonic potential in Figure 2.1. This concept is illustrated in Figure 2.4 by the example of different solvents surrounding a complex system such as the protein Photosystem I[16].

The optical response of nanoscopic objects on externally applied electromagnetic fields

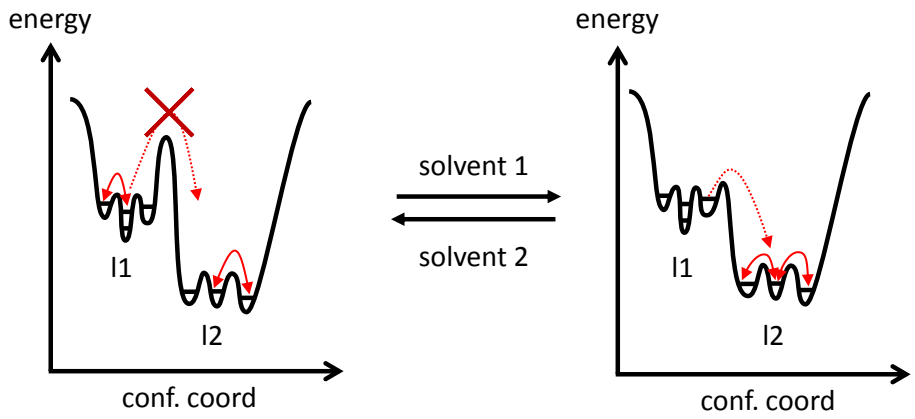

Figure 2.4: *Schematic illustration of the energy landscape of a complex macromolecular system such as PSI. In an initial condition (left) the transition between the sub-conformational tiers l1 and l2 is blocked. Changing the environment by replacing the surrounding matrix around the system can lower the barrier enabling transitions from l1 to l2. In comparison to Figure 2.1 the energy is here given as a function of conformational coordinates.*

can be categorized by both, the spectral distribution of absorption/emission and the relaxation dynamics in time, which are the main domains in nano- and quantum optics. As shown, these properties are not intrinsically determined by the nature of the quantum system, but rather by its interaction with the environment mainly by the photonic and phononic properties of the environment of the object. Thus, by observing spectral and time resolved information and for known influences of any extrinsic distortions, conclusions can be drawn e.g. about intra- and inter-molecular processes or vice versa how the environment must have been altered to achieve any desired observable effect on a known quantum system.

In chapter 6, a method is presented how the relaxation dynamics in the spectral and time domain for a fluorophore at the ensemble level and ambient conditions is described. This method bases on the possibility to alter the radiative decay rates of spectrally separated transitions by an altered photonic environment induced by a tunable Fabry-Pérot microresonator.

2.2 Förster resonance energy transfer

One prominent and often discussed process involving the relaxation and excitation of fluorophores is the Förster resonance energy transfer (FRET). The energy of an excited dipole can be transferred to a closely separated acceptor dipole by near-field dipole-dipole coupling, which was described in detail theoretically by Förster 1948[17]. The presence of an acceptor-dipole in close proximity to the donor-dipole means no homogeneous environment for both dipoles any more, requiring to adapt the formalism explained above. The probability of a successful energy transfer is depending on the spectral overlap $J(\lambda)$

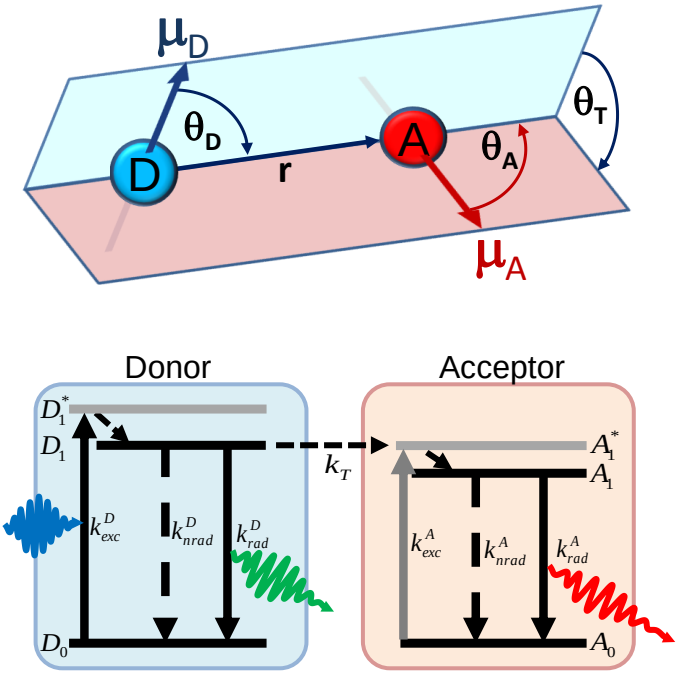

Figure 2.5: *Illustration of the orientation factor* κ *(top) and the FRET mechanism by an energy diagram (below). The donor-dipole (blue) is excited with* k^D_{exc} *(blue wave) to the intermediate state* D^*_1 *relaxing rapidly to* D_1*. Relaxation to the ground level* D_0 *can occur by fluorescence with* k^D_{rad} *(green wave), by non-radiative processes with* k^D_{nrad} *or by transferring the energy with* k_T *to a nearby acceptor (red), which can also relax radiatively (red wave) or non-radiatively.*

between the emission spectrum of the donor-chromophore $F_D(\lambda)$ and the absorption spectrum of the acceptor-chromophore given by the absorption coefficient $\varepsilon_A(\lambda)$, as this overlap is a measure of the coinciding eigenfrequencies of the respective dipole oscillations. The oscillation of the donor-dipole is generating an oscillating near-field at the location of the acceptor which is able to interact and couple to the acceptor-dipole that in turn can

start to oscillate with its distinct eigenfrequency. Due to the near-field nature of this effect, the distance r, the mutual orientation of the respective transition dipole moments given by the factor κ, the fluorescence quantum yield Q_D and the life-time τ_D of the donor's excited state, the refractive index of the medium between the chromophores n and the Avogadro constant N are the remaining parameters to describe the transfer rate constant k_T[17, 4]:

$$k_T = \frac{Q_D \kappa^2}{\tau_D r^6} \frac{9000(ln10)}{128\pi^5 N n^4} \int_0^\infty F_D(\lambda)\varepsilon_A(\lambda)\lambda^4 d\lambda. \tag{2.13}$$

The orientation factor κ^2 can be given by:

$$\kappa^2 = (cos\Theta_T - 3 \cdot cos\Theta_D \cdot cos\Theta_A)^2, \tag{2.14}$$

with the angle Θ_T between the transitions dipole moments μ_D and μ_A and the angles Θ_D and Θ_A describing the orientation of the transition dipole moments as sketched in Figure 2.5. FRET is commonly denoted as *weak coupling* meaning that the energy transfer is only one-directional and no energy level shift occurs. A purely phenomenological access to the dynamics of FRET can be reached in analogy to Equation (2.10) by describing the probabilities for the donor and acceptor to be in the excited or ground state by rate equations based on the term scheme in Figure 2.5 and by neglecting the populations of the intermediate states D_1^*,A_1^*:

$$\begin{aligned} \dot{D}_1(t) &= k^D_{\text{exc}}(t) D_0(t) - \left[k^D_{\text{rad}} + k^D_{\text{nrad}} + k_T A_0(t)\right] D_1(t)\,, \\ \dot{A}_1(t) &= \left[k^A_{\text{exc}}(t) + k_T D_1(t)\right] A_0(t) - \left[k^A_{\text{rad}} + k^A_{\text{nrad}}\right] A_1(t) \end{aligned} \tag{2.15}$$

Here, D_0, A_0 and D_1, A_1 denote the time dependent probabilities that the donor or acceptor are in their electronic ground (0) or excited state (1). The possible relaxation processes are quantified by the rate constants for radiative decay $k^{D,A}_{rad}$, non-radiative decay $k^{D,A}_{nrad}$, the transfer rate constant k_T and the excitation rates $k^{D,A}_{exc}$ by e.g. laser illumination which can be either time dependent (pulsed excitation) or time independent (continuous wave excitation). For a time independent illumination the equations can be solved analytically using the steady state approximation $\dot{D}_1 = \dot{A}_1 = 0$ (and in analogy to Equation (2.10) by $D_0(t) = 1 - D_1(t), A_0(t) = 1 - A_1(t)$):

$$D_1 = \frac{k^D_{exc}}{k^D_{exc} + k^D_{rad} + k^D_{nrad} + k_T(1 - A_1)}, \tag{2.16}$$

$$A_1 = \frac{k^A_{exc} + k_T D_1}{k^A_{exc} + k^A_{rad} + k^A_{nrad} + k_T D_1}. \tag{2.17}$$

The populations of the excited states D_1, A_1 are directly related to the corresponding fluorescence intensities of the donor and acceptor weighted by their fluorescence quantum

yield. In analogy to the fluorescence quantum yield the FRET-efficiency can be defined as:

$$E_{FRET} = \frac{k_T}{k_T + k_{rad} + k_{nrad}}. \tag{2.18}$$

For pulsed excitation the terms $k_{exc}^{D,A}(t)$ in Equations 2.15 have to be described with respect to the experimentally applied excitation source. To solve the differential equations for time depending populations numerical approaches can be used.

Although FRET is used for describing the energy transfer between two closely separated fluorescent molecules, the FRET formalism is often conveyed on energy transfer processes with comparable (near-field) mechanisms, which is a reason for its prominence[18, 19, 20]. An important application of FRET relies on the distance dependency by the r^{-6}-term allowing to experimentally access intermolecular distances obviously below the diffraction limit[21, 22]. FRET is therefore an often used technique for studying biological processes e.g. in living cells.

Since several years, an intensely discussed topic concerns the energy transfer process itself, especially, how FRET can be controlled. As we can see by Equation (2.15) a simple way to alter the efficiency of the transfer[5] is achieved by increasing (or decreasing) the excitation or relaxation rate constants of the chromophores leading to altered occupation probabilities of the excited/ground states of donor and acceptor. In chapter 7 and 8 this method is experimentally demonstrated and theoretically described for both, continuous wave and pulsed laser excitation of FRET-pairs, which are embedded in a photonic device ($\lambda/2$ Fabry-Pérot resonator) that mainly alters the radiative decay constants of the chromophores. A higher excitation rate for the donor causes an increased population probability of the donor and subsequently by FRET also for the acceptor. This can lead to the case when the acceptor is still excited when a re-excited donor is ready for starting the next FRET-cycle, which is suppressed by the excited acceptor.

However, the intrinsic properties of the dipole-dipole coupling given by the rate constant k_T are unaffected by this approach, which raises the question, how the near-field interaction between a donor and acceptor can be enhancement or suppressed directly. This consideration requires the evaluation of the electric fields generated by the donor dipole at the location of the acceptor dipole e.g. in terms of the Green's function. Hence, either the spectral properties of the chromophores have to be altered or an effective external distortion has to be introduced in order to change the effective fields at the location of the acceptor. One way to establish a controllable perturbation on the spectral proper-

[5] According to Equation (2.18) the FRET-efficiency is independent of the population dynamics. However, the phrase efficiency refers also to the observable fluorescence intensity ratios of donor and acceptor that very well depend on the population dynamics. Thus, Equation (2.18) has only experimental validity if the excitation power is infinitesimal low tending towards a single photon or for pulsed excitation.

ties of such systems can be achieved by applying external electric fields and using the Stark effect[23, 24]. Another perturbation affecting indirectly the spectral properties of the chromophores with respect to normal conditions can be introduced by cooling the FRET-system towards cryogenic temperatures. In this case, the crucial parameters describing the coupling in Equation (2.13) are the emission and absorption spectra of donor and acceptor which are broad bands at ambient conditions due to extremely fast spectral diffusion leading to a large spectral overlap. Reducing the temperature leads to a reduction of inhomogeneous broadening processes and a slowdown of spectral diffusion causing the spectral bands to become more narrow and thus, a reduced overlap between donor emission and acceptor absorption[25]. Nevertheless, the most effective approach to alter the dipole-dipole coupling is provided by a direct enhancement of the near-field at the location of the acceptor. It has been shown by several groups that plasmonic particles (see sections below) close to FRET-pairs are able to modify the dipole-dipole coupling by induced strong near-fields[26, 27, 28]. However, there has been a controversial debate since several years, how an altered LDOS is affecting the dipole-dipole coupling. A contribution to this debate is given in detail by the chapters 7 and 8. Here, the energy transfer dynamics are examined for FRET-pairs within a controlled photonic environment of a tunable $\lambda/2$-Fabry-Pérot micro-resonator.

2.3 Photosynthetic complexes

A prominent class of natural systems, for which the optical and the energetic behavior can be described by the FRET mechanism are photosynthetic complexes and light harvesting systems. These are macro-molecular systems which function as extremely efficient energy absorbers and converters, making them perfect model systems for future devices to generate energy from sunlight[29]. Over millions of year, within plants, algae and bacteria the internal and external arrangements of these systems were optimized for converting light into chemical energy. The oxygenic photosynthesis in plant cells is taking place at the thylakoid membrane between the chloroplast stroma and the thylakoid lumen. Beside other subunits in the membrane, the main photo-physics occur within the proteins Photosystems I (PSI) and II (PSII) where photons are absorbed, the respective energy transfered and converted. The reaction center in PSI catalyzes the electron transfer from the lumen to the stromal side of the membrane and is induced by light. PSII on the other side splits water also light-induced into protons and molecular oxygen. The structure and composition of these complexes that determine the functionality of the proteins differ slightly between the organisms in which they can be found. PSII within a large super-complex is forming dimers, whereby the respective monomer consists of 20 proteins binding 35 chlorophylls,

11 carotenoids, 14 lipids, 2 hemes, 1 non-heme iron and the Mn_4Ca cluster catalyzing the water oxidation[29]. The PSII core complex with the reaction center is surrounded by two proteins denoted as CP43 and CP47 working as antennas for absorbing the incident light[30]. The reaction center, denoted as P680, contains two chlorophyll dimers (P_{D1},P_{D2}) forming an excitonic dimer and absorbing at 680 nm[31]. In its oxidized state ($P680^+$) the reaction center has an estimated redox potential of 1.3 V[32]. The structure and appearance of PSI differs also for the respective photosynthesis running organisms. In general, the PSI complex forming monomers in plants and trimers in bacteria, is larger than the PSII complex and hosts 96 chlorophylls including the reaction center P700 (absorbing light at 700 nm)[33]. Like in PSII, the antenna complex surrounding the reaction center absorbs the energy of the incident photons which is transfered to P700.

The main interest in these two complexes arose since they have an extremely high quantum efficiency i.e. close to unity, which means that almost every absorbed photon generates a successful electron separation, and that PSII is the only natural biochemical system, which is able to split water. The extremely high transfer efficiency is supposed to be based on the specific arrangement of the Chlorophyll molecules. This idea is substantiated by the fact that disarranged Chlorophylls in solution show not even comparable efficiencies[34, 35]. Therefore, the single steps in the energy transfer chains, from the antennas to the reaction centers, are under special investigation since several decades. Beside the other subunits of PSI and PSII the Chlorophylls are the main transfer participants determining the energy transfer dynamics. They show absorption bands in the blue and red wavelength region as can be seen in Figure 2.6. The absorption of intact PSI (here from *Thermosynechococcus elongatus*) containing additional contributions by e.g. the carotenoids is shifted to red wavelengths with respect to bare Chlorophyll solution due to phononic interactions within the intact complex[35, 36]. One main feature of both photosystems beside their absorption, enabling optical experiments, is the fluorescence of individual Chlorophylls or Chlorophyll-pools whose optical properties correspond to their environment but also to their excitation and relaxation dynamics[37]. Spectroscopy of single complexes can be performed by reducing the temperature towards cryogenic conditions which leads to an increase of their fluorescence quantum yield. Also, the conformational changes in time are reduced sufficiently allowing to observe a single complex in a certain conformational state. Fluorescence measurements on photosystems reveal also spectral bands with wavelengths larger than the absorption wavelength of the corresponding reaction center[38, 39]. Such fluorescent chlorophyll compounds are thus thermodynamic traps especially at cryogenic temperatures for the excitation energy and allow us to directly observe individual steps within the energy transfer chain[40]. Such as the absorption, also the fluorescence spectra of PSI are strongly depending on temper-

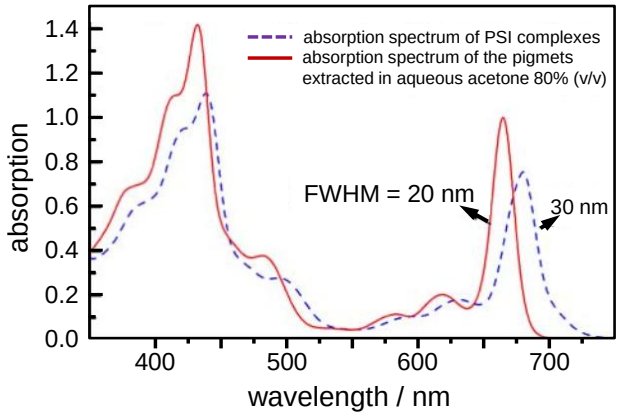

Figure 2.6: *Absorption of the extracted pigments from PSI in aqueous acetone (red lines) and the absorption of intact PSI complexes (violet dashed lines). The absorption in aqueous acetone is mainly determined by the Chlorophylls and the β-Carotenoids, adapted from ref.[35]*

ature, host organisms, surrounding matrix and the freezing conditions[41, 42, 43]. The main reason for such large spectral shifts between certain Chlorophylls is due to excitonic coupling between two or more specifically arranged chlorophyll molecules. The dipole-dipole coupling strength V, which is proportional to the rate of energy exchange, can be given by:

$$V_{AB} = \frac{1}{4\pi\varepsilon_0}\left[\frac{\hat{\mu}_A\hat{\mu}_B}{r^3} - 3\frac{(\hat{\mu}_A\hat{r}_{AB})(\hat{\mu}_B\hat{r}_{AB})}{r^5}\right]. \tag{2.19}$$

Here, $\hat{\mu}_{A,b}$ are the transition dipole moments of chlorophyll A and B and $\hat{r}_{AB}$ is the vector connecting the centers of A and B[44, 45]. As we will see in section 2.5, strongly coupled oscillators, such as transition dipoles, exhibit energy level splitting into a high and a low energy state which spectral separation depends on the coupling strength beside the phononic interaction to the environment. Obviously, some Chlorophyll-molecules are forming such excitonic dimers or trimers featuring lowered energies compared to the respective reaction center and representing traps for the absorbed energy, especially at cryogenic temperatures.

An issue widely discussed since several years is the question of how the energy transfer within photosynthetic complexes can be altered in a controlled way e.g. for examining the transfer pathways beyond the bare emission of the red-most-Chlorophylls and to understand why the related energy conversion exhibits such extremely high efficiencies. As indicated in the previous section, this can be achieved by combining PSI complexes with closely separated metal nanostructures[46, 47]. Another approach is presented in chap-

ter 11 whereas the fluorescence of PSI was examined embedded in a $\lambda/2$ Fabry-Pérot microresonator analogously to experiments on model FRET-pairs at ambient conditions.

2.4 Plasmonic particles

Beside organic molecular (quantum) systems metal nanoparticles are also able to interact with light in a comparable way, since they behave like antennas for light in the visible regime[48, 49]. A classical approach to describe the optical properties of such small metallic particles relies on combining Mie scattering theory[50] and the Drude model[51] for the dielectric properties of the particles since for describing their behavior quantum mechanics is not necessary. An incident electric field can spatially shift the conduction band electrons of the metal which can oscillate with respect to the frequency of an alternating electric field. This can be described by a polarization of the particle by the incident field[48]. However, the remaining inert positive charged ions of the crystal structure provide a restoring force for the electrons back to their initial spatial and energetic positions. If the frequency of the external driving field matches the eigenfrequency of this oscillation, the conduction band electrons are able to perform a coherent and resonant oscillation which is called a plasmon[6]. Thus, the excitation of this resonance frequency is crucially depending on the geometry and the dielectric properties of the particle, but also on the surrounding medium and the polarization and frequency of the incident field. This is schematically illustrated in Figure 2.7 for a rod shaped particle. The main dephasing mechanisms causing the decay of plasmons are scattering processes with other electrons, phonons, the surface and damping by radiation, each depending on a diverse set of parameters[52, 53, 54]. Therefore, the main problems of characterizing plasmon modes are the specification of the dielectric function of the metal in a medium and the oscillation behavior of the respective electrons within a certain volume i.e. their frequency depending polarizability[55, 56, 57, 48]. If the size of the particle is much smaller than the wavelength of the incident light, one can describe such localized plasmon oscillations by oscillating dipoles allowing to apply the formalism of Rayleigh scattering, in contrast to e.g. surface plasmons[58]. However, the optical properties of metals are even more complex. Although, even for particle sizes of few nanometers, one can describe them as condensed matter with certain bulk properties. According to the band structure of metals, absorption of light can also occur, which causes interband transitions of certain electrons leading to the generation of electron-hole pairs. They, in turn, can recombine either radiatively by emitting photons or non-radiatively by other relaxation channels involving

[6]This notation is analogous to phonons, which are the energy quanta of grid vibrations, and photons, which are quantified field oscillations. Plasmons are thus the quasi-particles describing the coherent oscillation of the conduction band electrons in metals and are the energy quanta of the plasma oscillation

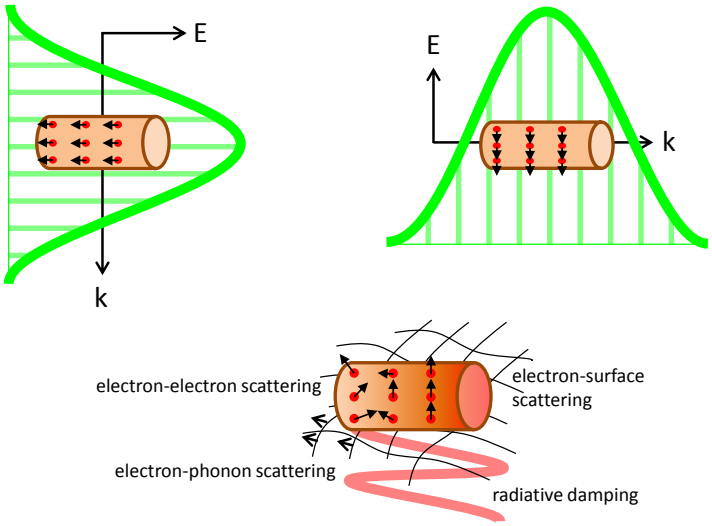

Figure 2.7: *Schematic illustration of the generation of longitudinal (upper left) and transversal (upper right) plasmon modes within a rod shaped nanoparticle by an incident electromagnetic wave (green) with different polarized field-vectors. For simplicity the size of the particle is displayed exaggerated, as compared to the wavelength of the electromagnetic field. The lower graph illustrates the main dephasing mechanisms leading to the decay of a plasmon oscillation, which are scattering of the conduction band electrons at the particle surface, with other electrons, with phonons or radiative damping[48, 49].*

e.g. the generation of phonons or plasmons[59]. Luminescence of metal surfaces[60] and nanoparticles[61, 62] can be observed when e.g. gold particles are excited with blue light but also with wavelengths close to the resonance frequencies of a plasmon mode. For rod shaped particles, luminescence spectra for three different excitation wavelengths and two different media are displayed in Figure 2.8. The short wavelength band around 520 nm corresponds to the plasmon mode for the short axis of the rod (transveral plasmon mode) while the long wavelength band corresponds to the long-axis plasmon mode (longitudinal plasmon mode) whereas the radiatively electron-hole-pair recombination is an underlying contribution[59]. The spectral position of the red wavelength band is mainly depending on the geometry and the dielectric function of the environment. This can be seen by the spectral difference of the red wavelength band for air and water as medium. Especially, the red wavelength band of the luminescence spectrum of such nanoparticles shows similarities to scattering spectra of the respective particle[63]. Most recent studies account this contribution to a radiatively decaying plasmon. This is indicated by the facts that the properties of luminescence spectra coincide mainly with white light scattering spectra. Both spectra show similar dependencies of the spectral position and FWHM-values of the respective bands on the geometry and size of the particle[61, 62, 64, 63].

The correlation between resonance energy and FWHM of a spectral band recorded by white light scattering is sketched for gold spheres and rods with different sizes in Figure 2.9. Rods with increasing aspect ratios show longer dephasing times and decreased resonance energies, while spheres in general exhibit faster dephasing times than rods. Thus, it can be claimed that the luminescence spectra of nanoparticles can be characterized by both, the plasmon mode resonances and the electron-hole pair excitation and recombination-dynamics[65, 59]. Presented spectroscopic measurements amended with simulations presented in chapter 12 of the long-wavelength luminescence band of gold nanorods at various temperatures are an additional indicator for the plasmonic origin of this luminescence band.

Nanoparticles are due to these properties often used tools for a variety of applications.

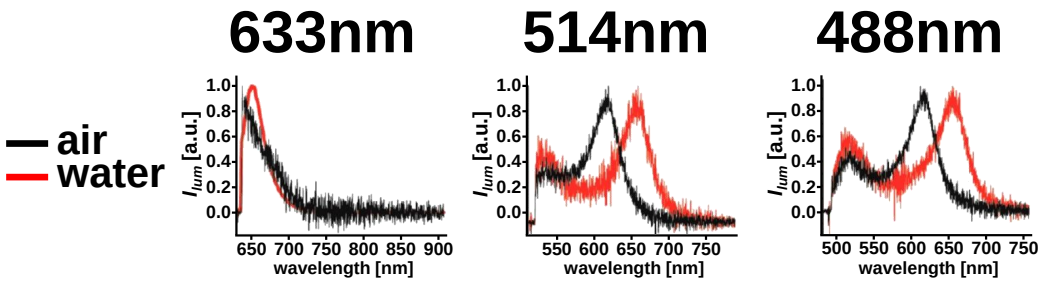

Figure 2.8: *Influence of the surrounding medium on the luminescence spectra of an individual gold nanorod excited with three different wavelengths probing the respective plasmon modes. The graph is adapted from ref.[66]*

The so-called antenna effect[67, 68] shall be mentioned in more detail, which is important for the further discussion. As explained above and in analogy to fluorophores, plasmonic particles are able to convert propagating optical fields into localized energy and vice versa by optical near-fields with an enhanced energy density[69]. A main difference to single quantum emitters is based on the possibility of generating extremely strong local electric fields around the particle, structure or surface, which effect can be easily explained by the large charge density oscillations associated with plasmons. These fields are specifically depending spatially and spectrally on the dielectric properties of the metal and the medium, but also on the size and shape of the particle or structure. As stated above, the optical properties of fluorescent molecules are crucially depending on the LDOS which makes metal nanoparticles and structures to powerful tools for enhancing the radiative or non-radiative relaxation processes of chromophores or energy transfer coupled systems such as FRET-pairs[70, 47, 71, 72, 73, 69]. A simple but commonly used hybrid model system is an emitting dipole localized above a metal surface[74, 9, 75]. In this case, the

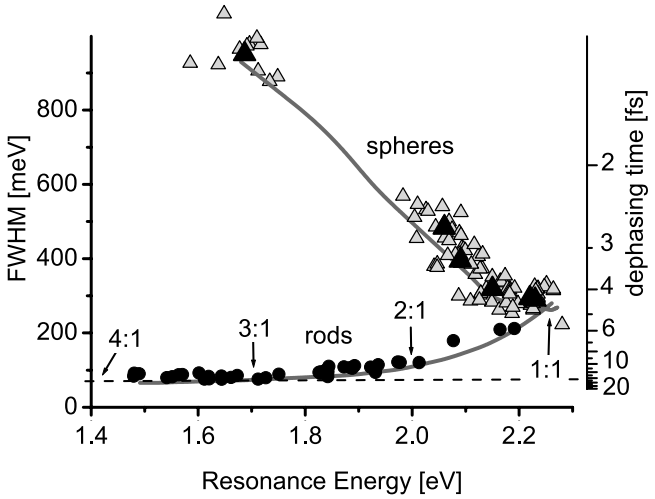

Figure 2.9: *Spectral linewidth of plasmon resonances (measured by light-scattering) of rod shaped and spherical gold nanoparticles with different aspect ratios and diameters as function of the resonance energy. The size for the spheres reduces from left to right (150, 100, 80, 60, 40, 20 nm). The lines represent theoretical calculations. The graph is adapted from ref.[52]*

LDOS influencing the emission properties of the dipole at the dipole's location is determined by both, the reflected light from the surface and the near-field generated by the plasmons, which are induced in the metal surface. For an arbitrarily shaped nanoparticle or structure in proximity to a randomly oriented dipole with arbitrary separations to the metal complex numerical calculations have to be performed to determine the quantitative influence on excitation, radiative and non-radiative relaxation[76].

2.5 Photonic devices

As introduced in the previous sections, hybrid systems of dipole emitters and metal nanoparticles can show completely altered spectral and temporal optical properties, which may be of high interest for engineers or experimental physicists as useful applications. An important issue in nano- and quantum optics is the question how the optical properties of sub-wavelength sized objects can be revealed, another issue how these properties can be controlled and used for further needs. Therefore, experimentalists developed a huge variety of devices, which either intervene the interplay of light and matter or make use of specific properties of matter to energetically, spatially and temporally tailor the properties of electromagnetic fields. In this thesis, all devices in which the properties of photons are

altered but not converted are denoted as photonic devices.[7] The most prominent combination of a photonic device with matter - i.e. the laser[77] - uses the process of stimulated emission for generating amplified coherent light of e.g. at specific wavelengths or pulse widths. As we have seen in the sections above, light emission of molecules and particles is always depending on the photonic environment, which can be modified e.g. by the surrounding dielectric material or by combining them with hybrid systems. However, the photonic mode density in Equation 2.7 can be controlled more directly by embedding the nano-object in a specific geometry, which is able to alter the LDOS. One type of devices can be categorized by its ability to enhance the near-field amplitudes of the electric fields in close proximity to the target object. An excellent example for this kind of device is realized by scanning-near field microscopy where a sharp tip with apex sizes of several nanometers is brought into close proximity to e.g. fluorescent molecules to directly interact with the near-field of the fluorophore[78, 79]. Another type is designed for enhancing the far-field amplitudes of the fields, which are in the regime of half a wavelength or larger and reach their maximum values at the location of the target. A prominent example for the second device can be found in micro-resonators allowing to control the energetic and spatial properties of enclosed electromagnetic fields by their geometry[8]. The main working principle of micro-resonators is based on the possibility to confine electromagnetic fields of decent frequencies inside a defined volume for a specific time and hence increase the photonic mode density[80]. The most simple geometry for such microresonators is the Fabry-Pérot design with two plane opposing mirrors of a certain separation ranging down to half a wavelength. One of the most important parameters characterizing such cavities is the Q-factor, which represents the degree of damping of the resonator. Regarding the fields confined in the (ideal) resonator as a damped Lorentzian oscillator the Q-factor can be described in terms of the time constant for the decay of the field energy stored in the cavity volume[81]. For resonators, the damping occurs by transmission of propagating waves due to a restricted reflectivity below unity and for realistic resonators also absorption of the field energy by the intra cavity medium or the materials of the cavity edges can occur. This behavior is illustrated in Figure 2.10 for ideal high (red) and low (blue) quality resonators. By Fourier Transformation the frequency spectrum can be determined consisting of a Lorentzian peak with resonance frequency ω_0 and the FWHM $\delta\omega$. The Q-factor is now given by:

$$Q = \omega_0/\delta\omega. \tag{2.20}$$

[7] According to this definition also simple and obviously trivial optical elements such as lenses, grids, mirrors or pinholes can also be denoted as photonic devices such as several hybrid systems.

[8] In this study, only resonators for the optical regime of light are discussed and used.

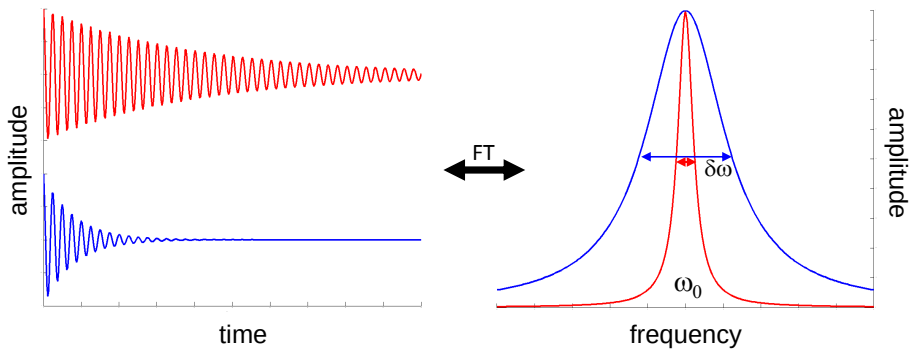

Figure 2.10: *Left: Simulated time decay of the electric field amplitude inside a resonator for high Q-factor (red) and low Q-factor(blue) with same frequency assuming a Lorentzian oscillation. Right: Fourier transformation leads to the frequency spectra whereby the high-Q resonator shows a reduced linewidth.*

Optically, the Q factor can be determined by measuring the transmission spectrum of a resonator by white light illumination whereas only those frequencies are transmitted, for which the energy density of the electric field at the resonance frequency is higher in the resonator than in the incident beam.
Understanding the interaction of electromagnetic fields and resonators can be achieved by regarding the optical fields in the cavity as standing waves that have to satisfy the Maxwell equations and the boundary conditions given by the geometry of the cavity. The respective photons and their density can also be described by oscillation modes, which are occupied by the photons[9]. Each mode can have its specified volume and energy density that correspond directly to the LDOS.
Thus, understanding the meaning of the LDOS is inevitable for the description of the impact of photonic devices on embedded matter and the illumination. For the most simple geometry such as the Fabry-Pérot resonator, the mode density can be determined by the basic assumption that only the magnitude of the z-component of the k-vector of a propagating wave has to be considered for the resonance condition (boundary condition). A photon can only enter the cavity if its corresponding electric field oscillation is able to establish a standing wave between the mirror surfaces and does not annihilate itself by destructive interference[10] Therefore, the LDOS is a measure for the probability that a photon

[9]The interaction of light with resonators is best understood using the wave image of light and describing a photon as the quantified energy of an electromagnetic wave, which are also the action quantum of the respective wave

[10]A wave generates spherical waves at boundaries such at the first mirror and are reflected at the second mirror. This causes interference between the waves, which can be constructive or destructive. Due to the law of conservation of energy a non-resonant wave is not annihilated by the resonator but reflected.

with specific frequency can exist in a specific (mode) volume[11]. This is also the reason why the process of spontaneous emission is not purely intrinsically determined. Photonic devices are - so to say - confined areas in which the probability density for energetically and spatially defined photons is enhanced or reduced with respect to free space. Thus, the LDOS can be formally given by the number density of optical modes with respect to energy dN/dE per volume unit V:

$$\rho = \frac{dN}{VdE}. \tag{2.21}$$

In Equation 2.8 the mode density for homogeneous isotropic space is given by: $\rho_0(\omega) = \frac{\omega^2}{\pi^2 c^3}$. In an ideal Fabry-Pérot resonator[82, 83], the LDOS is not isotropic and depends on the frequency and propagation direction of the photon with respect to the geometry. For electromagnetic waves obeying the resonance condition $|\vec{k}| = \pi/L$, the energy density dN/dE is proportional to the number of reflections of the photon between the two mirrors, and can thus be given in terms of the Q-factor (see Equation 2.20). The volume, which can be populated by (countably many) photons is called mode, according to the oscillation modes of the electromagnetic field. The volume V of the on-axis modes in a Fabry-Pérot resonator (k-vector perpendicular to mirror plane) can easily be given by the resonance condition for the first order interference ($L = \lambda/2$): $V = (\lambda/2)^3$, leading to the photonic mode density:

$$\rho_c(\omega) = \frac{2\omega^2}{\pi^2 c^3} Q.$$

By comparing the LDOS in a cavity and free space with respect to Fermi's Golden rule (see Equation 2.7), the well known Purcell factor[84] can be expressed by the ratio between the rate of spontaneous emission in free space Γ_{spE_0} and in the cavity Γ_{spE_c} and given by the wavelength λ within a material with refractive index n, the respective mode Volume V and the quality factor Q:

$$\frac{\Gamma_{spE_c}}{\Gamma_{spE_0}} = \frac{\rho_c}{\rho_0} = \frac{3}{4\pi^2}\left(\frac{\lambda}{n}\right)^3 \frac{Q}{V}. \tag{2.22}$$

For a realistic case where mirrors consist of metal films with complex dielectric functions and a certain thicknesses and where randomly oriented dipoles are located between those mirrors the effective LDOS has to be evaluated by the respective Green's function at the place of the emitter. We have seen that the photonic environment affects the spontaneous emission properties of enclosed emitters in the time and energy domain. This impact depends mainly on the quality of the cavity but also on the spectral and spatial distribution

[11] A photonic mode is thus comparable to atomic or molecular orbitals, which are spatial areas that can be occupied by an electron.

of the LDOS. As stated above, for a Fabry-Pérot resonator the quality factor as a measure for the damping of the cavity depends on the reflectivities of the mirrors, which are depending on the angle of incidence by the Fresnel-Equations, the wavelength and the effective length of the cavity (for a lossless intra-cavity medium). Using highly reflective mirrors e.g. with dielectric layers, Q-factors up to thousands can be reached with low mode volumes[80]. Another type of resonators exhibiting large Q-factors can be realized by the Whispering gallery geometry or photonic crystals. In reference [80] different kinds of resonators are presented with their mode volumes and Q-factors.

The change of the spontaneous emission process by coupling between the dipole and the cavity modes is denoted as weak coupling. In this coupling regime, the photon is emitted by the dipole into the cavity mode, which is an irreversible process. Increasing the coupling strength between the resonator and the embedded (quantum) object can lead to the strong coupling regime, which is a widely discussed topic in quantum optics due to additional effects on the spectral and temporal properties of the combined system. Understanding this interaction and its consequences can be done quantum mechanically but also classically. For describing the quantum mechanical problem one can regard in a first simplification the cavity as an external perturbation on an embedded two-level system. The system has the two eigenstates $|\phi_1\rangle$ and $|\phi_2\rangle$ of the Hamiltonian H_0 whose eigenvalues are the energies E_1 and E_2. The coupling or perturbation denoted by W (with $W_{12} = W_{21}^*$) has to be accounted by a new Hamiltonian H[85]:

$$\begin{aligned} H &= H_0 + W, \\ H &= \begin{pmatrix} E_1 + W_{11} & W_{12} \\ W_{21} & E_2 + W_{22} \end{pmatrix} \end{aligned} \tag{2.23}$$

This means that E_1 and E_2 are no longer eigenvalues (energies) of the two-level system within the coupled system and $\phi_{1,2}$ are no longer possible eigenstates. Solving Equation 2.23 yields the expressions for the new eigenvalues E_+ and E_- of the coupled system with Hamiltonian H and eigenstates ψ_+ and ψ_-:

$$\begin{aligned} E_+ &= \frac{1}{2}(E_1 + W_{11} + E_2 + W_{22}) + \frac{1}{2}\sqrt{(E_1 + W_{11} - E_2 - W_{22})^2 + 4|W_{12}|^2} \\ E_- &= \frac{1}{2}(E_1 + W_{11} + E_2 + W_{22}) - \frac{1}{2}\sqrt{(E_1 + W_{11} - E_2 - W_{22})^2 + 4|W_{12}|^2}. \end{aligned} \tag{2.24}$$

One has to keep in mind that the states with the states $\phi_{1,2}$ are stationary states for the unperturbed system. However, the introduction of W at a certain point of time has to induce a transition because $\phi_{1,2}$ are no longer possible eigenfunctions of the coupled system meaning that the time evolution of the system has to be considered. First, this formalism can be adapted for a cavity-atom-system by assigning one eigenstate to the cavity and the

second eigenstate to the atom assuming that only an excited cavity mode is able to interact with an atom in its excited state. In this simplification, we neglect e.g. a broadened energy continuum for possible eigenstates and assume further a large value of W with respect to the eigenvalues $E_{1,2}$. The atom in its excited state (at $t = 0$) and an excited cavity mode (at $t = 0$) can now dynamically exchange energy and both behave as one system with altered eigenstates and hence relaxation dynamics. The system consisting of the cavity mode and the excited level of the atom have their specific unperturbed decay rates γ_c and γ_a and an additionally rate of energy exchange given by the coupling rate constant κ. Due to the coupling between each subunit of the system to the environment, the phenomenologically observable strong coupling regime can only be reached if the coupling strength is much larger than the damping rates of the subunits.

However, strong coupling between two subsystems is not an exclusively quantum mechanical phenomenon and can also be described by classical equations of motions e.g. in acoustics, mechanics or electrodynamics. In a quantum mechanical approach the energies and the eigenstates of the coupled system are derived from the respective wave equations by means of the Schrödinger equation. In classical mechanics or electrodynamics the system is described by a coupled system of equations of motion, describing the dynamics of the perturbation. As a classical example one can consider two pendulums connected by a spring and observe that the system can exhibit a symmetric or anti-symmetric oscillation mode, with a high and a low energy. Modeling this behavior can be done by solving the differential equation for the amplitudes $x_{1,2}$ of both coupled pendulums:

$$m_1\ddot{x}_1(t) + 2\gamma_1\dot{x}_1(t) + k_1x_1(t) + \kappa(x_1(t) - x_2(t)) = 0, \tag{2.25}$$

$$m_2\ddot{x}_2(t) + 2\gamma_2\dot{x}_2(t) + k_2x_2(t) + \kappa(x_2(t) - x_1(t)) = 0. \tag{2.26}$$

$$\tag{2.27}$$

In this case, $m_{1,2}$ are the masses, $\gamma_{1,2}$ are the damping rate constants, $k_{1,2}$ are the spring constants determining the eigenfrequencies $\omega_{1,2}$ (by: $\omega_i = \sqrt{k_i/m_i}$), κ is the strength of the coupling spring and $x_{1,2}(t)$ are the time dependent amplitudes of the pendulums. These equations can be solved for the coupled eigenfrequencies if the intrinsic eigenfrequencies ω_i are much larger than the damping rates γ_i. Then, a complex frequency can be defined:

$$\widetilde{\omega}_i^{\,2} = \omega_i^2 - i\omega_i\gamma_i. \tag{2.28}$$

Now, the ansatz $x_i(t) = x_i^0 e^{-i\widetilde{\omega}_\pm t}$ is used including the frequencies $\widetilde{\omega}_\pm$ of the coupled system representing the two oscillation modes. The solutions can be given as:

$$\widetilde{\omega}_\pm^2 = \frac{1}{2}[\widetilde{\omega}_1^2 + \widetilde{\omega}_2^2 \pm \sqrt{(\widetilde{\omega}_1^2 - \widetilde{\omega}_2^2)^2 + 4g^2}], \tag{2.29}$$

where the parameter g is:

$$g = \sqrt{\kappa/m_1}\sqrt{\kappa/m_2}. \tag{2.30}$$

In general, every system of coupled Lorentzian oscillators such as pendulums or RLC circuits can be described by this equations by adapting the respective parameters to the problem.

The two sketched coupling regimes are in general sufficient to describe the impact of photonic devices on embedded nano-objects. The way, how the device is designed and the interaction occurs is always depending on the actual setup. Due to the huge variety of possible designs this thesis focuses on the simple geometry of the Fabry-Pérot resonators.

Chapter 3

Material and Methods

The previous section was dedicated to the description of the photo-physics of light-matter-interaction relevant to this thesis. The present section shall now investigate the same topic from the viewpoint of measuring, experimentally determining and analyzing the phenomena described above. In general, a simple optical setup e.g. a microscope consists of an excitation source, an optical path to guide the excitation radiation to the sample and finally an optical path to guide the response from the sample to the detectors, which analyze the detected signals with respect to the stated framework. To achieve the specific effects induced by external perturbations the experimentalist has always to consider additionally to extend the experimental setup in order to guaranty that in the best case only the alteration of a controllable set of intrinsic and extrinsic sample and environmental parameters occurs, which in reality is not always possible. In the following, the methods and techniques, which were used in this work to measure, control and evaluate the respective phenomena are sketched.

3.1 Confocal microscopy

First of all, each theoretical description in nano-optics starts by assuming e.g. a single molecule, atom or quantum object in a homogeneous environment interacting only with the incident light. This approach is often neglecting the experimental reality, which nevertheless is also a stimulus for the experimentalists to approximate and realize conditions to achieve such an idealized situation. Even if all the molecules of a macroscopic sample are intrinsically identical, they are always embedded in a different environment which furthermore is flexible over time mostly due to phononic interactions and can exhibit local inhomogeneities such that a single quantum object can sense many different environments at the same time. Thus, observing single and individual emitters over sufficiently short time scales in a most homogeneous matrix is essential for observing and characterizing the discussed effects. During the 20th century many developments within different technical branches allow one - at least since 1989 - to observe the fluorescence of a single

molecule[86, 87] which is nevertheless not a trivial task. First, in order to detect any fluorescence of a molecule one has to achieve that the specimen – exclusively – is absorbing a certain fraction of the incident light. After the invention of the laser[77] amended by further optical elements, enough photons of specific wavelengths, polarizations and phase can be generated and focused on a small volume to overcome the small absorption cross section of a single molecule. However, the single molecule has to be brought somehow into this volume exclusively. To focus a macroscopic laser beam of several millimeters in diameter to the unknown location of a nanoscopic single object, more advanced optical and electronic instruments have to be applied. A main restriction is the diffraction limit[88] preventing to project the power of a laser beam on an infinitesimally small spot by e.g. a lens. Due to the wave-nature of light the photons traveling towards the geometric focus point interfere with each other causing a characteristic intensity pattern with an intensity maximum at the location of the geometric focal spot but still with a finite diameter, which determines the resolution of the optical device i.e. a microscope. This causes that many photons with matching polarization and wavelength are not able to interact with the molecules absorption cross section and transition dipole moment, and that other molecules nearby may be also excited. Especially in the last decades many methods were developed to exhaust or overcome the diffraction limit. One basic method to increase the spatial resolution of a microscope consisting of optical elements to prepare and focus the laser beam on a sample containing the molecule, is confocal microscopy. Here, the sample is first illuminated by an objective lens with a high numerical aperture (NA) to achieve a small focal spot of the laser beam with diameters below a micrometer for the optical regime. The NA is defined as:

$$NA = n \cdot sin\alpha, \tag{3.1}$$

with n as the refractive index of the medium between the lens and the sample (whereas most objective lenses are corrected for a glass cover slip) and α as the largest angle which can be collected by the objective lens. According to wave-optics, a beam with a Gaussian intensity distribution exhibits a characteristic focal intensity distribution whereas the spot size depends on the NA of the optical device and the wavelength of light[89]. The lateral resolution of a microscope is therefore commonly given in terms of the full width at half maximum (FWHM) of the lateral (or axial) intensity cross section of the focal spot denoted as the point spread function (PSF). The most simple way to increase the resolution of a microscope at ambient conditions can be achieved by placing an immersion fluid with high refractive index between the objective lens and the first cover slide of the sample.[1]
To ensure that a molecule is located in the intensity maximum of the focal volume ei-

[1] Other techniques such as STED, STORM, PALM, etc. shall not be discussed in this thesis.

ther the laser beam can be spatially scanned or the sample over the fixed focal volume. Both scanning methods allow one to record location dependent images representing the detected photon intensity distributions. To improve the probability that only one molecule is located in the excitation volume, which is still larger than the molecule by at least two order of magnitude, the number of molecules in the sample volume has to be reduced. Nevertheless, one can not guarantee that exclusively one molecule within the complete sample volume is getting excited and emits fluorescence without more advanced techniques. Most commonly, the optical element focusing the laser on the molecule is also used for collecting the fluorescence, which is possible due to the coinciding locations of the excitation focus and the luminescence origin[2]. This method allows one to use only one objective lens, however, requires the spatial separation of laser light and fluorescence light, which can be achieved by implementing dichroic filters into the path of light reflecting the short wavelength laser light and transmitting the long wavelength fluorescence. The confocal principle also means that the image produced by the objective lens is not projected directly on a detector such as a camera but on a small pinhole, working as a spatial filter for nearly all photons, which are not originated out of the focal volume[3]. The photons passing the pinhole are now guided on the detectors, which can be a spectrograph with CCD-camera for recording spectral information of the fluorescence, or an avalanche photo-diode (APD) for acquiring spatially resolved intensity scan images or time resolved fluorescence decay curves. In Figure 3.1 the confocal microscopes used for acquiring the experimental results presented in this thesis are sketched.

The mechanical and electronic requirements for confocal microscopy depend on the investigated sample. If the sample promises a high amount of photons, which spectral distribution is narrow, commonly laser scanning is applied. Moving the focus over the sample is achieved by altering the entrance angle of the incident beam on the objective lens by a piezoelectric mirror and a telecentric system. This method is extremely fast and causes no vibrations to the spatially fixed sample. Nevertheless, the experimentalist using laser scanning has to accept the consequences of chromatic and spheric aberrations and a decreased effective NA. For less brighter samples such as singe molecules and for obtaining an improved image quality sample scanning is applied whereas the maximum NA and hence resolution can be reached.

Photodiodes exhibit high photon detection efficiencies for distinct broad wavelength regions and time resolutions below the nanosecond regime allowing to observe fluorescence

[2]The concept of coinciding locations of the focal volumes of the excitation and collection objective lens is the basic principle of confocal microscopy.

[3]The necessity to use pinholes is mainly due to the poor axial resolution of microscopes. For samples within thin films the pinhole can often be omitted, if the focal spot is sufficiently narrow. Also the pinhole can be omitted if the active area of the detector has the dimension of pinholes.

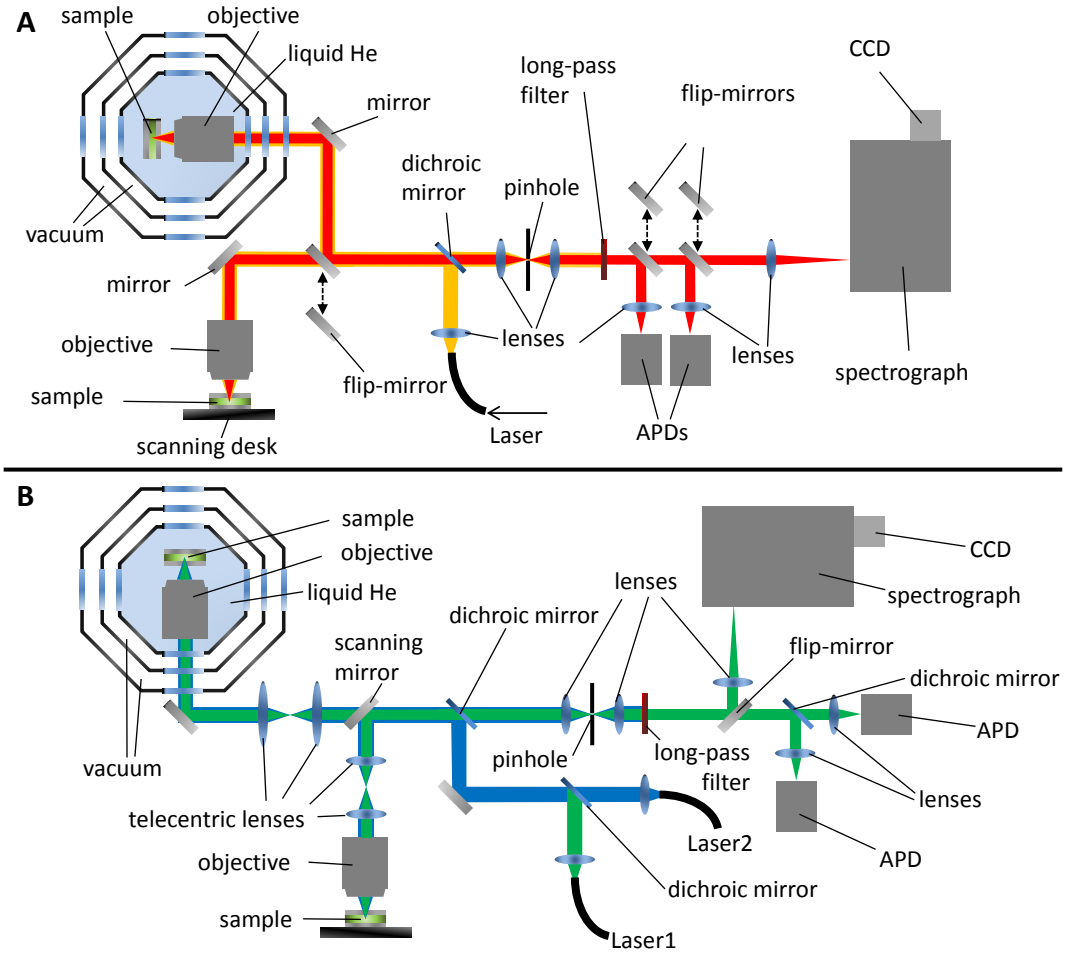

Figure 3.1: *Sketch of the used setups. A): The setup consists of two microscopes, one for low-temperature measurements and one for ambient conditions. Both are equipped with a scanning stage for sample scanning measurements including the microscope objectives (NA=0.8, 1.2) which are illuminated by the excitaiton source (665 nm). The detection path after passing the dicroic mirror and the pinhole for confocal microscopy and spectroscopy contains two APDs and one spectrograph with CCD-camera. B): The setup consists of two laser beams (488 nm and 532 nm) coupled into the excitation path. A scanning mirror and a telecentric system allows one to perform laser scanning of the sample inside a helium-bath cryostat. For ambient conditions the sample is mounted on a scanning stage allowing one to perform either beam or sample scanning with an objective lens with NA=1.46. The detection path contains two APDs and a spectrograph with CCD-camera.*

decay curves in combination with pulsed laser excitation. CCD-cameras on the other hand are designed for the respective requirements, either for spectroscopy or wide field imaging. Based on the confocal principle a microscope can be further extended by several features such as defined polarizations of the excitation by so-called doughnut modes al-

lowing to determine the orientation of dipole emitters[90, 91] or sharp metal tips for tip enhanced near-field microscopy[92].
While the spectroscopic characterization of fluorescence mainly depends on the detection efficiency of the camera and the resolution and reflectivity of the monochromator the time domain measurements host additional obstacles. Photodiodes using the avalanche effect exhibit a distribution of photon arrival times even for extremely narrow laser pulses in time. This leads to the observation of so-called instrument response functions (IRF) which represent the main restriction for a high time resolution[4]. In the ideal case, each photon arriving on the photodiode generates an electric signal, which can be registered by a suitable module in order to determine the arrival time of each detected photon either with respect to a synchronization pulse triggered by the laser emitting device or with respect to an absolute time scale. This technique, denoted as time correlated single photon counting (TCSPC) is a well established method for measuring fluorescence decay curves as function of time with typical time resolutions in the pico-second regime. To evaluate histograms of photon arrival times, the experimentalist needs to know the laser pulse width and repetition rate, the time resolution of the counter module and the IRF. The histogram with infinitesimal narrow time bins $I(t)$ of the recorded signal of a single fluorescent molecule obeying a mono-exponential decay behavior according to Equation (2.11) can be described by the convolution of a mono-exponential function with the IRF:

$$I(t) = I_0[exp(-\frac{1}{\tau}\cdot t) \otimes IRF(t)], \tag{3.2}$$

with I_0 as a scaling parameter, t as the infinitesimal narrow time channel and τ as the decay constant denoted as the excited state life-time of the molecule. For more complex systems compared to single molecules or for single molecules within an inhomogeneous environment, the decay laws have to be modified according to the expected relaxation dynamics e.g. poly-exponential decays. To overcome the restrictions set by the IRF e.g. pump-probe spectroscopy allows one to avoid the detection of the fluorescence in the time regime and is thus an often used technique for achieving a higher time resolution.

3.2 Low-temperature spectroscopy and microscopy

Confocal microscopy at ambient conditions still suffers the disadvantage that the experimentalist has to average the optical information of one molecule over the time of signal accumulation. However, some physical, inter- or intra-molecular processes are way faster than the acquisition time of the detectors, which has to be set long enough for acquiring spectra or decay curves with satisfying signal-to-noise ratios. This means that the observed object is able change its intrinsic properties such as conformation, structure or

geometry; but also the coupling to the extrinsic environment can change in time scales below the resolution of the acquisition cycle leading to a loss of information. The main reason for this time dependent behavior is due to the permanent coupling of the environment to the molecule mainly by phonons, which cause additional channels for energy entering or leaving the molecule and can catalyze the mentioned processes. To minimize these effects the amount of thermal energy by phonons and conformational fluctuations can be reduced e.g. by reducing the temperature and embedding the molecule in an immobilizing polymer[93, 94]. At ambient conditions a polymer matrix is able to reduce e.g. translation of the molecules and formation of flexible solvation shells but can enhance the phononic coupling to the rigid amorphous matrix and can cause hence local inhomogeneities around the single quantum objects. However, minimizing vibrations, rotations and comparable processes is only possible by cooling the sample towards zero Kelvin. Nevertheless, the dielectric, photonic and phononic properties of the surrounding matrix stay crucial parameters for the optical properties of the investigated specimens. Working at liquid helium temperatures (<4.2 K) allows the experimentalist to minimize the phononic coupling to the environment and the intrinsic vibronic dynamics. This allows one to prepare and freeze a sample in a certain condition and perform microscopy and spectroscopy. A second advantage of spectroscopy at cryogenic temperatures is a direct consequence of a reduced phononic coupling to electronic transitions. According to the definition of the fluorescence quantum yield the non-radiative relaxation rate can be reduced by decreasing its phononic contribution, which can be approximated by calculating the vibronic mode density[95, 96]. As described above, the fluorescence of most single molecules at low temperatures shows several features such as zero-phonon-lines (ZPL) and corresponding phonon-wings (PW) allowing one to determine the strength of electron-phonon coupling. Another observable temperature dependent phenomenon enabling the observation of ZPLs at all is spectral diffusion, which is generally better resolvable at cryogenic conditions for comparable host matrices due to slower diffusion rates[4] The thermal induced spectral diffusion effect is caused by conformational or structural changes in the sample or the surrounding solvat shell. At cryogenic temperatures the diffusion rates are often slow enough to detect spectral shifts of the fluorescence signal. These two effects dominating single molecule spectra at liquid helium temperature give some indication on the intrinsic energy landscape of the examined system but also on the

[4]The correlation between temperature and spectral diffusion rate is only valid for thermal induced changes in the conformational landscape of the environment and the specimens. However, there are other mechanisms responsible for comparable observations of jumping spectral lines or bands such as local inhomogeneities, concurring radiative processes, a complex relaxation dynamic by e.g. energy transfer processes or other external photo-induced processes. Also, the influence of the structure of the host matrix has to be regarded as well as the temperature influence.

interaction of the object with the surrounding matrix[13].
For biophysicists experiments at such low temperatures are of great interest especially for investigating complex molecules or molecule compounds such as proteins or photosynthetic complexes whereas e.g. nano- and quantum-optic physicists investigate fundamental optical processes in metal particles, structures, semiconductors or single atoms. At ambient conditions, biochemical systems exhibit mainly weak fluorescence (in their native condition and with exception of the class of auto-fluorescent proteins) and can be hardly investigated on the single molecule/complex level. At cryogenic temperatures, the combination of confocal microscopy and spectroscopy is therefore a powerful tool to investigate e.g. fundamental photo-physics of complex biological systems, in order to acquire insights on the functionality of the system. Nevertheless, combining microscopy with cryogenic temperatures, which can be achieved by a helium-bath cryostat such as the one sketched in Figure 3.2, causes several problems that can reduce the quality of confocally recorded scan images. The main reasons for a reduced resolution compared to microscopes working at ambient temperatures are mainly due to technical restrictions and temperature gradients[97]. First, high numerical aperture optics cannot be used until today at low temperatures due to extreme thermal stress on the optical elements and the respective mounts of objective lenses. Second, the usage of immersion oils is hampered by their high freezing temperatures and requires the positioning of the objective lens outside the cryogenic chamber, which on the other side requires objectives with large working distances, which additionally cause temperature gradients and mechanical instabilities[98]. Third, the recording principle of confocal images by sample scanning requires a scanning stage inside the cryogenic chamber whereas only since few years piezoelectric scanners can be produced, which are able to move reproducibly below 4 K. Beam scanning of the objective placed inside the cryogenic chamber implies, however, spherical and chromatic aberrations as well as a reduction of the effective NA. Another obstacle is the transfer of the sample into the cryogenic environment, which can be overcome either by movable elements inside the cryostat or by cooling the previously mounted sample inside the cryostat from ambient condition to the desired temperature. The second approach is often problematic for certain samples, especially for biological samples which can change their intrinsic properties uncontrollably during the cooling procedure or getting damaged. The imaging of unprepared cells at cryogenic temperatures is thus a problematic task due to crystallization of intracellular water. To guarantee a sparing freezing procedure of cells ultra-fast freezing techniques such as plunge-freezing can be used, which apply e.g. liquid propane for freezing the sample and is commonly used for cryo-electron microscopy[99, 97]. The combination of electron and light microscopy, called correlative microscopy, is an intensively used method at ambient conditions for accessing structural

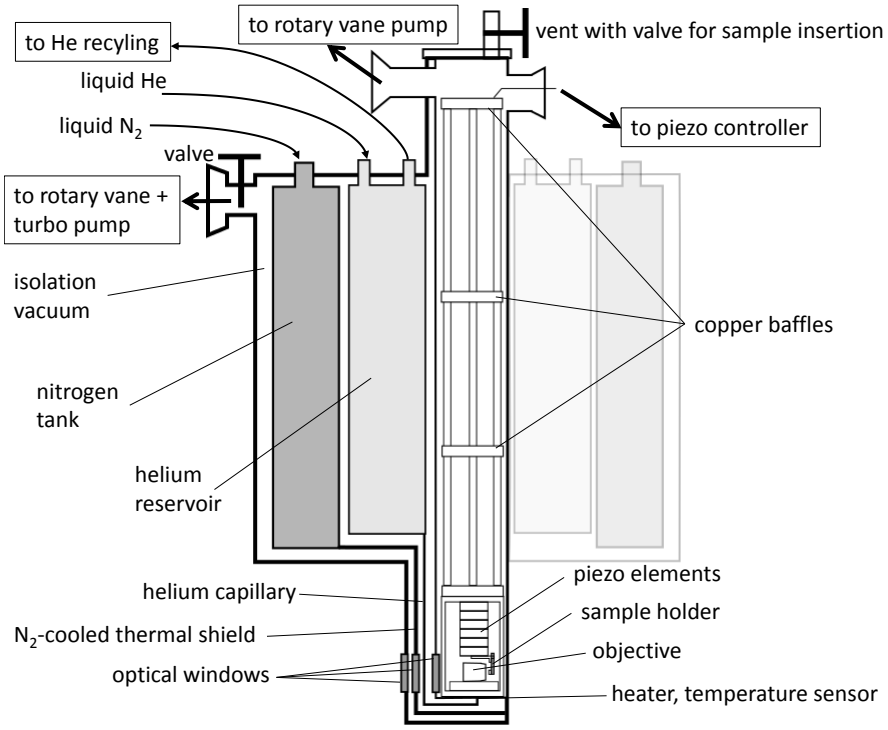

Figure 3.2: *Sketch of the Helium-bath cryostat. The outer most layer is the isolation vacuum with a pressure of 1e-5 mbar achieved a rotary vane and turbo pump. The second layer is the nitrogen tank for pre-cooling and providing an additional isolation (thermal shield) for the following helium tank. The third layer is the helium tank which is connected to inner most tube (sample area) by a small capillary with a needle valve. Inside the inner tube, the sample head is inserted with long polymer rods and several copper baffles for isolation. On top, there are two vents for connecting a rotary vane pump for reducing the pressure inside the sample area and for leading out the cables for controlling the piezoelectric elements of the scanning stage. Reducing the pressure in the sample area by pumping leads to a further reduction of the temperature in the sample area when filled with liquid helium. If the temperature is further decreased below 2.2 K the liquid helium becomes superfluid.*

and functional information of biological samples[100]. Therefore, since several years one main task in the field of microscopy is the realization of correlative microscopes for cryogenic temperatures[101]. In chapter 4 a new microscope prototype is presented enabling to solve some severe problems in low-temperature microscopy and spectroscopy. By this setup, we are able to insert frozen or vitrified samples into the pre-cooled cryostat and load a sample scanning stage in order to perform sample scanning microscopy down to 1.6 K. Based on this microscope a technique is introduced in chapter 5, which enables one to enhance the resolution of the microscope for cryogenic temperatures. The scanning stage

and the insertion mechanism allows us to load the stage with the sample together with a frozen droplet of an immersion fluid that can be warmed up over its melting point in order to immerse the volume between the microscope objective and the glass cover slip of the sample.

3.3 Fabry-Pérot $\lambda/2$-Micro-resonators

As described in the section on photonic devices, resonators for enclosing light in the optical regime can be used to alter the optical properties of embedded particles or molecules by a modified photonic environment. The most simple experimentally realizable class of resonators is the Fabry-Pérot geometry exhibiting certain advantages with respect to other resonator designs outlined in ref.[80]. Fabry-Pérot resonators are easy to produce since only two reflective layers as substrates are required that have to be plane and parallel at least in the microscopic view. The geometry of the resulting cavity is hence simple and easy to describe and characterizing the optical properties of such resonators can be achieved by illuminating the resonator with white light to observe the transmission pattern. The technical realization of a Fabry-Pérot for visible light in the $\lambda/2$ regime can be achieved by combining two silver coated glass cover slips. The $\lambda/2$ regime is reached by applying pressure on the middle of the slips and observing the transmission of the resonator by white light illumination. If the force is applied normal to the surfaces on a small spot the separation between the mirror layers can be decreased and controlled by observing the emergence of Newton Rings. When the silver surfaces reach a separation smaller than half a wavelength of the visible light, no rings emerge any more and the center of the rings stays black. To keep the mirror separation fixed either optical glue for ambient condition experiments or water/glycerol for cryogenic measurements can be used as intra cavity medium. The knowledge of the transmitted wavelength for a specific mirror separation is a requirement for determining the effective LDOS. Light regarded as electromagnetic waves can travel through (loss-less) media and interfere constructive or destructive with other traveling waves. They can also be refracted, scattered, absorbed or reflected at boundary surfaces depending on the dielectric function of the respective material, the angle of incidence and the polarization of the wave with respect to the plane of incidence. The behavior of electromagnetic waves for these processes can be described by the dielectric function of the passed materials, the Maxwell and Fresnel equations[102]. In general, if a Fabry-Pérot resonator with a mirror separation in the $\lambda/2$ region is illuminated with polychromatic light normal to the mirror surface, a photon can only exist in the cavity if its corresponding electromagnetic fields can exhibit a standing wave between the mirror surfaces. In an ideal resonator with infinitesimal thin and parallel mirror lay-

ers featuring a perfect reflectivity and for normal incidence neglecting phase changes the resonance condition is simply:

$$L = \lambda_0/2, \tag{3.3}$$

where L is the effective cavity length and λ_0 the wavelength of the photon passing the resonator, representing the on-axis mode (perpendicular to mirror surfaces) of the cavity. As sketched in Figure 2.10, the time dependent field amplitude in the resonator can be described by a Lorentzian lineshape in the frequency domain allowing one to observe a characteristic transmission spectrum with a spectral maximum at λ_0 and a FWHM corresponding to the Q-factor of the resonator ($Q = \lambda_0/FWHM$). To describe also the off-axis modes resonant in the cavity volume, a broad band emitter with isotropically distributed luminescence is placed in the center of the cavity. Thus, the resonance condition has to be defined in terms of the k-vector of the emitted electromagnetic wave with the wavelength λ and having the angle θ between its propagation direction and the cavity axis. This yields the following expressions:

$$k = \sqrt{k_x^2 + k_y^2 + k_z^2}, \tag{3.4}$$

$$k = \frac{k_z}{cos\theta}, \tag{3.5}$$

$$k = 2\pi/\lambda. \tag{3.6}$$

Here, $k_{x,y,z}$ are the components of the k-vector following the nomenclature of Figure 3.3 which can have complex values. The resonance condition is fulfilled if the z-component of $\mathbf{k}$ is fitting into the cavity:

$$k_z = m\frac{\pi}{L}, \tag{3.7}$$

whereby m denoted the number of interference, which is unity for a $\lambda/2$-resonator. For a certain length L and an enclosed photon with wavelength λ, the angle of emission (corresponding to $k_{x,y}$) is determined. This leads to the observation that the emission of a dipole can couple also to the angular distributed modes with wavelengths $\lambda_\theta \leq \lambda_0$ as sketched in Figure 3.3. Therefore, shorter wavelengths than the on-axis transmission wavelength λ_0 can be emitted by a luminescent object. As we have seen already, the emission properties of a dipole-emitter are depending on the photonic environment, which can be described either by the LDOS or by the electric field operator (see Fermi's Golden rule). Assuming a cavity with loss-less mirror materials and an isotropic radiating emitter oriented parallel to the y-axis with distance z_0 to the first mirror and an infinitesimal narrow emission spectrum, the in-plane electric fields can be calculated for each angle of emission θ and both polarization (S and P) with respect to the mirror surfaces and each

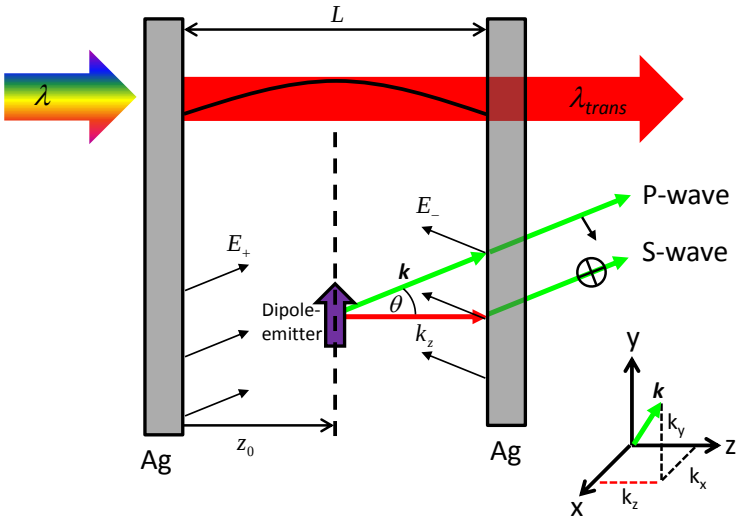

Figure 3.3: *Illustration of the resonance condition of a Fabry-Pérot resonator with two silver mirrors and their separation L. White light illumination (colored arrow) is able to excite only on-axis modes with* $\lambda_{trans} = 2L$*. The radiation of a dipole emitter (violet arrow) in the center at* $z_0 = L/2$ *can also couple to angular distributed modes. The effective fields inside the cavity can be described by calculating the interference of the traveling fields* E_- *and* E_+ *for P oder S-waves and the angle* θ *of the k-vector with respect to the z-axis.*

emission wavelength given by the k-vector[103]:

$$E^2_{S,||} = \frac{(1-r_{2,S})(1+r_{1,S}-2\sqrt{r_{1,S}}\,\cos(2kz_0\cos\theta)}{(1-\sqrt{r_{1,S}r_{2,S}})^2+4\sqrt{r_{1,S}r_{2,S}}\,\sin^2(kL\cos\theta)}|E_0^2|, \tag{3.8}$$

$$E^2_{P,||} = \frac{(1-r_{2,P})(1+r_{1,P}-2\sqrt{r_{1,P}}\,\cos(2kz_0\cos\theta)\cos^2\theta}{(1-\sqrt{r_{1,P}r_{2,P}})^2+4\sqrt{r_{1,P}r_{2,P}}\sin^2(kL\cos\theta)}|E_0^2|. \tag{3.9}$$

Here, $r_{i,P/S}$ denotes the reflectivity of the respective mirror for the polarization P or S, L is the effective cavity length and E_0 the initial field magnitude. To get the altered spontaneous emission rate of the dipole emitter, the field has to be integrated over all angles and respective wavelengths, averaged for both polarizations and combined with Fermi's Golden rule. For this ideal case the emission rate can be given by the integral over all angles and averaged over the polarizations[103, 104]:

$$\Gamma_{spE_c}(L) = \frac{3\Gamma_{spE_0}}{4}\int_0^{\pi/2} d\theta\sin\theta$$
$$\times\frac{(1-r_{2,S/P})[1+r_{1,S/P}-2\sqrt{r_{1,S/P}}\,\cos(2kz_0\cos\theta)][1+\cos^2\theta]}{(1-\sqrt{r_{1,S/P}r_{2,S/P}})^2+4\sqrt{r_{1,S/P}r_{2,S/P}}\,\sin^2(kL\cos\theta)}. \tag{3.10}$$

The pre-factor $3/4$ arises from constant factors and the integration over the half sphere. As a consequence, we can calculate the mode spectrum for each mirror separation, which

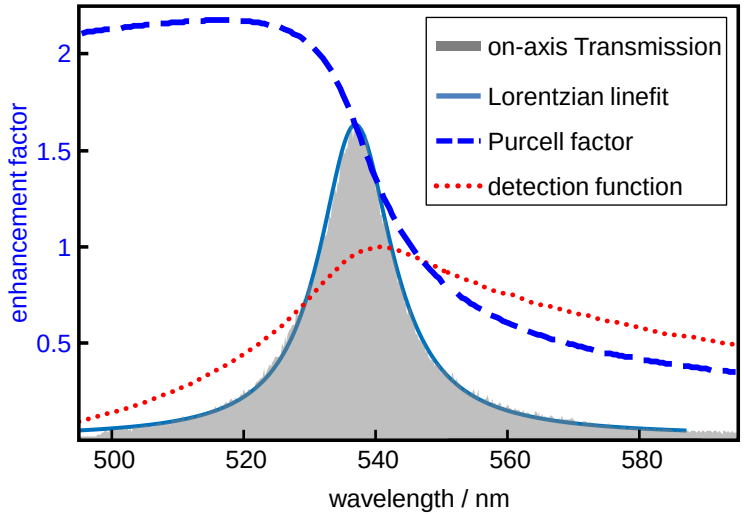

Figure 3.4: *Calculated mode spectrum (blue dashed line) of a Fabry-Pérot resonator in the $\lambda/2$-regime by integrating the electric fields given by Equation* (3.9) *over all real angles θ for a certain cavity length represented by a measured on-axis transmission spectrum (gray area) by white light illumination. Due to the limited collection angle of the objective lens (NA=1.46) the sensitivity function (red dots) is additionally required for describing the emission spectra of an embedded dipole. The mirrors of the resonator have the reflectivities of 0.95 and 0.9, respectively.*

can be given in terms of the on-axis transmission wavelength λ_0. The mode spectrum represents the wavelength dependent Purcell factor (see equation 2.22). A second consequence of the Fabry-Pérot geometry is the angular dependency of the radiated wavelength, which yields a spectral shape of the emission depending on the NA of the microscope objective due to its limited collection angle α. In Figure 3.4 the gray area represents a transmission spectrum of a resonator in the $\lambda/2$ region recorded by white light illumination. The Purcell factor for the respective resonator (with reflectivity of the mirrors being 0.95 and 0.9 and an emitter in the center of the cavity) is drawn as blue dashed line. The detection function for the objective lens with NA=1.46 is represented by the red dashed line.

When an emitter (here the organic dye Atto488) is placed halfway between the mirrors, the emission spectrum is shaped by the two effects of the resonator and is drawn in Figure 3.5 as red line. The same emitter in free space has an obviously different fluorescence spectrum represented by the black line recorded by the same experimental conditions (excited with 488 nm) in free space. As expected, the red wavelength flank of the free space spectrum is suppressed, while wavelengths close to the transmission maximum show enhanced intensity with respect to free space.

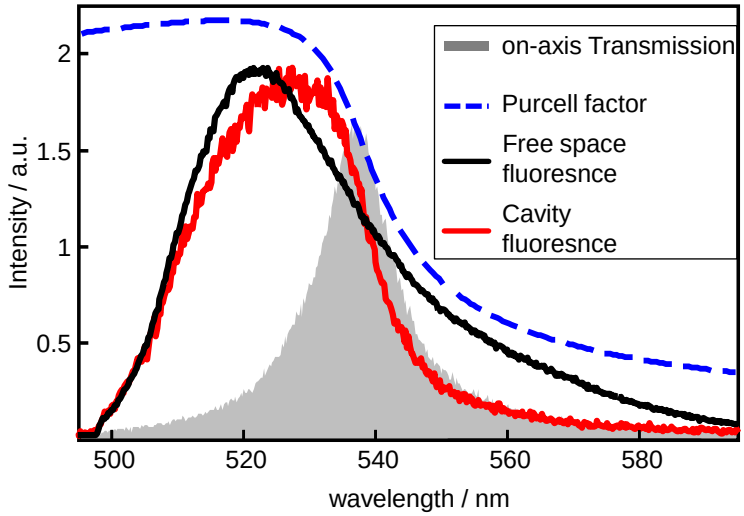

Figure 3.5: *Fluorescence spectra of the organic dye Atto488 in free space (black curve) and embedded in a microresonator (red curve), which exhibits a certain white light transmission spectrum (gray area). The cavity modified spectrum can be described by the impact of the wavelength dependent Purcell factor (blue dashed line) weighted by the angular sensitivity function. The dye molecules were excited with 488 nm.*

While the equations above neglect some aspects of reflected waves at surfaces, the real cavity length can be calculated by including the refractive index of the intra-cavity medium and the phase changes of waves at boundary surfaces reducing the effective cavity length[105]:

$$L = \left(m - \frac{\sum_{i=1} \Delta\phi_i(d_i, \theta, \lambda)}{2\pi} \right) \frac{\lambda}{2n\cos\theta}, \tag{3.11}$$

with n as the refractive index of the intra-cavity medium, θ as the angle of the incident light, ϕ_i as the phase change of waves at boundary surface i, d_i as the thickness of the respective silver mirror and m as the interference order.

A Fabry-Pérot micro-resonator, which allows tuning the mirror separations during the experiment with nanometer precision can be constructed by keeping one mirror fixed (e.g. by gluing on a mount) and moving the second mirror by piezoelectric stacks with respect to the other. A silver coated convex lens is used as a second mirror facilitating the localization and adjustment of the Newton Rings and the $\lambda/2$ region. For this thesis, two different designs were realized for implementing the resonator in an inverted and non-inverted microscope as displayed in Figure 3.6. To ensure chemical and mechanical stability of the mirror layers, the silver films were coated by electron beam evaporation on a thin layer of chromium (1 nm) and afterwards covered by a thin layer of gold (1 nm) and SiO_2 (60-100 nm). The medium for the intracavity space was chosen to be water as

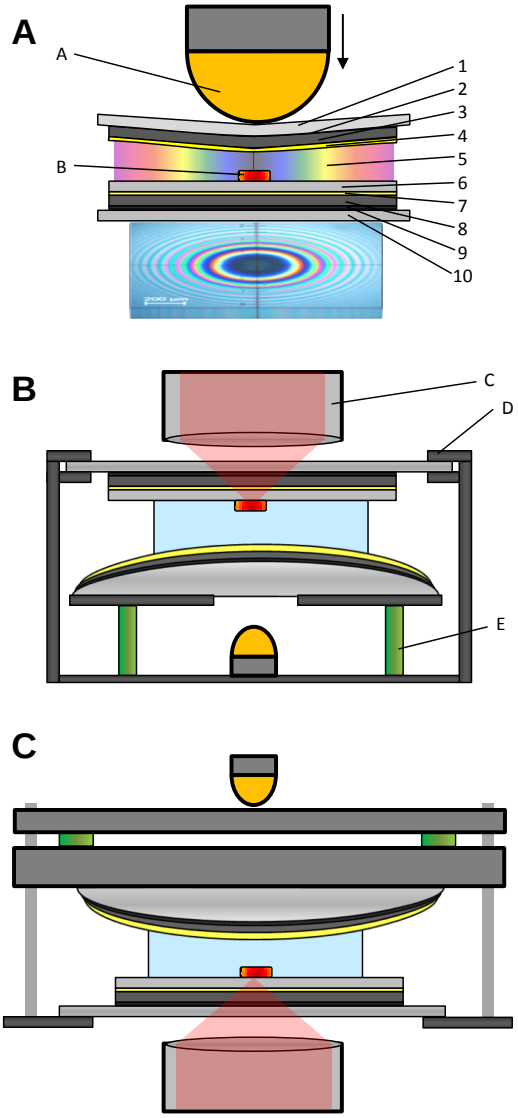

Figure 3.6: *Three resonator designs for different applications. A) Resonator with fixed mirror separation for e.g. cryogenic applications (setup A in Figure 3.1). The first order of interference is reached by applying pressure by a LED on the upper mirror and by observing the Newton Rings in transmission. B+C) Tunable resonator for inverted (setup A in Figure 3.1) and non-inverted (setup B in Figure 3.1) microscopes. For each resonator the layers were evaporated on the substrates by electron beam evaporation with the following sequence and respective thickness: 1) Glass cover slip; 2) 1 nm Cr; 3) 40 nm Ag; 4) 1 nm Au; 5) H_2O; 6) 40-80 nm SiO_2; 7) 1 nm Au; 8) 60 nm Ag; 9) 1 nm Cr; 10) Glass cover slip/ glass lens. The other elements are: A: LED; B: Sample; C: Objective lens (NA=0.8/1.46); D: Housing cage mounted on feedback-controlled scanning stage; E: Piezoelectric stacks.*

its refractive index matches better to the glass substrates than air does. Also, water has a lower viscosity than immersion oil facilitating the reaching of the $\lambda/2$-region. The sample was spin coated on the spacer layer of SiO_2, which additionally guaranties a fixed separation of the emitter to the silver layers minimizing fluorescence quenching induced by the metal surface and allowing to position the emitter in the center of the cavity. In Figure 3.7 a series of white light transmission spectra recorded by a confocal microscope is shown with linearly increasing mirror displacement meaning a reduction of the cavity length by moving one of the mirrors stepwise towards the other. For large mirror separations, several orders of interference are visible by multiple transmission maxima per spectrum. The spectral separation between two adjacent transmission maxima is denoted as the free spectral range (FSR) which values can be calculated by Equation (3.11) for m and $m \pm 1$ in order to determine the actual order of interference. The FSR between the transmission maxima of two following orders increases with decreasing cavity length, as can be seen

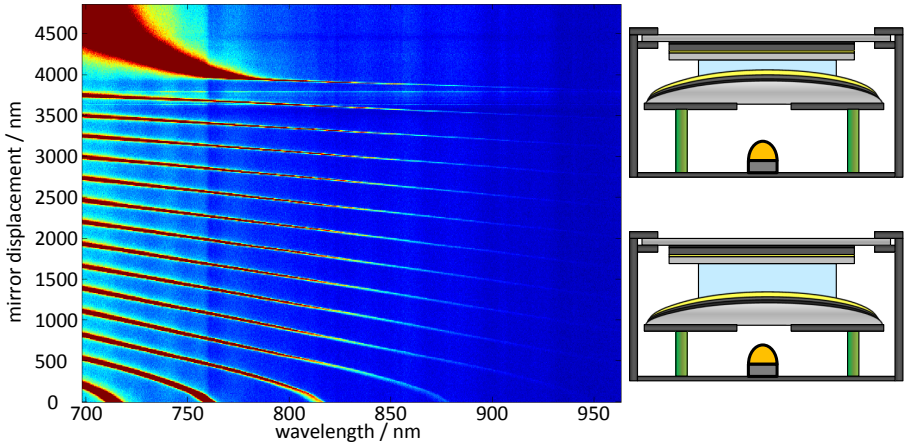

Figure 3.7: *White light transmission spectra as 2D intensity graph for a linear increase of the displacement of one resonator mirror while the second mirror is fixed. Thus, increasing the displacement means decreasing the cavity length as indicated in the inset on the right. In the initial position five orders of interference are visible in the observed spectral range. The mirror separation is now tuned by moving one mirror by piezoelectric stacks and monitoring the expansion by a sensor. After each displacement step (10 nm) leading to a reduction of the cavity length a white light transmission spectrum is recorded. The decrease of the cavity length can be seen by the continuous blue shift of the transmission maxima and the increase of the free spectral range between serial transmission maxima. For a large displacement with respect to the initial position only one order of interference and a deviation from the non-linear behavior is visible. This deviation is due to force applied by the intracavity medium (water) for small cavity lengths.*

in Figure 3.7. If the mirrors are getting in close proximity to each other, the water in the cavity is starting to apply pressure against the external force of the piezoelectric stacks leading to deviations in the linear shift of the transmission maxima.

Bibliography

[1] Bernard Valeur. *Molecular Fluorescence: Principles and Applications.* Wiley-VCH Verlag GmbH, 2002.

[2] Eugene Hecht. *Optics*. Addison-Wesley, 2001.

[3] J. B. Birks. *Photophysics of Aromatic Molecules*, volume 74. John Wiley & Sons Ltd, December 1970.

[4] J. R. Lakowicz. *Principles of Fluorescence Spectroscopy*. Springer, 3rd edition, September 2006.

[5] Michael Kasha. Characterization of electronic transitions in complex molecules. *Discuss. Faraday Soc.*, 9(0):14–19, 1950.

[6] H. D. Dahmen S. Brandt. *Elektrodynamik: Eine Einführung in Experiment und Theorie*. Springer, 2004.

[7] John David Jackson. *Classical Electrodynamics*. Wiley, 1999.

[8] H. Weyl. Ausbreitung elektromagnetischer wellen über einem ebenen leiter. *Ann. der Physik*, 365:481–500, 1919.

[9] J. Enderlein. New approach to fluorescence spectroscopy of individual molecules on surfaces. *Physical Review Letters*, 83(19):3804–3807, November 1999.

[10] J.J. Sakurai and S.F. Tuan. *Modern Quantum Mechanics*. Addison-Wesley, 1994.

[11] E. Fermi. Quantum theory of radiation. *Rev. Mod. Phys.*, 4:87–132, 1932.

[12] JoostS. de Klerk, ArjenN. Bader, Freek Ariese, and Cees Gooijer. High-resolution fluorescence studies on excited-state intra- and intermolecular proton transfer. In *Reviews in Fluorescence*, volume 2007, pages 271–298–. Springer New York, 2009.

[13] T. Basché, W. E. Moerner, M. Orrit, and U. P. Wild. *Single-Molecule Optical Detection, Imaging and Spectroscopy*. Wiley-VCH Verlag GmbH, 1997.

[14] K. Huang and A. Rhys. Theory of light absorption and non-radiative transitions in f-centres. *Proceedings of The Royal Society of London Series A-Mathematical and Physical Sciences*, 204(1078):406–423, 1950.

[15] M. Orrit, J. Bernard, and R. I. Personov. High-resolution spectroscopy of organic-molecules in solids - from fluorescence line narrowing and hole-burning to single-molecule spectroscopy. *Journal of Physical Chemistry*, 97(40):10256–10268, October 1993.

[16] J. B. Nieder, M. Hussels, R. Bittl, and M. Brecht. Effect of tmao and betaine on the energy landscape of photosystem i. *Biochimica Et Biophysica Acta-bioenergetics*, 1837(6):849–856, June 2014.

[17] T. Förster. Zwischenmolekulare Energiewanderung Und Fluoreszenz. *Annalen Der Physik*, 2(1-2):55–75, 1948.

[18] Bo Albinsson and Jonas K. Hannestad. Multistep fret and nanotechnology. In *FRET - Förster Resonance Energy Transfer*, pages 607–653. Wiley-VCH Verlag GmbH & Co. KGaA, 2013.

[19] W. Russ Algar, Melissa Massey, and Ulrich J. Krull. Semiconductor quantum dots and fret. In *FRET - Förster Resonance Energy Transfer*, pages 475–605. Wiley-VCH Verlag GmbH & Co. KGaA, 2013.

[20] B. Wieb van der Meer. Förster theory. In *FRET - Förster Resonance Energy Transfer*, pages 23–62. Wiley-VCH Verlag GmbH & Co. KGaA, 2013.

[21] M. L. Ruehr, D. R. Zakhary, D. S. Damron, and M. Bond. Cyclic amp-dependent protein kinase binding to a-kinase anchoring proteins in living cells by fluorescence resonance energy transfer of green fluorescent protein fusion proteins. *Journal of Biological Chemistry*, 274(46):33092–33096, November 1999.

[22] H. Sahoo. Forster resonance energy transfer - a spectroscopic nanoruler: Principle and applications. *Journal of Photochemistry and Photobiology C-photochemistry Reviews*, 12(1):20–30, March 2011.

[23] K. Becker, J. M. Lupton, J. Muller, A. L. Rogach, D. V. Talapin, H. Weller, and J. Feldmann. Electrical control of Förster energy transfer. *Nat. Mater.*, 5(10):777–781, October 2006.

[24] A. L. Rogach, T. A. Klar, J. M. Lupton, A. Meijerink, and J. Feldmann. Energy transfer with semiconductor nanocrystals. *Journal of Materials Chemistry*, 19(9):1208–1221, 2009.

[25] R. Metivier, F. Nolde, K. Mullen, and T. Basche. Electronic excitation energy transfer between two single molecules embedded in a polymer host. *Phys. Rev. Lett.*, 98(4):047802, January 2007.

[26] H. Y. Xie, H. Y. Chung, P. T. Leung, and D. P. Tsai. Plasmonic enhancement of forster energy transfer between two molecules in the vicinity of a metallic nanoparticle: Nonlocal optical effects. *Physical Review B*, 80(15):155448, October 2009.

[27] L. Zhao, T. Ming, L. Shao, H. J. Chen, and J. F. Wang. Plasmon-controlled forster resonance energy transfer. *Journal of Physical Chemistry C*, 116(14):8287–8296, April 2012.

[28] M. L-Viger, D. Brouard, and D. Boudreau. Plasmon-enhanced resonance energy transfer from a conjugated polymer to fluorescent multi layer core-shell nanoparticles: A photophysical study. *Journal of Physical Chemistry C*, 115(7):2974–2981, February 2011.

[29] Petra Fromme and Ingo Grotjohann. Overview of photosynthesis. In *Photosynthetic Protein Complexes*, pages 1–22. Wiley-VCH Verlag GmbH & Co. KGaA, 2008.

[30] E. Krausz, J. L. Hughes, P. Smith, R. Pace, and S. P. Arskold. Oxygen-evolving photosystem ii core complexes: a new paradigm based on the spectral identification of the charge-separating state, the primary acceptor and assignment of low-temperature fluorescence. *Photochemical & Photobiological Sciences*, 4(9):744–753, 2005.

[31] G. Raszewski and T. Renger. Light harvesting in photosystem ii core complexes is limited by the transfer to the trap: Can the core complex turn into a photoprotective mode? *Journal of the American Chemical Society*, 130(13):4431–4446, April 2008.

[32] F. Rappaport, M. Guergova-Kuras, P. J. Nixon, B. A. Diner, and J. Lavergne. Kinetics and pathways of charge recombination in photosystem ii. *Biochemistry*, 41(26):8518–8527, July 2002.

[33] A. W. Rutherford and P. Heathcote. Primary photochemistry in photosystem-i. *Photosynthesis Research*, 6(4):295–316, 1985.

[34] G. S. Beddaer and G. Porter. Concentration quenching in chlorophyll. *Nature*, 260(5549):366–367, 1976.

[35] E. Schlodder. Introduction to optical methods in photosynthesis. *Photosynthesis Research*, 101(2-3):93–104, September 2009.

[36] B. Gobets, I. H. M. van Stokkum, M. Rogner, J. Kruip, E. Schlodder, N. V. Karapetyan, J. P. Dekker, and R. van Grondelle. Time-resolved fluorescence emission measurements of photosystem i particles of various cyanobacteria: A unified compartmental model. *Biophysical Journal*, 81(1):407–424, July 2001.

[37] V. V. Shubin, S. D. S. Murthy, N. V. Karapetyan, and P. Mohanty. Origin of The 77-K Variable Fluorescence at 758-nm in the Cyanobacterium *Spirulina-Platensis*. *Biochimica et Biophysica Acta*, 1060(1):28–36, September 1991.

[38] N. V. Karapetyan, E. Schlodder, R. van Grondelle, and J. P. Dekker. *Advances in Photosynthesis and Respiration vol. 24, Photosystem I: The Light-Driven Plastocyanin:Ferredoxin Oxidoreductase*. Springer, 2006.

[39] K. Gibasiewicz, A. Szrajner, J. A. Ihalainen, M. Germano, J. P. Dekker, and R. van Grondelle. Characterization of low-energy chlorophylls in the psi-lhci supercomplex from chlamydomonas reinhardtii. a site-selective fluorescence study. *Journal of Physical Chemistry B*, 109(44):21180–21186, November 2005.

[40] V. V. Shubin, I. N. Bezsmertnaya, and N. V. Karapetyan. Isolation from spirulina membranes of 2 photosystem I-type complexes, one of which contains chlorophyll responsible for the 77-k fluorescence band at 760 nm. *Febs Letters*, 309(3):340–342, September 1992.

[41] L. O. Palsson, C. Flemming, B. Gobets, R. van Grondelle, J. P. Dekker, and E. Schlodder. Energy transfer and charge separation in photosystem I: P700 oxidation upon selective excitation of the long-wavelength antenna chlorophylls of Synechococcus elongatus. *Biophys. J.*, 74(5):2611–2622, May 1998.

[42] Eberhard Schlodder, Martin Hussels, Marianne Cetin, Navassard V. Karapetyan, and Marc Brecht. Fluorescence of the various red antenna states in photosystem i complexes from cyanobacteria is affected differently by the redox state of p700. *Biochimica et biophysica Acta*, 1807(11):1423–31, November 2011.

[43] Martin Hussels and Marc Brecht. Evidence for direct binding of glycerol to photosystem I. *Febs Letters*, 585(15):2445–2449, August 2011.

[44] B. Gobets, I. H. M. van Stokkum, F. van Mourik, J. P. Dekker, and R. van Grondelle. Excitation wavelength dependence of the fluorescence kinetics in photo-

system I particles from Synechocystis PCC 6803 and Synechococcus elongatus. *Biophys. J.*, 85(6):3883–3898, December 2003.

[45] S. G. Telfer, T. M. McLean, and M. R. Waterland. Exciton coupling in coordination compounds. *Dalton Transactions*, 40(13):3097–3108, April 2011.

[46] M. Brecht, M. Hussels, J. B. Nieder, H. Fang, and C. Elsässer. Plasmonic interactions of photosystem i with fischer patterns made of gold and silver. *Chem. Phys.*, 406:15 – 20, 2012.

[47] M. Hussels, J. B. Nieder, C. Elsässer, and M. Brecht. Interactions of photosystem i with plasmonic nanostructures. *Acta Physica Polonica A*, 122(2):269–274, August 2012.

[48] P. Zijlstra and M. Orrit. Single metal nanoparticles: optical detection, spectroscopy and applications. *Reports On Progress In Physics*, 74(10):106401, October 2011.

[49] G. V. Hartland. Optical studies of dynamics in noble metal nanostructures. *Chemical Reviews*, 111(6):3858–3887, June 2011.

[50] Bohren C and Huffman D. *Absorption and Scattering of Light by Small Particles*. New York: Wiley, 1998.

[51] Kittel. *Introduction to Solid State Physics*. Wiley, 1986.

[52] C. Sonnichsen, T. Franzl, T. Wilk, G. von Plessen, J. Feldmann, O. Wilson, and P. Mulvaney. Drastic reduction of plasmon damping in gold nanorods. *Physical Review Letters*, 88(7):077402, February 2002.

[53] E. A. Coronado and G. C. Schatz. Surface plasmon broadening for arbitrary shape nanoparticles: A geometrical probability approach. *Journal of Chemical Physics*, 119(7):3926–3934, August 2003.

[54] M. Z. Liu, M. Pelton, and P. Guyot-Sionnest. Reduced damping of surface plasmons at low temperatures. *Physical Review B*, 79(3):035418, January 2009.

[55] J. A. Osborn. Demagnetizing factors of the general ellipsoid. *Phys. Rev.*, 67(11-12):351–357, June 1945.

[56] U. Kreibig and M. Vollmer. *Optical Properties of Metal Clusters*. Springer, Berlin, 1995.

[57] Viktor Myroshnychenko, Jessica Rodriguez-Fernandez, Isabel Pastoriza-Santos, Alison M. Funston, Carolina Novo, Paul Mulvaney, Luis M. Liz-Marzan, and F. Javier Garcia de Abajo. Modelling the optical response of gold nanoparticles. *Chem. Soc. Rev.*, 37(9):1792–1805, 2008.

[58] G. Raschke, S. Kowarik, T. Franzl, C. Sönnichsen, T. A. Klar, J. Feldmann, A. Nichtl, and K. Kürzinger. Biomolecular recognition based on single gold nanoparticle light scattering. *Nano Lett.*, 3(7):935–938, May 2003.

[59] F. Wackenhut, A. V. Failla, T. Zuchner, M. Steiner, and A. J. Meixner. Three-dimensional photoluminescence mapping and emission anisotropy of single gold nanorods. *Applied Physics Letters*, 100(26):263102, June 2012.

[60] A. Mooradian. Photoluminescence of metals. *Phys. Rev. Lett.*, 22:185–187, Feb 1969.

[61] E. Dulkeith, T. Niedereichholz, T. A. Klar, J. Feldmann, G. von Plessen, D. I. Gittins, K. S. Mayya, and F. Caruso. Plasmon emission in photoexcited gold nanoparticles. *Physical Review B*, 70(20):205424, November 2004.

[62] A. Bouhelier, R. Bachelot, G. Lerondel, S. Kostcheev, P. Royer, and G. P. Wiederrecht. Surface plasmon characteristics of tunable photoluminescence in single gold nanorods. *Physical Review Letters*, 95(26):267405, December 2005.

[63] M. Yorulmaz, S. Khatua, P. Zijlstra, A. Gaiduk, and M. Orrit. Luminescence quantum yield of single gold nanorods. *Nano Letters*, 12(8):4385–4391, August 2012.

[64] G. S. He, J. Zhu, K. T. Yong, A. Baev, H. X. Cai, R. Hu, Y. P. Cui, X. H. Zhang, and P. N. Prasad. Scattering and absorption cross-section spectral measurements of gold nanorods in water. *Journal of Physical Chemistry C*, 114(7):2853–2860, February 2010.

[65] S. Link, M. B. Mohamed, and M. A. El-Sayed. Simulation of the optical absorption spectra of gold nanorods as a function of their aspect ratio and the effect of the medium dielectric constant. *Journal of Physical Chemistry B*, 103(16):3073–3077, April 1999.

[66] F. Wackenhut, A. V. Failla, and A. J. Meixner. Multicolor microscopy and spectroscopy reveals the physics of the one-photon luminescence in gold nanorods. *Journal of Physical Chemistry C*, 117(34):17870–17877, August 2013.

[67] M. B. Mohamed, V. Volkov, S. Link, and M. A. El-Sayed. The 'lightning' gold nanorods: fluorescence enhancement of over a million compared to the gold metal. *Chemical Physics Letters*, 317(6):517–523, February 2000.

[68] J. B. Nieder, R. Bittl, and M. Brecht. Fluorescence studies into the effect of plasmonic interactions on protein function. *Angewandte Chemie-international Edition*, 49(52):10217–10220, 2010.

[69] Lukas Novotny and Niek van Hulst. Antennas for light. *Nat Photon*, 5(2):83–90, February 2011.

[70] P. Anger, P. Bharadwaj, and L. Novotny. Enhancement and quenching of single-molecule fluorescence. *Physical Review Letters*, 96(11):113002, March 2006.

[71] A. M. Kern, D. Zhang, M. Brecht, A. I. Chizhik, A. V. Failla, F. Wackenhut, and A. J. Meixner. Enhanced single-molecule spectroscopy in highly confined optical fields: from lambda/2-fabry-perot resonators to plasmonic nano-antennas. *Chemical Society Reviews*, 43(4):1263–1286, 2014.

[72] P. Ghenuche, J. de Torres, S. B. Moparthi, V. Grigoriev, and J. Wenger. Nanophotonic enhancement of the forster resonance energy-transfer rate with single nanoapertures. *Nano Letters*, 14(8):4707–4714, August 2014.

[73] X. Zhang, C. A. Marocico, M. Lunz, V. A. Gerard, Y. K. Gun'ko, V. Lesnyak, N. Gaponik, A. S. Susha, A. L. Rogach, and A. L. Bradley. Experimental and theoretical investigation of the distance dependence of localized surface plasmon coupled forster resonance energy transfer. *Acs Nano*, 8(2):1273–1283, February 2014.

[74] K. H. Drexhage. Monomolecular layers and light. *Scientific American*, 222(3):108–&, 1970.

[75] B. C. Buchler, T. Kalkbrenner, C. Hettich, and V. Sandoghdar. Measuring the quantum efficiency of the optical emission of single radiating dipoles using a scanning mirror. *Phys. Rev. Lett.*, 95(6):063003–, August 2005.

[76] A. M. Kern, A. J. Meixner, and O. J. F. Martin. Molecule-dependent plasmonic enhancement of fluorescence and raman scattering near realistic nanostructures. *ACS Nano*, 6(11):9828–9836, November 2012.

[77] T. H. Maiman. Stimulated optical radiation in ruby. *Nature*, 187(4736):493–494, August 1960.

[78] E. Betzig and R. J. Chichester. Single molecules observed by near-field scanning optical microscopy. *Science*, 262(5138):1422–1425, November 1993.

[79] A. J. Meixner, M. A. Bopp, and G. Tarrach. Direct measurement of standing evanescent waves with a photon-scanning tunneling microscope. *Applied Optics*, 33(34):7995–8000, December 1994.

[80] K. J. Vahala. Optical microcavities. *Nature*, 424(6950):839–846, August 2003.

[81] K. K. Lehmann and D. Romanini. The superposition principle and cavity ring-down spectroscopy. *Journal of Chemical Physics*, 105(23):10263–10277, December 1996.

[82] Kikuo Ujihara. Spontaneous emission and the concept of effective area in a very short optical cavity with plane-parallel dielectric mirrors. *Japanese Journal of Applied Physics*, 30(5B):L901–, 1991.

[83] G. Bjork, H. Heitmann, and Y. Yamamoto. Spontaneous-emission coupling factor and mode characteristics of planar dielectric microcavity lasers. *Physical Review A*, 47(5):4451–4463, May 1993.

[84] E.M. Purcell. Proceedings of the american physical society. *Phys. Rev.*, 69:674–674, 1946.

[85] Frank Laloe Claude Cohen-Tannoudji, Bernard Diu. *Quantum Mechanics, Volume 1*. Wiley, 1977.

[86] W. E. Moerner and L. Kador. Optical detection and spectroscopy of single molecules in a solid. *Phys. Rev. Lett.*, 62:2535–2538, May 1989.

[87] M. Orrit and J. Bernard. Single pentacene molecules detected by fluorescence excitation in a para-terphenyl crystal. *Physical Review Letters*, 65(21):2716–2719, November 1990.

[88] E. Abbe. Beitr"age zur theorie des mikroskops und der mikroskopischen wahrnehmung. 9(1):413–418–, 1873.

[89] L. Bergmann and C. Schaefer. *Wellenoptik: Aus: Lehrbuch der Experimentalphysik : zum Gebrauch bei akademischen Vorlesungen und zum Selbststudium, Bd. 3*. Number Teil 1. Walter De Gruyter Incorporated, 1959.

[90] Raphael Gutbrod, Dmitry Khoptyar, Mathias Steiner, Anna M. Chizhik, Alexey I. Chizhik, Sebastian Baer, and Alfred J. Meixner. Three-dimensional orientation

of single molecules in a tunable optical lambda/2 microresonator. *Nano Letters*, 10(2):504–508, February 2010.

[91] T. Zuchner, A. V. Failla, and A. J. Meixner. Light microscopy with doughnut modes: A concept to detect, characterize, and manipulate individual nanoobjects. *Angewandte Chemie-international Edition*, 50(23):5274–5293, 2011.

[92] Nina Mauser and Achim Hartschuh. Tip-enhanced near-field optical microscopy. *Chem. Soc. Rev.*, 43(4):1248–1262, 2014.

[93] J. Friedrich, J. D. Swalen, and D. Haarer. Electron-phonon coupling in amorphous organic host materials as investigated by photochemical hole burning. *The Journal of Chemical Physics*, 73(2):705–711, 1980.

[94] T. Pullerits, R. Monshouwer, F. van Mourik, and R. van Grondelle. Temperature-dependence of electron-vibronic spectra of photosynthetic systems - computer-simulations and comparison with experiment. *Chemical Physics*, 194(2-3):395–407, May 1995.

[95] S. J. Jang, J. S. Cao, and R. J. Silbey. On the temperature dependence of molecular line shapes due to linearly coupled phonon bands. *Journal of Physical Chemistry B*, 106(33):8313–8317, August 2002.

[96] C. Roos, A. Kohn, J. Gauss, and G. Diezemann. The temperature dependence of vibronic lineshapes: Linear electron-phonon coupling. *Journal of Chemical Physics*, 141(15):154110, October 2014.

[97] R. Kaufmann, C. Hagen, and K. Grunewald. Fluorescence cryo-microscopy: current challenges and prospects. *Current Opinion In Chemical Biology*, 20:86–91, June 2014.

[98] M. A. Le Gros, G. McDermott, M. Uchida, C. G. Knoechel, and C. A. Larabell. High-aperture cryogenic light microscopy. *Journal of Microscopy-oxford*, 235(1):1–8, July 2009.

[99] S. A. Lancelle, D. A. Callaham, and P. K. Hepler. A method for rapid freeze fixation of plant-cells. *Protoplasma*, 131(2):153–165, 1986.

[100] C. van Rijnsoever, V. Oorschot, and J. Klumperman. Correlative light-electron microscopy (clem) combining live-cell imaging and immunolabeling of ultrathin cryosections. *Nature Methods*, 5(11):973–980, November 2008.

[101] A. Briegel, S. Y. Chen, A. J. Koster, J. M. Plitzko, C. L. Schwartz, and G. J. Jensen. Correlated light and electron cryo-microscopy. *Methods In Enzymology*, 481:317–341, 2010.

[102] Wolfgang Demtröder. *Experimentalphysik 2: Elektrizität und Optik*. Springer, 2008.

[103] G. Bjork. On the spontaneous lifetime change in an ideal planar microcavity - transition from a mode continuum to quantized modes. *Ieee Journal of Quantum Electronics*, 30(10):2314–2318, October 1994.

[104] Gunnar Bjork and Yoshihisa Yamamoto. Spontaneous emission in dielectric planar microcavities. In *Spontaneous Emission and Laser Oscillation in Microcavities*. CRC Press, 1995.

[105] M. Steiner, F. Schleifenbaum, C. Stupperich, A. V. Failla, A. Hartschuh, and A. J. Meixner. Microcavity-controlled single-molecule fluorescence. *Chemphyschem*, 6(10):2190–2196, October 2005.

Chapter 4

Confocal sample-scanning microscope for single-molecule spectroscopy and microscopy with fast sample exchange at cryogenic temperatures

In this chapter a confocal microscope is presented for scanning a sample within a helium bath cryostat, including the possibility to transfer the sample into the pre-cooled cryostat, which can be cooled down from 300 to 1.6 K. In contrast to laser scanning microscopes the setup contains a piezoelectric scanning stage to move the sample holder over the spatially fixed laser spot focued by a microscope objective in three space directions within nanometer and micrometer precision. The scan image quality and the effective numerical aperture of the microscope for single-molecule spectroscopy can be enhanced significatly by this method in contrast to beam scanning microscopes. The shuttle mechanism to insert or remove samples out of the cold sample area bases on magnets mounted on the sample scanning stage and the sample holder enabling to attach the sample carrier to the scanning stage. This approach allows also to rapidly transfer pre-frozen samples into a pre-cooled cryostat.

This chapter is based on:
Hussels, M., Konrad A., Brecht M. "Confocal sample-scanning microscope for single-molecule spectroscopy and microscopy with fast sample exchange at cryogenic temperatures" *Review of Scientific Instruments*, **2012**, *83*,123706.

Confocal sample-scanning microscope for single-molecule spectroscopy and microscopy with fast sample exchange at cryogenic temperatures

Martin Hussels, Alexander Konrad, and Marc Brecht[a)]
Universität Tübingen, Institut für Physikalische und Theoretische Chemie and LISA+ Center, Auf der Morgenstelle 18, 72076 Tübingen, Germany

(Received 28 June 2012; accepted 19 November 2012; published online 12 December 2012)

The construction of a microscope with fast sample transfer system for single-molecule spectroscopy and microscopy at low temperatures using 2D/3D sample-scanning is reported. The presented construction enables the insertion of a sample from the outside (room temperature) into the cooled (4.2 K) cryostat within seconds. We describe the mechanical and optical design and present data from individual Photosystem I complexes. With the described setup numerous samples can be investigated within one cooling cycle. It opens the possibility to investigate biological samples (i) without artifacts introduced by prolonged cooling procedures and (ii) samples that require preparation steps like plunge-freezing or specific illumination procedures prior to the insertion into the cryostat.
 [http://dx.doi.org/10.1063/1.4769996]

I. INTRODUCTION

The spectroscopy of individual molecules, nanoparticles, or proteins requires optical setups with the ability to separate single particles or molecules from their surrounding, suppress the background sufficiently, and collect the luminescence with high efficiency. One option to manage this is using the confocal principle.[1,2] Two main principles to scan the laser focus over the sample are used typically. One is to move the laser focus while the sample is fixed; this approach is often referred to as confocal laser scanning microscopy (CLSM). The second is to move the sample (sample scanning) while the position of the laser focus is fixed. Both scanning approaches are available at room and low temperatures. In the following, we focus on low temperature experiments.

At cryogenic temperatures, one has to face challenges due to the reduced imaging quality of available microscope objectives (MOs) and several limitations for using movable parts inside the cryostat. For CLSM, the beam is deflected by movable mirrors or lenses, which can be positioned outside the cryostat. The excitation laser focus is moved over the sample by the motion of these mirrors or lenses. As a consequence, no movable parts have to be placed inside the cryostat for 2D imaging of a sample making the construction of the probe-head easier. Therefore, this approach is quite often used for low temperature experiments.[3,4] In CLSM, the focus point is moved within the focal plane of the MO to acquire an image. The quality of the resulting image depends directly on the quality of the MO. Poor quality of commercially available MOs is a long-standing hurdle in low temperature microscopy. During the last years various approaches were reported using different types of MOs like mirror optics, gradient-index (GRIN) lenses or solid immersion lenses to overcome this drawback.[1,5–7] Unfortunately, none of these approaches yield an image quality comparable to that available at room temperature. This influence of the MO on the optical quality of the image can be reduced by using sample scanning instead of laser scanning. Therefore, the sample has to be mounted on a desk that can be moved for scanning. Then the fixed laser-beam can be aligned directly along the optical axis of the MO. In this approach, the off-axis performance of the MO is not important for the image quality. The desk moving the sample has to be implemented inside the cryostat, which implies technical difficulties in the probe-head design. The first setup using piezoelectric sliders and scanners with large range for single-molecule imaging and spectroscopy at low temperature was built by Segura *et al.* in 2000.[8] Today, dynamic piezoelectric sliders and scanners for implementation of sample scanning at low temperature providing lateral and vertical translations of the desk are commercially available;[9] and an extension to 3D scanning is also possible.

For sample scanning, the sample has to be mounted on the scanning desk. In the already described systems using sample scanning at low temperatures, the sample is mounted on the desk before insertion of the probehead into the cryostat and then cooled down. With this approach exchanging the sample during one cooling cycle, which usually lasts several days, is not possible. Samples mounted inside the cryostat from beginning of the cooling cycle are exposed for long time to a dry helium atmosphere. This exposure causes artifacts if the sample is sensitive to drying up like proteins and other biological samples. With the aim to avoid such artifacts, proteins are often embedded in polyvinyl alcohol (PVA) matrices instead of water-based buffer solutions. Unfortunately, PVA induces large changes into the structure of proteins; therefore this type of sample preparation is not able to produce valuable results as recently shown by us.[10] To avoid this, biological samples should be introduced into the pre-cooled cryostat hampering drying and enabling the observation in aqueous solution.

In this article, we report the construction of a fast transfer system for single-molecule spectroscopy and microscopy at low temperatures that enables the insertion of a sample

[a)]Telephone: +49-7071-29-76239. Fax: +49-7071-29-5490. E-mail: marc.brecht@uni-tuebingen.de.

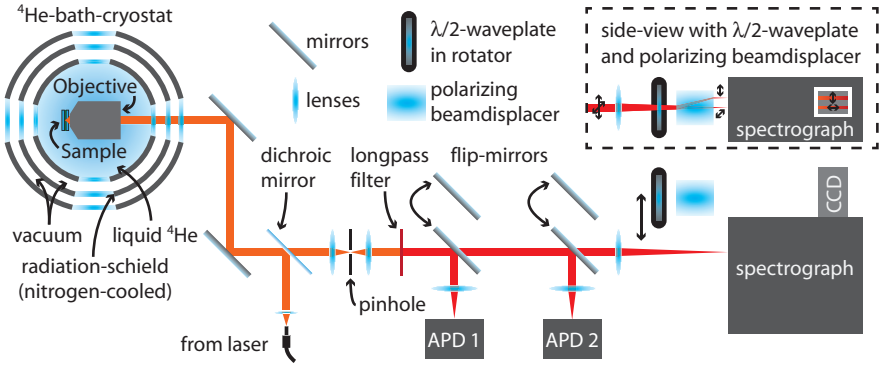

FIG. 1. Scheme of the setup for low temperature confocal imaging and spectroscopy. For details see Sec. II A.

from the outside onto the scanning desk in the cooled (4.2 K) cryostat. We report results of first experiments showing single-molecule data of Photosystem I protein complexes. With the described setup numerous samples can be investigated within one cooling cycle. Additionally, it opens the possibility to investigate biological samples very close to their native state.

II. DESCRIPTION OF THE SETUP

A. Design of the confocal microscope

Figure 1 shows the setup of our home-built confocal microscope. The microscope is mounted on a damped optical table. During measurement the sample and the MO (Mikrothek, 60× NA = 0.85) are immersed in liquid Helium inside a bath-cryostat (SVT-200, Janis). Temperatures below 4.2 K are generated by pumping the Helium gas with a Edwards TwoStage E2M80 combined with a Edwards EH250 booster pump. The temperature is measured close to the sample by a LakeShore Model 336 temperature controller equipped with a Cernox sensor (CX-1030-SD-HT 0.3L).

For excitation we use a fiber-coupled 665 nm *cw* diode-laser (iBEAM-660-3V2, TOPTICA Photonics). The laser is coupled into the setup using a dichroic mirror (ZQ670RDC, AHF Analysentechnik). The excitation light is then aligned along the optical axis of the MO to get an optimal focus. The emitted light passes the dichroic mirror, a 50 μm pinhole, and a longpass filter (HQ 695 LP, AHF Analysentechnik), and then it can be detected by two different avalanche photodiodes (APDs) and a CCD-camera mounted on a spectrograph. The different detectors for the emission light are selected by computer-controlled flip mirrors. The first APD (APD 1, COUNT-100C, Laser Components) is used for imaging of the sample and has a dark count rate <20 c/s. The second APD (APD 2, PD1CTC, Micro Photon Devices) is used for time correlated single photon counting (TCSPC) and fluorescence-lifetime imaging (FLIM) measurements and has pulse rise time <50 ps to gain good time resolution. For data acquisition of the APD signals a National Instruments NI6601 counter board and a Becker & Hickl TCSPC-module (SPC-130) are used. For TCSPC/FLIM-measurements a 670 nm pulsed diode laser (LDH-P-670, PicoQuant) is used for excitation instead of the *cw*-laser. For spectroscopy we use an Andor Newton back illuminated deep depleted CCD (DU920P-PR-DD) mounted on a Shamrock 500 spectrograph with 200 lines/mm and 400 lines/mm gratings. For polarization measurements a combination of a λ/2-waveplate (10RP52-2, Newport) on a motorized rotator (PRM1/MZ8, Thorlabs) and a polarizing beamdisplacer (BD27, Thorlabs) can be driven into the optical path in front of the spectrograph.

The polarizing beamdisplacer splits the light into two beams with perpendicular polarization, which can be acquired individually by the CCD-camera. In combination with the rotating λ/2-waveplate it is possible to measure the polarization spectrally resolved.

The whole setup is controlled by a self-developed LabVIEW software. The software controls all components described above. The special aim of the software is to simplify the acquisition of high resolution spectroscopic data on >100 individual molecules/proteins within several hours. To obtain such high numbers of different measurements the software provides different standard data acquisition types: 2D/3D intensity scan, time correlated single photon counting, single spectrum, spectra series, single spectrum with polarization splitting, and spectra series with polarization splitting and rotating λ/2-waveplate. The data are automatically saved in XML-format with current timestamp and all parameters set in the instrument (e.g., exposure time, CCD-parameters, sample name, etc.). The datasets are visualized and analyzed in a self-developed toolbox written in MATLAB. The toolbox provides a graphical user interface for displaying and statistical analysis of datasets.

B. Mechanical design of the probehead

The inner sample chamber of the cryostat has a diameter of 2.44 in. (∼62 mm) and a height of 40 in. (∼102 cm). The design of the whole probehead must fit these constraints resulting in a very compact arrangement of the required components. In addition, the construction should allow an easy positioning of the sample and a quick sample exchange.

The probehead is divided into two parts. The upper part is not described in detail here. This part is needed to launch the probehead into the cryostat, guide the cables from the scanners and the temperature sensor to the top flange, hold the baffles, and guide the transfer rod from the top flange to

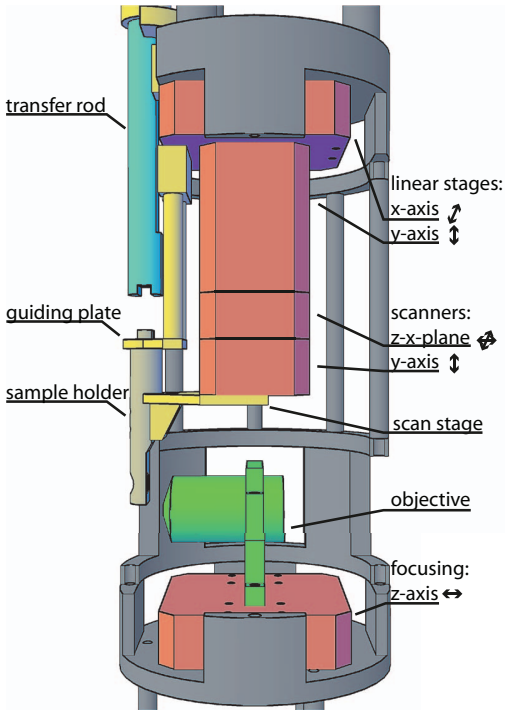

FIG. 2. Mechanical design of the lower part of the probehead used for low temperature microscopy. The dimension of the probehead must fulfill the constraints of inner sample chamber of the cryostat (diameter 2.44 in. (∼62 mm)). The whole arrangement is fitted together by a cage (grey) made of stainless steel. In the cage different types of piezo modules (red) are mounted to move the sample during sample transfer and sample scanning. One stage is mounted on the bottom of the cage carrying the MO (green). The sample holder (light grey) is mounted magnetically to the scan stage (yellow). The sample holder can be inserted or removed by a transfer rod (light green). The attachment of the sample holder to the transfer rod is realized by magnets that are fitted in the end of the holder and the rod (for detail see text).

the opening in the lower part. The lower part of the probehead is shown in Fig. 2. The whole arrangement of linear stages, scanners, the sample holder, and the mounting plate is housed in a cage (dark grey) made of stainless steel. The MO is mounted on a linear stage ANPx320 (attocube systems) for focusing (red) with the optical axis aligned parallel to the optical table. The laser beam can pass from the outside of the cryostat through the optical window into the opening at the backside of the MO. This position of the MO simplifies the arrangement of the optical path remarkably. The sample is mounted on a sample holder (light grey), which is magnetically mounted on the scan stage (yellow). Scanning and positioning of the sample are done using attocube systems linear stages and scanners (red). The linear stages are an ANPx320 (x-axis) and an ANPz101eXT (y-axis). These stages have a travel range of 12 mm with <100 nm precision allowing accurate positioning over large ranges. The scanners are an ANSxy100lr (z- and x-axis) and an ANSz100lr (y-axis). These scanners allow scanning of $30 \times 30 \times 30\,\mu m^3$ at low temperature and $50 \times 50 \times 50\,\mu m^3$ at room temperature. The motion control for both types of stages and scanners is done by an ANC350 controller. The combination of linear stages and scanners allows highly precise scanning of the sample besides large travel ranges. Precise scanning is the prerequisite for confocal imaging and the large travel ranges are necessary for the quick and easy sample transfer mechanism described below.

C. Sample transfer mechanism

The realization of the sample transfer system at low temperature is shown in Fig. 3. Three elements are essential for the mechanism introduced here; they are: transfer rod (light green), sample holder (light grey), and scan stage (yellow/red). The transfer rod has a diameter of 8 mm and a length of 120 cm. The upper part of the transfer rod is made of epoxy fiber glass reinforcement (HGW2375, Hesselmann). The lower part is made of stainless steel. At the bottom end of the transfer rod a groove of 3 mm fitting to the ridge of the sample holder is milled to avoid rotation of the sample holder during transfer. Two permanent magnets (NdFeB, magnets4you) with 3 mm diameter and height are fitted in this groove and in the bottom of the ridge of the sample holder to attach the sample holder to the transfer rod with a mounting force of ∼5 N. The whole transfer rod is inserted into the cryostat via an O-ring compression seal at the top flange. After insertion, the transfer rod is pushed down to the opening in the guiding plate (Figs. 2 and 3). The sample holder itself is made of a cylinder with 36 mm height and 7 mm diameter

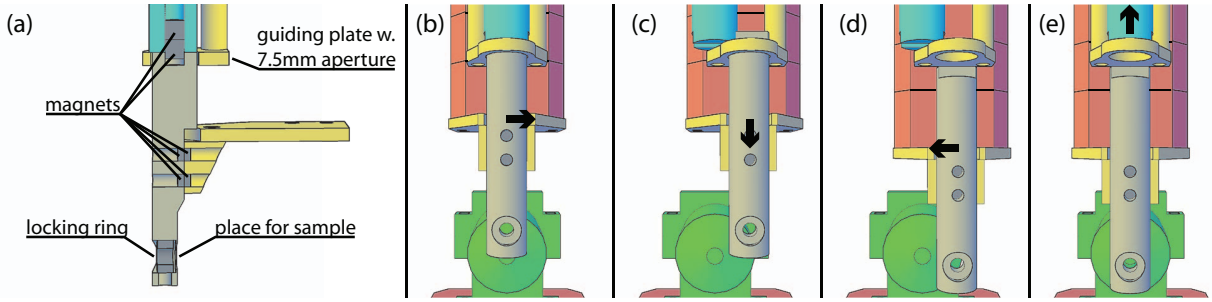

FIG. 3. Sample transfer system for low temperatures. (a) The mechanism consists of a transfer rod (light green), a sample holder (light grey), a guiding plate and the mounting at the scan stage (yellow). The transfer mechanism is based on magnets that are fitted at the connection of the sample holder with the transfer rod and the sample holder with the guiding plate. (b) and (c) Several movements are necessary to separate the sample holder from the transfer rod. The guiding plate is necessary to reduce the force acting on the piezo scanners during the cleavage of the magnets in the groove of the transfer rod and the sample holder. After the cleavage of these magnets, the sample holder can be driven out of the guiding plate and then it can be driven to the position required to perform the experiments.

(1 mm smaller than the transfer rod) to easily pass through the O-ring compression seal at the top flange. On the lower side the sample holder is milled along the center axis to get a plane that assures a stable attachment of the holder to the scan stage (see Fig. 3(a)). The sample is mounted on the back in a 5 mm diameter hole. To hold the sample in place a locking ring secured with a screw is mounted behind the sample. Two magnets (NdFeB, magnets4you) of 2 mm diameter and 1 mm height are fitted in the sample holder to attach it on the scanning stage (yellow). The magnets are arranged parallel to the sample plane to provide a stable mounting of the sample holder on the scan stage. On the opposite side, two magnets with 2 mm diameter and 1 mm height are fitted in the mounting element at the scan stage to get tight attachment of the sample holder with a mounting force of ∼2.5 N. The mounting element at the scan stage is made of two parts: a 2 mm stainless steel plate and a wedge whereon the sample holder is attached. The weights of the mounting elements and the sample holder are minimized to avoid an unwanted load on the scanners that increases their hysteresis during fast scanning.

D. Transfer of the sample holder

In the beginning of the transfer sequence, the sample holder is mounted on the transfer rod outside of the cryostat. Then the transfer rod is inserted into the cryostat through the O-ring compression seal at the top flange. To minimize the amount of air entering the inner chamber of the cryostat the O-ring compression seal is mounted on top of a ball valve, which is closed while inserting the transfer rod. After insertion of the holder to this position, the ball valve is opened and the transfer rod can be pushed easily into the cryostat until it reaches the final position at the guiding plate shown in Fig. 3(a). In this position all magnets of the sample holder are in contact with the corresponding magnets in the transfer rod and the scan stage. The force of the magnets in the scan stage is not sufficient to release the sample holder from the transfer rod by simple pulling back the transfer rod. The problem can be solved by moving the whole scan stage with the guiding plate along the groove of the transfer rod using the x-axis linear stage as shown in (b). The force required for cleavage of the magnets in this way is much smaller (∼1.2 N) than the force required for cleavage by pulling on the transfer rod (∼5 N). After the cleavage at position (c) the corresponding magnets in the transfer rod and in the sample holder show only weak contact. The guiding plate is necessary to hold the sample holder in upright position and to protect the scan piezo against the forces that occur during the process. After losing contact, the scan stage with the sample holder is moved along the y-axis (6 mm). Then the sample can be driven into the focal plane of the MO, the transfer rod can be pulled away, and the required experiments can be performed (c)–(e).

After finishing the experiments, the sample holder can be easily removed by driving the scanners into the starting position (b) and subsequent insertion of the transfer rod. When the transfer rod approaches the sample holder, it is pulled automatically into the mounting groove of the transfer rod by the strong attraction of the two magnets (their attraction is stronger than the attraction of the magnets at the mounting element). Then the sample holder can be pulled away.

III. RESULTS

A. Measurements on single pre-illuminated photosystem I complexes

The sample transfer mechanism introduced above enables the preparation and freezing of samples outside of the cryostat. Then, the frozen sample is inserted into the cryostat filled with liquid helium. In the following, we present results of an experiment performed on single protein complexes of photosystem I that were frozen in liquid nitrogen under white light illumination outside of the cryostat. Afterwards, the sample was transferred to the scanning desk. Figure 4(a) shows two emission spectra of a single photosystem I complex recorded under different excitation intensities. The upper trace is collected in 4 s with an excitation intensity of 300 μW whereas the lower trace is recorded in 600 s with an excitation

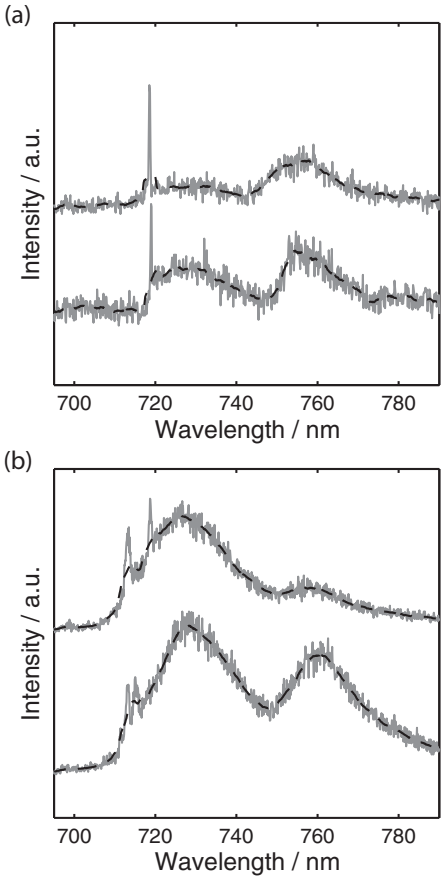

FIG. 4. Single-molecule fluorescence spectra of individual trimeric photosystem I complexs from *A. platensis*. (a) Spectra of one trimeric photosystem I complex of a sample frozen to 77 K under strong illumination with white light outside of the cryostat; excitation wavelength was 665 nm. The excitation power was varied between 300 μW (top trace) and 1 μW (bottom trace). (b) Spectra of one trimeric photosystem I complex taken from Ref. 11. The excitation power has been varied in a comparable way as in (a). For experimental details see Ref. 11. The accumulation time was chosen in each case so that a sufficient signal/noise ratio was achieved (2 s–10 min). Original data (solid curve), data smoothed by a moving average filter (dashed curve).

intensity of 1 μW. Emission spectra of several photosystem I complexes were investigated by the same variation of the illumination strength. Figure 4(b) shows two spectra, which were recorded in a comparable way but the sample was not frozen under illumination.[11]

The first single-molecule spectra of photosystem I at cryogenic temperature have been reported by Jelezko *et al.*[12] The fluorescence emission of photosystem I is due to several chlorophyll *a* molecules showing a remarkable redshift (for review see Refs. 13 and 14). Single-molecule spectroscopy offers the possibility to obtain more detailed information about the spectral characteristics of these redshifted antenna states.[15] Experiments on a large number of individual photosystem I complexes of *A. platensis* revealed sharp emission lines around 715 nm and two broad emission bands centered around 728 nm and 760 nm.[16] Indications for all of these emitters can be found in the spectra in Fig. 4. High excitation laser intensities of about 100 μW at 680 nm are often used to detect the weak fluorescence of single molecules (photosystems). Then, the excitation intensity in the focus is on the order of 6×10^2 W/cm^2.[17] This corresponds to a photon flux of about 6.8×10^{20} photons/(cm^{2}s). Because of the very large photon flux, most of the time P700 is in the oxidized state, for further details see Ref. 11. The most red-emitting state is very sensitive to the oxidation state of P700. In case of reduced P700, the emission of these states is intense, whereas in the oxidized state the fluorescence of the most red-emitting state is quenched.[18] As shown recently in Ref. 11 the quenching can be influenced by variation of the illumination strength due to the balance between oxidized and reduced state of P700. Strong illumination during freezing (without strong reductive like dithionite in the buffer solution) increases the probability of P700 to become oxidized. Then the variation of the excitation intensity should not affect the intensity distribution in the fluorescence emission dramatically. The intensity of the different emitters that contribute to the emission spectra of photosystem I complexes frozen under high illumination should show only a weak variation in their relative intensity distribution as seen in Fig. 4(a) as well as in all other photosystem I complexes that were recorded (data not shown). Without the illumination during freezing a variation of the relative intensity distribution as seen in Fig. 4(b) is expected.

IV. CONCLUSION

The described mechanical design of a fast transfer system is based on a simple mechanism. The setup enables experiments on samples that are prepared outside of a cryostat, afterwards they are transferred to the scanning desk in the already cold (4.2 K) cryostat. Transfer and launch of samples from the outside to the inside requires only some seconds. Removal of the sample takes the same time. This mechanism opens the possibility to investigate many samples within one cooling cycle as well as biological samples in almost native (vitrified) matrices at low temperatures.

ACKNOWLEDGMENTS

We thank Klaus Schaupp (head of the machine shop) for very helpful discussions concerning the design of the probehead. The great work of his team in manufacturing the parts of the probehead is gratefully acknowledged. The Brecht GmbH (http://www.brecht-brt.de) is gratefully acknowledged for manufacturing of parts of the probehead. We thank Alfred J. Meixner for fruitfull discussions and his continuous support. The samples were provided by Eberhard Schlodder, his continuous support is gratefully acknowledged. This work has been supported by the Deutsche Forschungsgemeinschaft (BR 4102/1–1 and BR 4102/2–1).

[1]P. Tamarat, A. Maali, B. Lounis, and M. Orrit, J. Phys. Chem. A **104**, 1 (2000).
[2]Y. Berlin, A. Burin, J. Friedrich, and J. Köhler, Phys. Life Rev. **4**, 64 (2007).
[3]F. Grazioso, B. R. Patton, and J. M. Smith, Rev. Sci. Instrum. **81**, 093705 (2010).
[4]V. Hirschfeld and C. G. Huebner, Rev. Sci. Instrum. **81**, 113705 (2010).
[5]J. Jasny, J. Sepiol, T. Irngartinger, M. Traber, A. Renn, and U. P. Wild, Rev. Sci. Instrum. **67**, 1425 (1996).
[6]M. Vacha, H. Yokoyama, T. Tokizaki, M. Furuki, and T. Tani, Rev. Sci. Instrum. **70**, 2041 (1999).
[7]S. Marcet, C. Ouellet-Plamondon, and S. Francoeur, Rev. Sci. Instrum. **80**, 063101 (2009).
[8]J. M. Segura, A. Renn, and B. Hecht, Rev. Sci. Instrum. **71**, 1706 (2000).
[9]A. Hogele, S. Seidl, M. Kroner, K. Karrai, C. Schulhauser, O. Sqalli, J. Scrimgeour, and R. J. Warburton, Rev. Sci. Instrum. **79**, 023709 (2008).
[10]M. Hussels and M. Brecht, Biochemistry **50**, 3628 (2011).
[11]E. Schlodder, M. Hussels, M. Cetin, N. V. Karapetyan, and M. Brecht, Biochim. Biophys. Acta **1807**, 1423 (2011).
[12]F. Jelezko, C. Tietz, U. Gerken, J. Wrachtrup, and R. Bittl, J. Phys. Chem. B **104**, 8093 (2000).
[13]N. V. Karapetyan, E. Schlodder, R. van Grondelle, and J. P. Dekker, *Photosystem I: The Light-Driven Plastocyanin:Ferredoxin Oxidoreductase*, Advances in Photosynthesis and Respiration Vol. 24, edited by J. H. Golbeck (Springer, 2006).
[14]B. Gobets and R. van Grondelle, Biochim. Biophys. Acta **1507**, 80 (2001).
[15]M. Brecht, V. Radics, J. B. Nieder, and R. Bittl, Proc. Natl. Acad. Sci. U.S.A. **106**, 11857 (2009).
[16]M. Brecht, M. Hussels, E. Schlodder, and N. V. Karapetyan, Biochim. Biophys. Acta **1817**, 445 (2012).
[17]M. Brecht, H. Studier, A. F. Elli, F. Jelezko, and R. Bittl, Biochemistry **46**, 799 (2007).
[18]V. V. Shubin, I. N. Bezsmertnaya, and N. V. Karapetyan, J. Photochem. Photobiol., B **30**, 153 (1995).

Chapter 5

Resolution enhancement for low-temperature scanning microscopy by cryo-immersion

The microscope presented in the previous chapter allows us to insert samples with previously attached fluids or solids attached on the sample cover slides. By using an objective lens with high numerical aperture and choosing a fluid with high refractive index and appropriate melting temperatures the area between the optical element of the microscope objective and the first sample cover slide can be immersed comparably to microscopes operating at ambient conditions. This approach leads to an increase of the effective numerical aperture of the objective lens with respect to dry conditions, whereas the resolution of confocal scan images at low temperatures can be enhanced. Due to the refractive index depending NA of the objective lens the excitation beam can be focused on the piezoelectric movable sample within a smaller spot in order to record spatially resolved the fluorescence of diffraction limited objects. The method of immersing a microscope objective at cryogenic temperatures (160 K) is experimentally demonstrated by using propanol as immersion fluid and single quantum dots as diffraction limited emitters. Analyzing the widths of the cross sections (point spread function) of confocally imaged single quantum dots yields a significantly increased effective numerical aperture of the immersed objective lens which is close to values determined at ambient conditions with a common immersion oil.

This chapter is based on:
Metzger, M., Konrad, A., Skandary S., Ashraf, I., Meixner, A.J., Brecht M. "Resolution enhancement for low-temperature scanning microscopy by cryo-immersion" *Optics Express*, **2016**, 24 (12), 13023-13032.

Resolution enhancement for low-temperature scanning microscopy by cryo-immersion

Michael Metzger,[1] Alexander Konrad,[1] Sepideh Skandary,[1] Imran Ashraf,[1] Alfred J. Meixner[1] and Marc Brecht[1,2,3,*]

[1]*Institute of Physical and Theoretical Chemistry, University of Tuebingen, Tuebingen, Germany*

[2]*Zurich University of Applied Science, Institute of Applied Mathematics and Physics, Winterthur, Switzerland*

[3]*Process Analysis and Technology (PA&T), Reutlingen Research Institute, Reutlingen University, Reutlingen, Germany*

[*]*marc.brecht@uni-tuebingen.de*

Abstract: Here we report a simple way to enhance the resolution of a confocal scanning microscope under cryogenic conditions. Using a microscope objective (MO) with high numerical aperture ($NA = 1.25$) and 1-propanol as an immersion fluid with low freezing temperature we were able to reach an imaging resolution at 160 K comparable to ambient conditions. The MO and the sample were both placed inside the inner chamber of the cryostat to reduce distortions induced by temperature gradients. The image quality of our commercially available MO was further enhanced by scanning the sample (sample scanning) in contrast to beam scanning. The ease of the whole procedure marks an essential step towards the development of cryo high-resolution microscopy and correlative light and electron cryo microscopy (cryoCLEM).

OCIS codes: (180.1790) Confocal microscopy; (180.2520) Fluorescence microscopy; (180.5810) Scanning microscopy; (110.0180) Microscopy; (330.6130) Spatial resolution.

References and links

1. M. Minsky, "Memoir on inventing the confocal scanning microscope," Scanning **10**(4), 128–138 (1988).
2. G. Lin, M. K. Chawla, K. Olson, C. A. Barnes, J. F. Guzowski, C. Bjornsson, W. Shain, and B. Roysam, "A multi-model approach to simultaneous segmentation and classification of heterogeneous populations of cell nuclei in 3D confocal microscope images," Cytometry A **71A**(9), 724–736 (2007).
3. A. Drechsler, M. A. Lieb, C. Debus, A. J. Meixner, and G. Tarrach, "Confocal microscopy with a high numerical aperture parabolic mirror," Opt. Express **9**(12), 637–644 (2001).
4. E. Abbe, "Beitraege zur Theorie des Mikroskops und der mikroskopischen Wahrnehmung," Arch. Mikrosk. Anat. **9**(1), 413–418 (1873).
5. M. Bates, B. Huang, G. T. Dempsey, and X. W. Zhuang, "Multicolor super-resolution imaging with photo-switchable fluorescent probes," Science **317**(5845), 1749–1753 (2007).
6. E. Betzig, G. H. Patterson, R. Sougrat, O. W. Lindwasser, S. Olenych, J. S. Bonifacino, M. W. Davidson, J. Lippincott-Schwartz, and H. F. Hess, "Imaging intracellular fluorescent proteins at nanometer resolution," Science **313**(5793), 1642–1645 (2006).
7. M. Friedenberger, M. Bode, A. Krusche, and W. Schubert, "Fluorescence detection of protein clusters in individual cells and tissue sections by using toponome imaging system: sample preparation and measuring procedures," Nat. Protoc. **2**(9), 2285–2294 (2007).

#261789 Received 18 Apr 2016; revised 27 May 2016; accepted 27 May 2016; published 6 Jun 2016

8. S. W. Hell, M. Dyba, and S. Jakobs, "Concepts for nanoscale resolution in fluorescence microscopy," Curr. Opin. Neurobiol. **14**(5), 599–609 (2004).
9. S. Manley, J. M. Gillette, G. H. Patterson, H. Shroff, H. F. Hess, E. Betzig, and J. Lippincott-Schwartz, "High-density mapping of single-molecule trajectories with photoactivated localization microscopy," Nat. Methods **5**(2), 155–157 (2008).
10. M. J. Rust, M. Bates, and X. W. Zhuang, "Sub-diffraction-limit imaging by stochastic optical reconstruction microscopy (STORM)," Nat. Methods **3**(10), 793–795 (2006).
11. M. Sackrow, C. Stanciu, M. A. Lieb, and A. J. Meixner, "Imaging nanometre-sized hot spots on smooth au films with high-resolution tip-enhanced luminescence and raman near-field optical microscopy," Chem. Phys. Chem. **9**(2), 316–320 (2008).
12. C. Stanciu, M. Sackrow, and A. J. Meixner, "High NA particle- and tip-enhanced nanoscale raman spectroscopy with a parabolic-mirror microscope," J. Microsc. **229**(2), 247–253 (2008).
13. R. Zondervan, F. Kulzer, M. A. Kol'chenko, and M. Orrit, "Photobleaching of rhodamine 6G in poly(vinyl alcohol) at the ensemble and single-molecule levels," J. Phys. Chem. A **108**(10), 1657–1665 (2004).
14. W. E. Moerner and M. Orrit, "Illuminating single molecules in condensed matter," Science **283**(5408), 1670–1676 (1999).
15. R. Kaufmann, C. Hagen, and K. Grunewald, "Fluorescence cryo-microscopy: current challenges and prospects," Curr. Opin. Chem. Biol. **20**, 86–91 (2014).
16. M. Hussels, A. Konrad, and M. Brecht, "Confocal sample-scanning microscope for single-molecule spectroscopy and microscopy with fast sample exchange at cryogenic temperatures," Rev. Sci. Instrum. **83**(12), 123706 (2012).
17. R. Kaufmann, P. Schellenberger, E. Seiradake, I. M. Dobbie, E. Y. Jones, I. Davis, C. Hagen, and K. Grunewald, "Super-resolution microscopy using standard fluorescent proteins in intact cells under cryo-conditions," Nano Lett. **14**(7), 4171–4175 (2014).
18. S. Weisenburger, B. Jing, A. Renn, and V. Sandoghdar, "Cryogenic localization of single molecules with angstrom precision," Proc. SPIE **8815**, 88150D (2013).
19. S. Weisenburger, B. Jing, D. Hanni, L. Reymond, B. Schuler, A. Renn, and V. Sandoghdar, "Cryogenic colocalization microscopy for nanometer-distance measurements," Chem. Phys. Chem. **15**(4), 763–770 (2014).
20. Y. Shibata, W. Katoh, T. Chiba, K. Namie, N. Ohnishi, J. Minagawa, H. Nakanishi, T. Noguchi, and H. Fukumura, "Development of a novel cryogenic microscope with numerical aperture of 0.9 and its application to photosynthesis research," BBA-Bioenergetics **1837**(6), 880–887 (2014).
21. M. Yoshita, T. Sasaki, M. Baba, and H. Akiyama, "Application of solid immersion lens to high-spatial resolution photoluminescence imaging of GaAs quantum wells at low temperatures," Appl. Phys. Lett. **73**(5), 635–637 (1999).
22. M. Vollmer, H. Giessen, W. Stolz, W. W. Ruhle, L. Ghislain, and V. Elings, "Ultrafast nonlinear subwavelength solid immersion spectroscopy at t = 8 K," Appl. Phys. Lett. **74**(13), 1791–1793 (1999).
23. W. X. Li, S. C. Stein, I. Gregor, and J. Enderlein, "Ultra-stable and versatile widefield cryo-fluorescence microscope for single-molecule localization with sub-nanometer accuracy," Opt. Express **23**(3), 3770–3783 (2015).
24. C. L. Schwartz, V. I. Sarbash, F. I. Ataullakhanov, J. R. Mcintosh, and D. Nicastro, "Cryo-fluorescence microscopy facilitates correlations between light and cryo-electron microscopy and reduces the rate of photobleaching," J. Microsc. **227**(2), 98–109 (2007).
25. A. Rigort, E. Villa, F. J. B. Bauerlein, B. D. Engel, and J. M. Plitzko, "Integrative approaches for cellular cryo-electron tomography: Correlative imaging and focused ion beam micromachining," Methods Cell Biol. **111**, 259–281 (2012).
26. L. F. van Driel, J. A. Valentijn, K. M. Valentijn, R. I. Koning, and A. J. Koster, "Tools for correlative cryo-fluorescence microscopy and cryo-electron tomography applied to whole mitochondria in human endothelial cells," Eur. J. Cell Biol. **88**(11), 669–684 (2009).
27. A. Briegel, S. Y. Chen, A. J. Koster, J. M. Plitzko, C. L. Schwartz, and G. J. Jensen, "Correlated light and electron cryo-microscopy," Methods Enzymol. **481**, 317–341 (2010).
28. M. Schorb and J. A. G. Briggs, "Correlated cryo-fluorescence and cryo-electron microscopy with high spatial precision and improved sensitivity," Ultramicroscopy **143**, 24–32 (2014).
29. P. Anger, A. Feltz, T. Berghaus, and A. J. Meixner, "Near-field and confocal surface-enhanced resonance raman spectroscopy at cryogenic temperatures," J. Microsc. **209**, 162–166 (2003).
30. M. A. Le Gros, G. McDermott, M. Uchida, C. G. Knoechel, and C. A. Larabell, "High-aperture cryogenic light microscopy," J. Microsc. **235**(1), 1–8 (2009).
31. E. A. Smith, B. P. Cinquin, M. Do, G. McDermott, M. A. Le Gros, and C. A. Larabell, "Correlative cryogenic tomography of cells using light and soft x-rays," Ultramicroscopy **143**, 33–40 (2014).
32. T. L. Jennings, S. G. Becker-Catania, R. C. Triulzi, G. L. Tao, B. Scott, K. E. Sapsford, S. Spindel, E. Oh, V. Jain, J. B. Delehanty, D. E. Prasuhn, K. Boeneman, W. R. Algar, and I. L. Medintz, "Reactive semiconductor nanocrystals for chemoselective biolabeling and multiplexed analysis," ACS Nano **5**(7), 5579–5593 (2011).
33. W. W. Yu, L. H. Qu, W. Z. Guo, and X. G. Peng, "Experimental determination of the extinction coefficient of

#261789 Received 18 Apr 2016; revised 27 May 2016; accepted 27 May 2016; published 6 Jun 2016

CdTe, CdSe, and CdS nanocrystals," Chem. Mater. **15**(14), 2854–2860 (2003).
34. M. Hussels, M. Brecht, "Vorrichtung und Verfahren zum Transferieren eines Probenhalters von einer Transportvorrichtung zu einer Scanvorrichtung," Patent DE102012218377 B3, April 17 (2014).
35. K. Moutzouris, M. Papamichael, S. C. Betsis, I. Stavrakas, G. Hloupis, and D. Triantis, "Refractive, dispersive and thermo-optic properties of twelve organic solvents in the visible and near-infrared," Appl. Phys. B **116**(3), 617–622 (2014).
36. V. Hirschfeld and C. G. Hubner, "A sensitive and versatile laser scanning confocal optical microscope for single-molecule fluorescence at 77 K," Rev. Sci. Instrum. **81**(11), p. 113705, Nov. 2010.
37. F. Grazioso, B. R. Patton, and J. M. Smith, "A high stability beam-scanning confocal optical microscope for low temperature operation," Rev. Sci. Instrum. **81**(9), 093705 (2010).
38. A. Konrad, F. Wackenhut, M. Hussels, A. J. Meixner, and M. Brecht, "Temperature dependent luminescence and dephasing of gold nanorods," J. Phys. Chem. B **117**(41), 21476–21482 (2013).
39. J. Dubochet, "The physics of rapid cooling and its implications for cryoimmobilization of cells," Methods Cell Biol. **79**(79), 7–21 (2007).
40. C. van Rijnsoever, V. Oorschot, and J. Klumperman, "Correlative light-electron microscopy (CLEM) combining live-cell imaging and immunolabeling of ultrathin cryosections," Nat. Methods **5**(11), 973–980 (2008).

1. Introduction

Light microscopy is an often used technique especially for investigating biological samples and in combination with spectroscopy for getting a deeper understanding of chemical and physical processes with high spatial resolution. Confocal microscopy developed by Marvin Minsky in 1957 [1] was a remarkable step in optical microscopy that increased the imaging contrast for gaining spatial information on luminescent samples. The principle of confocal microscopy relies on focusing a laser beam to a diffraction limited spot and recording light emerging mainly from that volume. In this technique out-of-focus light will be suppressed and hence increases the image contrast and enables to record 3D images of different structures such as biological cells by implementing a pinhole in front of the detector [2]. Therefore, a high numerical aperture (NA) microscope objective (MO) with corrected aberrations is required for high quality imaging with a high axial and lateral resolution. The NA describes the acceptance cone of an objective (see Eq. (1)):

$$NA = n\sin(\alpha), \tag{1}$$

where n is the refractive index of the medium between the lens and the sample and α is half the opening angle of a focusing element. Hence, for extended samples the NA in air ($n_{air} = 1$) can never be larger than unity, which could be achieved e.g. by a parabolic mirror [3]. In order to increase the NA and thus the resolution of a microscope beyond unity an additional immersion fluid, such as water or immersion oil is used. The principle of immersion requires to fill the volume between the MO and sample by a transparent medium with a high refractive index. Using immersion liquids also increases the collection efficiency of the MO by reducing refraction and reflection at the interfaces between MO and sample. Nevertheless, the lateral resolution of light microscopes is typically restricted to the diffraction limit given by [4]:

$$d = \frac{\lambda}{2NA}, \tag{2}$$

where λ is the wavelength of light in vacuum and d is the minimal distance at which to identical point like sources can be resolved. Since several years, the diffraction limit hampering high resolution microscopy of nanoscopic particles or structures (size below 200 nm) was overcome by various super-resolution techniques at ambient conditions [5–12]. However, many chromophores or auto-fluorescent proteins are difficult to observe at room temperature especially at the single molecule level due to their low signal intensities, various quenching effects and fast photo-bleaching [13]. Further problems related to biological samples are drifts and degradation during measurements. One common solution for all these problems can be achieved by

#261789 Received 18 Apr 2016; revised 27 May 2016; accepted 27 May 2016; published 6 Jun 2016

reducing the temperature. This reduces photobleaching and enhances the fluorescence signal up to two orders of magnitude. Low temperature experiments of biological samples allow us to record fluorescence images without additional labeling [14]. Furthermore, effects of many biological samples like drifting and degradation are also eliminated. However, confocal cryogenic microscopy is challenging due to technical and mechanical requirements of the low temperatures environment. Beam scanning and widefield imaging as common techniques at cryogenic temperatures cannot reach a high resolution and image quality comparable to ambient conditions because the MOs for low temperatures are insufficiently corrected for aberrations. The reason for that is, that most high-performance MOs are corrected for room temperatures and lose their high imaging properties under cryogenic conditions and getting easily damaged by thermal stress [15]. Using confocal sample scanning instead of beam-scanning the lower off-axis performance of the MO at low temperatures is not important for the image quality [16]. A further hurdle - if one aims to implement high-resolution techniques at low temperatures - is the low longterm stability of the whole setup. These instabilities are caused by temperature gradients at the interface between the room and the low temperatures segments of the setup [15]. Nevertheless, several approaches to increase the resolution of microscopes at cryogenic temperatures could be achieved. Kaufmann *et al.* [17] utilize the effect of photoswitching [18, 19] of fluorescent marker proteins by using a 0.75 NA MO for super-resolution fluorescence cryogenic-microscopy. Shibata *et al.* developed a microscope with NA of 0.9, where the MO is mounted inside of the cryogenic vacuum space [20]. One method exceeding an NA of unity, was achieved by using solid immersion lenses [21] exhibiting an NA of 1.23 [22] with the disadvantage of a very small field of view. A versatile widefield cryo-fluorescence microscope for single molecule localization with good thermal and mechanical stability was recently developed by Li *et al.* [23], featuring however an NA of only 0.7. A further often used technique combines low temperatures fluorescence microscopy with other imaging techniques like electron microscopy. One example bases on the application of long working distance MOs with NA of 0.7 [24] or 0.75 [25, 26] and is able to combine cryogenic fluorescence microscopy with cryo-electron microscopy [27]. Another setup developed by Schorb *et al.* applies a short working distance MO with an NA of 0.95 in combination with electron microscopy [28]. However, until today none of these techniques were able to provide a resolution and image quality compared to conventional microscopes at ambient conditions. Only with a parabolic mirror as focusing element a diffraction limited resolution and an NA close to unity was demonstrated at 8.5 K along with a large scanning range [29]. The decisive factor under cryogenic conditions is that the simple application of immersion fluids to provide an NA higher than unity is exceedingly problematic due to their high freezing temperatures. One promising brightfield imaging approach to increase the resolution under cryogenic temperatures by immersing the microscope was reported by Le Gros *et al.* [30, 31]. They use liquid propane or iso-pentane as immersion fluids and an MO placed outside the sample area, cooled with a copper cooling strip by liquid nitrogen. Summarizing, all these techniques may reach a resolution comparable to microscopes at ambient conditions but at the cost of scan range, image quality or mechanical stability.

In this study, we present a microscope setup, which allows us to immerse an MO ($NA = 1.25$) together with the sample both positioned inside the sample chamber of a cryostat. Thus, we are able to record confocal luminescence images with an imaging resolution comparable to ambient conditions and scan ranges only limited by the travel range of the piezo steppers (limited to 15×15 mm). Additionally, combining our large range scanning stage [16] with a sample transfer system allows us to load frozen or vitrified samples into the cold cryostat and remove them after the measurements without heating the samples to ensure a reproducible cryogenic cycle [34]. We demonstrate the capability of our approach by confocally imaged quantum dots (QD) at 160 K with 1-propanol immersed MO and could appoint a resolution enhancement of

#261789 Received 18 Apr 2016; revised 27 May 2016; accepted 27 May 2016; published 6 Jun 2016

1.3 in comparison to our $NA = 0.85$ air objective.

2. Experimental setup

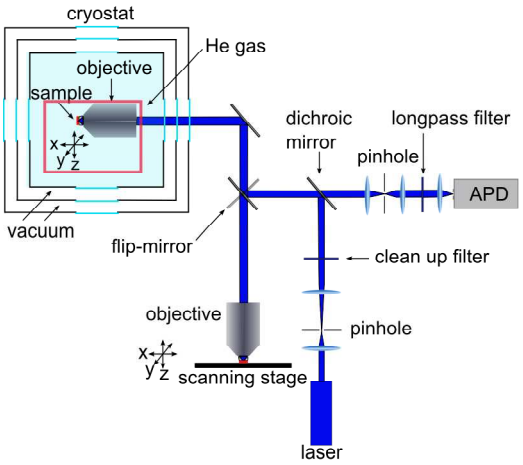

Fig. 1. Sketch of the low and room temperature setup for confocal imaging.

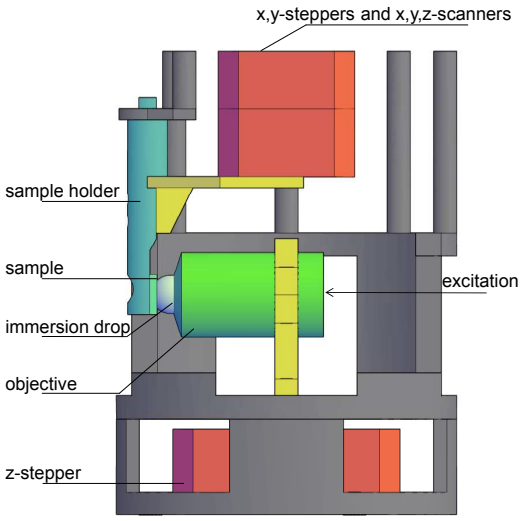

Fig. 2. Sketch of the focusing system (red quadrangle in Fig. 1) for low temperature microscopy adapted from [16]. With a special sample transfer system, consisting of x, y, z, steppers (red), to transfer frozen (also vitrified) samples into the precooled cryostat.

According to the manufacturer (ebioscience), the QDs have the following properties: Amine-Functionalized eFluor(R) 650NC nanocrystal consisting of CdSe/ZnS with a diameter of about 8.7 nm [32]. As a result, the QDs can be regarded as point light sources enabling us to estimate the resolution by means of the FWHM of the PSFs. The QDs exhibit a relativly high absorption

#261789 Received 18 Apr 2016; revised 27 May 2016; accepted 27 May 2016; published 6 Jun 2016

cross section, a large luminescence quantum yield, a molar extinction coefficient of 1.11E6 and an emission maximum around 650 nm without any sidebands and a high photostability [33]. A droplet (1 μl) of QDs solution diluted in H_2O/glycerol with concentration 1 $pmol/l$ to guaranty single particle microscopy was deposited between two 4 $\times$ 4 mm^2 (thickness 200 μm) glass coverslips cleaned with chromosulfuric acid. For the room temperature experiments, we used two 22 $\times$ 22 mm^2 coverslips and immersion oil (Zeiss Immersol 518 F). For the low temperature experiments, we used 1-propanol as immersion fluid due to its low melting point (147 K) and good transparency. The measurements were performed with a home-built confocal microscope consisting of a room and low temperature branch shown in Fig. 1. An enlarged section of the sample transfer system (red quadrangle in Fig. 1) and the low temperature sample head are shown in Fig. 2. Scanning the sample with nanometer precision was achieved at ambient condition by a feed-back controlled three axis scanning table (Physik Instrumente P-517.3CL, 100 $\times$ 100 $\times$ 20 μm) and at low temperatures by a multiaxis scanning stage (attocube steppers twice ANPx320 for x- and y-, ANPz101eXT for z-axis, scanners ANSxy100lr for x- and z-, ANSz100lr for y-axis) in a Helium-cryostat (Janis, SVT-200). The voltage dependent expansion of the scanners and their linearity were calibrated for low temperature (160 K) by scanning a copper grid (2000 lines/inch). The temperature dependent expansion deviation of the piezo scanners could be determined by the calibration measurements allowing us to calculate the spatial expansion of the scanners very accuratly. For the immersion measurements at room and low temperature we used an MO with high NA (Microthek, 100 $\times$, $NA = 1.25$) and as a reference at low temperature an air MO (Microthek, 60 $\times$, $NA = 0.85$) without immersion liquid. The temperature of 160 K in He atmosphere controlled by a cernox sensor (CX-1030-SD-HT 0.3L) is reached by cooling the outer temperature shield with liquid nitrogen. Temperature variations during the measurements can be minimized by an active temperature control sensor close to the sample [16]. The reliability of the microscope and the temperature control was demonstrated in a recent study [38]. A 488 nm *cw* laser diode (OBIS 488-20 LS) with a linear polarized Gaussian beam profile was used for exciting the QD. Their luminescence was collected by the very same MO passed a dichroic mirror, a 30 μm pinhole and a longpass filter (AHF F76-490) and was finally detected by an avalanche photodiode (APD, Laser Components, COUNT-100C). More details, of the setup were recently described by Hussels *et al.* [16].

3. Results

The immersion of the sample was achieved by applying a droplet of immersion liquid on the sample coverslip in three steps (Fig. 3). First we precool our sample holder with the mounted sample between two coverslips in a liquid nitrogen bath (Figs. 3(a) and 3(b)). After that a few droplets of 1-propanol were frozen directly on the coverslips (Figs. 3(c) and 3(d)).

A specially designed sample transfer mechanism allows us to insert the frozen sample into the precooled (140 K) cryostat without melting the immersion liquid [16]. Inside the cryostat the sample holder is translated towards the MO to achieve contact between the frozen immersion droplet and the MO. Then the sample chamber was heated slowly above the melting point (147 K) of 1-propanol to 160 K. Finally, we reduced the distance between sample and MO in order to bring the sample in the focus of the MO as shown in Fig. 2. Figure 4 shows confocal scanning images of luminescent QDs both at a temperature of 160 K with (right) and without immersion (left) excited with a 488 nm diode laser. The image on the left side was recorded with a commonly used air MO ($NA = 0.85$). On the right side, a segment of an image of the same QD sample recorded with a high numerical MO ($NA = 1.25$) immersed with 1-propanol is shown. Both images show symmetrical spots representing single QDs. However, the spot diameters become clearly smaller with higher theoretical NA (with immersion). Thus, no distortions, drifts or other instabilities even with the immersed MO for the respective temperature

#261789 Received 18 Apr 2016; revised 27 May 2016; accepted 27 May 2016; published 6 Jun 2016

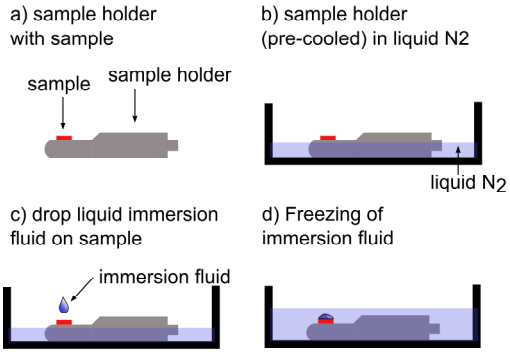

Fig. 3. Immersion procedure. a) Sample placed on sample holder b) precooled (liquid nitrogen) sample holder with sample c) applying of 1-propanol droplets directly on the glass coverslips d) freezing of 1-propanol.

disturb the measurements. However, the absolute intensities in Fig. 4 are not comparable due to different experimental conditions such as objective and sample changes. Furthermore not all QDs visible in the images are located in the focal plane causing individual excitation and luminescence yields.

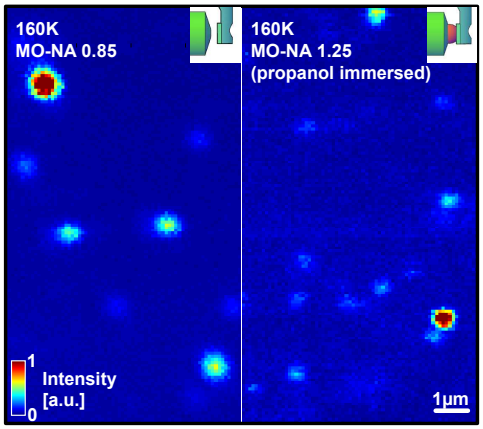

Fig. 4. Left: QD images recorded at 160 K with an air MO ($NA = 0.85$). Right: QD images recorded at 160 K with an immersion MO ($NA = 1.25$) with 1-propanol as immersion liquid.

To quantify the resolution of the respective MO reached by our experiments, we determine the point spread function (PSF) by scanning single QD in nanometer steps through the excitation focus. The excitation focus was generated by the linearly polarized ($\lambda = 488$ nm) beam with a diameter of 6 mm, filling the back aperture of the MO and can approximated by an Airy pattern with a nominal radius between the intensity maximum and the first intensity minimum of $r = 0,61 \cdot \frac{\lambda}{NA}$. As a reference measurement and to confirm the optical properties of the $NA = 1.25$ MO, we recorded several confocal images at 300 K immersed with standard immersion oil. Analyzing the line sections for these three conditions (160 K with 1-propanol immersion, 160 K without immersion and 300 K with oil immersion) allow us to determine the

#261789 Received 18 Apr 2016; revised 27 May 2016; accepted 27 May 2016; published 6 Jun 2016

full width of half maximum (FWHM) of the PSF for each single spot as a measure for the resolution. In Fig. 5 three spots are shown exemplarily for each condition, representing a single QD (Figs. 5(A1)–5(C1)) together with the line sections (Figs. 5(A2)–5(C2)) indicated by a white line in Figs. 5(A1)–5(C1). Figure 5(A1) shows the spatially resolved luminescence of a single QD at 160 K recorded with an air MO. The corresponding line section (Fig. 5(A2)) showing the luminescence intensity as function of the x-axis scanner position in μm (blue line) was fitted by a Gaussian (red line) in order to determine the FWHM of the lateral PSF. The usage of a Gaussian to reproduce the PSF is a well-founded approximation due to our linear Gaussian excitation beam and the small size of the emitter working as a point light source [8]. Figure 5(B1) shows one spot out of many from an image recorded with the 1-propanol immersed $NA = 1.25$ MO of the same QD sample. Figures 5(C1) and 5(C2) show images and corresponding line sections recorded with the same MO at 300 K immersed with standard immersion fluid (Zeiss Immersol^{T}M 518 F). Obviously these three line sections are all symmetric and scale inversely with the theoretical effective NA as expected. Figures 5(A3)-(C3) show the distribution of the FWHM for each condition.

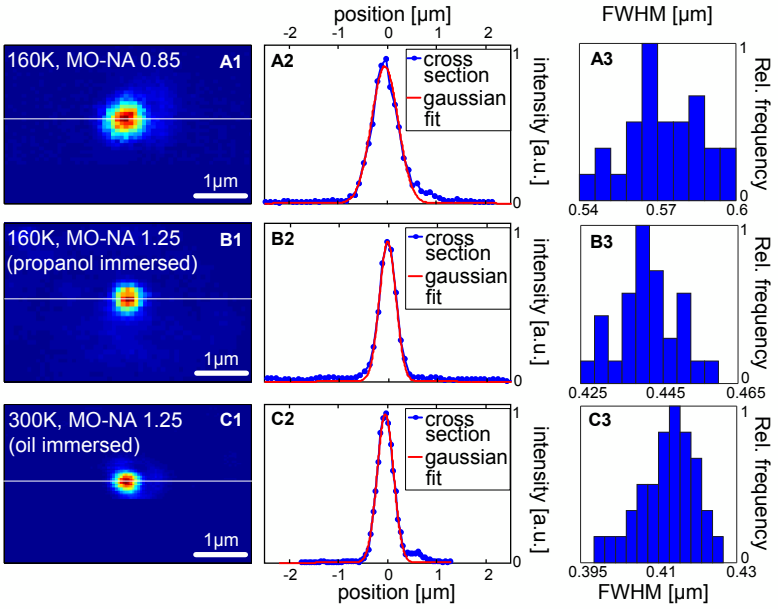

Fig. 5. Left: Three confocal luminescence images showing each a single QD recorded for different conditions. A1) enlarged section of a QD at 160 K recorded with an air MO with an $NA = 0.85$. A2) line section (blue line) indicated by the white line in Fig. A1 with Gaussian fit (red line, $FWHM = 0.574$ μm) to determine the PSF. A3) distribution of the FWHM measured with an air MO. B1) confocal image of a QD at 160 K with 1-propanol immersed MO ($NA = 1.25$). B2) line section (blue line) indicated by the white line in Fig. B1 with Gaussian fit (red line, $FWHM = 0.442$ μm). B3) distribution of the FWHM measured with an immersion MO immersed with 1-propanol. C1) confocal image of a QD at 300 K with the same MO ($NA = 1.25$) oil immersed. C2) line section (blue line) indicated by the white line in Fig. C1 with Gaussian fit (red line, $FWHM = 0.415$ μm). C3) distribution of the FWHM measured with an immersion MO immersed with immersion oil.

Table 1 summarizes the results for the three different measuring conditions. The column in bold shows the results of our 1-propanol immersed measurements with a resolution enhance-

#261789 Received 18 Apr 2016; revised 27 May 2016; accepted 27 May 2016; published 6 Jun 2016

ment of 1.3 in comparison to our air objective and a comparable resolution to ambient conditions (right column).

Table 1. Comparison of our experimental results with an air objective, an oil immersed objective and the same objective immersed with 1-propanol.

	air objective	**immersion objective**	immersion objective
Temperatur [K]	160	**160**	300
Immersion Liquid	–	**1-propanol**	immersion oil
Refractive Index [at 300 K]	1.0	**1.3851 [35]**	1.518
FWHM [nm]	574	**442**	415
resolution enhancement	–	**1.3**	1.38

4. Discussion

The scan images recorded with the 1-propanol immersed MO show obviously comparable quality, scan range and resolution with respect to experiments at ambient conditions. Hence, we can claim that the lateral resolution of the immersed MO under cryogenic conditions is enhanced by a factor of 1.3 with respect to our standard air objective with $NA = 0.85$. Furthermore, all recorded images show no distortions, drifts or thermally induced variations of the sample position or the scanner translation. This is a result of the microscope design whereby the optical elements, the sample and the scanning stage are in a controllable thermally stable equilibrium.

The resolution enhancement arises from the increased refractive index of the 1-propanol with respect to helium as the medium between MO and sample coverslip. The NA depends linearly on the refractive index contributes linearly to the resolution of images acquired by fluorescence microscopy. The mismatch of the refractive indices between glass and 1-propanol are leading only to a reduced effective NA with respect to standard oil. We used 1-propanol as immersion fluid due to its melting point and its hydrophobic properties (high stability on glass substrates). Due to the lower refractive index of 1-propanol ($n_{532\ nm,300\ K} = 1.385$ [35] as compared to immersion oil ($n_{546{,}1\ nm,298\ K} = 1.518$) and the large number of optical elements (cryo windows) we estimated an enhancement factor around 1.3 compared to 1.38 with oil. To our knowledge we found no appropriate refractive index for 160 K. Hence, we make the following assumption using the TOC-value of 1-propanol of -4×10^{-4} resulting in a refractive index of 1.46 for 160 K [35].

For measuring our sample under cryogenic conditions, which is previously immersed outside the croystat a sample transfer system is indispensable. Our patented sample transfer system in combination with a sample scanning stage, instead of beam-scanning [36, 37], allows us to quickly insert (and remove) samples with attached frozen immersion droplets, into the precooled cryostat. Additionally, the optical properties of the whole setup will be increased by using sample scanning. Typical microscopes with cryo stages commonly use air MOs with a long working distance limiting the NA < 1 [24–26]. However, cryogenic systems with a high long term stability and NA close to unity usually do not feature the possibility of a transfer system [20]. Our method combines short working distance immersion MOs with an NA of 1.25 and a sample scanning stage allowing us to keep the whole microscope at a defined temperature. As a result, we have a mechanically stable system without temperature gradients resulting in a high imaging quality and stability which is a prerequisite for high resolution techniques such as STORM. In order to image vitrified cells (below 135 K [39]) however the immersion fluid has to be varied to reach a temperature below 135 K.

The improved spatial resolution of the developed method will be further applicable to correlative microscopy [27], which is a recently emerging technique combining cryo-electron to-

#261789 Received 18 Apr 2016; revised 27 May 2016; accepted 27 May 2016; published 6 Jun 2016

mography and fluorescence microscopy.

5. Conclusion

We demonstrated the resolution enhancement by applying an immersion fluid under cryogenic temperatures. This could be shown by determing the FWHM of confocally imaged QDs whereas an effective resolution enhancement of 1.3 compared to an air objective was achieved. Key to our experiment is the transfer mechanism which allows to insert a cooled sample with a frozen droplet of immersion liquid into the precooled cryostat and to bring it into contact with the objective lense. By our method of resolution enhancement at low temperature new opportunities can be realized e.g. the observation of biological systems, which can be imaged by their auto-fluorescence without additional labeling. The used sample transfer system together with our presented technique to immerse MOs at low temperature is therefore also of great relevance for correlative light and electron cryo microscopy (cryoCLEM) [27, 40]. With our long-term stable system without any temperature gradients super resolution methods like STED and STORM, which require a mechanical stability and high NA MO are also conceivable.

Acknowledgments

We gratefully acknowledge financial support by Baden-Wuerttemberg Stiftung and Deutsche Forschungsgemeinschaft. We thank the Kay Gruenewald group (division of structural biology, University of Oxford), especially Christoph Hagen and Rainer Kaufmann for helpful discussions.

#261789 Received 18 Apr 2016; revised 27 May 2016; accepted 27 May 2016; published 6 Jun 2016

Chapter 6

Revealing the radiative and non-radiative relaxation rates of the fluorescence dye Atto488 in a $\lambda/2$ Fabry-Pérot-resonator by spectrally an time resolved measurements

In this chapter the impact of an altered photonic environment by a tunable microresonator on the spectral and temporal properties of the fluorescence of an organic dye molecules, Atto488, is presented by means of confocal microscopy. The free space fluorescence spectrum of the fluorophore Atto488 is structured by several radiative transitions from an electronic excited state into serried vibronic levels of the electronic ground state, which are spectrally not resolvable with common microscopy and spectroscopy at ambient conditions. The modified photonic mode density induced by a $\lambda/2$ Fabry-Pérot resonator alters the fluorescent deactivation of the excited molecule leading to modified fluorescence spectra and relaxation rates according to the Purcell factor. This is observed by in the spectral and time domain as function of the cavity on-axis transmission wavelength. A model is presented based on the possibility to describe and reproduce the shape of spectral bands depending on the impact of the Purcell factor for the respective cavity lengths. The model also includes the modifications of the radiative rates of the spectral bands and the impact of the metal surfaces of the resonator on the non-radiative relaxation rate. Thus, this method allows to resolve the spectral properties of the radiative transitions of the fluorophore, quantify the radiative and non-radiative relaxation properties and control the observed spectral and temporal response of the molecules emission.

This chapter is based on:
Konrad, A., Metzger, M., Kern, A.M., Brecht M., Meixner A.J. "Revealing the radiative and non-radiative relaxation rates of the fluorescent dye Atto488 in a $\lambda/2$ Fabry-Pérot-resonator by spectral and time resolved measurements", *Nanoscale*, **2016**, 8, 14541-14547.

Nanoscale

PAPER

View Article Online
View Journal | View Issue

Cite this: *Nanoscale*, 2016, **8**, 14541

Revealing the radiative and non-radiative relaxation rates of the fluorescent dye Atto488 in a $\lambda/2$ Fabry–Pérot-resonator by spectral and time resolved measurements†

Alexander Konrad,*[a] Michael Metzger,[a] Andreas M. Kern,[a] Marc Brecht[a,b] and Alfred J. Meixner*[a]

Received 22nd March 2016,
Accepted 1st July 2016

DOI: 10.1039/c6nr02380k

www.rsc.org/nanoscale

Using a Fabry–Pérot-microresonator with controllable cavity lengths in the $\lambda/2$-regime, we show the controlled modification of the vibronic relaxation dynamics of a fluorescent dye molecule in the spectral and time domain. By altering the photonic mode density around the fluorophores we are able to shape the fluorescence spectrum and enhance specifically the probability of the radiative transitions from the electronic excited state to distinct vibronic excited states of the electronic ground state. Analysis and correlation of the spectral and time resolved measurements by a theoretical model and a global fitting procedure allows us to reveal quantitatively the spectrally distributed radiative and non-radiative relaxation dynamics of the respective dye molecule under ambient conditions at the ensemble level.

1. Introduction

The ability to reveal and control the optical properties of matter is the key for design and development of novel nanoscale photonic devices.[1–3] In particular, single quantum emitters such as fluorescent molecules,[1,4] quantum dots[5] or noble metal particles[6] are essential candidates for such applications. Besides the temperature dependent influence of the chemical environment of the host material, the fluorescence properties of a molecule depend in particular on the direct photonic environment.[7] Several approaches to sense or control optical properties such as fluorescence spectra or excited state lifetimes of electronically excited molecules have been described over the last few decades. In general, the two regimes of optical fields *i.e.* the near- and far field regimes, can be distinguished, which affect the radiative and non-radiative relaxation processes of fluorophores.[8] Near-field induced influences caused by strong localized fields on molecular dipoles were investigated, which can be generated by closely separated antenna-like objects such as nanoparticles,[8–10] nanostructures,[11,12] surfaces,[13] tips,[14] other molecules[4,15,16] or large molecular systems.[17,18] The optical near-field of such an antenna is able to couple to the near-field of the molecule transition dipole leading to enhanced or quenched emission.[8] On the other side, a quantum emitter can also be perturbed by optical far-fields of *e.g.* lasers,[19] resonators *via* the Purcell effect[20–23] or electric fields.[24,25] However, in order to sense or control the fluorescence properties of molecules, one requires both, the intrinsic properties of the emitter and the optical properties of the external perturbation[26] determined by the local density of optical states (LDOS).

Specifically, modeling and experimentally distinguishing between the radiative and non-radiative perturbation induced by a photonic device is a difficult task.[27] First of all, a description of the fluorescence properties in the time and spectral domain of molecules is hampered especially under ambient conditions, where fluorescent transitions are affected by inhomogeneous broadening. To date under ambient conditions the composition of the emission spectra could be described explicitly, though only at the single particle level, only for certain model systems with spectrally separable bands.[28] Thus, resolving closely separated spectral bands is not always possible. Secondly, relaxation from an electronically excited state can occur by non-radiative relaxation, which cannot be observed directly by optical means. Experimentally determined fluorescence lifetimes by time domain measurements only represent the total relaxation rate of the electronic transition. Thus, correlating the spectral and the time domain data of one chromophore cannot be achieved without further methods such as a controllable perturbation on the system.

[a]*Universität Tübingen, Institut für Physikalische und Theoretische Chemie, Auf der Morgenstelle 18, 72076 Tübingen, Germany.*
E-mail: alexander.konrad@uni-tuebingen.de, alfred.meixner@uni-tuebingen.de
[b]*Process Analysis and Technology (PA&T), Reutlingen Research Institute, Reutlingen University, Alteburgstr. 150, 72762 Reutlingen, Germany*

†Electronic supplementary information (ESI) available. See DOI: 10.1039/C6NR02380K

And thirdly, the ability to reproducibly control the impact of a photonic environment needs both, a full description of the perturbation and an appropriate instrumental device.

Several attempts have been reported addressing these issues. One method focuses on using plasmonic based nanoresonators,[29,30] nanocrystals[31] and nanoapertures[32,33] to shape and control the fluorescence of molecules. In particular, nanoantennas combined with scanning probes are promising devices to detect the near-field of fluorescent molecules.[34] Summarizing these studies, nanoscopic antennas with determinable impact on the near- and far-field of emitters can be used to obtain a deeper insight by modifying the dynamics of fluorescent and non-fluorescent deactivation mechanisms. The major advantage of such antennas is their very large field enhancement at certain localized hot spots and thus their strong impact on fluorescence. However, using metallic antennas in an extremely close proximity can cause besides quenching severe chemical interactions with the specimen leading to conformational changes or even chemical degradation.[35,36] Another problem arises from the positioning of the metal–antenna system with respect to the molecule, which has to be in a controlled manner with sub-nanometer precision due to the competitive enhancement of deactivation processes.[8] Additionally, the precise position and geometry of the antenna with respect to a molecule are often not well defined; also the inter- and intra-molecular dynamics of the specimen in time and space have to be known to achieve a quantitatively assessable impact on fluorescence. Other methods to gain information on fluorescent molecules are saturation spectroscopy, where the fluorescence intensity is detected as a function of excitation flux[37] or alternatively low-temperature single molecule spectroscopy,[38,39] where the inhomogeneous broadening of the spectra can be minimized in order to gain information on the spectral and temporal properties of a molecule. However, both methods also have their difficulties such as heating and photobleaching in the case of saturation spectroscopy or the use of experimentally demanding equipment in the case of low temperature single molecule spectroscopy.

Therefore, Fabry–Pérot-type $\lambda/2$-microresonators are promising candidates to investigate these issues avoiding an altered chemical environment by metal particles and without the requirement of single molecules or cryogenic temperatures. Their simple geometry allows one to tune reproducibly the cavity resonance *via* a mirror separation and thus the effective Purcell effect.[40,41] Several studies have demonstrated the ability of such microresonators to shape emission spectra of luminescent systems and enhance or suppress excited state relaxation dynamics such as the lifetimes of fluorescent molecules.[4,16,22,28] However, a study revealing the optical properties of a fluorescent molecule in both, the spectral and time domains under ambient conditions at the ensemble level is still missing. To this end, the fluorescence of the rhodamine derivative known under the commercial name Atto488 (see Fig. 1(a1); purchased from ATTO-TEC, Siegen, Germany) was analyzed in free space and in a tunable $\lambda/2$-microresonator by confocal scanning microscopy and spectroscopy combined

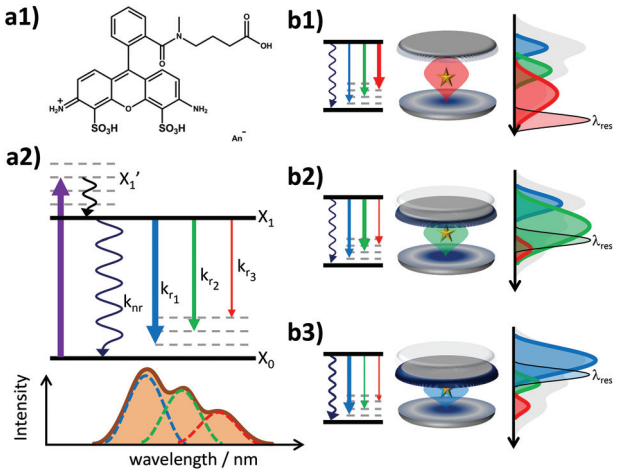

Fig. 1 (a1) Chemical structure of the dye molecule Atto488 (ATTO-TEC GmbH, Siegen, Germany). (a2) Jablonski-like diagram for a fluorescent chromophore X with an electronic ground state X_0 and excited state X_1. After pulsed excitation (violet arrow) into the excited vibronic level X_1' the system relaxes to the purely electronic level X_1. The electronic relaxation occurs either non-radiatively or radiatively into possible vibronic levels of the electronic ground state. The probability of each fluorescent decay is indicated by the thickness of the arrows which is a measure for the rate constants k_{r_i}. Each fluorescent transition can be described by a spectrally broadened Gaussian band due to thermal energy level fluctuations and phonon interactions with the environment. (b1–b3) Impact of a variable microresonator with the on-axis spectral emission of a fluorescent emitter by enhancing resonant and suppressing off-resonant radiative transitions. For smaller emitter–mirror separation the non-radiative quenching by the metal surface comes also into play.

with time correlated single photon counting (TCSPC). Rhodamine dyes exhibit a large quantum yield and have been exceedingly used in the last few decades.[42] The fluorescence decay of Atto488 obeys a mono-exponential time law, where the lifetime is in the regime of nanoseconds and is thus experimentally accessible by the Purcell effect. For a large number of different cavity lengths, the fluorescence of Atto488 was evaluated using a theoretical model[18,28] allowing us to assign quantitatively the relaxation properties of the excited molecule in both, the time and spectral domains, even for spectrally overlapping fluorescence bands. The quantitative assignment includes the characterization of the spectral distribution of the fluorescence as well as the radiative and non-radiative relaxation properties as a function of cavity separation. This approach finally allows us to correlate the optical information of the time and the spectral domains, which are connected *via* the wavelength dependent Purcell effect on the radiative decay rates and the shaping of the fluorescence spectra.

The fluorescence spectrum of Atto488 under ambient conditions is composed of several radiative transitions from the first electronically excited state to a sequence of vibronic levels of the electronic ground state with decreasing energy. Due to a large inhomogeneous broadening of these transitions, they cannot be resolved spectrally in free space. However, the controllable wavelength dependent perturbation *via* the Purcell

effect allows us to overcome this issue. The energy level diagram in Fig. 1(a2) illustrates the transition from the electronically excited state to the vibronic levels of the electronic ground state yielding different emission spectra for free space and in a microresonator for three different mirror separations (b1–b3). Each inhomogeneously broadened radiative transition (k_{1-3}) can be described in the spectral domain by a Gaussian with the parameters amplitude, spectral position and full width at half maximum (FWHM). For each microresonator setting, given by the on-axis transmission wavelength, the Purcell factor can be calculated as a function of the emission wavelengths.[18,28,40] This allows us to determine the effective enhancement and shaping for each vibronic band by calculating the modification of the radiative decay rate according to eqn (1):

$$k^{*}_{\mathrm{r}_i}(\lambda_{\mathrm{trans}}) = k_{\mathrm{r}_i}\frac{\int P(\lambda,\lambda_{\mathrm{trans}})S_{0_i}(\lambda)\mathrm{d}\lambda}{\int S_{0_i}(\lambda)\mathrm{d}\lambda}, \quad (1)$$

where $k^{*}_{\mathrm{r}_i}(\lambda_{\mathrm{trans}})$ is the modified decay rate for the electronic transition i, k_{r_i} is the free space decay rate (*i.e.* without resonator) for transition i, $P(\lambda,\lambda_{\mathrm{trans}})$ is the wavelength dependent Purcell factor for a given transmission wavelength and $S_{0_i}(\lambda)$ is the spectral shape representing the transition i, which is here the average of an ensemble of molecules. We assume that the spectrum of transition i under ambient conditions at the ensemble level can be described by a Gaussian.[43,44] Our model also implies that the resonator has no impact on both, the mechanisms of inhomogeneous broadening and the intrinsic eigenfrequency of the electronic transition dipole moment due to the weak coupling to the optical fields. The degree of inhomogeneous broadening for an ensemble spectrum is dependent on the interaction of the molecule with its chemical environment in a matrix, the temperature, and the ratio between the rate of spectral diffusion and the integration time. None of these parameters are altered when the experiments are performed in the resonator with respect to free space. Additionally, we assume that a transition into a higher vibronic level has a spectrum with a larger FWHM due to an increasing number of phonons accompanying the electronic transition.

Access to quantitative decay rate constants can be gained by measuring the fluorescence lifetimes of the molecules for respective transmission wavelengths $k^{*}_{\mathrm{tot}}(\lambda)$ in free space k_{tot}. The total decay rate is composed of the modified radiative rate constants for the single electronic transitions based on eqn (2):

$$k^{*}_{\mathrm{tot}}(\lambda_{\mathrm{trans}}) = k^{*}_{\mathrm{nr}}(\lambda_{\mathrm{trans}}) + \sum_{i}^{n} k^{*}_{\mathrm{r}_i}(\lambda_{\mathrm{trans}}), \quad (2)$$

where k^{*}_{nr} is the non-radiative contribution, which is independent of the Purcell effect but dependent on the distance between the emitter and the metal surfaces. The evaluation method for determining the free space spectral shapes S_{0_i} and the decay rates of each process is based on reproducing the measured spectral shapes $S_0(\lambda)$ and decay constants k_{tot} of the fluorescence in free space and for various cavity lengths the spectral shapes $S^{*}(\lambda,\lambda_{\mathrm{trans}})$ and decay constants $k^{*}_{\mathrm{tot}}(\lambda_{\mathrm{trans}})$. This is done by a global fitting procedure, which first fits the spectral parameters for the individual bands for the free space spectrum. Second, the resonator shaped spectra and the respective transition rates are calculated using the Purcell factor for each transmission wavelength. Third, the deviation between the resulting simulated spectral shapes/total decay rates and the measured spectral shapes/decay rates is minimized by varying the respective spectral parameters for the Gaussians and the quantum yield. The benefit of this method is that the evaluation is completely independent of intensity dependent parameters such as the excitation power or the number of molecules in the focal volume.[29,30,34] Since the intensity ratio of the vibronic bands given by the spectral shape of one and the same spectrum only depends on $P(\lambda,\lambda_{\mathrm{trans}})$ and their given intensity ratio in free space their spectral parameters can be determined by the outlined fitting procedure. A detailed description on the deduction of the used model function is given in the ESI.†

2. Results

Experimentally, a large number of fluorescence spectra and decay curves are recorded at various resonator configurations for the global fitting-algorithm. The used procedure, performed in the energy regime, optimizes the parameters of the Gaussians representing the free space spectral bands as shown in Fig. 2 and further the values for the respective rate constants. For a more detailed description of the confocal microscope and the resonator design see the ESI.† In Fig. 2 the impact of a $\lambda/2$-microresonator with a transmission wavelength around 540 nm on the fluorescence spectrum is demonstrated. In the upper panel the free space fluorescence spectrum of Atto488 in a PVA-matrix (red lines) is shown and can be described by the superposition of three Gaussians (black dashed curves). The spectral appearance of an electronic transition is modified, first, by an altered fluorescence intensity according to the overlap of the respective band with the Purcell factor (eqn (1)). Hence, an additional detection function is required to take into account the angular distributed fluorescence and the angle dependent collection efficiency of the objective lens. Since a molecule can emit not only into the longitudinal mode of the resonator but also into the off-axis modes, whose wavelengths are blue shifted with respect to the longitudinal mode, the signal collected by the objective lens has an increasing blue shifted tail with increasing NA. In the lower panel of Fig. 2 the fluorescence spectrum (red line) is shown for a transmission wavelength around 540 nm as indicated by the gray shaded Lorentzian together with the calculated Purcell factor (blue curve), the detection function (red dots) and the modified spectral bands (black dashed lines) from the upper panel. It can be seen that the contribution around 549 nm is nearly completely suppressed by the Purcell factor, while the contribution around 530 nm is enhanced.

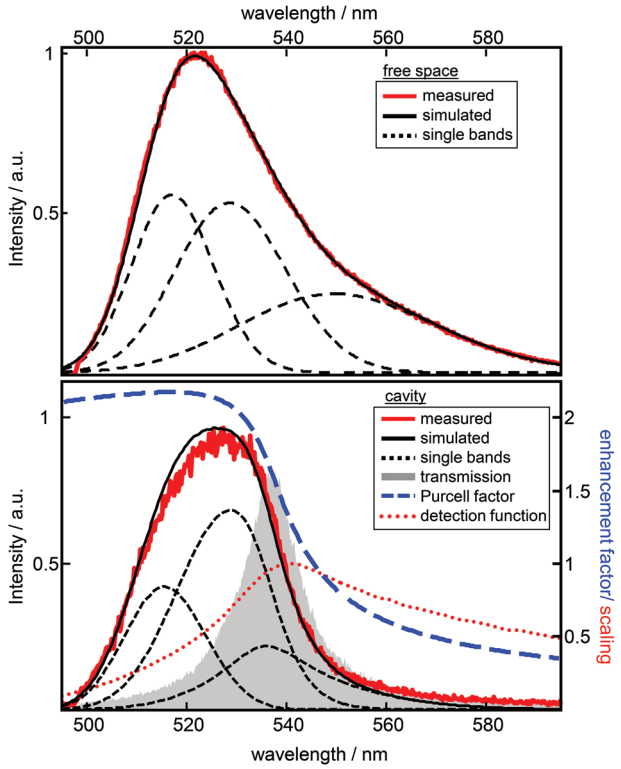

Fig. 2 Modelling of spectra. The graph on top shows an experimental free space emission spectrum of Atto488 together with three Gaussians (black dashed lines) representing the vibronic bands and their summation (black solid line). The properties of the three Gaussians are further used for the simulation of the cavity modified spectra. The graph below shows the relevant functions for reproducing the cavity modified emission spectrum (red) together with the fitted spectrum (black). As gray area the Lorentzian shaped white light transmission spectrum is shown, which is used to calculate the Purcell factor (blue dashed line) and the detection function (red dots, scaling according to the Purcell factor). For this resonator setting, an effective mirror separation of 142 nm can be calculated. Due to the wavelength depending radiative enhancement and the detection function the three Gaussian vibronic bands (black dashed lines) building the complete spectrum are modified in their intensity ratio and shape with respect to the free space spectrum.

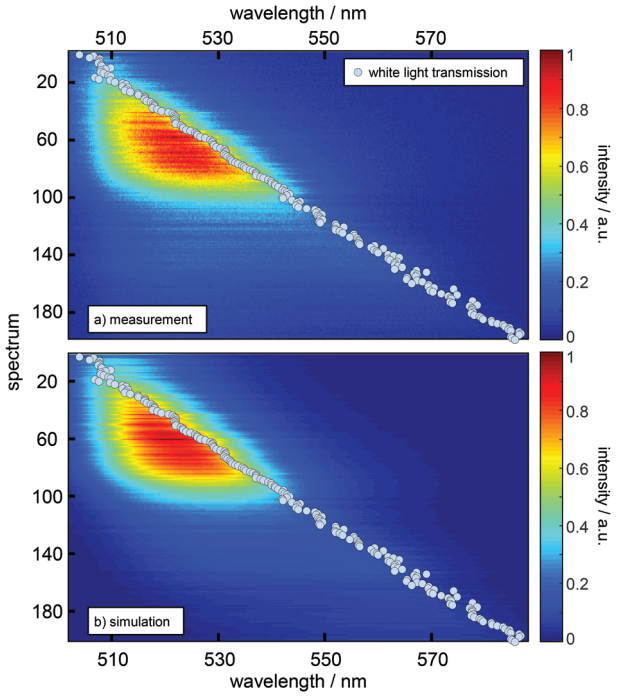

Fig. 3 Comparison of a sequence of measured emission spectra (a) and a sequence of calculated spectra (b) as a function of the resonance wavelength (grey dots) as obtained from the on-axis transmission recorded for the respective resonator setting. The *y*-axis represents the number of acquired spectra in this series and scales with the stepwise increase of mirror separation. Each spectrum in (b) is composed of the same three Gaussian vibronic bands as in Fig. 2 with relative intensities scaled by the Purcell factor calculated for the respective resonance wavelength and detection function.

Hence, the cavity dependent fluorescence spectrum can be calculated from the measured free space spectrum and the respective transmission spectrum of the resonator. In Fig. 3a sequences of measured (a) and calculated (b) fluorescence spectra are shown as a function of the measured transmission wavelength of the resonator. Each simulated spectrum is based on the modification of the same three Gaussians from Fig. 2. The respective measured on-axis transmission wavelengths λ_{res} are displayed as gray circles and were acquired by Lorentzian linefits to white light transmission spectra at the very same resonator setting at which the respective fluorescence spectra were recorded.

In Fig. 4, time resolved fluorescence decay curves for free space and the resonator settings λ_{res} = 510 nm (blue) and 560 nm (green) are shown together with mono-exponential curves (red curves) fitted to the data by the convolution of the

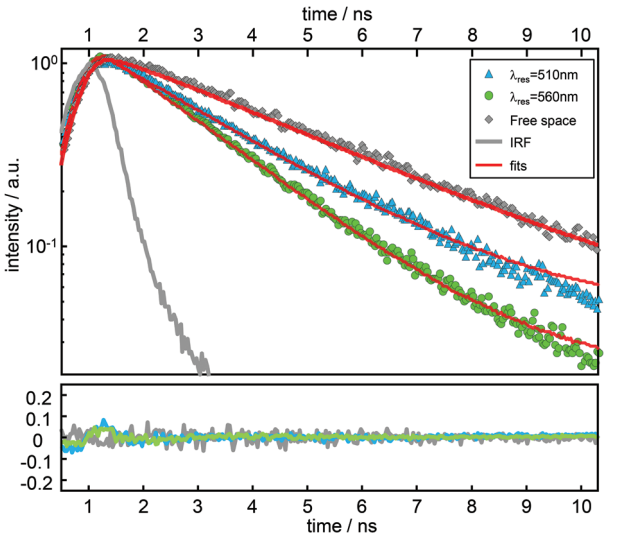

Fig. 4 Fluorescence decay curves fitted by model functions obtained by convolution of the instrument response function (gray line) and mono-exponential decay curves. Shown are the decay curves and fits for free space (gray squares, k_{tot} = 0.31 ns^{-1}) and the resonator settings λ_{res} = 510 nm (blue triangles, k_{tot} = 0.41 ns^{-1}) and 560 nm (green circles, k_{tot} = 0.55 ns^{-1}).

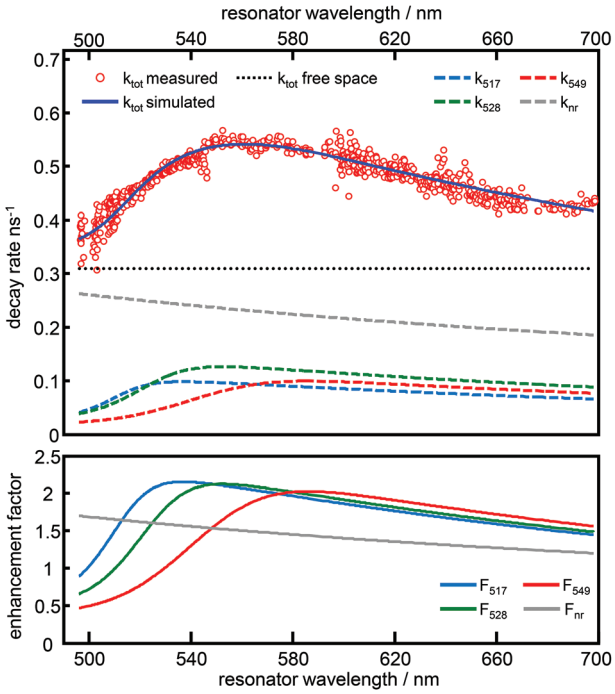

Fig. 5 Top: Total decay rate constants (red circles) of the dye Atto488 inside a $\lambda/2$-microresonator determined by mono-exponential fits of TCSPC histograms recorded at different on-axis cavity transmission wavelengths. The blue line shows the simulated curve which is the sum of the single contributions: the radiative rate constants for the 517 nm (dashed light blue), the 528 nm (green dashed line), the 549 nm band (red dashed line) and the non-radiative rate constant (gray dashed line). The black dashed lines show the free space total decay rate. Bottom: Calculated enhancement factors depending on the on-axis transmission wavelength for the radiative band with 517 nm (blue line), 528 nm (green line) and 549 nm (red line) emission maximum. The gray line shows the non-radiative enhancement factor.

model function with the instrument response function (gray line). In the upper panel of Fig. 5 we show the quantitative evaluation of all experimental decay rates as a function of the cavity resonance, whereby the total decay rate is enhanced for all resonator settings with respect to free space. Hence, an enhanced non-radiative decay of the excited emitter, induced by a decreasing mirror–emitter separation must be also taken into account, which reflects quenching by the silver surface with decreasing mirror separation. With decreasing transmission wavelengths, the distance between the emitters and the silver mirrors are also decreasing and thus enhance near-field coupling between the molecule and the metal surface. As a reasonable assumption, we model the course of the non-radiative decay rate as a function of transmission wavelength with respect to the r^{-3}-distance dependency of the near-field amplitude.[8,45,46] Thus, in the lower panel of Fig. 5 the respective enhancement and inhibition for each relaxation mechanism including the non-radiative decay due to quenching by the metal mirrors is shown. The total decay rates in the cavity (red dots) as a function of transmission wavelengths are in excellent agreement with the superposition of the individual relaxation processes, which are the three radiative transitions (blue, green and red dashed curves) and the non-radiative decay (gray dashed line).

As can be seen in Fig. 3 and 5, both simulations accurately reproduce the fluorescence properties of Atto488 embedded in a tunable $\lambda/2$-microresonator. The quality of the fitting procedure is based on a large number of recorded datasets (800 fluorescence spectra and decay curves) allowing us to also determine the non-radiative relaxation rate constant as a function of transmission wavelength.

3. Discussion

The impact on the spectral behavior of the cavity embedded fluorophore is in agreement with several previous studies such as the spectral shaping and the modification of the radiative decay rate.[23,28,47] Additionally, the behavior of the non-radiative rate is in accordance with the results of other studies.[9,48–50] A major difference between our photonic microresonators and plasmonic nanoantennas is the separation of the molecules from the metal. In our experiment, we reach a minimum emitter–metal separation of 60 nm (for resonator on-axis transmission of 500 nm). Hence, the near-field of the molecule at the mirror surface (silver) is small just as the spectral overlap between the fluorescence of the molecule and the plasmon resonance of silver. Therefore quenching due to dissipative energy transfer to the metal plays a minor role. In contrast, for very close metal–molecule proximity as in plasmonics (<10 nm), near-field coupling or the coupling to non-radiative or evanescent modes, which can lead to quenching has to be taken into account. This means, the far-field contribution of the LDOS at the position of the emitter mainly determining the observed spectral properties is induced by the mirror separation of the cavity and the mirror–mirror separation, while a weak near-field contribution is induced by the presence of silver surfaces, whose plasmonic impact on the spectral properties is negligible and independent of the mirror–mirror separation.[4,16]

To date, the quantitative and rigorous separation between radiative and non-radiative relaxation processes for fluorophores in one and the same experimental series could not be performed to the best of our knowledge in the spectral and time-domain. However, numerical simulations are able to reproduce the total decay rates of excited organic dyes within $\lambda/2$-microresonators in order to determine the free space quantum yield.[23] For Atto488 in an aqueous solution, the quantum yield was determined by Chizhik *et al.* to be 70%, who performed their experiments in aqueous solution in contrast to our experiments that were performed in a PVA-matrix.

Our study demonstrates that we can correlate the spectral distribution and the decay mechanisms of a fluorescent dye molecule under ambient conditions at the ensemble level and we find a quantitative agreement with our simulations. This could be accomplished at the ensemble level, under ambient conditions, on a system with largely inhomogeneously broadened overlapping fluorescence bands and with a finely tunable

and simple to build photonic device avoiding chemical interaction with the molecules. Also, our approach does not require high excitation fluxes or cryogenic temperatures. Under such conditions emitters can show dramatically altered spectral behavior with respect to ambient conditions and free space hampering the extrapolation to normal conditions. The advantage of using excitation power independent properties is obvious that for low excitation power at the ensemble level, the quality of the results can be enhanced due to the possibility of recording a large number of datasets in different controllable environments.

Our approach also describes the effective perturbation on the examined system and the kinetic relaxation parameters requiring only a large number of recorded datasets due to the fitting procedure. However, tuning and controlling the cavity resonance is easy and reproducible with our resonator design and allows us to record more than the required number of datasets. By finally combining the spectral and temporal information we are able to gain a deeper insight into the dynamics of the vibronic progression of a fluorescence spectrum and furthermore to have the opportunity to tune controllably the near- and far-field induced photonic influence of our resonators on the deactivation mechanisms of the excited fluorophores.

Acknowledgements

Financial support from the German Research Council (DFG) for ME1600/13-1 and Heisenberg-Programm (BR 4102/1-1 and BR 4102/2-1) is gratefully acknowledged.

References

1 K. J. Vahala, *Nature*, 2003, **424**, 839–846.
2 M. Barth, S. Schietinger, S. Fischer, J. Becker, N. Nusse, T. Aichele, B. Lochel, C. Sonnichsen and O. Benson, *Nano Lett.*, 2010, **10**, 891–895.
3 G. M. Akselrod, C. Argyropoulos, T. B. Hoang, C. Ciraci, C. Fang, J. Huang, D. R. Smith and M. H. Mikkelsen, *Nat. Photonics*, 2014, **8**, 835–840.
4 A. Konrad, M. Metzger, A. M. Kern, M. Brecht and A. J. Meixner, *Nanoscale*, 2015, **7**, 10204–10209.
5 P. Lodahl, A. F. van Driel, I. S. Nikolaev, A. Irman, K. Overgaag, D. Vanmaekelbergh and W. L. Vos, *Nature*, 2004, **430**, 654–657.
6 P. Zijlstra and M. Orrit, *Rep. Prog. Phys.*, 2011, **74**, 106401.
7 J. R. Lakowicz, J. Malicka, I. Gryczynski, Z. Gryczynski and C. D. Geddes, *J. Phys. D: Appl. Phys.*, 2003, **36**, R240–R249.
8 A. M. Kern, D. Zhang, M. Brecht, A. I. Chizhik, A. V. Failla, F. Wackenhut and A. J. Meixner, *Chem. Soc. Rev.*, 2014, **43**, 1263–1286.
9 P. Anger, P. Bharadwaj and L. Novotny, *Phys. Rev. Lett.*, 2006, **96**, 113002.
10 A. M. Kern and O. J. F. Martin, *Nano Lett.*, 2011, **11**, 482–487.
11 M. Frimmer, Y. T. Chen and A. F. Koenderink, *Phys. Rev. Lett.*, 2011, **107**, 123602.
12 M. Brecht, M. Hussels, J. B. Nieder, H. Fang and C. Elsässer, *Chem. Phys.*, 2012, **406**, 15–20.
13 E. Fort and S. Gresillon, *J. Phys. D: Appl. Phys.*, 2008, **41**, 013001.
14 X. Wang, K. Braun, D. Zhang, H. Peisert, H. Adler, T. Chasse and A. J. Meixner, *ACS Nano*, 2015, **9**, 8176–8183.
15 R. Roy, S. Hohng and T. Ha, *Nat. Methods*, 2008, **5**, 507–516.
16 F. Schleifenbaum, A. M. Kern, A. Konrad and A. J. Meixner, *Phys. Chem. Chem. Phys.*, 2014, **16**, 12812–12817.
17 E. Schlodder, M. Hussels, M. Cetin, N. V. Karapetyan and M. Brecht, *Biochim. Biophys. Acta*, 2011, **1807**, 1423–1431.
18 A. Konrad, A. L. Trost, S. Skandary, M. Hussels, A. J. Meixner, N. V. Karapetyan and M. Brecht, *Phys. Chem. Chem. Phys.*, 2014, **16**, 6175–6181.
19 A. C. Millard, L. Jin, J. P. Wuskell, D. M. Boudreau, A. Lewis and L. M. Loew, *J. Membr. Biol.*, 2005, **208**, 103–111.
20 D. I. Schuster, A. Wallraff, A. Blais, L. Frunzio, R. S. Huang, J. Majer, S. M. Girvin and R. J. Schoelkopf, *Phys. Rev. Lett.*, 2005, **94**, 123602.
21 S. Noda, M. Fujita and T. Asano, *Nat. Photonics*, 2007, **1**, 449–458.
22 S. Bär, A. Chizhik, R. Gutbrod, F. Schleifenbaum, A. Chizhik and A. J. Meixner, *Anal. Bioanal. Chem.*, 2010, **396**, 3–14.
23 A. I. Chizhik, I. Gregor, B. Ernst and J. Enderlein, *ChemPhysChem*, 2013, **14**, 505–513.
24 K. Becker, J. M. Lupton, J. Müller, A. L. Rogach, D. V. Talapin, H. Weller and J. Feldmann, *Nat. Mater.*, 2006, **5**, 777–781.
25 A. Laucht, F. Hofbauer, N. Hauke, J. Angele, S. Stobbe, M. Kaniber, G. Bohm, P. Lodahl, M. C. Amann and J. J. Finley, *New J. Phys.*, 2009, **11**, 023034.
26 E. Fermi, *Rev. Mod. Phys.*, 1932, **4**, 87–132.
27 A. Caze, R. Pierrat and R. Carminati, *Photonics and Nanostructures-Fundamentals and Applications*, 2012, **10**, 339–344.
28 A. I. Chizhik, A. M. Chizhik, A. M. Kern, T. Schmidt, K. Potrick, F. Huisken and A. J. Meixner, *Phys. Rev. Lett.*, 2012, **109**, 223902.
29 M. Ringler, A. Schwemer, M. Wunderlich, A. Nichtl, K. Kurzinger, T. A. Klar and J. Feldmann, *Phys. Rev. Lett.*, 2008, **100**, 203002.
30 C. Sauvan, J. P. Hugonin, I. S. Maksymov and P. Lalanne, *Phys. Rev. Lett.*, 2013, **110**, 237401.
31 L. Aigouy, A. Caze, P. Gredin, M. Mortier and R. Carminati, *Phys. Rev. Lett.*, 2014, **113**, 076101.
32 P. Holzmeister, E. Pibiri, J. J. Schmied, T. Sen, G. P. Acuna and P. Tinnefeld, *Nat. Commun.*, 2014, **5**, 5356.
33 J. Wenger, D. Gerard, J. Dintinger, O. Mahboub, N. Bonod, E. Popov, T. W. Ebbesen and H. E. Rigneault, *Opt. Express*, 2008, **16**, 3008–3020.

34 D. Cao, A. Caze, M. Calabrese, R. Pierrat, N. Bardou, S. Collin, R. Carminati, V. Krachmalnicoff and Y. De Wilde, *ACS Photonics*, 2015, **2**, 189–193.
35 L. Shang, Y. Z. Wang, J. G. Jiang and S. J. Dong, *Langmuir*, 2007, **23**, 2714–2721.
36 S. Chah, M. R. Hammond and R. N. Zare, *Chem. Biol.*, 2005, **12**, 323–328.
37 P. Winckler and R. Jaffiol, *Anal. Chem.*, 2013, **85**, 4735–4744.
38 W. E. Moerner and T. Basche, *Angew. Chem., Int. Ed.*, 1993, 32, 457–476.
39 T. Basche, *Single Mol.*, 2001, **2**, 237–240.
40 G. Bjork, *IEEE J. Quantum Electron.*, 1994, **30**, 2314–2318.
41 A. Konrad, A. M. Kern, M. Brecht and A. J. Meixner, *Nano Lett.*, 2015, **15**, 4423–4428.
42 J. Lakowicz, *Principles of Fluorescence Spectroscopy*, Springer, 2006.
43 J. M. Hayes, J. K. Gillie, D. Tang and G. J. Small, *Biochim. Biophys. Acta*, 1988, **932**, 287–305.
44 T. P. Krüger, V. I. Novoderezhkin, C. Ilioaia and R. van Grondelle, *Biophys. J.*, 2010, **98**, 3093–3101.
45 R. R. Chance, A. Prock and R. J. Silbey, *J. Chem. Phys.*, 1974, **60**, 2744–2748.
46 A. Campion, A. R. Gallo, C. B. Harris, H. J. Robota and P. M. Whitmore, *Chem. Phys. Lett.*, 1980, **73**, 447–450.
47 M. Steiner, F. Schleifenbaum, C. Stupperich, A. V. Failla, A. Hartschuh and A. J. Meixner, *J. Lumin.*, 2006, **119**, 167–172.
48 K. H. Drexhage, *Sci. Am.*, 1970, **222**, 108–118.
49 B. C. Buchler, T. Kalkbrenner, C. Hettich and V. Sandoghdar, *Phys. Rev. Lett.*, 2005, **95**, 063003.
50 E. Castanie, V. Krachmalnicoff, A. Caze, R. Pierrat, Y. De Wilde and R. Carminati, *Opt. Lett.*, 2012, **37**, 3006–3008.

Supplementary information: Revealing the radiative and non-radiative relaxation rates of the fluorescence dye Atto488 in a λ/2 Fabry-Pérot-resonator by spectrally and time resolved measurements†

Alexander Konrad,[a*] Michael Metzger,[a] Andreas M. Kern[a], Marc Brecht[a], and Alfred J.Meixner[a‡]

1 Theoretical modeling and analysis

1.1 Free space dipole emitters in the spectral and the time domain

The spectral shape of a vibronic band i in free space and ambient conditions can be approximated by a Gaussian $S_{0_i}(\lambda)$ with amplitude h_{0_i}, spectral position p_i and the full width at half maximum (FWHM) w_i, which is related to the standard deviation c_i. The complete spectrum S_0 for a fluorophore composed of several vibronic bands is then the superposition of all vibronic bands n:

$$S_0(\lambda) = \sum_{i=1}^{n} S_{0_i}(h_{0_i}, p_{0_i}, w_{0_i}, \lambda), \tag{1}$$

with:

$$S_{0_i}(\lambda) = h_{0_i} e^{-(\frac{\lambda - p_i}{2c_i})^2}, \tag{2}$$

$$c_i = \frac{w_i}{2\sqrt{2\ln 2}}, \tag{3}$$

and:

$$\int S_{0_i}(\lambda) d\lambda = h_{0_i} w_i \frac{\sqrt{2\pi}}{2\sqrt{2\ln 2}}. \tag{4}$$

The FWHM is a direct measure for the thermal fluctuations of the energy levels accompanying the transition, wherby the broadening increases most often with increasing energy distance to the 0-0 transition. Further, the integrated intensity of the respective Gaussian i is a measure for the amount of emitted photons for the corresponding spectral transition i with respect to the overall intensity. Thus, the probability of one transition with respect to all other radiative transitions can be given by the ratio:

$$f_{0_i} = \frac{\int S_{0_i}(\lambda) d\lambda}{\int S_0(\lambda) d\lambda}. \tag{5}$$

Regarding the time domain of fluorescent transitons, the excited state X_1 is relaxing to X_0 with a certain rate constant, depending on the relaxation mechanism with its probability. The single radiative transition i occurs with the rate constant k_{r_i} while the non-radiative decay channels are summarized here by the rate constant k_{nr}. The time decay of excited chromophores can be measured by time correlated single photon counting (TCSPC) yielding time dependent decay curves $N(t)$, where $N(t)$ is the number of registered fluorescence photons in the time interval dt. They can be described by the convolution of the pure intensity decay $I_0(t)$ of a chromophore and the instrument response function (IRF) $H(t')$. The most simple decay laws describing $I_0(t)$ are single or multi-exponential functions. The time law for a common chromophore with n vibronic transitions can be derived by stating and solving the differential equation for the time dependent decay of the excited state population X_1:

$$\frac{X_1(t)}{dt} = -(k_{nr} + \sum_{i}^{n} k_{r_i}) X_1(t) = -k_0 X_1(t). \tag{6}$$

By integrating one can find the solution:

$$X_1(t) = e^{-k_{nr}t} \prod_{i}^{n} e^{-k_{r_i}t} = e^{-k_{tot}t}, \tag{7}$$

with k_{tot} as the experimentally accessible total decay constant. Thus, measured decay curves can be described by the convolution of I_0 with the IRF:

$$N(t) = N_0 \int_0^{t'} [e^{-k_{nr}(t-t')} \prod_{i}^{n} e^{-k_{r_i}(t-t')}] H(t') dt', \tag{8}$$

with N_0 as the intensity at $t = 0$. The radiative rate k_{r_i} is directly connected to the spectral intensity of the very same vibronic transition i of the overall spectral intensity. Therefore, the ratio given in equation 5 f_{0_i} can be written also as:

$$f_{0_i} = \frac{k_{r_i}}{\sum k_{r_i}} = \frac{\int S_{0_i}(\lambda) d\lambda}{\int S_0(\lambda) d\lambda}. \tag{9}$$

Together with the quantum yield Ω defined by the ratio of the radiative decay rates and the sum of all decay rates one can write:

$$\Omega = \frac{\sum k_{r_i}}{k_{nr} + \sum k_{r_i}} = \frac{\sum k_{r_i}}{k_{tot}}. \tag{10}$$

1.2 Purcell factor

According to Fermis Golden Rule, the emission properties of a dipole-emitter are depending on the photonic environment. For a two-level system the emission rate of such a transition can be expressed as[1,2]:

$$\Gamma_{spE} = \frac{2\pi}{h^2} |\langle \boldsymbol{\mu} \cdot \boldsymbol{E} \rangle|^2 \rho(\omega). \tag{11}$$

The term in the bra-kets denotes the matrix element of the perturbation between final and initial state, induced by the electric field $\boldsymbol{E}$ and the dipole operator $\boldsymbol{\mu}$. The electric field operator for the spontaneous emission in a Fabry-Pérot cavity can be given analytically[3]. Assuming a cavity with loss-less mirror materials and an isotropic radiating emitter oriented parallel to the y-axis with distance z_0 to the first mirror and an infinitesimally narrow emission spectrum, the in-plane electric fields can be calculated for each angle of emission θ and both polarization (s and p) with respect

[a] Universität Tübingen, Institut für Physikalische und Theoretische Chemie, Auf der Morgenstelle 18. 72076 Tübingen. Germany.
* alexander.konrad@uni-tuebingen.de
‡ alfred.meixner@uni-tuebingen.de

to the mirror surfaces and each emission wavelength given by the k-vector:

$$E_{s,||}^2 = \frac{(1-r_{2,s})(1+r_{1,s}-2\sqrt{r_{1,s}}\,\cos(2kz_0\cos\theta)}{(1-\sqrt{r_{1,s}r_{2,s}})^2+4\sqrt{r_{1,s}r_{2,s}}\,\sin^2(kL\cos\theta)}|E_0^2|, \quad (12)$$

$$E_{p,||}^2 = \frac{(1-r_{2,p})(1+r_{1,p}-2\sqrt{r_{1,P}}\,\cos(2kz_0\cos\theta)\cos^2\theta}{(1-\sqrt{r_{1,p}r_{2,p}})^2+4\sqrt{r_{1,p}r_{2,p}}\sin^2(kL\cos\theta)}|E_0^2|. \quad (13)$$

Here, $r_{i,p/s}$ denotes the reflectivity of the respective mirror for the polarization p or s, L is the effective cavity length and E_0 the initial field magnitude. To get the wavelength dependent Purcell factor $P(\lambda,L)$ for the dipole emitter, the field has to be integrated over all angles θ for the respective emission wavelengths, averaged for both polarizations. The effective cavity length L can be determined by fitting the expressions for the optical fields to a measured transmission spectrum using reflection coefficients provided by the transfermatrix-method (TMM) and for $\theta = 0$.
Inside a cavity, the radiative rates are specifically altered due to the changed photonic mode density affecting the rate constants and the spectral shape of the fluorescence bands, depending on the resonator length L. For simplicity, the mean Purcell factor is calculated for random dipole orientations ϕ, emission angles θ with respect to the collection efficiency of the objective lens and axial positions of the emitter z_0, which is hosted inside a thin film of several nanometers with a distance of ~ 60 nm to the first mirror. Further the radiative enhancement factor is simplified further as $P(\lambda,L)$.

1.3 Impact on dipole emitters and analysis

The aim is now, to correlate the spectral and temporal information gained by the mirror separation dependent fluorescence spectra and decay curves. The modification of a single vibronic band $S^*_{cav_i}(\lambda,L)$ by the cavity how it appears in an experimental spectrum can be described by the spectral shape S_{0_i} of the radiative transition i weighted by $P(\lambda,L)$ and regarding the detection efficiency of this transition. First, we determine the modified radiative rate constant by the overlapp of the Purcell factor and the spectral band, multiplied by its free space rate k_{r_i}:

$$k^*_{r_i}(L) = k_{r_i}\frac{\int P(\lambda,L)S_{0_i}(\lambda)d\lambda}{\int S_{0_i}(\lambda)d\lambda}. \quad (14)$$

And the modified histogram can be easily given by:

$$N^*(t,L) = N_0^*\int_0^{t'} e^{-k^*_{nr}(L)\cdot(t-t')}\prod_i^n e^{-k^*_{r_i}(L)\cdot(t-t')}H(t')dt', \quad (15)$$

and the total decay rate by:

$$k^*_{tot}(L) = k^*_{nr}(L) + \sum_i^n k^*_{r_i}(L). \quad (16)$$

In analogy to equation 9 we can write:

$$f_i^* = \frac{k^*_{r_i}(L)}{\sum k^*_{r_i}(L)} = \frac{\int S_i^*(\lambda,L)d\lambda}{\int S^*(\lambda,L)d\lambda}. \quad (17)$$

Here, S^* and S_i^* refer to the cavity modified shapes without respect to the detection, because the detection probability should not alter the fluorescence properties of the emitter in the resonator. Since a molecule can also emit into angular distributed off-axis modes, both, the collection efficiency of the objective lense and the asymetry of the spectrally distributed mode spectrum of the cavity affect the shape of the detected spectral band. The fluorescence spectrum can not be regarded as a Gaussian any more, whereby the transition energy p_i and the FWHM w_i of the experimental band $S^*_{cav_i}$ are not altered by the photonic mode density. Therefore, the cavity distorted band $S^*_{cav_i}$ with respect to the complete normalized spectrum can be described by a Gaussian with altered intensity weighted by a normed angular sensitivity function $D_N(\lambda,L)$ and the normed Purcell factor $P_N(\lambda,L)$. The detection function $D(\lambda,L)$ can be calculated by the deviation of the emission angle θ with respect to the on-axis emission and is close to unity for resonant or red shifted wavelengths while it decreases for blue shifted wavelengths. Thus, we first use the scaling factor introduced in equation 17 to account for the altered intensity ratio with respect to the other bands of the complete spectrum:

$$S_i^*(\lambda,L) = f_i^*\frac{S_{0_i}(\lambda)}{\int S_{0_i}(\lambda)d\lambda}P_N(\lambda,L), \quad (18)$$

which leads to:

$$S^*_{cav_i}(\lambda,L) = S_i^*(\lambda,L)D_N(\lambda,L), \quad (19)$$

and finally:

$$S^*_{cav}(\lambda,L) = \sum_i^n S^*_{cav_i}(\lambda,L). \quad (20)$$

In order to correlate now the spectral and temporal information, we connect the intensity ratio for each band with the experimentally accessible total decay rates k_{tot} and $k^*_{tot}(L)$. Therefore, we can express equation 18 in the following way:

$$S_i^*(\lambda,L) = \frac{k^*_{r_i}(L)}{k^*_{tot}(L)-k^*_{nr}(L)}\frac{S_{0_i}(\lambda)}{\int S_{0_i}(\lambda)d\lambda}P_N(\lambda,L), \quad (21)$$

and by using equation 14:

$$S_i^*(\lambda,L) = \frac{k_{r_i}\int P(\lambda,L)S_{0_i}(\lambda)d\lambda}{k^*_{tot}(L)-k^*_{nr}(L)}\frac{S_{0_i}(\lambda)}{(\int S_{0_i}(\lambda)d\lambda)^2}P_N(\lambda,L). \quad (22)$$

Regarding the free space rate $k_{r_i} = f_{0_i}\sum k_{r_i}$ and equation 5 we can further write:

$$S_i^*(\lambda,L) = \frac{\sum k_{r_i}\int P(\lambda,L)S_{0_i}(\lambda)d\lambda}{k^*_{tot}(L)-k^*_{nr}(L)}\frac{S_{0_i}(\lambda)}{\int S_{0_i}(\lambda)d\lambda\int S_0(\lambda)d\lambda}P_N(\lambda,L). \quad (23)$$

The non-radiative rate $k^*_{nr}(L)$ is describable by a model function following the near-field amplitude decay from the molecule to a mirror surface according to L^{-3} [4], an additional scaling factor a and the free space decay rate representing the various non-radiative decay mechanisms in free space:

$$k^*_{nr}(L) = aL^{-3} + k_{nr}. \quad (24)$$

To final model function can then be expressed with the quantum yield $\Omega = \frac{\sum k_{r_i}}{k_{tot}}$ as:

$$S_i^*(\lambda,L) = \frac{\Omega k_{tot} \int P(\lambda,L) S_{0_i}(\lambda) d\lambda}{k_{tot}^*(L) - (aL^{-3} + (1-\Omega)k_{tot})} \times \frac{S_{0_i}(\lambda) P_N(\lambda,L)}{\int S_{0_i}(\lambda) d\lambda \int S_0(\lambda) d\lambda}. \quad (25)$$

For the equations 25, 19 and 20 the Purcell factor $P(\lambda,L)$ and the detection function $D(\lambda,L)$ are determinable by the model sketched above, the mirror separation L is determinable by measuring the on-axis transmission wavelength, the total decay rates k_{tot} and k_{tot}^* can be determined by evaluating the fluorescence decay curves and the experimental shapes $S^*(\lambda,L)$ and $S_0(\lambda)$ (equation 1) by recording the fluorescence spectra. It can be seen also from equation 25 that all spectra are normed, which leads to a purely dependency on the shaped of the spectra and not on the measured overall intensity.

Now, this set of model functions can be fitted to the experimental data in order to determine the $3n$ parameters for the Gaussians S_{0_i}, the course of the non-radiative decay rate k_{nr}^* and the quantum yield Ω. For minimizing the error and optimizing the fit-paramters (11 parameters for $n = 3$) one needs a large number of datasets at different mirror separations (800 spectra/decay curves for transmission wavelengths between 500 and 700 nm). However, the procedure can be additionally optimized by setting reasonable limits and constraints for the respective parameters. The results for the fitting procedure can be seen in the main article in Figure 2, 3 $(S_{0_i}(\lambda), S_{cav_i}^*(\lambda,L))$ and 5 $(k_{r_i}^*(L), k_{nr}^*(L))$.

2 Experimental Methods

The fluorescence of Atto488 (ATTO-TEC, Siegen, Germany) was examined by a confocal microscope shown in Fig. 1a), after excitation by a 488 nm pulsed laser diode (PicoQuant, LDH-P-C-485) operating with a repetition rate of 40 MHz and a pulse width of ~100 ps (PicoQuant, PDL 828 Sepia II). The laser beam with a power of 20 μW was guided by a beamsplitter (AHF, zt488RDC) to the objective lens (Zeiss, plan-apochromat 63x/1.46 immersion oil), which focuses the excitation beam to a diffraction limited volume within the sample. The subsequent fluorescence was collected by the same objective lens and guided back through a pinhole and a long-pass filter (AHF, F76-490) on the detectors, an APD (Perkin Elmer, SPCM-AQRH) and a spectrograph (Princeton Instruments, Acton SP2500) equipped with a CCD-camera (Princeton Instruments, ProEM). A counting module (PicoQuant, HydraHarp400) recorded the signal of the photodiode in order to perform TCSPC. For free space measurements, a droplet (40 μL) of aqueous solution of Atto488 (with concentration of 1e-7 mol/L diluted in 4% PVA) was spin-coated (5 minutes with 6000 rpm) on a cleaned (with chromosulfuric acid) and washed (with tridistilled water) glass cover slip (Menzel, 22x22 mm) to produce a thin film of several nanometers. For the resonator experiments shown in Fig. 1b), we have used a coated glass cover slip (Menzel, 22x22 mm) and coated glass lens (Thorlabs, LA1433, f=150 mm, R=77.3 mm) as mirrors for the Fabry-Pérot-resonator. The respective layers were deposited on the substrates by electron beam

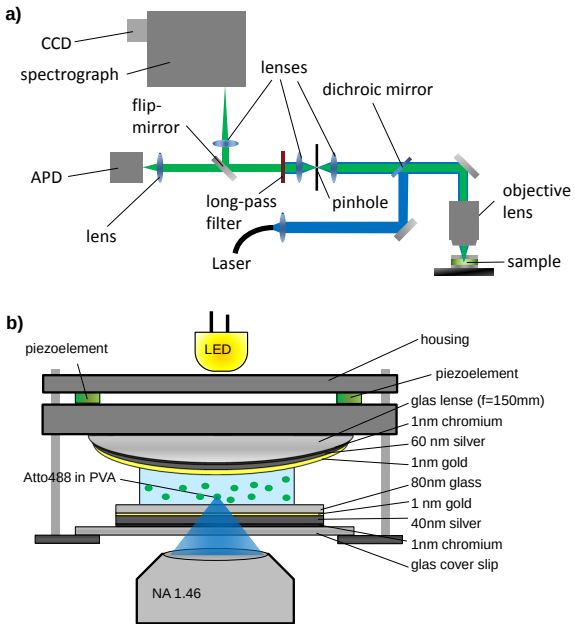

Fig. 1 *Scheme of the experimental setup. a) Scheme of the optical path: The excitation source, a pulsed 488 nm laser diode, is triggered by the Sepia II module which is synchronized with the counter module Hydra Harp 400. The beam is guided by a beamsplitter into the confocal microscope. For excitation and fluorescence collection the same objective (NA=1.46) is used. The fluorescence is deflected through a pinhole and a longpass filter on the detectors, an APD and a spectrograph with equipped thermoelectrically cooled CCD-camera. b) Drawing of the resonator design. The mirrors consist of the following layers: 1) glass cover slide; 2) 1 nm chromium; 3) 40 nm silver; 4) 1 nm gold; 5) 80 nm SiO_2; 6) 1 nm gold; 7) 60 nm silver; 8) 1 nm chromium; 9) glass lens (f=150 mm) hence, the mirror surface can be considered to be parallel within the investigated sample section being less than 100μmin diameter. The cavity length is tuned by the piezoelectric stacks implemented in a mirror mount. The sample is placed about half way between the mirrors on the bottom mirror, which is immersed in the intra-cavity medium (water). The bottom mirror is fixed on a plate which is mounted on a three-axis feed-back controlled scanning stage.*

evaporation (Edwards, EB3) monitored by a crystal quartz oscillator with the following sequence: 1 nm chromium, 40 nm silver (60 nm for lens), 1 nm gold and 80 nm glass (for cover slip mirror). The lens was fixed on a kinematic mount including piezoelectric elements (Thorlabs, KC1-T-PZ) in order to alter reproducibly the cavity length. The cavity resonance was checked for every mirror setting by recording white light transmission spectra. Since the radius of the mirror is much larger than the mirror spacing and the diameter of the laser focus the cavity can be described by a plane parallel Fabry-Pérot interferometer with concentric rings fulfilling the idealized resonance conditions $L = m \cdot \lambda/2$ (with $m = 1,2,3...$)[5]. The transmission spectra were recorded by illuminating the resonator by a broadband LED from the back side of the resonator. To record fluorescence spectra and decay curves for different cavity lengths, the fluorophore containing sample was laterally scanned by a feedback controlled piezoelectric scanning stage through the spatially fixed diffraction limited focal confocal volume. The complete setup was controlled by

a custom LabView-program allowing us to record a large number of datasets. The data analysis and fitting of the spectra and TCSPC histograms was performed by a custom Matlab program.
For a beam diameter in the resonator of around 500 nm the average number of molecules is roughly 100 (as obtained from spincoating a dye solution with a concentration of $1 \cdot 10^{-7} mol/l$ in 4% PVA) in the detection volume at locations of the sample which yield high fluorescence intensity. With an excitation power of ca. 5 μW entering the resonator we have a photon flux of around $1.25 \cdot 10^{21} ph \cdot s^{-1} \cdot cm^{-2}$. For the excitation wavelength of 488 nm and one molecule with absorption cross section of $3.4 \cdot 10^{-16} cm^{-2}$ this gives an excitation rate between $4.3 \cdot 10^{5} s^{-1}$ (off-resonant) and $8.6 \cdot 10^{6} s^{-1}$ (resonant). Together with the excitation rate and the repetition rate of the laser (40 MHz) we estimate that every pulse excites around 10 molecules.

References

1 E. Fermi, *Rev. Mod. Phys.*, 1932, **4**, 87–132.

2 M. Fox, *Quantum Optics - An Introduction*, Oxford University Press, New York, 2006.

3 G. Bjork, *Ieee Journal of Quantum Electronics*, 1994, **30**, 2314–2318.

4 A. Campion, A. R. Gallo, C. B. Harris, H. J. Robota and P. M. Whitmore, *Chemical Physics Letters*, 1980, **73**, 447–450.

5 S. Bar, A. Chizhik, R. Gutbrod, F. Schleifenbaum, A. Chizhik and A. J. Meixner, *Analytical and Bioanalytical Chemistry*, 2010, **396**, 3–14.

Chapter 7

Dynamic control of Förster energy transfer in a photonic environment

In this chapter the fluorescence of a Förster energy transfer coupled system - the protein DsRed - embedded in a tunable $\lambda/2$ Fabry-Pérot resonator is investigated. The fluorescence spectra are recorded and analyzed at a cavity adjustment where the photonic mode spectrum is resonant to the emission of the donor of DsRed. The efficiency is the transfer given in term of the fluorescence intensity ratio between donor and acceptor fluorescence, is investigated as a function of excitation power promoting the donor in the excited state. A rate equation model for continuous wave excitation allows us to determine the ratio between the probabilities to find the donor and acceptor in their excited states. It can be seen that the efficiency can be well described by the modified radiative relaxation rates of donor and acceptor, the increasing excitation rates of the donor due to an increasing laser power and both, a constant non-radiative relaxation of donor and acceptor and a cavity independent energy transfer rate. While the coupling between the donor and the acceptor chromophore is not affected significantly by the photonic environment, the radiative relaxation rates of both chromophores are modified by the resonator altering hence the complete relaxation dynamics of the FRET-system. According to the rate equations, high excitation rates increase the probability that an excited donor is hampered to transfer its energy to an acceptor that is still excited by a previous transfer. By choosing a certain cavity length and excitation power the efficiency of a FRET-transfer can be controlled in a precise manner without altering the intrinsic dipole-dipole coupling for continuous wave laser excitation.

This chapter is based on:
Schleifenbaum, F., Kern, A.M., Konrad A., Meixner A.J. "Dynamic control of Förster energy transfer in a photonic environment", *Physical Chemistry Chemistry Physics*, **2014**, *16*,12812.

PCCP

PAPER

View Article Online
View Journal | View Issue

Cite this: *Phys. Chem. Chem. Phys.*, 2014, **16**, 12812

Dynamic control of Förster energy transfer in a photonic environment

Frank Schleifenbaum, Andreas M. Kern, Alexander Konrad* and Alfred J. Meixner*

Received 26th March 2014,
Accepted 29th April 2014

DOI: 10.1039/c4cp01306a

www.rsc.org/pccp

In this study, the effect of modified optical density of states on the rate of Förster resonant energy transfer between two closely-spaced chromophores is investigated. A model based on a system of coupled rate equations is derived to predict the influence of the environment on the molecular system. Due to the near-field character of Förster transfer, the corresponding rate constant is shown to be nearly independent of the optical mode density. An optical resonator can, however, effectively modify the donor and acceptor populations, leading to a dramatic change in the Förster transfer rate. Single-molecule measurements on the autofluorescent protein DsRed using a $\lambda/2$-microresonator are presented and compared to the theoretical model's predictions. The observed resonator-induced dequenching of the donor subunit in DsRed is accurately reproduced by the model, allowing a direct measurement of the Förster transfer rate in this otherwise inseparable multichromophoric system. With this accurate yet simple theoretical framework, new experiments can be conceived to measure normally obscured energy transfer channels in complex coupled quantum systems, *e.g.* in photovoltaics or light harvesting complexes.

1 Introduction

Since the early work of Förster,[1] the interaction between closely spaced fluorescent molecules *via* dipole–dipole coupling (fluorescence/Förster resonant energy transfer, FRET) has been a topic of great interest.[2–9] The efficiency of the energy transfer depends on the spectral overlap between the emission of the donor chromophore and the absorption of the acceptor chromophore as well as on the distance and the mutual orientation of their respective transition dipole moments. While it is easily possible to design and prepare synthetic FRET-pairs and study the optical properties of the individual chromophores separately, this is not possible for many biological molecules such as the red fluorescent protein DsRed from the Discosoma reef coral. DsRed is known to form tetramers consisting of two different types of subunits containing a chromophore exhibiting fluorescence emission either in the green or red spectral regime.[10–12] These spectral properties along with the steric composition as derived from X-ray data suggest a non-radiative Förster energy transfer within a tetrameric unit which has indeed been experimentally proven by different spectroscopic approaches using single molecule and ensemble techniques.[2,11,13,14] However, it is not possible to separate the tetramers into functional monomers by chemical or biochemical means to make the isolated chromophoric species addressable for further investigation.

Universität Tübingen, Institut für Physikalische und Theoretische Chemie, Auf der Morgenstelle 18, 72076 Tübingen, Germany. E-mail: x@uni-tuebingen.de; Fax: +49-7071-29-5490; Tel: +49-7071-29-76

A promising approach to spectrally isolate individual chromophoric subunits in biological FRET-systems is to modify the local photonic mode characteristics and density by using a $\lambda/2$-microresonator. We have previously demonstrated the optical confinement effect on both the fluorescence spectrum and the emission rate of single (synthetic) dye molecules by embedding them in a transparent polymer between two planar silver mirrors separated by half of the emission wavelength.[15,16] The influence of the modified photonic mode density on a system consisting of coupled molecular dipole emitters is theoretically well described[17–22] and several experimental demonstrations on the ensemble level have been reported to date.[23–26]

In this article, we report the first investigation of the autofluorescent protein DsRed embedded in a $\lambda/2$-microresonator by steady-state and time resolved spectroscopy down to the single molecule level. We use a novel microresonator design that allows coupling the fluorescence of individual chromophores to on- and off-axis cavity modes while maintaining physiological conditions for the embedded biomolecules. We show that, in this way, it is possible to spectrally isolate the two coupled chromophoric subunits of DsRed without destroying the composition of the tetrameric protein complex.

2 Rate equation model

To study the effect of a photonic environment on a FRET-coupled system, we introduce a rate equation model describing the energetic processes of the system. Shown in Fig. 1, this

model comprises two three-level subsystems D and A representing the donor and acceptor molecules, respectively. Each subsystem X (X = D, A) can be excited at the rate $X_0 k_{exc} = X_0 J\sigma$, where X_0 is the probability to find the subsystem in its electronic ground state, k_{exc} is the excitation rate constant, J is the incident illumination photon flux at the absorption wavelength and σ is the corresponding absorption cross section. Optical excitation of X_0 leads to a vibronic level in the first electronically excited state X_1' which thermally relaxes rapidly within some picoseconds to X_1, from which it may decay nonradiatively or radiatively at the rates $X_1 k_{nr}$ and $X_1 k_{rad}$, respectively. Here, k_{nr} and k_{rad} are the nonradiative and radiative decay rate constants, respectively. In addition, the subsystems D and A are coupled *via* the nonradiative channel representing Förster resonant energy transfer, described by the rate constant k_T as a measure of the dipole–dipole coupling strength. This Förster transition rate is defined as the probability per time interval that an acceptor molecule is transferred from its ground state A_0 to its electronically excited state A_1 by absorbing a photon of the optical near-field of the donor chromophore with state D_1. The transition rate is then given by $D_1 A_0 k_T$.

The population probability dynamics for the excited states D_1 and A_1 of the subsystems can be written by a system of coupled differential equations,

$$\begin{aligned} \dot{D}_1 &= k^{D}_{exc} D_0 - [k^{D}_{rad} + k^{D}_{nr} + k_T A_0] D_1, \\ \dot{A}_1 &= [k^{A}_{exc} + k_T D_1] A_0 - [k^{D}_{rad} + k^{D}_{nr} +] A_1, \end{aligned} \tag{1}$$

where a dotted value denotes a derivative in time. Here, superscripts D and A denote values corresponding to the donor and acceptor subsystems, respectively. In equilibrium, the populations are described by the steady-state solution to eqn (1), obtained for $\dot{D}_1 = \dot{A}_1 = 0$. With $X_0 + X_1 = 1$, donor and acceptor excited-state populations can then be written as

$$\begin{aligned} D_1 &= \frac{k^{D}_{exc}}{k^{D}_{exc} + k^{D}_{rad} + k^{D}_{nr} + k_T(1 - A_1)}, \\ A_1 &= \frac{k^{A}_{exc} + k_T D_1}{k^{A}_{exc} + k^{A}_{rad} + k^{A}_{nr} + k_T D_1}. \end{aligned} \tag{2}$$

When placed in a modified photonic environment, *e.g.* a resonant cavity, the parameters in eqn (2) can change. First, the intensity of the incident light can be enhanced or suppressed when the cavity is excited on or off resonance, varying the incident photon flux J and thus k_{exc}. With the intensity enhancement factor $F_{exc} = I(\mathbf{r})/I_{fs}(\mathbf{r})$ denoting the incident intensity at the position $\mathbf{r}$ of the quantum system in a photonic environment compared to free space, the modified excitation rate constant can be expressed as $k_{exc} = F_{exc} k_{exc,fs}$.

Second, the radiative decay rate constant k_{rad} is proportional to the local density of optical states (LDOS) ρ corresponding to the transition energy. In a photonic background, ρ is a function of space and the emitter's orientation and can vary by many orders of magnitude, dramatically changing the behavior of the coupled quantum system. Introducing the LDOS enhancement factor $F_{rad} = \rho(\mathbf{r})/\rho_{fs}(\mathbf{r})$ induced by the photonic environment at the position of the emitter, the radiative decay rate constant can be expressed as $k_{rad} = F_{rad} k_{rad,fs}$. The value F_{rad} is also known as the Purcell factor.

Finally, the Förster transfer rate constant k_T can be influenced by the photonic background as well. While FRET is a nonradiative process, often described as a near-field dipole–dipole interaction, it is nevertheless influenced by modifications to the electromagnetic field: if a photonic system enhances the donor dipole's near-field, it will equally enhance the induced dipole moment in the acceptor, thus increasing the FRET speed. The photonic enhancement $F_T = |\mathbf{E}^{D}(\mathbf{r}^{A})|^2/|\mathbf{E}^{D}_{fs}(\mathbf{r}^{A})|^2$ of the donor's dipole field intensity at the position of the acceptor compared to free space thus also describes the enhancement of the FRET channel, $k_T = F_T k_{T,fs}$, assuming that there is no change in polarization.

The radiative and FRET enhancement factors can be conveniently computed given the photonic system's electromagnetic response in the form of its dyadic Green's function $\mathbf{G}$. This 3×3-tensorial function describes the electric field at an arbitrary position $\mathbf{r}'$ induced by a single dipole emitter in the photonic system,

$$\mathbf{E}(\mathbf{r}') = \omega^2 \mu(\mathbf{r}) \mathbf{G}(\mathbf{r}', \mathbf{r}) \cdot \mathbf{p}. \tag{3}$$

Here, $\mathbf{r}$ is the position of the dipole emitter, $\mathbf{p}$ is its dipole moment, $\hbar\omega$ is the transition energy and $\mu(\mathbf{r})$ is the magnetic permeability at the position of the emitter. The LDOS can directly be computed as

$$\rho(\mathbf{r}) = \frac{6\pi\omega}{\hbar c^2} \mathrm{Im}\{G_{\hat{\mathbf{p}}}(\mathbf{r}, \mathbf{r})\}, \tag{4}$$

where $G_{\hat{\mathbf{p}}} = \hat{\mathbf{p}} \cdot \mathbf{G} \cdot \hat{\mathbf{p}}$ and $\hat{\mathbf{p}} = \mathbf{p}/|\mathbf{p}|$ is a unit vector in the direction of the emitter's dipole moment. In free space, eqn (4) results analytically in $\rho_{fs}(\mathbf{r}) = \omega^2/(\hbar c^3)$; the LDOS is then homogeneous and isotropic. With eqn (4), the radiative enhancement factor can then be written as

$$F_{rad} = 6\pi \frac{c}{\omega} \mathrm{Im}\{G_{\hat{\mathbf{p}}}(\mathbf{r}, \mathbf{r})\}. \tag{5}$$

The FRET enhancement factor F_T can also be derived from eqn (3) with $\mathbf{r}$ and $\mathbf{r}'$ describing the positions of the donor and the acceptor, respectively:

$$F_T = \frac{\mu(\mathbf{r}^{D})}{\mu_{fs}(\mathbf{r}^{D})} \frac{|\mathbf{G}(\mathbf{r}^{A}, \mathbf{r}^{D}) \cdot \mathbf{p}^{D}|^2}{|\mathbf{G}_{fs}(\mathbf{r}^{A}, \mathbf{r}^{D}) \cdot \mathbf{p}^{D}|^2}. \tag{6}$$

The first term in eqn (6) can usually be neglected as the magnetic permeability is seldom changed in a photonic system.

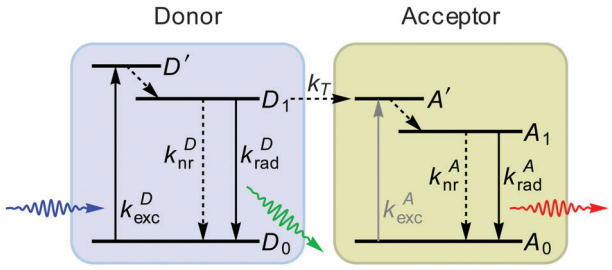

Fig. 1 System used to model the FRET-coupled system. Radiative transitions are shown as solid lines, nonradiative transitions as dashed lines. In our study, the acceptor is not directly excited, hence its excitation channel is drawn in gray.

In the second term, the absolute value of the donor's dipole moment cancels out, and so F_T depends solely on $|\mathbf{G}|^2$ in the direction of the donor's dipole moment.

The dyadic Green's function $\mathbf{G}$ can be obtained using a number of analytical or numerical approaches. For the simple case of an ideal Fabry–Pérot microresonator, analytical calculations have been presented.[27] For more complex resonator geometries including multiple layers and interfaces, the transfer matrix method (TMM) provides a quasi-analytical solution. For arbitrary photonic systems, numerical methods such as the finite-difference time-domain (FDTD)[28] or surface integral equation (SIE)[29] approach may be required for satisfactory results.

2.1 λ/2-Microresonator

Due to the simple geometry of a λ/2-microresonator, its electromagnetic response can be calculated analytically.[27] The angular dependence of its modes' resonances limits the Purcell factor of a planar Fabry–Pérot-type resonator to at most $F_{rad} = 3$, even for perfectly reflecting mirrors. Emission inhibition, on the other hand, can be very effective, reaching values of nearly $F_{rad} \approx 0$. The size of a λ/2-microresonator is on the order of the emitted light's wavelength, thus only the far field of an embedded emitter can populate its modes: as the near field's amplitude decays with R^{-3}, it will have nearly vanished even before reaching the resonator's mirrors for the first time. A comparison of a dipole emitter's far field to its near field shows that the intensity of the far field which is only one wavelength λ away is more than 8 orders of magnitude weaker than that of the near field at a distance of λ/100. One can thus see that even a large resonant enhancement of the cavity modes will have only a minuscule effect on the FRET rate constant k_T.

Changes in the FRET rate $D_1A_0k_T$ in a λ/2-microresonator will therefore not be caused by a change in the rate constant, but instead by the changes in the donor and acceptor populations D_1 and A_0, respectively.[30] In particular, efficient emission inhibition of the donor's emission wavelength can effectively increase its excited state population D_1, leading to an increase in FRET. Similarly, inhibiting acceptor fluorescence can lead to a depletion of the ground state population A_0, preventing Förster transfer.

3 Experimental results

To observe the effects predicted by our model, we experimentally studied the fluorescence of a Förster-coupled system in a λ/2-microresonator. As a FRET system, we chose the autofluorescent protein DsRed, a complex molecule containing two spectrally isolated chromophoric subunits with fluorescence maxima at 505 nm and 580 nm, respectively. These two subunits can couple nonradiatively, allowing energy to be transferred from the energetically higher subunit to the lower subunit *via* FRET. The gray shaded area in Fig. 2(b) shows the free-space emission spectrum of DsRed when illuminated at 473 nm, clearly displaying the two fluorescence peaks.

The photonic background in our study was defined by a λ/2 Fabry–Pérot microresonator enclosing the DsRed molecules.

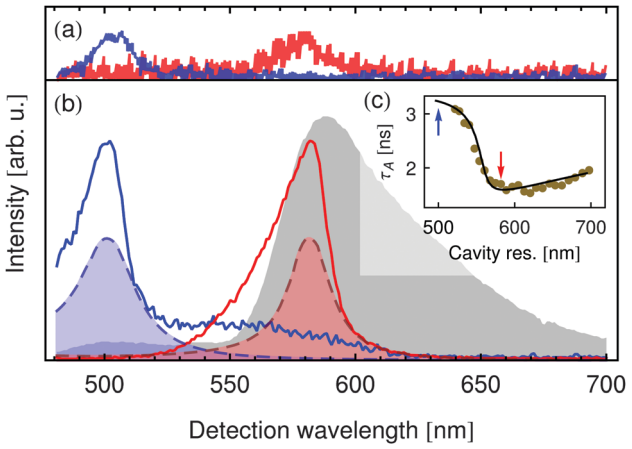

Fig. 2 Measured spectra: (a) single DsRed tetramers in a λ/2-microresonator tuned to the donor emission wavelength (blue curve) and acceptor emission (red curve). (b) Ensemble DsRed in free space (gray shaded area) and in λ/2-microresonator tuned to the donor emission wavelength (blue curve) and acceptor emission (red curve), along with the respective white-light transmission spectra (shaded dashed lines). (c) Ensemble DsRed acceptor fluorescence lifetime τ_A for different cavity resonance wavelengths. Blue and red arrows correspond to the two resonator configurations shown in (a) and (b).

A schematic diagram of the sample-microresonator system is shown in Fig. 3. While one of the resonator's mirrors is flat, the other is minimally curved with a radius of $R = 150$ mm. This curvature is slight enough that the mirrors can still be assumed to be parallel, yet causes a well-defined variation in the mirror separation $L(x,y)$ in the resonator plane. The longitudinal

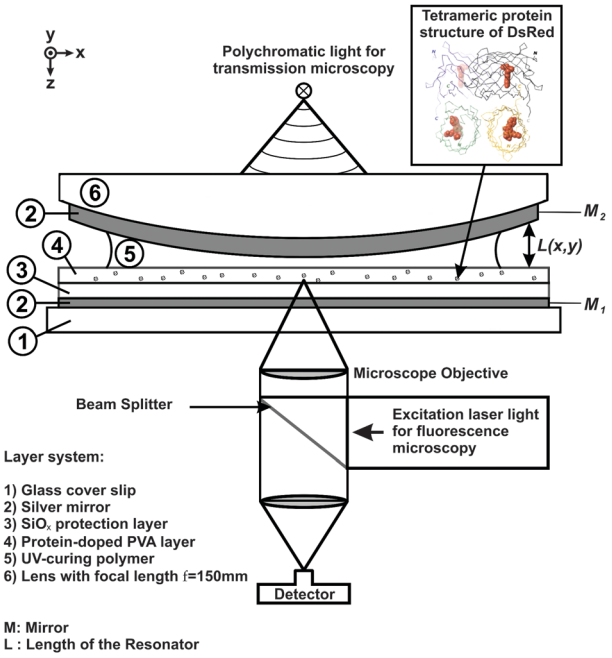

Fig. 3 Experimental setup consisting of a λ/2 microresonator with embedded DsRed molecules in a physiological environment. The resonator is placed in a confocal laser microscope with an additional white-light source for measuring its transmission spectra.

resonance wavelength can thus be tuned by scanning the detection point across the resonator.

The blue and red solid lines in Fig. 2(b) show the fluorescence spectra of DsRed in the microresonator for two different mirror separations L. The corresponding white-light transmission spectra, indicating the resonator's longitudinal resonances for the two mirror separations, are shown by the shaded dashed lines of the same color. The amplitudes of these spectra are not shown to scale but magnified to aid interpretation. Immediately, one can see that by choosing the correct resonance wavelength, one emission peak can be greatly enhanced while the other is nearly completely suppressed. For the blue curve, the normally dominant peak at 580 nm is so effectively suppressed by the resonator that it is visible only as a slight hump on the blue peak's flank. For the red curve, the off-resonance peak at 505 nm has completely disappeared. In both curves, the resulting peaks are asymmetric, showing a steep flank on the red side and a slow roll-off on the blue side. This is typical for emitters in a $\lambda/2$-resonator as the longitudinal resonance wavelength also corresponds to the resonator's cutoff wavelength: light with a wavelength longer than the longitudinal resonance cannot populate any mode in the resonator. Shorter wavelengths, however, can populate off-axis modes which are no longer parallel to the z-axis but which can nevertheless be collected by the high NA of the used objective.

The spectra of single DsRed tetramers shown in Fig. 2(a) in blue (donor resonat) and red (acceptor resonat) illustrate that the influence of the resonator on transfer coupled systems is observable even on the single particle level. This enables a precise control and study of individual chromophores within one distinct transfer coupled complex, whose optical properties may vary by *i.e.* induced environmental influences. To verify that the influence of the resonator on the molecules' emission spectra is indeed an effect of their varied emission rates and not simply a filtering of the emitted light, the acceptor fluorescence lifetime τ_A was studied as a function of the cavity resonance wavelength, *viz.* Fig. 2(c). The points show measured lifetimes and the curve is a calculation using the transfer matrix method (TMM) assuming a free-space fluorescence lifetime of $\tau^A_{rad,fs}$ = 6.7 ns and an emission quantum yield of $\Phi^A_{rad,fs}$ = 25.2%. The dramatic change in the measured lifetime agrees perfectly with the calculation's prediction. The red and blue arrows indicate the two resonator configurations at which the spectra in Fig. 2(b) were recorded, corresponding to the cases of inhibition (blue) and enhancement (red) of strong acceptor emission.

To study the resonator's effect quantitatively and to verify the rate-equation model presented above, we study the resonator-induced dequenching of the donor chromophore: when the resonator is tuned to the emission peak at 505 nm, Fig. 2(b) shows that besides amplifying the donor emission, the acceptor fluorescence is effectively suppressed. If the quantum yield of the acceptor chromophore is sufficiently high, the lifetime of the A_1 state will then be considerably increased. From eqn (1) one follows that an excited acceptor choromophore cannot participate in FRET and so this decay channel is lost to the donor. The resulting shift in the relative transition

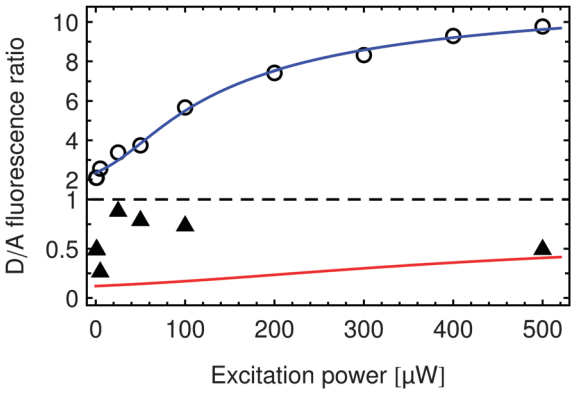

Fig. 4 Measured donor-to-acceptor fluorescence ratios of DsRed in free space (triangles) and in a microresonator tuned to the donor emission wavelength (circles) for varying illumination power P_{exc}. Blue line is the predicted behavior for the presented rate-equation model.

efficiency causes an increase in donor emission intensity compared to acceptor fluorescence. Fig. 4 shows the donor-to-acceptor fluorescence ratios for DsRed in a microresonator tuned to 505 nm (circles) and in free space (triangles), measured for increasing excitation power. In free space, this ratio remains in the order of 0.5 for all illumination power. With the acceptor fluorescence suppressed by the resonator, however, the donor dominates the fluorescence by a ratio of up to 10/1 in the measured range.

Typically, this behavior is difficult to observe in free space, since, on the one hand, the fluorescence lifetime of a typical acceptor dye is rather short and, on the other hand, the fluorescence lifetime of a typical (unquenched) donor, being in the same range, is too long. Hence, the acceptor has already relaxed to the ground state while the donor is still excited, allowing for another energy transfer which quenches the emission of the donor. However, using a microresonator system, it is possible to precisely adjust the radiative rates of the respective chromophores. Thus, one can significantly shorten the lifetime of the donor chromophore while the lifetime of the acceptor chromophore is lengthened.

One might argue that the larger D/A fluorescence ratio in the resonator is simply due to the fact that the donor fluorescence is enhanced and the acceptor fluorescence is suppressed by the resonator, even without a change in the FRET efficiency. This static effect, however, should not depend on the illumination power P_{exc}. In fact, the effect of static fluorescence enhancement can be observed for $P_{exc} \to 0$. The modified fluorescence speed k_{rad} thus causes a change from $f_D/f_A \approx 0.5$ to $f_D/f_A \approx 2.0$, while the illumination-dependent modification of the FRET efficiency increases the ratio to $f_D/f_A \approx 10$.

The dynamic behavior observed in the measurement is accurately reproduced by the rate equation model presented in this paper. The blue line in Fig. 4 shows the donor-to-acceptor fluorescence ratio $D_1 k^D_{rad}/(A_1 k^A_{rad})$ predicted by our model for decay efficiencies $\Phi_x = k_x/k_{tot}$ given in Table 1. These values correspond to excited state fluorescence lifetimes of 2.8 ns and 2.6 ns for the uncoupled donor and acceptor, respectively, with fluorescence quantum yields (without FRET) of 18.1% and

Table 1 Free-space decay efficiencies used in our model to reproduce the measured behavior

Chromophore	$\Phi_{rad,fs}$ (%)	$\Phi_{nr,fs}$ (%)	$\Phi_{T,fs}$ (%)
Donor	2.6	11.8	85.6
Acceptor	25.2	74.8	—

25.2%. The FRET rate constant k_T then corresponds to a value of 2.1 GHz, in agreement with previously measured data.[31] With these values, the model's predictions are in excellent agreement with our experimental results.

Having confirmed the accuracy of our model, we can now explore the parameter space of the studied system. In Fig. 5, we plot the donor-to-acceptor fluorescence ratio (red surface, left scale) and the FRET efficiency,

$$\Phi_T = \frac{k_T A_0}{k_T A_0 + k_{rad}^D + k_{nr}^D}, \quad (7)$$

(green surface, right scale) for typical values of the resonator mirror separation L and illumination power P_{exc}.

Many interesting features can be observed in this representation. First, one can see that the large increase in the D/A fluorescence ratio is only possible if the resonator is tuned to the correct wavelength. A large enhancement can be seen if the acceptor fluorescence is effectively inhibited while allowing, or even enhancing, donor emission. For larger L, both donor and acceptor emissions are allowed, and so the D/A ratio is similar to that in free space (*cf.* triangles in Fig. 4). For very small L, both donor and acceptor emissions are suppressed. While the D/A ratio is not strongly enhanced in this case, it shows a saturation onset at very low power P_{exc}. This is due to the fact that, with fluorescence being inhibited, Förster transfer plays the dominant role in the energy dynamics of the coupled system. As the resonator modes prevent the acceptor from decaying radiatively, the resulting FRET inhibition is clearly visible already at very low power. Finally, one can see that the FRET efficiency Φ_T varies greatly across the shown parameter space. Depending on the incident power, tuning the resonator mirrors allows us to reduce the FRET efficiency between 50% and 75%. It should be pointed out that this is not a modification of the FRET rate constant k_T as per the factor F_T (here, $F_T = 1$), as the resonator is not capable of sufficiently modifying the near field of the donor dipole. Much more, it is an active modification of the other transition parameters D_1 and A_0, allowing us to selectively change the rate and efficiency of the Förster transfer.

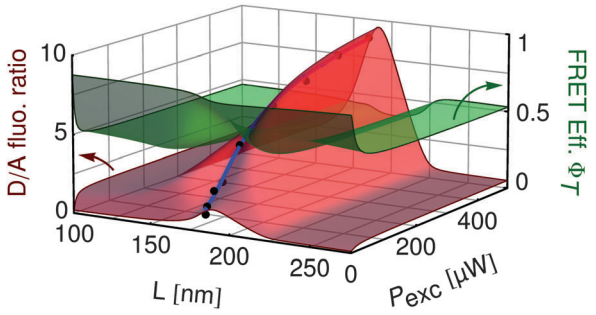

Fig. 5 Simulated D/A ratio (red surface) and FRET efficiencies (green surface) for different resonator widths d and excitation power P_{exc}.

Acknowledgements

Financial support from the German Research Council (DFG) for ME1600/13-1 is gratefully acknowledged.

References

1 T. Förster, Intermolecular energy migration and fluorescence, *Ann. Phys.*, 1948, **2**, 55–75.
2 T. A. Schüttrigkeit, U. Zachariae, T. von Feilitzsch, J. Wiehler, J. von Hummel, B. Steipe and M. E. Michel-Beyerle, Picosecond time-resolved fret in the fluorescent protein from discosoma red (wt-dsred), *ChemPhysChem*, 2001, **5**, 325–328.
3 S. Brasselet, E. J. G. Peterman, A. Miyawaki and W. E. Moerner, Single-molecule fluorescence resonant energy transfer in calcium concentration dependent cameleon, *J. Phys. Chem. B*, 2000, **104**, 3676–3682.
4 J. Hofkens, M. Cotlet, T. Vosch, P. Tinnefeld, K. D. Weston, C. Ego, A. Grimsdale, K. Müllen, D. Beljonne, J. Luc Brédas, S. Jordens, G. Schweitzer, M. Sauer and F. C. de Schryver, Revealing competitive Förster-type resonance energy-transfer pathways in single bichromophoric molecules, *Proc. Natl. Acad. Sci. U. S. A.*, 2003, **100**(23), 13146–13151.
5 E. B. van Munster and T. W. Gadella, Fluorescence lifetime imaging microscopy (flim), *Adv. Biochem. Eng./Biotechnol.*, 2005, **95**, 143–175.
6 E. A. Jares-Erijman and T. M. Jovin, Fret imaging, *Nat. Biotechnol.*, 2003, **21**(11), 1387–1395.
7 A. A. Deniz, T. Laurence, G. S. Beligere, M. Dahan, A. B. Martin, D. S. Chemla, P. E. Dawson, P. G. Schultz and S. Weiss, Single molecule protein folding: diffusion Förster energy transfer studies of the denaturation of chymotrypsin inhibitor 2, *Proc. Natl. Acad. Sci. U. S. A.*, 2000, **97**, 5179–5184.
8 R. Gronheid, J. Hofkens, F. Köhn, T. Weil, E. Reuther, K. Müllen and F. C. de Schryver, Intramolecular forster energy transfer in dendritic systems at the single molecule level, *J. Am. Chem. Soc.*, 2002, **124**, 2418–2419.
9 J. R. Lakowicz, *Principles of Fluorescence Spectroscopy*, Kluwer Academic, New York, 2nd edn, 1999.
10 G. Baird, D. Zacharias and R. Tsien, Biochemistry, mutagenesis, and oligomerization of dsred, a red fluorescent protein from coral, *Proc. Natl. Acad. Sci. U. S. A.*, 2000, **97**(22), 11984–11989.
11 B. Lounis, J. Deich, F. I. Rosell, S. G. Boxer and W. E. Moerner, Photophysics of dsred, a red fluorescent protein, from the ensemble to the single-molecule level, *J. Phys. Chem. B*, 2001, **105**, 5048–5054.
12 M. Matz, A. Fradkov, Y. Labas, A. Savitsky, A. Zaraisky, M. Markelov and S. Lukyanov, Fluorescent proteins from non-bioluminescent anthozoa species, *Nat. Biotechnol.*, 1999, **17**, 969–973.

13 C. Blum, V. Subramaniam, F. Schleifenbaum, F. Stracke, B. Angres, A. Terskikh and A. J. Meixner, Single molecule fluorescence spectroscopy of mutants of the discosoma red fluorescent protein dsred, *Chem. Phys. Lett.*, 2002, **362**, 355–361.

14 F. Schleifenbaum, *Energy transfer in the red fluorescent protein DsRed in confined optical fields*, Life Sciences, Rhombos, Berlin, 2008, vol. 3.

15 M. Steiner, F. Schleifenbaum, C. Stupperich, A. V. Failla, A. Hartschuh and A. J. Meixner, Microcavity-controlled single-molecule fluorescence, *ChemPhysChem*, 2005, **6**, 2190–2196.

16 M. Steiner, F. Schleifenbaum, C. Stupperich, A. V. Failla, A. Hartschuh and A. J. Meixner, A new microcavity design for single molecule detection, *J. Lumin.*, 2006, **119**(120), 167–172.

17 G. S. Agarwal and S. D. Gupta, Microcavity-induced modification of the dipole-dipole interaction, *Phys. Rev. A: At., Mol., Opt. Phys.*, 1998, **57**(1), 667–670.

18 M. J. A. Dood, J. Knoester, A. Tip and A. Polman, Förster transfer and the local optical density of states in erbium doped silica, *Phys. Rev. B: Condens. Matter Mater. Phys.*, 2005, **71**, 1151021.

19 S. D. Druger, S. Arnold and L. M. Folan, Theory of enhanced energy transfer between molecules embedded in spherical dielectric particles, *J. Chem. Phys.*, 1987, **87**(5), 2649–2659.

20 T. Kobayashi, Q. Zheng and T. Sekiguchi, Resonant dipole-dipole interaction in a cavity, *Phys. Rev. A: At., Mol., Opt. Phys.*, 1995, **52**(4), 2835–2846.

21 P. T. Leung and K. Young, Theory of enhanced energy transfer in an aerosol particle, *J. Chem. Phys.*, 1988, **89**(5), 2894–2899.

22 A. C. Pineda and D. Ronis, Classical model for energy transfer in microsperical droplets, *Phys. Rev. E: Stat. Phys., Plasmas, Fluids, Relat. Interdiscip. Top.*, 1995, **52**(5), 5178–5194.

23 P. Andrew and W. L. Barnes, Förster energy transfer in an optical microcavity, *Science*, 2000, **290**, 785–788.

24 W. L. Barnes and P. Andrew, Energy transfer under control, *Nature*, 1999, **400**, 505–506.

25 M. Hopmeier, W. Guss, M. Deussen, E. O. Göbel and R. F. Mahrt, Enhanced dipole-dipole interaction in a polymer microcavity, *Phys. Rev. Lett.*, 1999, **82**(20), 4118–4121.

26 A. Konrad, A. L. Trost, S. Skandary, M. Hussels, A. J. Meixner, N. V. Karapetyan and M. Brecht, Manipulating the excitation transfer in Photosystem I using a Fabry–Perot metal resonator with optical subwavelength dimensions, *Phys. Chem. Chem. Phys.*, 2014, **16**, 6175–6181.

27 G. Bjork, On the spontaneous lifetime change in an ideal planar microcavity-transition from a mode continuum to quantized modes, *IEEE J. Quantum Electron.*, 1994, **30**(10), 2314–2318.

28 A. Taflove and S. C. Hagness, *Computational Electrodynamics: The Finite-Difference Time-Domain Method*, Artech House, Boston, 2nd edn, 2000.

29 A. M. Kern and O. J. F. Martin, Surface integral formulation for 3D simulations of plasmonic and high permittivity nanostructures, *J. Opt. Soc. Am. A*, 2009, **26**(4), 732–740.

30 C. Blum, N. Zijlstra, A. Lagendijk, M. Wubs, A. P. Mosk, V. Subramaniam and W. L. Vos, Nanophotonic control of the forster resonance energy transfer efficiency, *Phys. Rev. Lett.*, 2012, **109**(20), 203601.

31 F. Schleifenbaum, *Energy transfer in the red fluorescent protein DsRed in confined optical fields*, Phd thesis, 2008.

Chapter 8

Controlling the energy transfer dynamics of Förster resonance energy transfer inside a tunable $\lambda/2$ Fabry-Pérot-resonator

In this chapter the energy transfer dynamics of a FRET-coupled pair of fluorophores is examined in the time domain by pulsed excitation of the donor within the FRET-pair. The FRET-pair is embedded in a tunable $\lambda/2$ Fabry-Pérot resonator able to alter the radiative relaxation rates of the donor and the acceptor. In order to determine the impact of the photonic environment on the energy transfer rate constant of a FRET-pair, the decay traces representing the deactivation of the donor chromophore as function of cavity length were evaluated. In contrast to the previous chapter the FRET pair was excited by a pulsed laser beam for different cavity lengths in order to record fluorescence decay curves by TCSPC additionally to fluorescence and white light transmission spectra. The transfer rate constants were determined according to the rate equation model by comparing the decay constants of the donor within the FRET pair with the decay constants of the donor without a nearby acceptor for both, free space and for various cavity lengths. The determined transfer rates constants show no significant dependency on the cavity length confirming the assumption stated in the previous chapter that the modification of the LDOS induced by the resonator is not large enough to interfere directly into the dipole-dipole coupling.

This chapter is based on:
Konrad A., Metzger, M., Kern, A.M., Brecht M., Meixner A.J. "Controlling the energy transfer dynamics of Förster resonance energy transfer inside a tunable $\lambda/2$ Fabry-Pérot-resonator", *Nanoscale*, **2015**, *7*, 10204-10209.

Nanoscale

PAPER

View Article Online
View Journal | View Issue

Cite this: *Nanoscale*, 2015, **7**, 10204

Controlling the dynamics of Förster resonance energy transfer inside a tunable sub-wavelength Fabry–Pérot-resonator†

Alexander Konrad,*[a] Michael Metzger,[a] Andreas M. Kern,[a] Marc Brecht[b] and Alfred J. Meixner*[a]

Received 30th March 2015,
Accepted 30th April 2015

DOI: 10.1039/c5nr02027a

www.rsc.org/nanoscale

In this study we examined the energy transfer dynamics of a FRET coupled pair of chromophores at the single molecule level embedded in a tunable sub-wavelength Fabry–Pérot resonator with two silver mirrors and separations in the $\lambda/2$ region. By varying the spectral mode density in the resonator *via* the mirror separation we altered the radiative relaxation properties of the single chromophores and thus the FRET efficiency. We were able to achieve wavelength dependent enhancement factors of up to three for the spontaneous emission rate of the chromophores while the quenching due to the metal surfaces was nearly constant. We could show by confocal spectroscopy, time correlated single photon counting and time domain rate equation modeling that the FRET rate constant is not altered by our resonator.

1 Introduction

Förster resonance energy transfer (FRET) is probably the most prominent energy transfer mechanism between two fluorophores and is a widely used technique in life-science for determining small molecular distances.[1] This energy transfer is crucially dependent on the separation and orientation of two coupled chromophores and is mediated by near-field dipole–dipole coupling.[2] The Förster-transfer and similar energy-transfer mechanisms are important processes in nature *i.e.* photosynthesis[3] and might be applied in photonic devices.[4] During the last few years several studies have examined the influences of different environments on the FRET rate constant *i.e.* by coupling FRET-pairs to plasmonic particles.[5,6] But how the energy transfer rate constant can be altered by changing the local density of optical states (LDOS) is still under debate. Even contradicting statements can be found in the literature claiming no[7–9] or a linear[10–12] dependence of the transfer rate constant on the LDOS. One explanation for these contradictions can be found in the problem of describing the effective impact of the LDOS which is only a vague quantity if its spectral and spatial distribution affecting a dipole-emitter is not clarified. Thus, it is more explicit to separate the LDOS into energetically and spatially distributed modes with a certain density capable of coupling to the near-field and/or the far-field of an emitter.[13,14] Separating or specifically ruling out one of these influences is therefore inevitable for a deeper understanding of how the energy transfer process can be controlled. Another problem concerns the properties of the FRET-pair and the experimental determination of the transfer rate constant. Most commonly two spectrally matching fluorophores are labeled at two complementary DNA-strands ensuring a specific hybridization to adjust a fixed inter-chromophore distance. The often assumed rigid distance and its labeling with chromophores are nevertheless questionable regarding *e.g.* the hybridization thermodynamics,[15,16] structural and conformational changes of DNA[17] confirmed by *e.g.* fluorescence microscopy experiments[18–20] revealing a broad distribution of FRET efficiencies of such labeled strands.

In this article, we examine the transfer dynamics of a FRET pair embedded in a $\lambda/2$-Fabry–Pérot-microresonator[21–24] by means of confocal microscopy and spectroscopy combined with pulsed laser excitation (λ = 488 nm, pulse width <100 ps, repetition rate 40 MHz) and time correlated single photon counting (TCSPC) for single molecule conditions. The FRET-pair, the resonator design and an energy level diagram are sketched in Fig. 1. Four types of samples were investigated: bare donors and FRET-pairs in free space and embedded in the microresonator. In all cases the concentration of donor chromophores or FRET-pairs was $\sim 10 \times 10^{-9}$ mol l^{-1} corresponding to an average number of around one chromophore or FRET-pair in a diffraction limited confocal volume, allowing

[a]*Universität Tübingen, Institut für Physikalische und Theoretische Chemie, Auf der Morgenstelle 18, 72076 Tübingen, Germany. E-mail: alexander.konrad@uni-tuebingen.de, alfred.meixner@uni-tuebingen.de*
[b]*Zürcher Hochschule für Angewandte Wissenschaften, Institute of Applied Mathematics and Physics, Technikumstrasse 13, 8401 Winterthur, Switzerland*

†Electronic supplementary information (ESI) available. See DOI: 10.1039/c5nr02027a

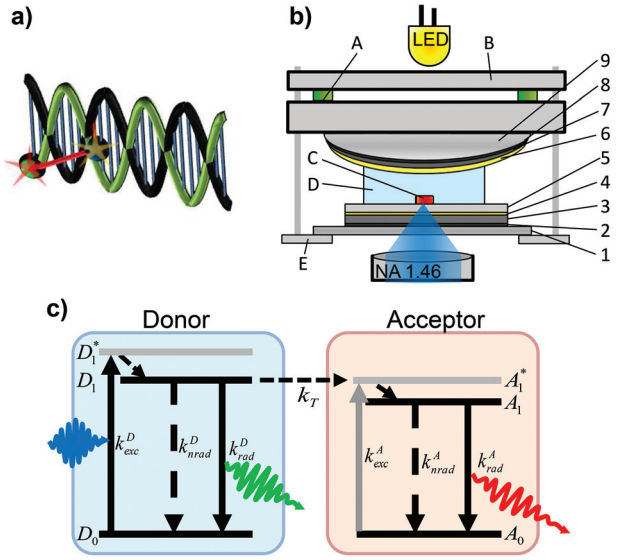

Fig. 1 (a) Double DNA-strand, with two FRET-coupled chromophores: Atto488 (donor) and Atto590 (acceptor) labeled to the green strand. (b) Fabry–Pérot-resonator: the mirrors consist of the following layers: (1) glass cover slide; (2) 1 nm Cr; (3) 40 nm Ag; (4) 1 nm Au; (5) 80 nm SiO_2; (6) 1 nm Au; (7) 60 nm Ag; (8) 1 nm Cr; (9) glass lens (f = 150 mm). The cavity length is tuned by using the piezoelectric stacks (A) implemented in a mirror mount (B). The sample (C) with embedded FRET-pairs or single donors within a thin film of PVA immersed with water (D) for reducing refractive index mismatches is placed on the bottom mirror which is mounted on the feed-back controlled sample scanning stage (E) of a confocal microscope. The same objective lens is used for excitation and fluorescence collection. A photodiode is used to measure white light transmission spectra of the resonator as a function of mirror spacing and hence determine the respective cavity resonance wavelength λ_{res}. (c) Simplified energy-level scheme of a FRET-system consisting of one donor and one acceptor. By absorbing a photon (blue wave) the donor is excited from the ground state D_0 to the intermediate vibronic level D_1^* from where it relaxes quickly to the first electronically excited state D_1. Transitions back to D_0 can occur by either fluorescence with k^D_{rad} or various non-radiative decay channels with k^D_{nrad}. From the electronic excited state D_1 the energy can also be transferred with k_T to the acceptor chromophore, which is excited from the ground state A_0 to the intermediate vibronic level A_1^* from where the first electronically excited state A_1 is populated. Relaxation to A_0 can occur radiatively or non-radiatively.

us to measure fluorescence spectra and decay traces at the single-molecule level. The FRET-pairs consist of the fluorescent dyes Atto488 (donor) and Atto590 (acceptor) labeled on the same DNA-strand to prevent detection of false hybridized FRET-pairs or bare donors in the FRET-experiment. To stabilize this double labeled strand we hybridized a complementary unlabeled DNA-strand to the dye labeled strand. For further details concerning the sample design see the ESI.† The microresonator displayed in Fig. 1b allows us to control the LDOS at the location of the sample and its effect on the embedded emitters by controlling the mirror separation by piezo elements. The resonator exhibits a mirror separation dependent radiative enhancement of the spontaneous emission (*i.e.* the Purcell factor[25]) ranging from a factor of 3 to nearly zero.[14,26–28]

For analyzing the fluorescence in the time and spectral domain of a FRET-pair shown in Fig. 1c consisting of one donor, one acceptor and a one-directional energy transfer channel the transfer dynamics have to be expressed by the probabilities of finding one chromophore in its excited state given by the following rate equations:

$$\begin{aligned}\dot{D}_1(t) &= k^{\mathrm{D}}_{\mathrm{exc}}(t)D_0(t) - \left[k^{\mathrm{D}}_{\mathrm{rad}} + k^{\mathrm{D}}_{\mathrm{nrad}} + k_{\mathrm{T}}A_0(t)\right]D_1(t),\\ \dot{A}_1(t) &= \left[k^{\mathrm{A}}_{\mathrm{exc}}(t) + k_{\mathrm{T}}D_1(t)\right]A_0(t) - \left[k^{\mathrm{A}}_{\mathrm{rad}} + k^{\mathrm{A}}_{\mathrm{nrad}}\right]A_1(t).\end{aligned} \quad (1)$$

where $D_{0,1}$ and $A_{0,1}$ are the probabilities of finding the donor and the acceptor chromophores in the electronic ground or excited state. The donor is excited by the focused pulsed laser beam with a time dependent rate $k^{\mathrm{D}}_{\mathrm{exc}}(t)$ to a higher vibronic level D_1^* of the first excited state. According to Kasha's rule vibronic relaxation occurs very fast such that the population can be neglected with respect to the lowest electronically excited state.[29] The donor may relax to its ground state with a non-radiative $k^{\mathrm{D}}_{\mathrm{nrad}}$, a radiative $k^{\mathrm{D}}_{\mathrm{rad}}$ and an energy transfer rate constant k_{T} exciting in turn the acceptor to the vibronic level A_1^* of the excited state. The acceptor can relax from its pure electronically excited state A_1 by non-radiative or radiative decay channels to its ground state A_0. Eqn (1) can be solved analytically for a quasi-stationary equilibrium $\dot{D}_1(t) = \dot{A}_1(t)$, whereas the time evolution of $D_1(t)$ and $A_1(t)$ can be found only numerically. The energy transfer rate constant k_{T} as a measure of the dipole–dipole coupling depends on the spectral overlap of the donor fluorescence and acceptor absorption, the dipole–dipole separation in space and the mutual orientation of the transition dipole moments. The rate constant reaches its maximum value when the transition dipole moment of the acceptor is oriented parallel to the near-field induced by the donor or reaches zero if the transition dipole moment and field are perpendicular to each other.

In an altered photonic environment the decay rate constants have to be adapted to their dependency on the LDOS. The enhancement of the radiative rate can be calculated analytically[30] while in our Fabry–Pérot resonators the contributions to non-radiative relaxation by quenching due to the interaction of the emitters with the metallic mirrors are small.[9,31,32] This is because of the comparably large distances from the emitters to the metal surface which range between 70 and 125 nm adjusted by using a SiO_2-spacer layer on top of the silver. In the following, all radiative rate constants are denoted as functions of the on-axis transmission wavelength of the resonator λ_{res} which is experimentally directly accessible by white light transmission spectra of the resonator.

The total decay constant (or lifetime by $\tau^{\mathrm{D_A}} = (k^{\mathrm{D_A}})^{-1}$) for the donor in a FRET-pair can be expressed as

$$k^{\mathrm{D_A}} = k^{\mathrm{D}} + k_{\mathrm{T}} = k^{\mathrm{D}}_{\mathrm{rad}} + k^{\mathrm{D}}_{\mathrm{nrad}} + k_{\mathrm{T}}, \quad (2)$$

which is the sum of the total decay constant of the bare donor k^{D} and the transfer rate constant k_{T} offering an additional decay channel. Therefore, the transfer rate constants can be determined by the experimentally accessible decay constants

of the donor fluorescence for a specific resonance wavelength λ_{res} of the Fabry–Pérot cavity as

$$k_T(\lambda_{res}) = k^{D_A}(\lambda_{res}) - k^{D}(\lambda_{res}). \quad (3)$$

Recording the on-axis transmission wavelengths allows one to calculate the radiative enhancement factor as a function of mirror separation.[24,30] For determining the transfer rate constants for a large number of different FRET-pairs and cavity lengths, the resonator was mounted on a scanning stage of a home built confocal microscope equipped with a spectrograph and a thermoelectrically cooled CCD-detector for recording fluorescence and transmission spectra and an avalanche photodiode (APD) for recording fluorescence decay curves by TCSPC. The pulsed and linearly polarized Gaussian laser beam was focused on the sample by using an objective lens (NA 1.46) which was able to collect also cavity off-axis emission. By installing a band-pass filter transmitting from 520–540 nm in front of the APD and switching between the photodiode and the CCD-camera it was possible to record fluorescence spectra of a FRET-pair and the decay curves at the very same lateral position representing exclusively the total decay of the donor chromophore inside the FRET-pair. A more detailed description of the microscope is given in the ESI.† First, the resonator was tuned to on-axis transmission wavelengths of around 500 nm for the lateral position of the detection volume by white light illumination. After that, the corresponding decay curve and fluorescence spectrum were recorded subsequently at the very same lateral position with integration times of 1 s by laser illumination. Then the confocal probing volume was laterally shifted by 1 μm and again the transmission and fluorescence were recorded. By a custom program (Labview) automatizing the procedure it was possible to investigate over 10 000 spatially separated volumes during all experiments. For the experiment with the FRET-pairs in the resonator ~200 measured decay curves exceeded the threshold (30 counts per s in first time-bin) for determining the respective decay rate constants.

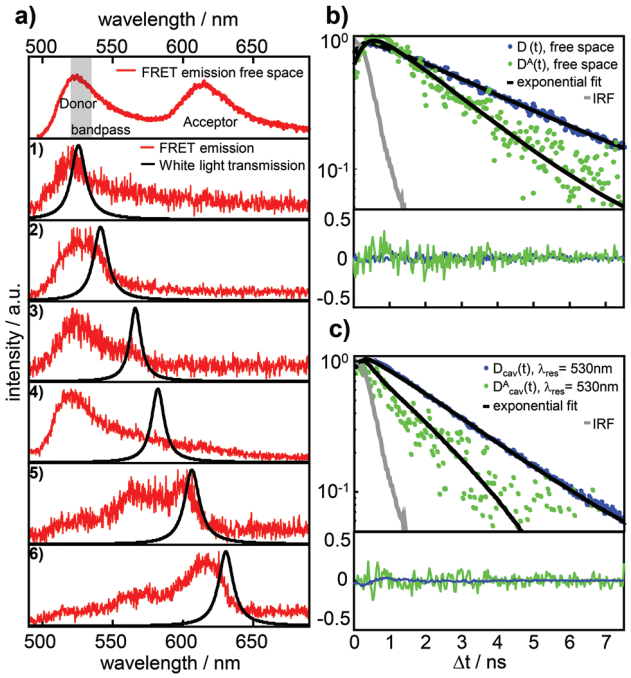

Fig. 2 (a) Top panel: free space ensemble fluorescence spectrum (red lines) of the FRET-pair Atto488 (donor) and Atto590 (acceptor). The gray area indicates the transmission of the bandpass filter placed in front of the APD to record decay curves of the donor fluorescence only. The six fluorescence spectra in the lower panels are from the same FRET-pair in a microresonator for different on-axis wavelengths of the resonator as illustrated by the black lines of the corresponding white light transmission spectra depending on the respective mirror separations. The change of the fluorescence spectra is in agreement with the expected effect of the cavity induced photonic environment, which is well described in the literature.[26–28] (b) Free space decay curves of donor fluorescence without (blue dots) and with (green dots) a coupled acceptor, recorded with a bandpass filter in front of the APD. (c) Fluorescence decay curves of donor D emitted photons without (blue dots) a coupled acceptor and the photons emitted by the donor D^A within the FRET-pair (green dots) in a microresonator with on-axis resonance wavelength 530 nm and a bandpass filter in front of the APD to select the donor fluorescence only. The black lines in (b) and (c) represent mono-exponential decay curves convolved with the instrument response function (IRF, gray line) fitted to the experimental data yielding the decay constants τ^D and τ^{D^A}.

2 Results

Fig. 2a shows a free space ensemble spectrum of our FRET-pair consisting of the dyes Atto488 (donor) and Atto590 (acceptor) averaged over all measured confocal volumes to guarantee a homogeneous distribution of FRET-pairs in the sample volume. The emission with maximum intensity around 528 nm and a less intense vibronic contribution around 560 nm are assigned to the donor fluorescence while the red shifted contribution with its maximum around 620 nm is emitted by the acceptor. The gray shaded area represents the transmission range of the bandpass-filter installed in front of the APD selecting the donor fluorescence only for the time resolved measurements. In Fig. 2a the lower six panels show the fluorescence spectra (red lines) of FRET-pairs in the resonator recorded as a function of increasing mirror spacing, indicated by Lorentzian linefits to white light transmission spectra (black lines). The cavity fluorescence spectra (1)–(4) show only the blue wavelength bands of the donor. The donor's red wavelength vibronic band around 560 nm and the complete acceptor emission are suppressed. The cavity fluorescence spectra (5) and (6) show enhanced emission of the donor's long wavelength band and a part of the acceptor emission band around 610 nm. This behavior is in accordance with the resonance conditions for emission of fluorescent dipoles inside Fabry–Pérot-resonators, the mode spectrum given by the Purcell factor for this geometry and the angular detection efficiency of the objective lens.[23,30,33] Fig. 2b shows measured fluorescence decay curves of the bare donor (blue dots) and the donor coupled to the acceptor (green dots) in free space, respectively. Both traces can be well fitted (black curves) to the

convolution of a mono-exponential model function and the instrument response function (IRF, gray line). In panel (c) measured fluorescence decay curves of the bare donor (blue dots) and the donor coupled to an acceptor (green dots) in the resonator with an on-axis transmission wavelength of 530 nm matching the donor emission are displayed together with the fitted curves (black lines) consisting of a mono-exponential model function convolved with the IRF (gray line). Evaluating all recorded decay curves exceeding the pre-defined threshold in free space and in the cavity allows us to determine the statistically significant distributions. The determined 1200 bare donor decay constants k^{D} (blue bars) and 800 FRET-coupled donor decay constants k^{D_A} (green bars) in free space are shown in Fig. 3a by their relative occurrence. According to eqn (2) and the narrow distribution of the decay constants of the bare donor k^{D} the transfer rate constants k_T (brown bars) could be determined for each measured k^{D_A} as well as the FRET efficiency (yellow bars, lower panel) defined as $E = k_T/[k^{D} + k_T]$. For the bare donor, the distribution of the decay rates yields an average value of $k^{D} = 0.309 \pm 0.016$ ns^{-1}, for the FRET-coupled donor decay rates $k^{D_A} = 0.524 \pm 0.137$ ns^{-1} and for the efficiency $E = 0.448 \pm 0.083$. The significantly wider distribution of the FRET-coupled donor decay constants reflects the variation of the transfer rate constants and is in accordance with a mutual distribution of transition dipole moment orientations between the donor and acceptor in an amorphous polymer matrix.

Fig. 3b shows the cavity modified lifetimes of the bare donors $\tau^{D}(\lambda_{res})$ (blue dots) and of the donors within the FRET-pair $\tau^{D_A}(\lambda_{res})$ (green dots) as a function of resonator wavelength. The bare donor lifetimes follow closely analytically calculated profile depending on the cavity length[30] (black curve) for molecules centered in the resonator with transition dipole moments parallel to the mirror surfaces. The gray line shows the modeled lifetimes $\tau^{D_A}(\lambda_{res})$ assuming a cavity length independent transfer rate constant k_T with the mean free space value. The largest number of data points appear for cavity resonance wavelengths <600 nm *i.e.* when the cavity and the donor emission are in resonance.

Due to the narrow distribution of the bare donor decay rates $k^{D}(\lambda_{res})$ around the analytical solution, the transfer rate constants $k_T(\lambda_{res})$ can be determined by eqn (3) for each $k^{D_A}(\lambda_{res})$ and are displayed in Fig. 4 as yellow dots in the center graph. The transfer rate constants determined in this way can be divided roughly into two sections. The dots in the left section (blue shaded area) represent those rate constants which were determined for a resonator setting $\lambda_{res}(L) < 570$ nm *i.e.* when the donor emission is in resonance with the cavity. The dots in the right section (red shaded area) represent the transfer rate constants that have been determined where $\lambda_{res}(L) > 570$ nm *i.e.* when the acceptor emission is in resonance with the cavity. On the left side, the distributions of the transfer

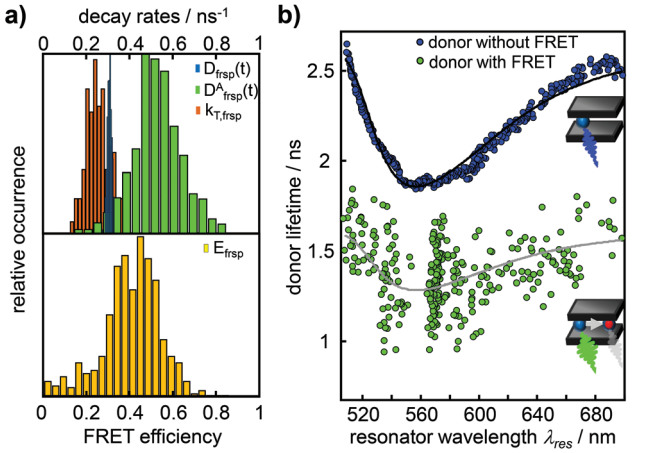

Fig. 3 (a) Histogram of total donor decay rates from different confocal volumes containing single bare donors (blue bars, $k^{D} = 0.309 \pm 0.016$ ns^{-1}) and single FRET-pairs (green bars, $k^{D_A} = 0.524 \pm 0.137$ ns^{-1}) in free space. The brown bars show the distribution of the energy transfer rates ($k_T = 0.249 \pm 0.079$ ns^{-1}) determined by eqn (3). The panel below shows the distribution of the energy transfer efficiency in free space E_{frsp} (yellow bars, $E_{frsp} = 0.448 \pm 0.083$ with: $E_{frsp} = k_T/[k^{D} + k_T]$). (b) Lifetimes τ^{D} and τ^{D_A} from mono-exponential fits of decay curves of single donor molecules without (blue dots) and with a coupled acceptor (green dots) as function of the on-axis resonance wavelength of the microresonator. The black line shows the simulated decay constant of the excited state of the donor inside the resonator. The gray line shows the simulation for the relaxation constant of the excited donor when coupled to an acceptor. The simulation of the lifetime of the FRET-coupled donor is based on the mono-exponential approximation and is the sum of the simulation of the pure donor (black line) and the mean transfer rate constant, determined from free space measurements.

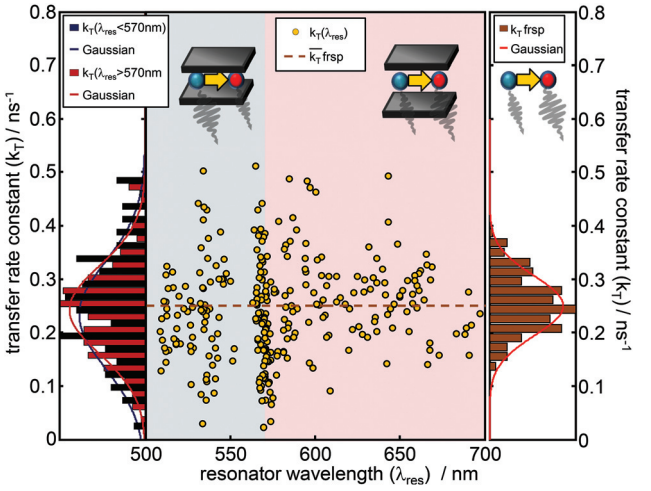

Fig. 4 Transfer rate constants $k_T(\lambda_{res})$ (yellow dots) as a function of cavity resonance wavelength for the FRET-pair Atto488 and Atto590 inside an optical $\lambda/2$ microresonator. The yellow dots spread symmetrically around the free space mean value indicated by the brown dashed line and show no wavelength dependence. The dark blue bars (left panel) show the transfer rate constant distribution for $\lambda_{res} < 570$ nm with a mean value $k_T(<570\text{ nm}) = 0.233 \pm 0.141$ ns^{-1} and the red bars show the respective transfer rate constant distribution for $\lambda_{res} > 570$ nm with a mean value $k_T(>570\text{ nm}) = 0.242 \pm 0.112$ ns^{-1}. The histogram on the right shows the distribution of k_T with a mean value of 0.249 ± 0.079 ns^{-1} in free space.

rate constants of both sections (donor resonance: dark blue; acceptor resonance: dark red) are visualized by histograms. The corresponding Gaussians show a mean transfer rate constant k_T of 0.233 ± 0.141 ns^{-1} (λ_{res} < 570 nm) and 0.242 ± 0.112 ns^{-1} (λ_{res} > 570 nm), respectively. On the right side, the distribution of the free space transfer rate constant (brown bars) is shown for comparison. The free space mean value is indicated as a dashed line in the center graph. All three distributions spread around the free space value, shaped symmetrically and show a large overlapping with mean values much closer to each other than their FWHM. Hence, the transfer rate constants determined for different transmission wavelengths show no significant dependence on the resonator wavelength.

3 Discussion

The presented results reflect the attempt to avoid the following three main obstacles of determining FRET-rate constants as a function of the LDOS achieved by the sample preparation, the design of the microresonator and the measurement procedure.

1: the intrinsic properties of a single FRET-pair and the corresponding transfer properties may vary with time due to conformational changes, bending or stretching of the DNA or the linker groups attached to the chromophores. This issue was faced by fixing the coupled chromophores in a PVA-matrix, preventing geometrical changes of the pair itself and the fluorophores with respect to each other over time. The TCSPC-histograms of the fluorescence decays (Fig. 2b) recorded with a collection time of 1 s are well described by a mono-exponential model function. Variations of orientation or distances within the FRET-pair during the acquisition time would lead to a multi-exponential decay behavior. The wide distributions of FRET-rate constants in free space and in the resonator can exclusively be ascribed to different conformational dispositions of the chromophores labeled to the DNA embedded in a rigid PVA matrix and reflect the results of previous studies.[34,35]

2: the number of fluorescent dyes/FRET-pairs in the detection volume was chosen to be small enough to prevent averaging. Two or more FRET-pairs in the same detection volume would most likely have different donor decay rates resulting in double or multi exponential fluorescence decay curves. Thus, only decay curves fitting to the mono-exponential model function were further used in the evaluation. The distributions of the donor decay rates with and without the acceptor in free space and in the cavity show no significant asymmetric distortions or bimodal behavior. The design of the FRET-pair itself (see the ESI†) guarantees that we detected only fluorescent donors with linked acceptors. Hence, we can claim that our results were acquired at the single molecule level and the number of data-points and resonator separations are large enough allowing us to make statistically significant statements.

3: the influence of the photonic environment can be precisely controlled in particular for different lateral and axial locations and random orientations of the embedded emitters with respect to the resonator geometry defining the LDOS. The setup of our resonator allows one to accurately position the molecules in the center of the resonator by a thin PVA-film of several nanometer thickness and by spin coating on a well defined spacer layer of SiO_2 to ensure a well defined distance between the emitters and the mirrors. The near-field of a dipole can excite plasmons in the metal if the distance to the surface is small enough leading to a reduced fluorescence lifetime.[36] However, the distance between the chromophores and the mirrors is so large (80 nm, 80–240 nm) that non-radiative quenching by the silver mirrors has only a minor effect and is almost independent of the cavity resonance.[14,26–28] The measured lifetimes of the donor without the acceptor in the resonator (Fig. 3b), $\tau^D(\lambda_{res})$, agree well with the model predicting radiative enhancement/inhibition according to the Purcell factor and a constant non-radiative decay.[14,26–28] The maximum enhancement of the LDOS in our approach tends toward a factor of 3, which seems to be still not enough to influence the FRET rate constant k_T.[9]

Due to these points, the reported results substantiate the assumption that the transfer rate constant of a closely spaced FRET pair is not influenced by the LDOS in our low-quality resonator. Nevertheless recent studies determined a scaling of the FRET-rate constant with the LDOS. Ghenuche *et al.* used FRET-pairs coupled to zero-mode waveguides milled in gold with diameters between 150 and 400 nm and determined an aperture size dependent rate constant.[12] Zhang *et al.*[11] observed altered energy transfer rates between donor–acceptor containing layers and an intermediate gold nanoparticle layer. This putative contradiction to our result is easily resolvable by regarding the effective mode distribution induced by the photonic environment. Our approach minimizes the coupling between the near-field modes of the emitter and the metal as the amplitude of the near field decays with R^{-3} and the cavity length is in the range of half a wavelength. Also Blum *et al.*[8] found no enhancement of the FRET-rate constant in their experiments. They used one silver mirror with different separations to the FRET-pairs in order to vary the LDOS and achieved a maximum total enhancement factor of 1.5 assuming a constant non-radiative decay rate due to comparably large emitter–mirror separations. The main advantage of our method compared to most of the previously used techniques is based on the ability to control the LDOS in real-time at the location of one and the same quantum system by increasing or decreasing the mirror separations by using piezoelectrically movable mirrors and simultaneously observing white light transmission spectra. The approaches with nanoholes or nanoparticles on the other side benefit mainly from near-field coupling effects between the metal and emitter due to a smaller metal–emitter separation. This important insight allows one to tailor specific photonic devices for enhancing individual optical properties of FRET-coupled fluorophores without altering the intrinsic coupling properties of the FRET pair itself.

4 Conclusion

Using tunable Fabry–Pérot-λ/2-microresonators allows one to examine, control and characterize the spectral and temporal optical properties of *e.g.* natural energy-transfer coupled systems without changing the coupling mechanisms determined by their intrinsic structure.[9,24] We could show that the FRET rate constant is not altered by the effective LDOS of our resonator by time resolved measurements on fluorescent single FRET-pairs at different mirror separations.

Acknowledgements

Financial support from the German Research Council (DFG) for ME1600/13-1 is gratefully acknowledged. Special thanks are directed to Barbara Pohl (Biomers, Ulm, Germany) for her advice and discussions concerning the design and fabrication of the FRET-pair.

References

1 R. Roy, S. Hohng and T. Ha, *Nat. Methods*, 2008, **5**, 507–516.
2 J. Lakowicz, *Principles of Fluorescence Spectroscopy*, Springer, 2006.
3 I. H. Stein, C. Steinhauer and P. Tinnefeld, *J. Am. Chem. Soc.*, 2011, **133**, 4193–4195.
4 M. Heilemann, P. Tinnefeld, G. S. Mosteiro, M. Garcia-Parajo, N. F. Van Hulst and M. Sauer, *J. Am. Chem. Soc.*, 2004, **126**, 6514–6515.
5 H. Y. Xie, H. Y. Chung, P. T. Leung and D. P. Tsai, *Phys. Rev. B: Condens. Matter*, 2009, **80**, 155448.
6 V. Faessler, C. Hrelescu, A. A. Lutich, L. Osinkina, S. Mayilo, F. Jackel and J. Feldmann, *Chem. Phys. Lett.*, 2011, **508**, 67–70.
7 M. J. A. de Dood, J. Knoester, A. Tip and A. Polman, *Phys. Rev. B: Condens. Matter*, 2005, **71**, 115102.
8 C. Blum, N. Zijlstra, A. Lagendijk, M. Wubs, A. P. Mosk, V. Subramaniam and W. L. Vos, *Phys. Rev. Lett.*, 2012, **109**, 203601.
9 F. Schleifenbaum, A. M. Kern, A. Konrad and A. J. Meixner, *Phys. Chem. Chem. Phys.*, 2014, **16**, 12812–12817.
10 P. Andrew and W. L. Barnes, *Science*, 2000, **290**, 785–788.
11 X. Zhang, C. A. Marocico, M. Lunz, V. A. Gerard, Y. K. Gun'ko, V. Lesnyak, N. Gaponik, A. S. Susha, A. L. Rogach and A. L. Bradley, *ACS Nano*, 2014, **8**, 1273–1283.
12 P. Ghenuche, J. de Torres, S. B. Moparthi, V. Grigoriev and J. Wenger, *Nano Lett.*, 2014, **14**, 4707–4714.
13 A. Caze, R. Pierrat and R. Carminati, *Photonics Nanostruct. Fundam. Appl.*, 2012, **10**, 339–344.
14 A. M. Kern, D. Zhang, M. Brecht, A. I. Chizhik, A. V. Failla, F. Wackenhut and A. J. Meixner, *Chem. Soc. Rev.*, 2014, **43**, 1263–1286.
15 K. J. Breslauer, R. Frank, H. Blocker and L. A. Marky, *Proc. Natl. Acad. Sci. U. S. A.*, 1986, **83**, 3746–3750.
16 W. Rychlik, W. J. Spencer and R. E. Rhoads, *Nucleic Acids Res.*, 1990, **18**, 6409–6412.
17 J. SantaLucia and D. Hicks, *Annu. Rev. Biophys. Biomol. Struct.*, 2004, **33**, 415–440.
18 R. M. Clegg, A. I. H. Murchie, A. Zechel and D. M. J. Lilley, *Proc. Natl. Acad. Sci. U. S. A.*, 1993, **90**, 2994–2998.
19 C. R. Sabanayagam, J. S. Eid and A. Meller, *J. Chem. Phys.*, 2005, **122**, 061103.
20 I. V. Gopich and A. Szabo, *Proc. Natl. Acad. Sci. U. S. A.*, 2012, **109**, 7747–7752.
21 A. Chizhik, F. Schleifenbaum, R. Gutbrod, A. Chizhik, D. Khoptyar, A. J. Meixner and J. Enderlein, *Phys. Rev. Lett.*, 2009, **102**, 073002.
22 S. Bar, A. Chizhik, R. Gutbrod, F. Schleifenbaum, A. Chizhik and A. J. Meixner, *Anal. Bioanal. Chem.*, 2010, **396**, 3–14.
23 A. I. Chizhik, A. M. Chizhik, A. M. Kern, T. Schmidt, K. Potrick, F. Huisken and A. J. Meixner, *Phys. Rev. Lett.*, 2012, **109**, 223902.
24 A. Konrad, A. L. Trost, S. Skandary, M. Hussels, A. J. Meixner, N. V. Karapetyan and M. Brecht, *Phys. Chem. Chem. Phys.*, 2014, **16**, 6175–6181.
25 E. M. Purcell, *Phys. Rev.*, 1946, **69**, 681–681.
26 M. Steiner, F. Schleifenbaum, C. Stupperich, A. V. Failla, A. Hartschuh and A. J. Meixner, *ChemPhysChem*, 2005, **6**, 2190–2196.
27 M. Steiner, F. Schleifenbaum, C. Stupperich, A. V. Failla, A. Hartschuh and A. J. Meixner, *J. Lumin.*, 2006, **119**, 167–172.
28 M. Steiner, A. V. Failla, A. Hartschuh, F. Schleifenbaum, C. Stupperich and A. J. Meixner, *New J. Phys.*, 2008, **10**, 123017.
29 M. Kasha, *Discuss. Faraday Soc.*, 1950, **9**, 14–19.
30 G. Bjork, *IEEE J. Quantum Electron.*, 1994, **30**, 2314–2318.
31 M. Paulus, P. Cay-Balmaz and O. J. F. Martin, *Phys. Rev. E: Stat. Phys., Plasmas, Fluids, Relat. Interdiscip. Top.*, 2000, **62**, 5797–5807.
32 J. R. Lakowicz, *Anal. Biochem.*, 2001, **298**, 1–24.
33 A. Konrad, F. Wackenhut, M. Hussels, A. J. Meixner and M. Brecht, *J. Phys. Chem. C*, 2013, **117**, 21476–21482.
34 A. A. Deniz, M. Dahan, J. R. Grunwell, T. J. Ha, A. E. Faulhaber, D. S. Chemla, S. Weiss and P. G. Schultz, *Proc. Natl. Acad. Sci. U. S. A.*, 1999, **96**, 3670–3675.
35 A. K. Wozniak, G. F. Schroder, H. Grubmuller, C. A. M. Seidel and F. Oesterhelt, *Proc. Natl. Acad. Sci. U. S. A.*, 2008, **105**, 18337–18342.
36 K. H. Drexhage, *Sci. Am.*, 1970, **222**, 108–118.

Supplementary information

Controlling the dynamics of Förster resonance energy transfer inside a tunable sub-wavelength Fabry-Perot-resonator

Alexander Konrad[1], Michael Metzger[1], Andreas M. Kern[1], Marc Brecht[2], and Alfred J. Meixner[1]*

1: University of Tuebingen, IPTC, Auf der Morgenstelle 18, 72076 Tuebingen, Germany

2: Zürcher Hochschule für Angewandte Wissenschaften, Institute of Applied Mathematics and Physics, Technikumstrasse 13, 8401 Winterthur, Switzerland.

E-mail: alfred.meixner@uni-tuebingen.de

Phone: +49 7071-29-76903. Fax: +49 7071-29-5490

Experimental setup

The microresonator design and the confocal microscope with optical path for excitation and detection is outlined in Figure 1). Due to fast bleaching (1-5 seconds with 20μW excitation) of the low concentrated sample (bare donor and FRET-pair), we acquired histograms for more than thousand different diffraction limited spots in free space and in the resonator. Additionally on each location of the resonator a white light transmission spectrum of the Fabry-Perot resonator was acquired in order to determine for each decay curve the on-axis resonance wavelength λ_{res}. The histograms of

*To whom correspondence should be addressed

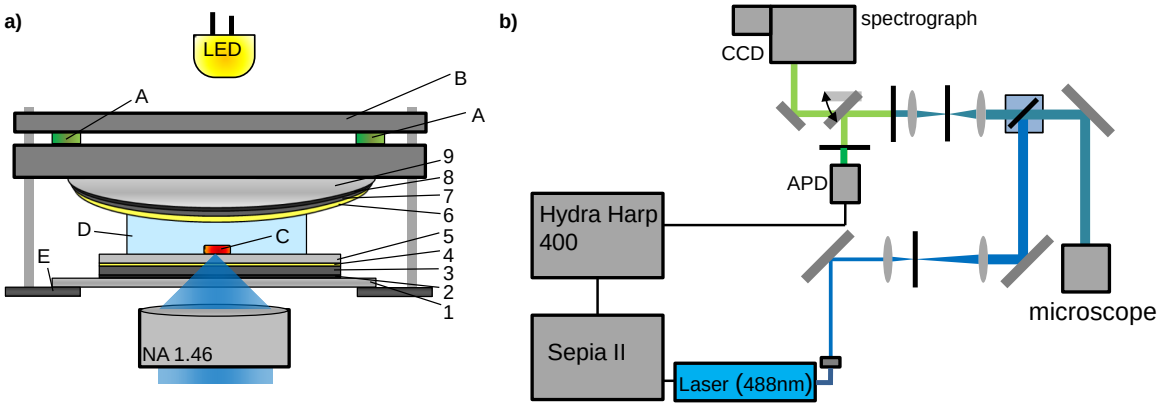

Figure 1: *Scheme of the experimental setup. a) Drawing of the resonator design. The mirrors consist of the following layers: 1) glass cover slide; 2) 1 nm chromium; 3) 40 nm silver; 4) 1 nm gold; 5) 80 nm SiO_2; 6) 1 nm gold; 7) 60 nm silver; 8) 1 nm chromium; 9) glass lens (f=150 mm) hence, the mirror surface can be considered to be parallel within the investigated sample section being less than 100µmin diameter. The cavity length is tuned by the piezoelectric stacks (A) implemented in a mirror mount (B). The sample (C) is placed about half way between the mirrors on the bottom mirror, which is immersed in the intra-cavity medium (D) (water). The bottom mirror is fixed on a plate (E) which is mounted on a three-axis feed-back controlled scanning stage. b) Scheme of the optical path: The excitation source, a pulsed 488 nm laser diode, is triggered by the Sepia II module which is synchronized with the counter module Hydra Harp 400. The beam is enlarged by a telecentric system and guided by a beamsplitter into the confocal microscope. For excitation and fluorescence collection the same objective (NA=1.46) is used. The fluorescence is deflected through a pinhole and a longpass filter on the detectors, an APD and a spectrograph with equipped thermoelectrically cooled CCD-camera.*

the bare donor show a high signal-to-noise ratio of around 100 while histograms of the donor in the FRET pair show a roughly 20 times lowered signal-to-noise ratio due to the lowered quantum yield of the donor and the bandpass filter in front of the APD additionally reducing the amount of detected donor photons by about 50%.

Sample

As stated in the main article, the thermodynamics and kinetics of the hybridization process of two DNA-strands may lead to false base sequences or incomplete reactions. Hence for ensemble measurements the determining of transfer rates is hampered by averaging over the lifetimes of bare donors and donors with various acceptor distances. To ensure that every measured fluorescence

photon originates from a similarly configured FRET-pair we used a sample design with both chromophores labeled at the same DNA-strand. A second chromophore-less DNA-strand is hybridized to the chromophore labeled DNA-strand to stabilize its conformation. The FRET-pair consisting of Atto488 and Atto590 with the DNA-base sequence is displayed in Figure 2. The hybridized pairs are diluted in Tris-buffer (with 1e-7 mol/L) and were embedded in a thin PVA film (aqueous 4%PVA solution) by spin-coating (5 min, 6000 rpm) on the substrates. The samples were used after evaporation of the solvent having a concentration of around 10e-9 mol/L.

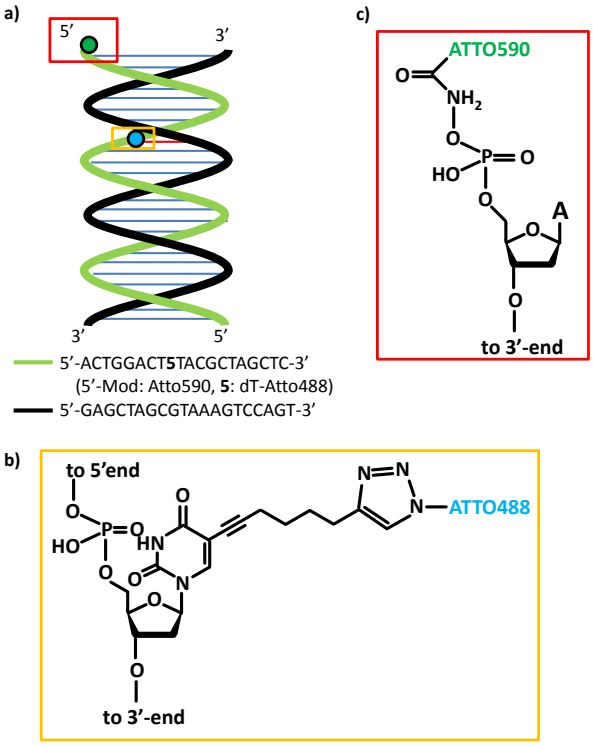

Figure 2: *Scheme of the FRET pair. a) Schematic drawing of the hybridized DNA-double strand. The green string is labeled at base number 8 with the fluorophore Atto488 and at the 5'-end with the fluorophore Atto590. The black strand was chosen to contain the complementary base sequence to guaranty conformational stability with the dye-labeled green strand. b) Structure of the binding linker between the base thymine and the fluorophore Atto488. c) Structure of the binding linker between the 5'end of the green string in a) and the fluorophore Atto590.*

Chapter 9

Spectroscopic properties of photosystem II core complexes from Thermosynechococcus elongatus revealed by single-molecule experiments

In this chapter the fluorescence of single photosystem II core complexes from the cyanobacterium *Thermosynechococcus elongatus* at 1.6 K was observed and analyzed together with absorption spectra in regard of the heterogeneity and dynamics of the respective spectral properties. Combining low temperature microscopy with single-molecule techniques allows to observe the temporal dynamics of the fluorescence spectra of such complex structures like PSII, which can be resolved due to sufficiently low spectral diffusion rates. According to the reduced phononic impact of the surrounding matrix and the intrinsic conformational changes the spectral properties of the fluorescence of single complexes can be observed, which show characteristic ZPLs contributed by different emitting Chlorophyll pools. By analyzing the spectral ZPL distribution it can be seen that the lowest energy traps are not the only observable contributions; three bands F685, F689 and F695 can be assigned. The observed spectral dynamics of the ZPLs substantiate remarkable effects on the energy transfer dynamics and energy trapping between the antenna sub-units CP43 and CP47 and the reaction center. However, the average fluorescence spectrum formed out of all single spectra show a reduced intensity of the F695 band compared to ensemble spectra which can be explained by an increased probability of triplet-states on the carotenoids due to the high excitation power. Such accumulated triplet-states are able to quench the emission of certain Chlorophyll pools in close proximity.

This chapter is based on:
Brecht, M., Skandary, S., Hellmich, J., Glöckner C., Konrad, A., Hussels, M., Meixner, A.J., Zouni, A., Schlodder, E. "Spectroscopic properties of photosystem II core complexes from Thermosynechococcus elongatus revealed by single-molecule experiments" *Biochimica et Biophysica Acta*, **2014**, *1837*,773-781.

Biochimica et Biophysica Acta 1837 (2014) 773–781

Contents lists available at ScienceDirect

Biochimica et Biophysica Acta

journal homepage: www.elsevier.com/locate/bbabio

Spectroscopic properties of photosystem II core complexes from *Thermosynechococcus elongatus* revealed by single-molecule experiments

Marc Brecht [a,b,*], Sepideh Skandary [a], Julia Hellmich [c], Carina Glöckner [c], Alexander Konrad [a], Martin Hussels [a], Alfred J. Meixner [a], Athina Zouni [c,d], Eberhard Schlodder [c]

[a] Universität Tübingen, IPTC and Lisa + Center, Auf der Morgenstelle 18, Tübingen, Germany
[b] Zurich University of Applied Sciences, Technikumstrasse 13, 8401 Winterthur, Switzerland
[c] Technische Universität Berlin, Max-Volmer-Institut, Straße des 17. Juni 135, Berlin, Germany
[d] Humboldt Universität zu Berlin, Institut für Biologie, Philippstr. 13, 10099 Berlin, Germany

ARTICLE INFO

Article history:
Received 30 October 2013
Received in revised form 28 January 2014
Accepted 31 January 2014
Available online 6 February 2014

Keywords:
Photosystem II core complex
CP43
CP47
Single-molecule spectroscopy
Low temperature spectroscopy
Fluorescence quenching

ABSTRACT

In this study we use a combination of absorption, fluorescence and low temperature single-molecule spectroscopy to elucidate the spectral properties, heterogeneities and dynamics of the chlorophyll *a* (Chl*a*) molecules responsible for the fluorescence emission of photosystem II core complexes (PS II cc) from the cyanobacterium *Thermosynechococcus elongatus*. At the ensemble level, the absorption and fluorescence spectra show a temperature dependence similar to plant PS II. We report emission spectra of single PS II cc for the first time; the spectra are dominated by zero-phonon lines (ZPLs) in the range between 680 and 705 nm. The single-molecule experiments show unambiguously that different emitters and not only the lowest energy trap contribute to the low temperature emission spectrum. The average emission spectrum obtained from more than hundred single complexes shows three main contributions that are in good agreement with the reported bands F685, F689 and F695. The intensity of F695 is found to be lower than in conventional ensemble spectroscopy. The reason for the deviation might be due to the accumulation of triplet states on the red-most chlorophylls (e.g. Chl29 in CP47) or on carotenoids close to these long-wavelength traps by the high excitation power used in the single-molecule experiments. The red-most emitter will not contribute to the fluorescence spectrum as long as it is in the triplet state. In addition, quenching of fluorescence by the triplet state may lead to a decrease of long-wavelength emission.

1. Introduction

Photosystem II (PS II) is the membrane protein complex of higher plants, green algae and cyanobacteria that uses solar energy to catalyze the electron transfer from water to plastoquinone [1,2]. The photo-oxidized electron donor of PS II ($P680^+$) is one of the most powerful oxidizing species capable of driving the oxidation of water to oxygen. The structure of dimeric PS II core complexes (PS II cc) from cyanobacteria has been determined by X-ray crystallography to a resolution of up to 1.9 Å [3,4]. Fig. 1 shows the chlorophyll containing subunits of PS II cc according to the structural model at 2.9 Å resolution [4]. Subunits CP43 and CP47 contain 13 and 16 chlorophyll *a* (Chl*a*) molecules, respectively. The PS II reaction center (RC), which is formed by the subunits D1, D2 and Cyt *b559*, binds six Chl*a* and two pheophytin *a* molecules. The RC is surrounded by the subunits CP47 and CP43. The primary function of CP47 and CP43 is to harvest light and transfer the absorbed energy to the RC, where the photochemical charge separation takes place.

The optical properties of PS II cc, its individual subunits (CP43, CP47) and the RC have been studied in detail [5–15]. The shape of the fluorescence emission spectrum depends remarkably on temperature [6,7,10–13]. Two spectral components at 685 nm and 695 nm, called F685 and F695, were used to explain the temperature dependence. Andrizhiyevskaya et al. [11] concluded that F695 originates from excitations that are irreversibly transferred to the red-absorbing 690 nm chlorophylls of CP47 and that F685 originates from excitations that are slowly transferred to the RC, where they are irreversibly trapped by charge separation. At 4 K almost all excitations that reach the 690 nm chlorophylls of CP47 will remain on this chlorophyll, whereas some excitations will become trapped on the red-most chlorophylls of CP43. Information about the optical properties of CP43 and CP47 core antennae was obtained from high-resolution spectroscopy in the frequency domain [6,16]. Excitation dependent fluorescence line narrowing spectra of PS II from spinach gave first evidence that CP43 holds two emitting states with different inhomogeneous distributions at low temperatures

Abbreviations: PS I, photosystem I; PS II, photosystem II; PS II cc, photosystem II core complex; CP43 CP47, chlorophyll binding subunits of PS II; ZPL, zero-phonon line; RC, reaction center; Chl*a*, chlorophyll *a*; Car, carotenoid

* Corresponding author.
E-mail address: marc.brecht@uni-tuebingen.de (M. Brecht).

0005-2728/$ – see front matter © 2014 Elsevier B.V. All rights reserved.
http://dx.doi.org/10.1016/j.bbabio.2014.01.025

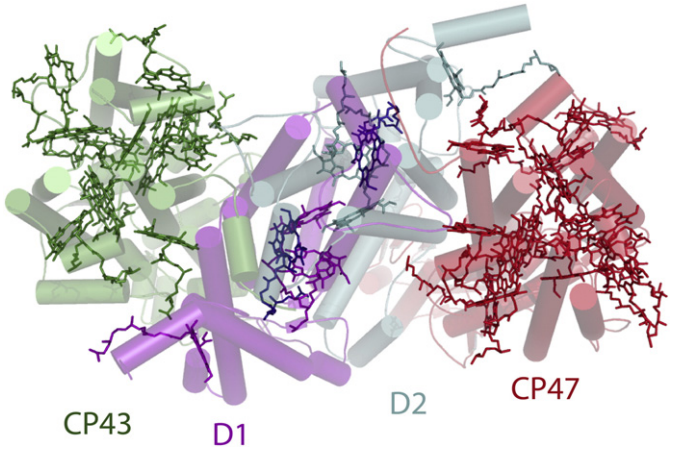

Fig. 1. Chlorophyll containing subunits of PS II cc. The Chl*a* molecules coordinated by the subunits CP43, D1, D2 and CP47 (cartoon mode) are shown in green, purple, cyan and red, respectively. The two Pheophytin (Pheo) a molecules are colored in dark blue. The figure was made with PyMol using the coordinates of the structural model of PS II cc from *Thermosynechococcus elongatus* at 2.9 Å resolution (Ref. [4], (PDB code 3BZ1)).

[6]. Komura et al. [12] performed picosecond time-resolved fluorescence spectroscopy on spinach PS II at 4, 40, and 77 K and identified an additional fluorescence band at 689 nm (F689). The fast decay of F689 suggests an energy transfer directly from F689 to P680 [12]. The complex interrelation between the different subunits and the strong influence of the inhomogeneous widths of the different red-states makes a set of optical techniques necessary to solve their function in the excitation energy transfer.

In this study we investigate the optical properties of intact, oxygen-evolving PS II cc dimers of *Thermosynechococcus elongatus* at the single-molecule level. Single-molecule techniques overcome the inhomogeneous broadening. This is especially useful if the influence of inhomogeneity is covered by ensemble averaging [17]. At ambient temperatures, the susceptibility of the chromophores to fluctuations of the protein moiety and its surrounding media leads to line broadening (spectral diffusion) [18–20]. Lowering the temperature is one possibility to reduce the impact of fluctuations on the chromophores' site energies. Low temperature experiments have the additional advantage to minimize photobleaching and limitations in the observation time [21]. Assuming that all fluctuations are suppressed, the emission profile of a single emitter composed out of a sharp zero-phonon-line (ZPL) and a phonon-wing becomes observable. The ZPL belongs to an electronic transition between the vibronic ground state of the first electronic excited state and the vibronic ground state of the electronic ground state. This kind of emission is not accompanied by the creation or annihilation of phonons. The phonon wing on the low-energy side of the ZPL is due to the reorganization of the surrounding induced by the excitation of the chromophores from the ground to the excited state. The reorganization leads to the excitation of phonons (lattice vibrational modes). Due to the small line width of the ZPLs, it is possible to observe the process of spectral diffusion in slow-motion as nicely shown by experiments on LH2 and PS I at 1.4 K [22,23]. The widths of those spectral jumps reach into the range of several nanometers indicating remarkable changes in the site energy of the emitting chlorophyll molecules. In a recent study on PS I, we were able to show that a large portion of the spectral dynamics in the lower hierarchical levels is connected to fluctuations of protons located close to the chromophores [24]. Such protons can be found e.g. in hydrogen bonds between the chromophore and nearby amino acid residues, or structural water molecules [24,25]. The consideration of site-energy changes induced by all of these fluctuations is necessary to understand the optical properties of these proteins, especially if the chromophores take part in energy transfer. Coupled chromophores are found in almost all pigment proteins that are involved in light harvesting. Then, spectral jumps of only one chromophore are able to redirect the actual pathways of a traveling exciton and as a consequence it takes influence on the function of the whole protein complex [26,27].

2. Material and methods

2.1. Single-molecule fluorescence spectroscopy

Dimeric PS II cc from *T. elongatus* have been isolated and purified as described in Ref. [28]. The purified PS II cc dimers were diluted in buffer solution containing 100 mM PIPES (pH7.0), 5 mM $CaCl_2$, 0.5 M betaine, and 0.03% β-DM. For single molecule experiments, PS II complexes were diluted in buffer to a final PS II concentration of about 3 pM. About 1 μl of this suspension was placed between cover slips made of glass. Finally the sample was transferred directly into the cryostat and rapidly plunged into liquid helium. Experiments were carried out using a home-built confocal microscope operating at 1.6 K as described recently in Ref. [29].

The excitation intensity of the laser, measured before entering the cryostat, was 100 μW resulting in a flux of approximately $6.6 \cdot 10^{20}$ photons/(cm^2 s). The excitation wavelength was 665 nm for all experiments. The highest resolution of the spectrometer (Shamrock 500 spectrograph with 200 lines/mm and 400 lines/mm gratings in combination with Andor Newton back illuminated deep depleted CCD) is ~0.05 nm. In a sequence of spectra, the usual exposure time for each spectrum is 2 s resulting in a typical S/N ratio of >6 for single PS II cc dimers at the given excitation power referred to as time resolution in the following context.

2.2. Measurement of steady state absorption and fluorescence spectra

Absorption spectra were recorded with a spectral resolution of 1 nm on a Cary-1E-UV/VIS spectrophotometer (Varian, Inc.). Fluorescence spectra were recorded in a FluorMax 2 (Jobin Yvon) photon counting spectrofluorometer. The spectra were corrected for the spectral sensitivity based on the measurement of a calibrated light source. For the measurements, PS II complexes were diluted to a final Chl concentration of about 5 μM with buffer containing 20 mM MES-NaOH (pH 6.5), 10 mM $MgCl_2$, 10 mM $CaCl_2$, 0.02% (w/w) β-DM and glycerol (final concentration about 65% (v/v)), to obtain a transparent glass at low temperatures. For experiments at cryogenic temperatures, the cuvette was placed in a variable temperature liquid nitrogen bath cryostat (Oxford DN1704) or an Oxford liquid helium flow cryostat (Oxford CF1204). A home-built cryostat holder was used in the spectrophotometer and spectrofluorometer.

3. Results and discussion

3.1. Ensemble absorption and emission spectra of PS II cc

Fig. 2 presents temperature-dependent absorption and fluorescence emission spectra of PS II cc dimers from *T. elongatus*. At 5 K the Q_Y absorption exhibits peaks at 674 nm and 684 nm and shoulders near 669 nm, 677 nm, 680 nm and 694 nm. The second derivative of the 5 K spectrum shows minima at the specified wavelengths indicating various pigment pools (not shown).

The emission band at 290 K is centered at around 683 nm. At 50 K, two bands located at 685 nm and 694 nm are resolved. These bands are generally named F685 and F695. The 20 K fluorescence spectrum exhibits the maximum at 691 nm. The overall behavior is in good agreement with measurements on PS II samples from spinach [5,11]. The band at 695 nm (F695) has been assigned to the lowest lying energy state of the chlorophylls in CP47 [5,11] that is associated with Chl29 by several groups (using the nomenclature used in Loll et al. [30]) [2,7,31,32]. Low energy chlorophylls become traps for the excitation energy, if the thermal

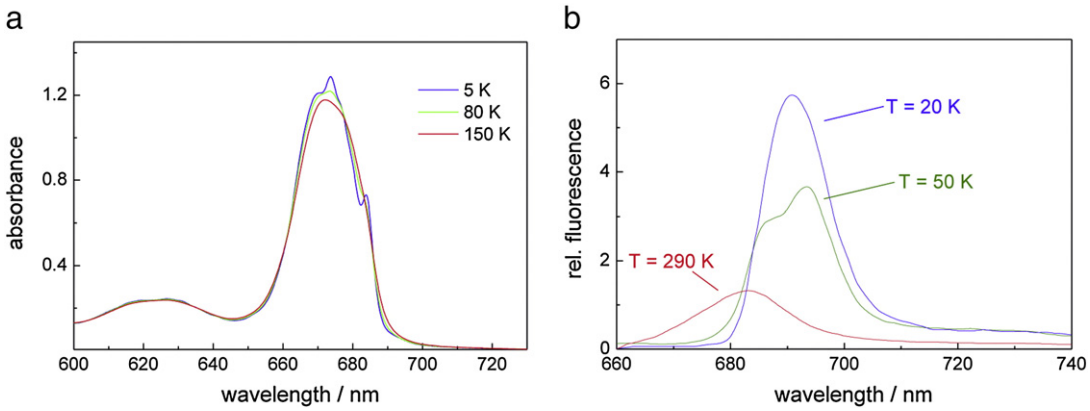

Fig. 2. (a) The panel on the left shows absorption spectra of dimeric PS II cc from *T. elongatus* at 5 K, 80 K and 150 K. The Q_y absorption band is centered at about 673 nm. (b) The panel on the right shows fluorescence spectra of dimeric PS II cc from *T. elongatus* at 20 K, 50 K and 290 K.

energy (kT) is not sufficient to enable uphill energy transfer to the RC. Lowering the temperature from 50 K to 5 K causes the fluorescence to increase and its maximum to shift to the blue to 691 nm at 20 K and 687 nm at 5 K (see Fig. 2b and Refs. [5,10–12]). This blue shift and fluorescence increase may be interpreted by the assumption that chlorophylls, absorbing at slightly shorter wavelengths than the lowest energy chlorophyll start to successively trap the excitation energy if the temperature is lowered. There are two possibilities for this case: (a) These chlorophylls are all part of the inhomogeneous distribution of transition energies of the lowest lying energy state of the chlorophylls in CP47 or (b) structurally different chlorophylls in the PS II antenna become a trap, which are not connected by fast energy transfer with the lowest state in CP47.

3.2. Emission spectra of individual PS II cc dimers

Fig. 3 shows a selection of six fluorescence emission spectra (denoted I–VI) of different single PS II cc dimers. The acquisition time for the spectra was 40 s. Single PS II cc dimers can be detected at low temperature using the fluorescence emission of several Chl*a* molecules acting as traps for the excitation energy at cryogenic temperatures with a significant fluorescence quantum yield.

The emission spectra of single PS II cc are characterized by ZPLs covering the whole range of fluorescence from 680 to 750 nm. Each spectrum exhibits unique features. In the wavelength range 680 to 690 nm all spectra show several ZPLs. Their number varies between two (spectrum VI) and six to seven (spectrum I). At wavelengths larger than 690 nm clearly visible lines are only observed in spectra I–III. Their intensities are reduced compared to the lines in the range 680–690 nm.

Fig. 4 shows a series of fluorescence emission spectra recorded on one single PS II cc within 2, 10, 50, 100 and, 200 s. The spectra show one pronounced line at ~684 nm and a line with smaller intensity at ~682 nm. The line width (fitted by a Gaussian) increases in the spectra taken at 2 and 200 s from ~0.35 nm (for both lines) to 1.15 nm (line at 682 nm) and 1.20 nm (line at 684 nm). The time dependent broadening of the lines indicates that spectral diffusion is the main underlying broadening process. Further details about the number and spectral positions of emitters responsible for the fluorescence emission of single PS II cc dimers are obtained from the analysis of their polarization. Fig. 5 shows the fluorescence emission of a single PS II cc dimer in dependence of the polarizer angle in front of the spectrograph. This angle is defined with respect to an arbitrary laboratory axis and is uncorrelated to the polarization of the excitation light [33]. In Fig. 5, the dependence of the whole emission spectra as a function of the polarizer orientation is shown. Three pronounced contributions at 684.7 nm, 686.2 nm and, 689.7 nm can be distinguished. The intensity of these contributions vanishes at specific angles almost completely; therefore a strong linear polarization can be assumed. Similar intensity variations were observed for all PS II cc investigated in this way. A strong polarization of the fluorescence emission from the different Chls requires either a single emitter as the origin of the emission or a number of emitters with parallel transition dipole moments. Since the PS II cc are randomly oriented in our samples, it is unlikely that the transition moments of several emitters would appear parallel in all cases. Therefore, the number of emitters responsible for the fluorescence emission of a single PS II cc can be determined by this method. A detailed study on this topic is in preparation.

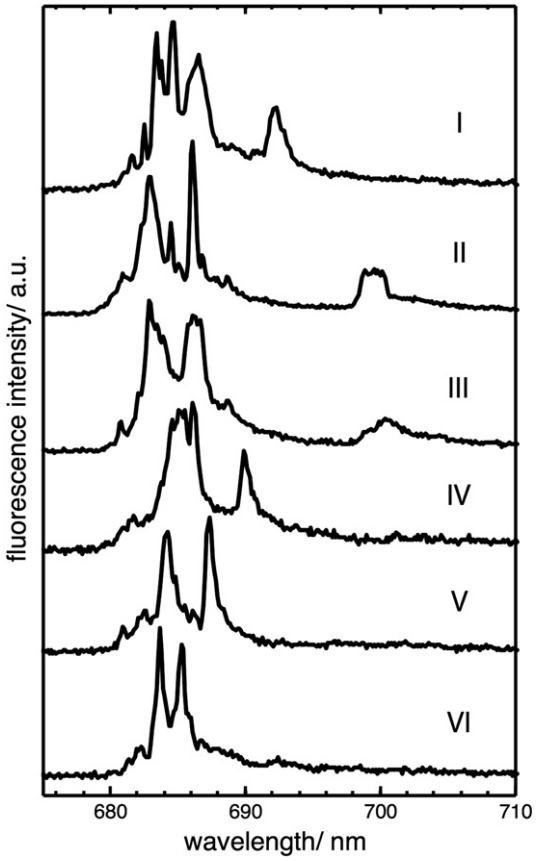

Fig. 3. Single-molecule fluorescence emission spectra from PS II cc dimers of *Thermosynechococcus elongatus*. Spectra were recorded on different individual complexes. The accumulation time was 40 s for each complex. For better comparability, the spectra that exhibited intensity differences were scaled to a similar magnitude. Excitation wavelength 665 nm; temperature 1.6 K.

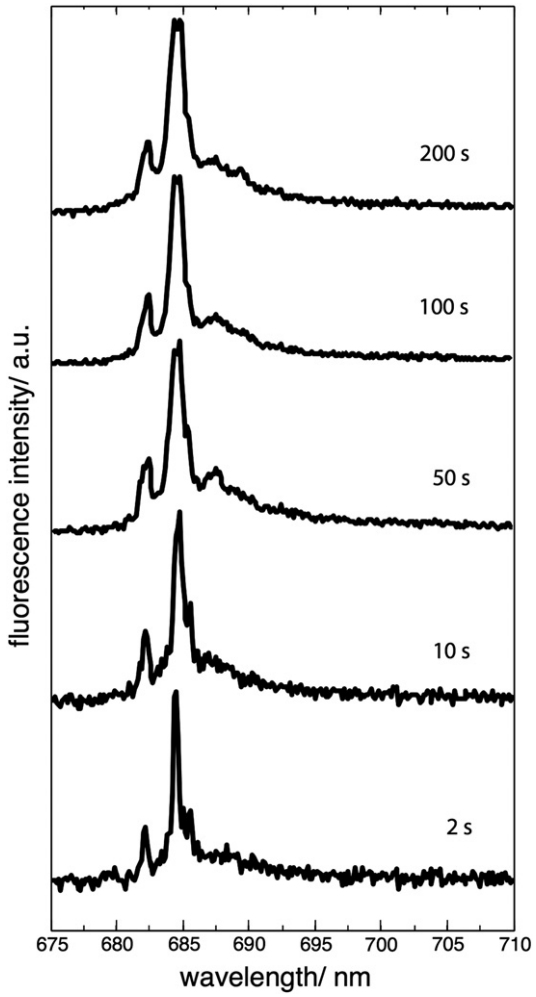

Fig. 4. Dependence of fluorescence emission spectra of one single PS II cc dimer on acquisition time. Excitation wavelength 665 nm; temperature 1.6 K.

3.3. Spectral dynamics and intensity variations of ZPLs

The basis of the dynamical process leading to the spectral broadening can be analyzed in our setup with sufficient S/N ratio using an acquisition time of 2 s. In order to analyze the spectral dynamics in the emission of PS II cc sequences of fluorescence spectra of 140 complexes were recorded. In Fig. 6 two representative examples of the time-dependent behavior of ZPLs are shown. The sequences consist of 100 spectra consecutively recorded with 2 s acquisition time. The average spectra are shown on top. The average spectrum (Fig. 6a) is dominated by two intense emitters at 682.9 nm (fwhm = 1.34 nm) and 686.2 nm (fwhm = 0.35 nm) and one broad line at 699.8 nm (fwhm = 1.66 nm). In the sequence it becomes obvious that these emitters show quite different spectral diffusion behavior. The intense line around 682.9 nm remains in the first 80 s within a limited spectral range. In the interval 100–160 s, its spectral width is expanded. Starting at 160 s up to the end of the sequence, the bandwidth is reduced again. The line around 686.2 nm remains for the most of the time at one spectral position. Only in time intervals e.g. 60–65 s, 140–148 s the line undergoes discrete jumps in frequency. In all cases the jump width is ~0.8 nm. The third line at 699.8 nm shows also pronounced spectral diffusion, but even more striking are the intensity variations of this line. In the first 80 s, the line has a low intensity. During the interval 80–150 s, the intensity is increased and the line shows several jumps in frequency until the intensity drops down completely. The sequence (Fig. 6b) shows an example for ZPLs without changes in the wavelength position during time. The average spectrum shows two intense ZPLs at 682.6 nm (fwhm = 1.0) and 684.4 nm (fwhm = 0.6) as well as a ZPL with lower intensity at 690.1 nm (fwhm = 0.6). All three lines are visible during the whole time of data acquisition. The lines at 682.6 nm and at 690.1 nm show almost no change in wavelength during time, whereas for the line at 684.4 nm slight changes are observed. Both lines show intensity variations of almost 100%, whereas the line at 690.1 nm emits with almost constant intensity.

Different lines in single-molecule spectra (e.g. see Fig. 3) may be the result of spectral diffusion (i), static disorder (ii), or different emitters (iii): (i) As can be seen in Fig. 6 spectral jumps are typically less than 1.5 nm. Lines, which are close together, may be assigned to a single emitter whose site-energy changes due to protein dynamics during the accumulation period. In general, spectral diffusion leads to a time dependent broadening of the lines (see Fig. 4) and not to separated lines. (ii) Chlorophylls bound at the same site in both monomers of the PS II dimer might have different transition energies. A Gaussian distribution is often used to describe the extent of static disorder within an ensemble with a full width at half maximum of about 200 cm^{-1} corresponding to about 10 nm [13]. (iii) Different low energy traps bound at CP43 and CP47 give rise to separated lines if the low energy states are not connected to each other by efficient energy transfer leading rapidly to thermal equilibrium. Taking the above-mentioned processes together it is reasonable that at least 2–3 emitters contribute to the emission spectra shown in Fig. 3; nevertheless an uncertainty in the determination of their correct number remains. To remove this remaining uncertainty, polarization dependent measurements (shown above) are a perfect tool to unravel overlapping signals and to account for the correct number of emitters.

The movement of the ZPLs is characterized by discrete spectral jumps with different widths and not by continuous changes in their positions (Fig. 6). A plausible explanation of the spectral dynamics observed in LH2 based on the hierarchy of tiers in the energy landscape of a protein is given in Ref. [22]. We adopt this explanation for the observed spectral dynamics in PS II. High energetic barriers between the different conformational substates characterize the highest tier in the energy landscape. Under the given low-temperature conditions, the barriers cannot be crossed and the system rests in one given conformational substate in the first tier. Two different situations are illustrated

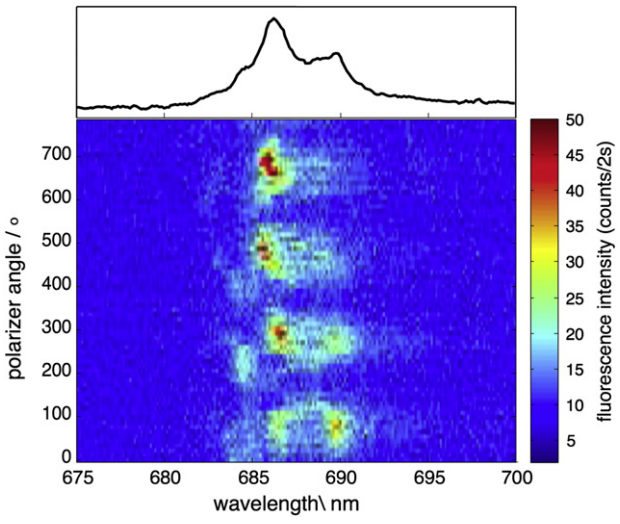

Fig. 5. Sequence of fluorescence emission spectra of a single PS II cc dimer as a function of the orientation of the polarizer in front of the spectrograph. The acquisition time was 2 s for each spectrum. Excitation wavelength 665 nm; temperature 1.6 K. The individual spectra were recorded in steps of 10°. The angle of the polarizer is shown on the left side.

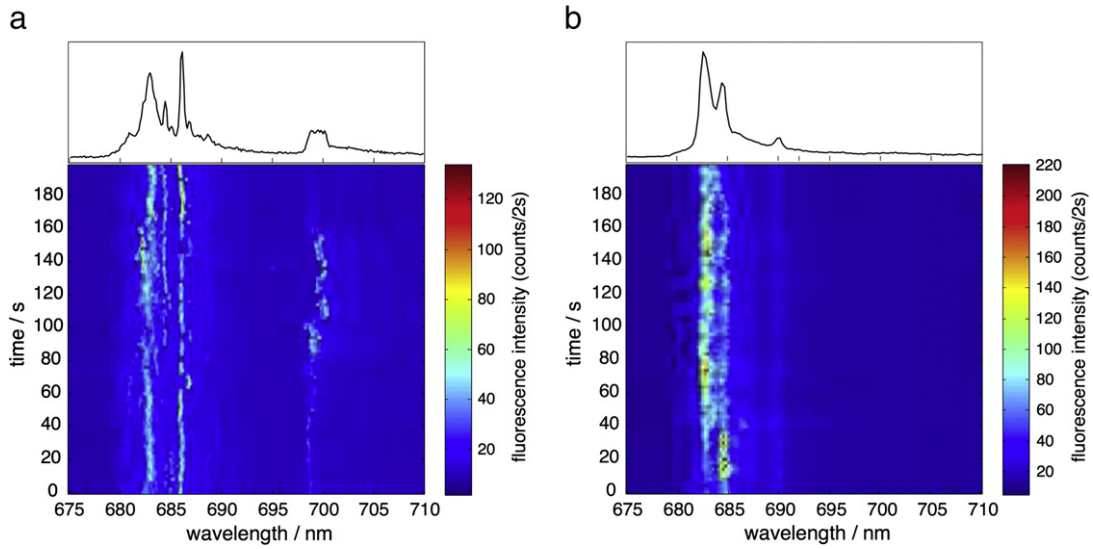

Fig. 6. Plots of time-dependent fluorescence emission spectra of single PS II cc dimers. The time sequences of 100 spectra with an accumulation time of 2 s for each spectrum are displayed for both complexes. Excitation wavelength 665 nm; temperature 1.6 K.

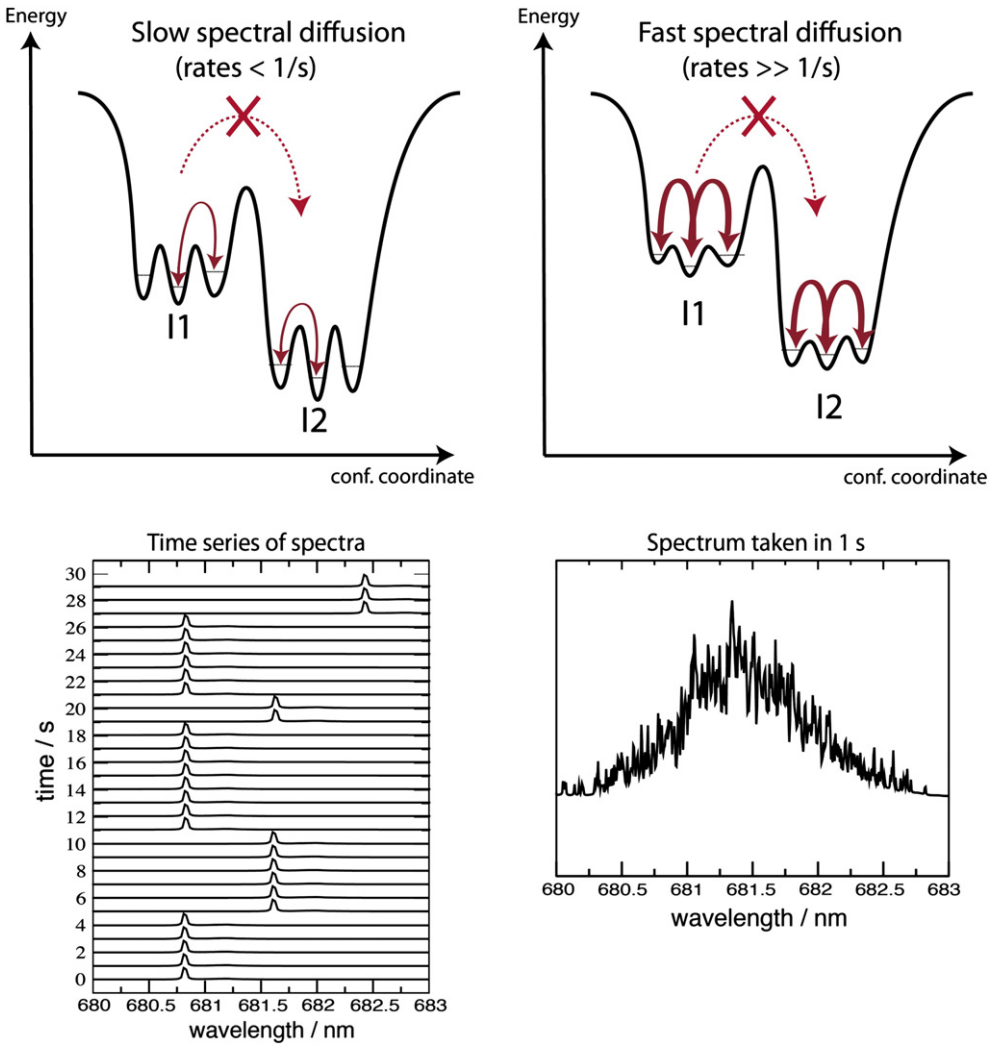

Fig. 7. Schematic illustration of the protein energy landscape. I1, I2 represent different intermediate states in the first tier. The energetic barrier between I1 and I2 cannot be crossed at low temperatures, but the barriers within I1 and I2 can be crossed (red arrows), yielding the observed jumps of the ZPLs in the emission spectra (see also Fig. 6). The barrier heights within I1 and I2 determine the rates of the conformational changes. (Left) The barriers within I1/I2 are high. Jumps occur with low rates. If the rates are in the range of the acquisition time (here ~2 s) stable ZPLs and discrete jumps can be observed in the resulting emission spectra (slow spectral diffusion). (Right) Reduced barrier heights yields increased rates, if the barriers are crossed with rates much higher than the acquisition time only broadened lines can be observed (fast spectral diffusion).

in Fig. 7. The energetic barriers between the different substates within the second tier are lower. As a consequence, these barriers can be crossed under the experimental conditions. The crossing of these barriers induces the observed line broadenings (Fig. 4) and spectral jumps (Fig. 6). The jumps are induced by small conformational changes that are possible in the second tier. Nevertheless, these changes are able to induce jumps covering a major fraction of the whole inhomogeneous line width [24]. The observation of stable ZPLs or broadened lines depends on the rates of these jumps [34].

The contributions of CP43 and CP47 are both inhomogenously broadened and their emission bands show certain overlap. The complex temperature dependence of PS II fluorescence is interpretable by noting that excitation transfer from CP43 and CP47 to the RC is slow, and strongly dependent on the precise energy at which a slow-transfer pigment in CP43 or CP47 is located within its inhomogeneous distribution [2,11,32,35]. The observed intensity variations of the emitters in Fig. 6 are most probably induced by slight changes in the site energies of the Chl*a* involved in the excitation energy transfer [26]. Especially, site-energy fluctuations of the low energy states of CP43 and CP47 will have a remarkable effect on the excitation energy transfer between the subunits and the RC.

3.4. Single-molecule average emission spectrum

As shown e.g. for PSI, the average spectrum can be reconstructed by the summation of ≥100 spectra of individual pigment protein complexes [36]. Fig. 8 shows the average emission spectrum obtained by summation of all spectra of single PS II cc dimer. The maximum fluorescence intensity is located around 685 nm. A pronounced shoulder is observed on the long-wavelength side between 690 and 695 nm. The fwhm of the peak is about 8 nm.

A satisfactory Gaussian decomposition of the average emission spectrum can be achieved by using at least three contributions (see Fig. 8). The maxima of the Gaussian bands are around 684.7, 689.3, and 691.4 nm. Vibrational contributions are taken into account by the fourth component at 701.8 nm. The overall agreement between the spectrum and the fitting function is quite good; a minor deviation is visible only at around 691 nm. The three Gaussian bands cover the wavelength regions, in which ZPLs are predominantly observed in the emission spectra of single PS II cc dimer (see Figs. 3, 5 and 6).

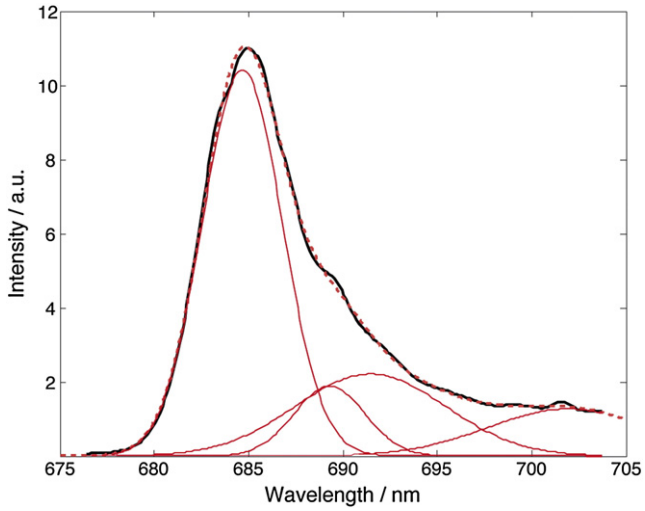

Fig. 8. The summation (average) of all fluorescence spectra taken on individual single PS II cc dimers (black) fitted by four Gaussian functions. The individual Gaussians are given in red, the summation of all Gaussians is given by the red-dotted curve. The wavelength positions and the widths of the Gaussians are: 684.7 nm/6.0 nm, 689.3 nm/5.3 nm, 691.4 nm/11.2 nm, and 701.9 nm/12.0 nm.

The contribution around 684.7 nm is in good agreement with the position of F685 assigned to a contribution from CP43 [2,11,32]. The shape of the emission spectrum shows a certain dependence on the wavelength of the excitation light. The highest intensity of the CP43 contribution was reported for excitation in the wavelength range between 665 and 673 nm [11]. In our experiment, we used 665 nm for excitation; therefore, the contributions of CP43 should also be enhanced. The second contribution is found at around 689.3 nm. The wavelength position and the width of this contribution are in good agreement with the F689 contribution reported by Komura et al. [12]. The third band is centered at around 691.4 nm. It has been proposed that the band F695 shifts from ~695 nm at 70 K to ~692 nm at 5 K [10]. This assignment can be used for the interpretation of the contributions in the single-molecule spectra e.g. Fig. 5. The weak contribution at 684.7 nm and the intense line at 686.2 nm fall into the wavelength range assigned to CP43, whereas the component with the lowest energy belongs most likely to CP47. Therefore, it can be concluded that the fluorescence of PS II results from different sites between which the energy transfer is frozen out (see Introduction section).

The complex temperature dependence of PS II fluorescence can be interpreted by noting that excitation transfer from CP43 and CP47 to the RC is slow, and strongly dependent on the precise energy at which a low-energy pigment in CP43 or CP47 is located within its inhomogeneous distribution [2]. Therefore, future single-molecule experiments will be helpful to get further insights into the influence of the inhomogeneity of the different spectral bands on the energy transfer in PS II.

The single-molecule average emission spectrum shown in Fig. 8 is significantly different from ensemble emission spectra measured by conventional fluorescence spectrometer. In ensemble experiments, the maximum emission for PS II cc was found between 687.5 nm and 690 nm below 20 K (see Fig. 2 and Refs. [10–12,37]); i.e. a few nm shifted to the red. The fwhm of the ensemble spectra is about 14 nm, i.e. nearly a factor two larger than that of the single-molecule average emission spectrum shown in Fig. 8. A notable exception is the recently reported fluorescence spectrum of PS II cc from *T. vulcanus* that was obtained by time integrals of time-wavelength 2-D images obtained with a Streak camera set-up [32]. This spectrum is virtually identical to our single-molecule average emission spectrum shown in Fig. 8. It should also be noted that emission spectra reported for the RC and CP43 from spinach PS II exhibit the maxima at 683.7 nm and 682.8 nm [6,11]. The line width of the RC is larger, whereas the line width of CP43 is close to the low value found by the single-molecule experiments.

The emission spectra of single PS II cc dimers (see Fig. 3) and the single-molecule average emission spectrum (see Fig. 8) clearly demonstrate that three or more emitters contribute to the fluorescence spectrum of PS II core complexes at low temperature. This indicates that the excitation energy is trapped at different low energy states in the PS II core antenna. Due to their low Q_Y transition energy, uphill excitation energy transfer to the RC becomes impossible at cryogenic temperatures. These states are not connected to each other by efficient energy transfer leading to thermal equilibration, because otherwise the excitation energy would be localized at 5 K on the lowest energy state being the only emitting state.

The sum of all contributions determines the shape of the fluorescence spectrum. The reason for the observed difference between the single-molecule average spectrum and the ensemble spectrum is most likely that the intensities of the contributions are different, as different quenching mechanisms might be effective under the respective conditions of the experiments.

Upon illumination at cryogenic temperatures, the light-induced formation of $P680^+Q_A^-$ in PS II is followed by charge recombination, as the electron transfer from Q_A^- to Q_B and from Y_Z to $P680^+$ is inhibited. The extent of $P680^+Q_A^-$ formation decreases progressively with

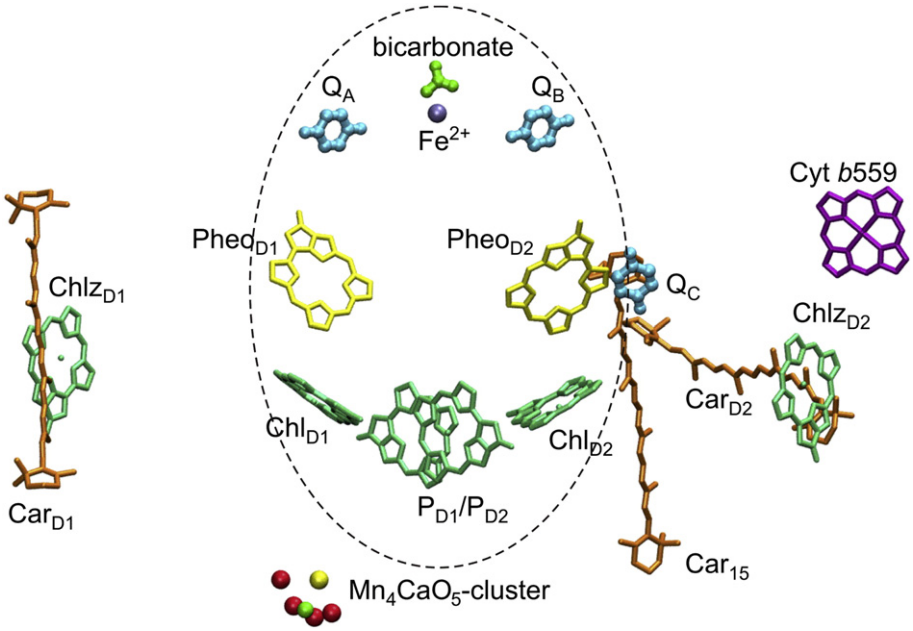

Fig. 9. Arrangement of the cofactors of the RC of PS II cc including the presumably involved co-factors of the secondary electron transfer (view perpendicular to the pseudo-C2 axis) based on the structural model of PS II cc from *T. elongatus* at 2.9 Å resolution (Ref. [4], (PDB code 3BZ1)). Shown are the two Chl*a*s constituting P680, P_{D1}/P_{D2} (green), the two peripheral Chls, Chl_{ZD1} and Chl_{ZD2} (green), the β-carotene (Car) molecules identified so far in the RC, Car (orange), and cytochrome (Cyt) b559 (violet).

successive turnovers. The reason is the oxidation of secondary electron donors (Car, Chl_Z, Cyt *b*559, Y_Z) by $P680^+$, which occurs with low quantum yield in competition to the charge recombination of $P680^+Q_A^-$. Thereby, long-living states as e.g. $Q_A^-P680Car^+$, $Q_A^-P680Cyt\ b559^+$, or $Q_A^-P680Chl_Z^+$ are accumulated after several turnovers [38]. Fig. 9 shows the arrangement of the mentioned cofactors in the X-ray structure. In the presence of Q_A^- (closed PS II), the primary radical pair $P680^+Pheo^-$ can still be formed, but stabilization of the charge separation is not possible. Fluorescence induction experiments have shown that the fluorescence yield increases upon reduction of Q_A [39,40]. The increase is stronger for PS II frozen with Cyt *b*559 in the reduced state than for PS II frozen with Cyt *b*559 oxidized. In the first case, it is $Q_A^-P680Cyt\ b559^+$, whereas in the second case, it is $Q_A^-P680Car^+$ and $Q_A^-P680Chl_Z^+$, that is predominantly accumulated upon illumination at low temperature. This difference might be due to trapped Chl^+ and Car^+, which are known to be efficient quencher of the excitation energy [41,42].

There is no need for high excitation intensities, to accumulate the discussed long-living states. Therefore, reduced Q_A and oxidized secondary donors are most likely present while measuring fluorescence spectra by conventional ensemble spectroscopy as well as single-molecule spectroscopy. Thus, the described light-induced reactions in the RC cannot explain the differences in the shape of the emission spectra (single-molecule vs. ensemble).

However, in single-molecule experiments the photon flux has to be much higher than in conventional fluorescence spectroscopy in order to achieve a satisfactory signal-to-noise ratio. In our experiments, the flux was approximately $6.6 \cdot 10^{20}$ photons/(cm^2 s). With an absorption cross section σ for PS II of about $7 \cdot 10^{-15}$ cm^2 at 665 nm, the excitation rate $\sigma \cdot I$ is of the order of 10^6 s^{-1}. A relatively high excitation power was also used for the time-resolved fluorescence measurements with the streak camera set-up by Shibata et al. [32]. With an excitation power of 0.5 W/cm^2 at 430 nm, the excitation rate is about $1.4 \cdot 10^4$ s^{-1}.

Under such conditions, the accumulation of triplet states, ^{3}Chl and ^{3}Car, in CP47 and CP43 can be expected. The structural data of PS II show that about one third of the chlorophylls in CP47 (Chl17, Chl22, Chl26, Chl27 and Chl29) as well as in CP43 (Ch33, Chl43, Chl47, and Chl49) are in close contact ($\leq$5 Å) to a β-carotene [43]. This structural information is in line with triplet-minus-singlet absorbance difference spectra of isolated CP43 and CP47 [6,16]. Carotenoid triplets formed by triplet transfer from chlorophylls as well as chlorophyll triplets decaying with half-lives in the ms range have been characterized by their absorbance difference spectra [6,16]. Chlorophyll triplets in CP47 and CP43 are certainly accumulated at an excitation rate above 10^4 s^{-1}. In single-molecule experiments even the decay rate of ^{3}Car at cryogenic temperatures is almost a factor of 10 lower than the excitation rate of 10^6 s^{-1} [16]. When the low energy chlorophylls in CP47 and CP43 itself are kept in the triplet state due to the high photon flux directed to the traps, the emission of these lowest lying states (e.g. F695) will be drastically reduced in the single-molecule experiment. Alternatively, it is quite possible that chlorophylls in the vicinity of the low energy states are predominantly in the triplet state. ^{3}Chl is also known to be an efficient quencher of the excitation energy [44], i.e. the emission of the low energy states might be quenched and their contribution to the fluorescence spectrum might be significantly reduced. Nevertheless, emission lines are observed in the respective spectral region; as a consequence photodamage of these chromophores can be ruled out by our single-molecule data.

As a consequence, the accumulation of triplet states in CP47 and CP43 holds the potential to change the shape of the emission spectra remarkably. In future experiments, the difference between the shape of the single-molecule average spectrum and the ensemble spectra will be used to determine the spectral characteristics of the emitters that undergo triplet formation.

The strongest reduction of the emission intensity is found for the contribution assigned to CP47 (Fig. 3). The most likely candidate for the low energy trap in CP47 is Chl29. Chl29 is located at the outside of PS II far away from the RC. At ambient conditions, the excitation transferred to Chl29 can easily be transferred back to the RC. It is interesting, why the lowest energy trap in PS II is located at the edge of PS II. One reason might be that Chl29 is a member of an additional quenching site formed by the whole photosynthetic unit including the peripheral light-harvesting complexes CP26, CP29 and LHC II. In the architecture of PS II supercomplexes of higher plants a small distance

between CP29 and CP47 was found [45]. A small distance between CP29 and CP47 could allow for efficient energy transfer between them [32].

4. Conclusion

A combination of absorption, fluorescence and low temperature single-molecule spectroscopy was used to investigate the spectral properties, heterogeneities and dynamics of the fluorescence emission of intact PS II cc from *T. elongatus*. At the ensemble level, the absorption and fluorescence spectra show a temperature dependence similar to plant PS II.

With single-molecule techniques, we are able to observe individual PS II cc. The emission spectra of these individual complexes are dominated by ZPLs showing dynamic site-energy changes. The ZPLs can be assigned to F685, F689 and F695. It is not sufficient to explain the observed spectra by assuming only one lowest trap. Single-molecule spectroscopy is especially helpful in assigning the components in the emission of PS II, because the inhomogeneous broadenings of CP43 and CP47 are responsible for the complex temperature dependence of the absorption and emission spectra of PS II. The observed spectral dynamics of ZPLs (site-energy changes) have remarkable effects on the excitation energy transfer and trapping between CP43, CP47 and the RC.

The average emission spectrum based on single PS II cc dimers shows a reduced intensity of F695 compared to reported ensemble data. The deviation can be explained by quenching of fluorescence by triplet states accumulated on Car or the red-most Chl*a* molecules like on Chl29 in CP47 induced by the excitation laser light.

Acknowledgement

This work was supported by the Heisenberg-Programm of the Deutsche Forschungsgemeinschaft DFG (BR 4102/1-1 and BR 4102/2-1) and by the DFG within the framework of the cluster of excellence on unifying Concepts in catalysis (UniCat) project B1, coordinated by the TU Berlin and Sfb 1078, project A5 (A.Z.).

References

[1] F. Rappaport, B.A. Diner, Primary photochemistry and energetics leading to the oxidation of the $(Mn)_4Ca$ cluster and to the evolution of molecular oxygen in photosystem II, Coord. Chem. Rev. 252 (3–4) (2008) 259–272.
[2] T. Renger, E. Schlodder, Optical properties, excitation energy and primary charge transfer in photosystem II: theory meets experiment, J. Photochem. Photobiol. B 104 (1–2) (2011) 126–141.
[3] Y. Umena, K. Kawakami, J.R. Shen, N. Kamiya, Crystal structure of oxygen-evolving photosystem II at a resolution of 1.9 Å, Nature 473 (7345) (2011) 55–60.
[4] A. Guskov, J. Kern, A. Gabdulkhakov, M. Broser, A. Zouni, W. Saenger, Cyanobacterial photosystem II at 2.9-angstrom resolution and the role of quinones, lipids, channels and chloride, Nat. Struct. Mol. Biol. 16 (3) (2009) 334–342.
[5] E.J.G. Peterman, H. van Amerongen, R. van Grondelle, J.P. Dekker, The nature of the excited state of the reaction center of photosystem II of green plants: A high-resolution fluorescence spectroscopy study, Proc. Natl. Acad. Sci. U.S.A. 95 (11) (1998) 6128–6133.
[6] M.L. Groot, R.N. Frese, F.L. de Weerd, K. Bromek, A. Pettersson, E.J.G. Peterman, I.H.M. van Stokkum, R. van Grondelle, J.P. Dekker, Spectroscopic properties of the CP43 core antenna protein of photosystem II, Biophys. J. 77 (6) (1999) 3328–3340.
[7] F.L. de Weerd, M.A. Palacios, E.G. Andrizhiyevskaya, J.P. Dekker, R. van Grondelle, Identifying the lowest electronic states of the chlorophylls in the CP47 core antenna protein of photosystem II, Biochemistry 41 (51) (2002) 15224–15233.
[8] J.L. Hughes, B.J. Prince, S.P. Arskold, E. Krausz, R.J. Pace, R. Picorel, M. Seibert, Photo-conversion of chlorophylls in higher-plant CP43 characterized by persistent spectral hole burning at 1.7 K, J. Lumin. 108 (1–4) (2004) 131–136.
[9] J.L. Hughes, B.J. Prince, E. Krausz, P.J. Smith, R.J. Pace, H. Riesen, Highly efficient spectral hole-burning in oxygen-evolving photosystem II preparations, J. Phys. Chem. B 108 (29) (2004) 10428–10439.
[10] E. Krausz, J.L. Hughes, P.J. Smith, R.J. Pace, S.P. Arskold, Assignment of the low-temperature fluorescence in oxygen-evolving photosystem II, Photosynth. Res. 84 (1–3) (2005) 193–199.
[11] E.G. Andrizhiyevskaya, A. Chojnicka, J.A. Bautista, B.A. Diner, R. van Grondelle, J.P. Dekker, Origin of the F685 and F695 fluorescence in photosystem II, Photosynth. Res. 84 (1–3) (2005) 173–180.
[12] M. Komura, Y. Shibata, S. Itoh, A new fluorescence band F689 in photosystem II revealed by picosecond analysis at 4–77 K: function of two terminal energy sinks F689 and F695 in PSII, Biochim. Biophys. Acta Bioenerg. 1757 (12) (2006) 1657–1668.
[13] G. Raszewski, B.A. Diner, E. Schlodder, T. Renger, Spectroscopic properties of reaction center pigments in photosystem II core complexes: revision of the multimer model, Biophys. J. 95 (1) (2008) 105–119.
[14] N.C. Dang, V. Zazubovich, M. Reppert, B. Neupane, R. Picorel, M. Seibert, R. Jankowiak, The CP43 proximal antenna complex of higher plant photosystem II revisited: modeling and hole burning study. I, J. Phys. Chem. B 112 (32) (2008) 9921–9933.
[15] B. Neupane, N.C. Dang, K. Acharya, M. Reppert, V. Zazubovich, R. Picorel, M. Seibert, R. Jankowiak, Insight into the electronic structure of the CP47 antenna protein complex of photosystem II: hole burning and fluorescence study, J. Am. Chem. Soc. 132 (12) (2010) 4214–4229.
[16] M.L. Groot, E.J.G. Peterman, I.H.M. van Stokkum, J.P. Dekker, R. van Grondelle, Triplet and fluorescing states of the CP47 antenna complex of photosystem-II studied as a function of temperature, Biophys. J. 68 (1) (1995) 281–290.
[17] P. Tamarat, A. Maali, B. Lounis, M. Orrit, Ten years of single-molecule spectroscopy, J. Phys. Chem. A 104 (1) (2000) 1–16.
[18] H.P. Lu, X.S. Xie, Single-molecule spectral fluctuations at room temperature, Nature 385 (6612) (1997) 143–146.
[19] D. Rutkauskas, V. Novoderezhkin, R.J. Cogdell, R. van Grondelle, Fluorescence spectroscopy of conformational changes of single LH2 complexes, Biophys. J. 88 (1) (2005) 422–435.
[20] F. Schleifenbaum, C. Blum, V. Subramaniam, A.J. Meixner, Single-molecule spectral dynamics at room temperature, Mol. Phys. 107 (18) (2009) 1923–1942.
[21] Y. Berlin, A. Burin, J. Friedrich, J. Köhler, Low temperature spectroscopy of proteins. part II: experiments with single protein complexes, Phys. Life Rev. 4 (1) (2007) 64–89.
[22] C. Hofmann, T.J. Aartsma, H. Michel, J. Köhler, Direct observation of tiers in the energy landscape of a chromoprotein: a single-molecule study, Proc. Natl. Acad. Sci. U.S.A. 100 (26) (2003) 15534–15538.
[23] M. Brecht, H. Studier, A.F. Elli, F. Jelezko, R. Bittl, Assignment of red antenna states in photosystem I from *Thermosynechoccocus elongatus* by single-molecule spectroscopy, Biochemistry 46 (3) (2007) 799–806.
[24] M. Brecht, H. Studier, V. Radics, J.B. Nieder, R. Bittl, Spectral diffusion induced by proton dynamics in pigment–protein complexes, J. Am. Chem. Soc. 130 (2008) 17487–17493.
[25] A.R. Faro, V. Adam, P. Carpentier, C. Darnault, D. Bourgeois, E. de Rosny, Low-temperature switching by photoinduced protonation in photochromic fluorescent proteins, Photochem. Photobiol. Sci. 9 (2) (2010) 254–262.
[26] M. Brecht, V. Radics, J.B. Nieder, R. Bittl, Protein dynamics-induced variation of excitation energy transfer pathways, Proc. Natl. Acad. Sci. U.S.A. 106 (29) (2009) 11857–11861.
[27] T.P.J. Kruger, C. Ilioaia, L. Valkunas, R. van Grondelle, Fluorescence intermittency from the main plant light-harvesting complex: sensitivity to the local environment, J. Phys. Chem. B 115 (18) (2011) 5083–5095.
[28] J. Kern, B. Loll, C. Luneberg, D. DiFiore, J. Biesiadka, K.D. Irrgang, A. Zouni, Purification, characterisation and crystallisation of photosystem II from *Thermosynechococcus elongatus* cultivated in a new type of photobioreactor, Biochim. Biophys. Acta Bioenerg. 1706 (1-2) (2005) 147–157.
[29] M. Hussels, A. Konrad, M. Brecht, Confocal sample-scanning microscope for single-molecule spectroscopy and microscopy with fast sample exchange at cryogenic temperatures, Rev. Sci. Instrum. 83 (2012) 123706.
[30] B. Loll, J. Kern, W. Saenger, A. Zouni, J. Biesiadka, Towards complete cofactor arrangement in the 3.0 Angstrom resolution structure of photosystem II, Nature 438 (7070) (2005) 1040–1044.
[31] G. Raszewski, T. Renger, Light harvesting in photosystem II core complexes is limited by the transfer to the trap: can the core complex turn into a photoprotective mode? J. Am. Chem. Soc. 130 (13) (2008) 4431–4446.
[32] Y. Shibata, S. Nishi, K. Kawakami, J.R. Shen, T. Renger, Photosystem II does not possess a simple excitation energy funnel: time-resolved fluorescence spectroscopy meets theory, J. Am. Chem. Soc. 135 (2013) 6903–6914.
[33] M. Brecht, V. Radics, J.B. Nieder, H. Studier, R. Bittl, Red antenna states of photosystem I from Synechocystis PCC 6803, Biochemistry 47 (20) (2008) 5536–5543.
[34] M. Brecht, Spectroscopic characterization of photosystem I at the single-molecule level, Mol. Phys. 107 (2009) 1955–1974.
[35] E. Krausz, J.L. Hughes, P. Smith, R. Pace, S.P. Arskold, Oxygen-evolving photosystem II core complexes: a new paradigm based on the spectral identification of the charge-separating state, the primary acceptor and assignment of low-temperature fluorescence, Photochem. Photobiol. Sci. 4 (9) (2005) 744–753.
[36] M. Hussels, M. Brecht, Effect of glycerol and PVA on the conformation of photosystem I, Biochemistry 50 (18) (2011) 3628–3637.
[37] J.P. Dekker, A. Hassoldt, A. Pettersson, H. van Roon, M.L. Groot, R. van Grondelle, On the nature of the F695 and F685 emission of photosystem II, photosynthesis: from light to biosphere, 1 (1995) 53–56.
[38] B. Hillmann, E. Schlodder, Electron-transfer reactions in photosystem-II core complexes from Synechococcus at low-temperature—difference spectrum of P680(+) Q(a)(−)/P680 Q(a) at 77 K, Biochim. Biophys. Acta Bioenerg. 1231 (1) (1995) 76–88.

[39] S. Okayama, W.L. Butler, The influence of cytochrome b 559 on the fluorescence yield of chloroplasts at low temperature, Biochim. Biophys. Acta Bioenerg. 267 (3) (1972) 523–529.
[40] F. Müh, M. Cetin, E. Schlodder, Temperature dependence of fluorescence induction in photosystem II core complexes from *Thermosynechococcus elongatus*, in: A. van der Est, D. Bruce (Eds.), Proceedings of the 13th International Congress of Photosynthesis in Montreal, Canada, International Society of Photosynthesis, 2005, pp. 309–311, (Vol.).
[41] R.H. Schweitzer, G.W. Brudvig, Fluorescence quenching by chlorophyll cations in photosystem II, Biochemistry 36 (38) (1997) 11351–11359.
[42] R. Steffen, H.J. Eckert, A.A. Kelly, P. Dormann, G. Renger, Investigations on the reaction pattern of photosystem II in leaves from *Arabidopsis thaliana* by time-resolved fluorometric analysis, Biochemistry 44 (9) (2005) 3123–3133.
[43] F. Müh, T. Renger, A. Zouni, Crystal structure of cyanobacterial photosystem II at 3.0 Å resolution: a closer look at the antenna system and the small membrane-intrinsic subunits, Plant Physiol. Biochem. 46 (3) (2008) 238–264.
[44] E. Schlodder, M. Cetin, M. Byrdin, I.V. Terekhova, N.V. Karapetyan, P700(+)- and (3) P700-induced quenching of the fluorescence at 760 nm in trimeric photosystem I complexes from the cyanobactenium *Arthrospira platensis*, Biochim. Biophys. Acta Bioenerg. 1706 (1-2) (2005) 53–67.
[45] S. Caffarri, R. Kouril, S. Kereiche, E.J. Boekema, R. Croce, Functional architecture of higher plant photosystem II supercomplexes, EMBO J. 28 (19) (2009) 3052–3063.

Chapter 10

Variation of Exciton-Vibrational Coupling in Photosystem II Core Complexes from Thermosynechococcus elongatus as Revealed by Single-Molecule Spectroscopy

In this chapter the spectral properties of single Photosystem II core complexes from *Thermosynechococcus elongatus* are further described regarding the ZPL distribution. Reducing the temperature to 1.6 K and observing only the fluorescence of single complexes allows to record spectral resolved time traces with sufficiently resolved ZPLs showing slow spectral diffusion. The ZPLs are observable due to lowered excition-vibrational coupling, which however show spectral diffusion as a consequence of a certain energy landscape of the proteins conformational space. Ruling out spectral diffusion on single ZPLs allows further to determine for each contribution the coupling between matrix and electronic transition by calculating the Huangs-Rhys-factors. The determined values show no correlation between coupling strength and spectral position of the ZPL, whereas the conclusion can be derived about the nature of the interactions responsible for the respective contributors assigned to be an electrostatic interaction.

This chapter is based on:
Skandary, S., Hussels, M., Konrad, A., Renger, T., Müh, F., Bommer, M., Zouni, A., Meixner, A.J., Brecht, M. "Variation of Exciton-Vibrational Coupling in Photosystem II Core Complexes from Thermosynechococcus elongates as Revealed by Single-Molecule Spectroscopy" *The Journal of Physical Chemistry B*, **2015**, *119*(11), 4203-4210.

THE JOURNAL OF PHYSICAL CHEMISTRY B

Article

pubs.acs.org/JPCB

Variation of Exciton-Vibrational Coupling in Photosystem II Core Complexes from *Thermosynechococcus elongatus* As Revealed by Single-Molecule Spectroscopy

Sepideh Skandary,[†] Martin Hussels,[†] Alexander Konrad,[†] Thomas Renger,[‡] Frank Müh,[‡] Martin Bommer,[§] Athina Zouni,[§] Alfred J. Meixner,[†] and Marc Brecht*[,†,∥]

[†]IPTC and Lisa+ Center, Universität Tübingen, Tübingen, Germany

[‡]Institut für Theoretische Physik, Johannes Kepler Universität, Linz, Austria

[§]Institut für Biologie, Humboldt Universität zu Berlin, Berlin, Germany

[∥]Zurich University of Applied Science Winterthur (ZHAW), Winterthur, Switzerland

Supporting Information

ABSTRACT: The spectral properties and dynamics of the fluorescence emission of photosystem II core complexes are investigated by single-molecule spectroscopy at 1.6 K. The emission spectra are dominated by sharp zero-phonon lines (ZPLs). The sharp ZPLs are the result of weak to intermediate exciton-vibrational coupling and slow spectral diffusion. For several data sets, it is possible to surpass the effect of spectral diffusion by applying a shifting algorithm. The increased signal-to-noise ratio enables us to determine the exciton-vibrational coupling strength (Huang–Rhys factor) with high precision. The Huang–Rhys factors vary between 0.03 and 0.8. The values of the Huang–Rhys factors show no obvious correlation between coupling strength and wavelength position. From this result, we conclude that electrostatic rather than exchange or dispersive interactions are the main contributors to the exciton-vibrational coupling in this system.

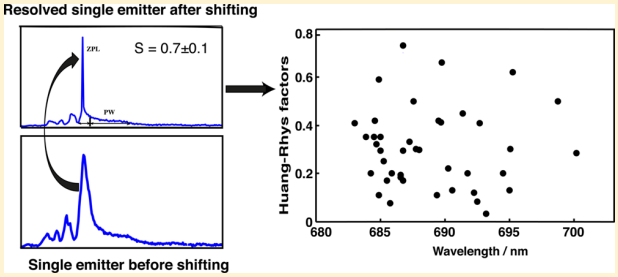

In photosynthetic light-harvesting complexes (also termed antenna proteins), an intricate interplay between different pigment molecules is responsible for light absorption and efficient excitation energy transfer (EET) to the reaction center (RC).[1,2] In oxygenic photosynthesis of cyanobacteria, green algae, and higher plants, the harvested energy is used to oxidize water and reduce plastoquinone in a membrane-embedded pigment–protein complex (PPC) called photosystem II (PSII).[3,4] The functional unit of PSII is a core complex (PSIIcc) that forms dimers (dPSIIcc), which in turn assemble into rows in cyanobacteria[5,6] or are part of a supercomplex with peripheral antennae in higher plants.[7,8] PSIIcc contains, besides the RC, two core antenna subunits referred to as CP43 and CP47 which are responsible for ultimately transferring the excitation energy to the RC, where the charge separation is initiated.[9−12] To understand EET in these systems, it is necessary to know the electronic energy levels of the involved, coupled chlorophyll (Chl) *a* pigments and the interactions of the electronic transitions with vibrational motions of the PPC.[13−15] Important information is obtained from the spectral properties of the fluorescence emitters of the antenna system.[16−18] The fluorescence spectrum of dPSIIcc exhibits a complicated temperature dependence in both plants[18,19] and cyanobacteria.[12,20] Both cases are characterized by a fluorescence maximum at 685 nm at higher temperatures (above 140 K) and the emergence of a second 695 nm fluorescence peak upon cooling down to 77 K. Further cooling reduces the intensity at 695 nm, so that mainly one peak at 685 nm is left at around 4 K. This complex behavior was explained[12] in terms of two distinct pools of Chls, F685 and F695, emitting at different wavelengths and both absorbing at lower wavelengths than the primary electron donor state in the RC. Therefore, these Chls are referred to as red-absorbing or red Chls. Whereas F695 carries the oscillator strength of one Chl, F685 has a larger oscillator strength due to a delocalized exciton state. At 4 K the fluorescence maximum is determined by the state with the higher oscillator strength, i.e., F685. Upon increasing the temperature, EET from F685 to the RC and subsequent quenching by electron transfer sets in and thereby diminishes the fluorescence intensity of this state. Since energy transfer from F695 is frozen out below 77 K, this state is still fully fluorescent and the fluorescence maximum shifts to the red between 4 and 77 K.[12] Note that isolated CP47 complexes do not show such a behavior, since no EET to the RC and subsequent quenching by electron transfer is possible. Instead,

Received: October 22, 2014
Revised: February 20, 2015

DOI: 10.1021/jp510631x
J. Phys. Chem. B XXXX, XXX, XXX−XXX

in isolated intact[21] CP47 complexes, the position of the fluorescence maximum was shown[22] to remain constant at 695 nm for $T \leq 75$ K and to move to shorter wavelengths at higher temperatures due to thermal population of higher exciton states.

Besides F685 and F695, a third emitter was identified in plant material, termed F689, that can be detected only in time-resolved fluorescence experiments below 77 K.[23] F685 was assigned to Chls in CP43,[24] whereas F695 was assigned to Chls in CP47.[24−26] Two tentative models assigned F689 to either CP43 or CP47 and left open the possibility that Chls of CP47 contribute to F685.[23] Similar assignments were made on the basis of theoretical studies aimed at the description of a variety of spectroscopic properties of dPSIIcc.[9,12] Reports using excitation-dependent fluorescence line narrowing (FLN)[17] and picosecond time-resolved fluorescence spectroscopy[23] at low temperatures showed inhomogeneous widths of the red chlorophyll bands, where different contributions showed strong overlap. The energy landscape of the CP43 protein was investigated with spectral hole-burning (SHB) and hole-recovery experiments in combination with thermocycling,[27] revealing distribution functions for the barrier heights separating different conformational substates of the protein. So far, these experiments were interpreted by assuming a single value for the Huang−Rhys factor S characterizing the strength of the exciton-vibrational coupling. In the present work, we want to investigate whether not only the electronic transition energy of a protein-bound pigment in PSIIcc but also its coupling to the protein vibrations can vary along the energy landscape of the protein. For Chl *a* in an organic glass and LH2 complexes of purple bacteria, such a variation was reported in combined hole burning, fluorescence line narrowing,[28] and in single molecule spectroscopy (SMS).[29]

SMS is an excellent technique to cope with inhomogeneous spectral widths and reveals subtle spectral details often obscured by averaging over heterogeneous ensembles.[30,31] At room temperature, spectral diffusion and photobleaching hamper the collection of detailed spectroscopic information for most single molecules.[32−35] Lowering the temperature reduces the impact of spectral diffusion,[35−37] and the emission profile of a single emitter composed of a sharp zero-phonon line (ZPL) and a so-called phonon wing (PW) becomes observable.[28,38−40] The ZPL belongs to pure electronic transitions. The PW on the low-energy side of the ZPL belongs to electronic transitions with excitations of vibrational quanta. This coupling is due to the interaction of the chromophore with its surrounding. The ZPL and PW can only be distinguished at low temperatures because of the temperature dependence of the homogeneous lineshape causing the PW to mask the zero-phonon contributions completely at temperatures above 100 K. The ratio between the intensity of the ZPL and PW depends on the strength of exciton-vibrational coupling expressed by the Huang−Rhys factor (S).[41−43] The dimensionless factor S is a measure for the linear exciton-vibrational coupling strength and characterizes the average number of vibrational quanta excited during a particular electronic transition.[44]

Even at low temperatures, the spectral properties of protein bound chromophores depend on time. The time dependence concerns the emission wavelength, intensity, exciton-vibrational coupling, and rate of spectral diffusion.[45,46] The most obvious effect visible in the spectra of single chromophores is spectral diffusion. The fluctuations of the site energy cause spectral jumps extending into the range of several nanometers.[45,46]

The ZPL and PW can be observed in time-dependent spectra series if the rate of spectral diffusion is smaller than the rate of data acquisition, whereas a complete broadening of the ZPLs results if the rate of spectral diffusion surpasses the rate of data acquisition.

In this study, we investigate the spectroscopic properties of dPSIIcc from *Thermosynechoccocus elongatus* at low temperature (1.6 K) at the single-complex level. All recorded fluorescence spectra series consist of sharp ZPLs that cover the whole emission range. We were able to overcome the effect of spectral diffusion for a selected number of lines using a shifting algorithm.[47,48] As a result, the resolved emission profiles of single emitters become visible and the Huang−Rhys factor S can be determined with high accuracy.

MATERIALS AND METHODS

Sample Preparation. Preparation and crystallization of dPSIIcc from *T. elongatus* are described elsewhere.[49] Extensive biochemical characterization of dPSIIcc are summarized in ref 50. For single-molecule spectroscopy redissolved crystals in buffer solution containing 100 mM PIPES (pH 7.0), 5 mM $CaCl_2$, 0.5 M betaine, and 0.03% β-DM showing high oxygen evolution activity were used.[49] The final dPSIIcc concentration was ∼3 pM. For single-molecule experiments less than 1 μL of the sample was sandwiched between two coverslips. Finally, the sample was transferred directly into the cryostat and rapidly plunged into liquid helium. Experiments were carried out using a home-built confocal microscope operating at 1.6 K as described recently.[51] A 665 nm CW diode laser set to 100 μW emission power was used to record spectra series with 100 spectra per data set.

Data Evaluation Process. Two algorithms have been used to evaluate the data sets. Both are implemented using the MATLAB software package. The first algorithm uses smoothing and filtering to detect spectral positions of ZPLs in spectra series and is described in ref 48. By applying it to all data sets a ZPL histogram has been achieved, which is discussed in the Results section.

The second algorithm is useful to overcome the broadening of spectra of single emitters, which are affected by spectral diffusion, for long accumulation times. It works on time-dependent spectra series where the position of the maximum intensity of an emitter is detected in a user-selected wavelength range. Then the single spectra are shifted in a circular manner that the intensity maxima are at the same position. Circular shifting means data points shifted out of the matrix boundaries are moved to the opposite end of the matrix. In the next step the shifted spectra are summed up, giving a spectrum of the single emitter with better signal-to-noise ratio. Finally, a linear baseline correction is applied. To achieve highly resolved single emitter profiles, the shifting wavelength range is selected around the ZPL and the PW, and single spectra showing low intensity or multiple positions of the single emitter are excluded.

To determine the Huang−Rhys factor the intensities of the ZPL, I_{ZPL}, and the PW, I_{PW}, are calculated by numerical integration and the Huang−Rhys factor, S, is obtained by

$$e^{-S} = \frac{I_{ZPL}}{I_{ZPL} + I_{PW}} \quad (1)$$

DOI: 10.1021/jp510631x
J. Phys. Chem. B XXXX, XXX, XXX−XXX

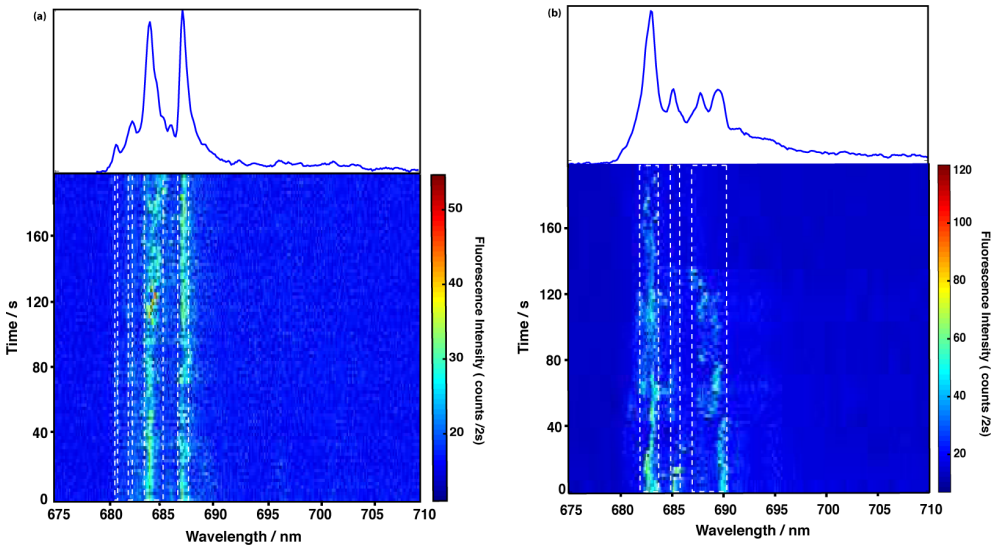

Figure 1. Fluorescence emission spectra of two individual dPSIIcc at low temperature (1.6 K). In both cases, 100 fluorescence emission spectra with an accumulation time of 2 s for each spectrum were recorded subsequently (λ_{exc} = 665 nm). The fluorescence intensity is color-coded (see color code to the right side of each graph). The confined spectral positions of the ZPLs are indicated by the white dashed lines. The average spectrum (on top) is obtained by summation of all spectra in one data set.

RESULTS

Individual dPSIIcc were detected by low temperature confocal microscopy.[20] Figure 1 shows two examples of the time-dependent fluorescence emission of single dPSIIcc. The data set shown in Figure 1a shows four ZPLs. Two sharp and relatively stable ZPLs at 684 and 687.5 nm can be found in the spectra series and the average spectrum, whereas the two weak ZPLs at 681 and 682.4 nm are hardly visible due to their low S/N ratio in time-dependent spectra series. In the data set shown in Figure 1b, one intense ZPL at 683 nm and two weaker ZPLs at 685.4 and 689.3 nm are observable. The first ZPL at 683 nm is relatively stable during the whole series, whereas the two other ZPLs at 685.4 and at 689.3 nm are distorted after 15 and 134 s, respectively. In the mean spectrum on top, the peak at 687.9 nm results from the ZPL which started at 689.3 nm.

ZPLs are clearly visible in all recorded spectra series in the wavelength range from 675 to 710 nm. They show dynamical variations of their spectral position and intensity, but their distribution as well as their time-dependent behavior varies from complex to complex. The variation of each ZPL position is confined to a certain spectral range as indicated by the white dashed lines in Figure 1. The width of this range was determined for clearly distinguishable ZPLs and is 2.5 ± 1.1 nm in the wavelength region from 680 to 705 nm.

The probability of finding a ZPL in a wavelength interval was evaluated for all measured spectra series. For this purpose, the spectral positions of the ZPLs were determined for all data sets by the first algorithm mentioned in the Materials and Methods section. Figure 2 shows the relative occurrence of ZPLs together with the average spectrum calculated for all data taken from single dPSIIcc during this study. The histogram shows the relative distribution of ZPL spectral positions as a function of wavelength between 675 and 710 nm. The ZPLs dominantly occurred in the range between 682 and 687 nm, which corresponds to the peak of the average spectrum with the maximum position at 684.7 nm, and their occurrence decreases at 689 to 701 nm. As it has been discussed in our previous report,[20] the amplitude of the fluorescence from the lowest

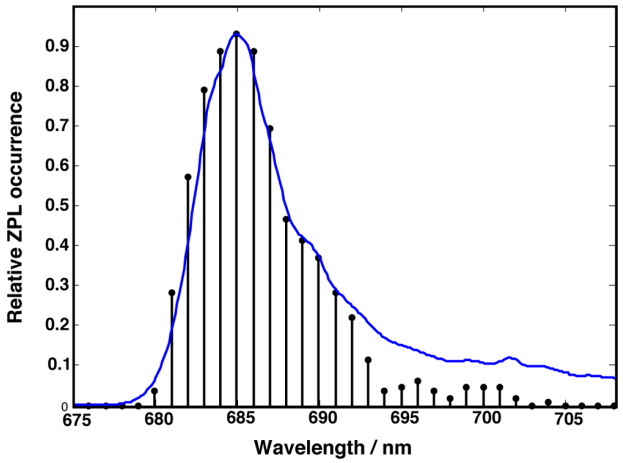

Figure 2. Comparison of the ZPL distribution (histogram) and the average emission spectrum for dPSIIcc. The average spectrum (solid line) represents the sum of all measured (142 data sets) emission spectra from single dPSIIcc at 1.6 K.

emitter F695 in PSIIcc is diminished in our SMS experiments, probably because of the accumulation of triplet states. At low temperatures, a significant part of the excitation is trapped on energetically low-lying antenna chlorophylls because uphill energy transfer to the reaction center is impossible. Because of the longer lifetime of the excited chlorophyll, the yield of fluorescence and triplet formation increases. Carotenoid triplets are formed subsequently by triplet−triplet transfer. The lifetime of Chl triplets decaying by triplet energy transfer to carotene is most likely in the submicrosecond domain.[52]

The determination of the Huang−Rhys factor requires the intensity of the ZPL, I_{ZPL}, and PW, I_{PW}. Determining the position and intensity of ZPLs is straightforward because the whole intensity of a ZPL is emitted within a small spectral range. However, the PWs are less intense and spread over a broader wavelength range than ZPLs. As a consequence,

DOI: 10.1021/jp510631x
J. Phys. Chem. B XXXX, XXX, XXX−XXX

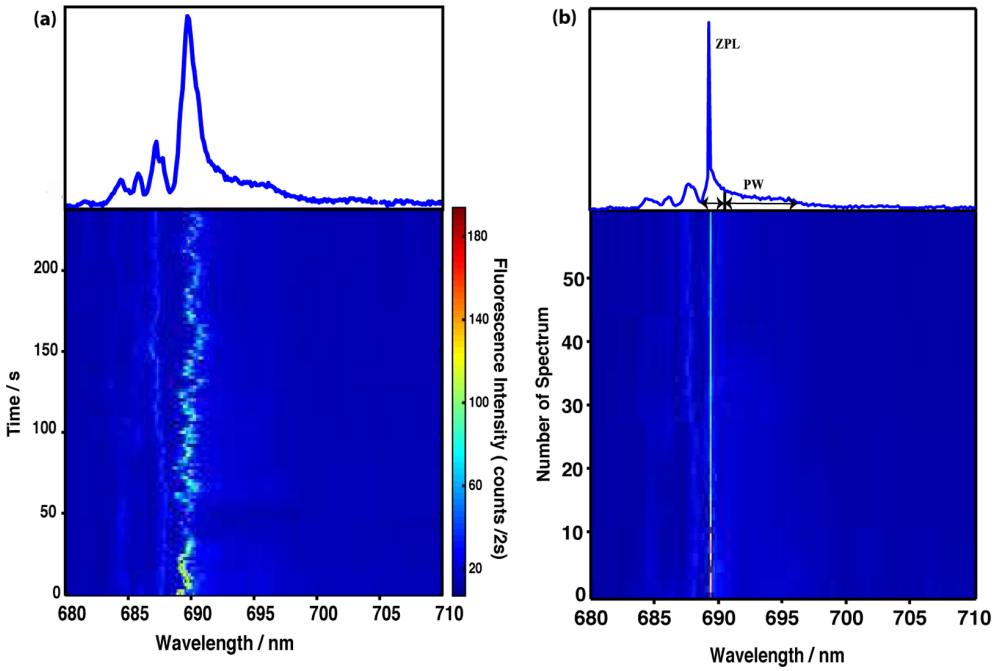

Figure 3. (a) Time-dependent fluorescence emission spectra of an individual dPSIIcc with 2 s time resolution. The average spectrum is given on top. (b) The same data set as (a) after applying the shifting procedure. The bar in the top separates the ZPL and the PW, and the double arrows indicate the spectral range of ZPL and PW. For further details, see the Supporting Information. For the depicted single-emitter profile, we calculated $S = 0.7 \pm 0.1$ with the mean position of ZPL at 689.8 ± 1.2 nm.

determination of PWs is more sensitive to interference with other emitters and background noise; therefore, it is difficult to determine their position and intensity because spectra with good signal-to-noise ratio are needed.

The average spectrum of time-dependent spectra series does not allow us to determine the Huang–Rhys factor because of spectral diffusion leading to multiple peaks and broadening of the spectra as can be seen in Figure 1. It is possible to resolve a ZPL and its accompanying PW if the emission is stable and the background signals can be separated. For this purpose, the position of ZPL is determined for all time-dependent spectra series (see Figure 3). Then all spectra are shifted along the wavelength axis and to one common mean position. After shifting, the background signals are subtracted by applying linear baseline correction.

Figure 3a shows one of the selected time-dependent spectra series with the average spectrum on top. Four ZPLs at 684.5, 685.9, 687.3, and 689.8 nm can be distinguished. However, the only suitable ZPL for applying the shifting algorithm is at 689.8 nm (mean position) because there is no overlap with the other emitters. The wavelength range from 688 to 698 nm was selected for the shifting procedure. Figure 3b shows the series after the shifting, together with the average spectrum (on top). It should be noted that due to shifting along wavelength, the original wavelength scale changed and the time scale converts to number of spectrum. The line at 689.8 nm in Figure 3a changed to a well-resolved line in Figure 3b showing ZPL and pronounced PW with obviously enhanced resolution and signal-to-noise ratio. The signal strength of the individual spectra is too low to resolve the shape of the PW correctly. Using the nicely resolved single ZPL and corresponding PW, we are able to determine the Huang–Rhys factor, *S*. Because of spectral interference of ZPLs and PWs, Huang–Rhys factors are calculated for several estimated borders between positions of ZPLs and PWs, and that is the reason for the relatively large error of the *S* values. For the depicted single-emitter profile, it is $S = 0.7 \pm 0.1$ with the mean position of ZPL at 689.8 ± 1.2 nm.

All data sets were scanned for ZPLs suitable to apply our shifting procedure. Overall, 41 ZPLs were found where *S* could be determined. Figure 4 shows a 2D-scatter plot (*S* versus wavelength) of all 41 ZPLs. The histograms in Figure 4 show the amount of resolved ZPLs according to their wavelength and Huang–Rhys factor values. The distribution of the contribution over the wavelength is in a reasonable agreement with ZPL occurrence in Figure 2. The ZPLs are found in the range of 682–700 nm; the *S* values vary between 0.03 and 0.8. Most of

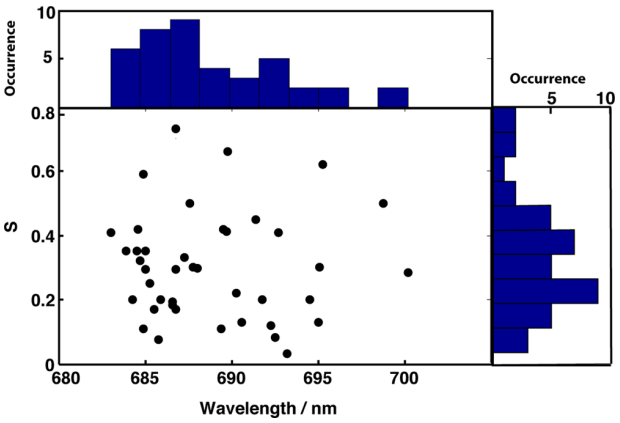

Figure 4. 2D-scatter plot of the wavelength-dependent distribution of the Huang–Rhys factor *S* for dPSIIcc. *S* was determined for 41 resolved emitters in 142 data sets of single dPSIIcc (for more details see text). For both dimensions, histograms are given additionally.

DOI: 10.1021/jp510631x
J. Phys. Chem. B XXXX, XXX, XXX–XXX

the ZPLs occurred at 685 ± 1 nm, and their mean S value is 0.3, in agreement with hole-burning spectra on isolated CP43 complexes, which were analyzed assuming a single S-value.[27,53] Here, we have resolved the distribution of possible S-values of this state. We find a broad range of S-values for F685 as well as for the other emitting states, suggesting that the electron-vibrational coupling varies substantially along the multidimensional energy landscape of the protein. The lowest Huang–Rhys factor of a single dPSIIcc is S = 0.03 ± 0.01 at 693.2 ± 2.1 nm, and the highest is S = 0.8 ± 0.1 at 686.8 ± 0.7 nm (see Figure 4).

In contrast to earlier results obtained for the LH2 antenna of purple bacteria,[29] there is no obvious correlation between S and the ZPL emission wavelength except that the points are somewhat more crowded in the 685 nm region with S < 0.4 (Figure 4). One can find quite different values of S for the same ZPL position. For example, at 684.9 nm, we find S = 0.11 as well as S = 0.59. On the other hand, essentially the same value of S is found for ZPLs at different positions, e.g., S = 0.35 at 684.5 ± 1.2 and 683.9 ± 1.1 nm. In the range between 685 and 689 nm, the weakest exciton-vibrational coupling is S = 0.07 and the strongest S = 0.8. Nearly the same variation of exciton-vibrational coupling is found in the range between 690 and 700 nm with minimally S = 0.03 and maximally S = 0.62.

DISCUSSION

At 1.6 K the spectra are dominated by sharp ZPLs which are characteristic features of single molecules at low temperature. The ZPLs in the data sets of single dPSIIcc differ in their intensity and spectral positions (see Figure 1).

Multiple lines in different data sets can be the result of (i) spectral diffusion, (ii) static disorder, or (iii) different emitters.[20] (i) Most of the lines which are close to each other can be assigned to single emitters whose site energy changes due to dynamic variations as can be seen in Figure 1. Spectral diffusion is the main reason for variable shapes and positions of ZPLs observable in emission spectra of individual dPSIIcc. Mostly, spectral diffusion leads to time-dependent broadening of the emission (see Figure 1) and not to separated lines. (ii) Chlorophylls bound at the same site might have different transition energies. This includes the possibility that equivalent (symmetry-related) sites in the two dimer halves of dPSIIcc emit at different wavelengths. A Gaussian distribution is often used to describe the extent of static disorder within an ensemble with a fwhm of about 200 cm^{-1},[54] corresponding to about 10 nm wavelength range. (iii) Different low-energy traps corresponding to different Chls in dPSIIcc give rise to separated lines if the low-energy states are not connected to each other by efficient energy transfer leading rapidly to thermal equilibrium.

Stable ZPLs with small discrete jumps are observed (see Figure 1a) if the rate of spectral diffusion is in the range of the experimental accumulation time or slower (slow spectral diffusion). On the other hand, only broadened lines are visible if the rate of spectral diffusion is faster than the rate of data acquisition (fast spectral diffusion).[55]

Our shifting algorithm aims at a correction of the spectra for the effects of spectral diffusion to facilitate the determination of S. Clearly, the algorithm can only correct for the resolvable slow spectral diffusion, while the shifted spectra remain broadened by fast spectral diffusion. Nonetheless, by applying this procedure, we were able to determine the line shapes and Huang–Rhys factors for 41 individual emitters with high accuracy based on 142 recorded data sets.

Earlier analyses of bulk spectra suggest the presence of at least three different emitting entities, F685, F689, and F695,[9,12,23−26] corresponding to three different low-energy traps in dPSIIcc. This suggestion is supported by the present data; i.e., the ZPLs are distributed over a large wavelength range that can be divided roughly into three regions around 685, 689, and 695 nm, which might correspond to F685, F689, and F695, respectively. However, a clear-cut assignment of ZPLs to energy traps is not possible. An assignment would be facilitated by a correlation between ZPL position and S, but no such correlation is observed. There is merely a crowding of data points in the lower left corner of the scattering plot (Figure 4), suggesting that pigments contributing to F685 have preferentially a weak exciton-vibrational coupling (i.e., S < 0.4). This result is in agreement with hole-burning studies of isolated CP43 assigning $S \approx 0.3$ to the so-called A-state of CP43,[27,53] which likely corresponds (or at least contributes) to F685.[9]

The red-most state in dPSIIcc, i.e., F695, is assigned to the low-energy trap in CP47. This is proposed[9,10] to be due to Chl29 (in the nomenclature of Loll et al.[56]), but there are other assignments.[57] Hole-burning studies on isolated CP47 suggest this trap to have a relatively strong exciton-vibrational coupling with $S \approx 1.0$.[21] This is only partly in agreement with our results, since all our emitters, including those at low energies, where F695 is expected, have smaller S values. Hence, we have to conclude that we only see a nonrepresentative selection of ZPLs for the state F695 in our single-molecule experiments. As has been discussed in our previous publication,[20] the selection may occur due to the high excitation rate necessary for SMS. Triplet states could be accumulated at the low-energy state F695 of CP47, which, therefore, fluoresces less. It is expected that the Chl triplet states accumulating at F695 are quenched by nearby carotenoids to prevent photodamage that can occur if the triplet state of Chl is reacting with triplet oxygen to form the poisonous singlet oxygen. Of course, we cannot entirely exclude that such or other type of photodamage occurs. In this case, our interpretation of the data relies on the assumption that the photodamage stays local and, therefore, has no influence on the Huang–Rhys factors of the other low-energy sites, which is reasonable. It is an open question why the remaining emitters of F695 exhibit a weaker electron-vibrational coupling than the ensemble on average. It seems that the states with higher exciton-vibrational coupling can more easily undergo an intersystem crossing to the triplet state, probably because the excess energy can be better dissipated by the protein environment during the transition. Finally, we note that also the low-energy emitting states show a random variation of S values.

In contrast to the present data, positive correlations between the wavelength of the ZPL position and the Huang–Rhys factor were reported for the LH2 antenna of purple bacteria[29] and for Chl *a* in a glassy matrix of 1-propanol.[28] The question arises: Under which circumstances is there a correlation between the solvatochromic shift (i.e., the environment-induced shift of the ZPL position) of the transition energy of a pigment and the strength of the dynamic modulation of this transition energy by environmental vibrations (represented by S)? In the case of LH2, most likely the mixing between exciton states and interchromophore charge transfer (CT) states is responsible for the red-shift as well as for the enhanced electron-vibrational coupling. If the CT state is energetically

DOI: 10.1021/jp510631x
J. Phys. Chem. B XXXX, XXX, XXX−XXX

above the exciton state, this mixing leads to a red-shift of the exciton state. The CT state borrows some oscillator strength from the exciton state, and the exciton state borrows some electron-vibrational coupling strength from the CT state.[58] Note that a CT state, due to its polar nature, exhibits a very strong electron-vibrational coupling.

In the case of Chl *a* in the organic glass, electrostatic as well as dispersive interactions are responsible for the electrochromic shift. Whereas the dispersive interaction, due to the higher polarizability of the excited state (with respect to the ground state) of the chromophore, leads to a red-shift of the transition energy, the electrostatic interaction can lead to both blue- and red-shifts.

As a general rule we expect a positive correlation between the red-shift and the Huang–Rhys factor, if a decrease in the distance between the chromophore and the environmental atoms (leading to an increase in the fluctuation of the transition energy) leads to a red-shift in the transition energy of the chromophore. In the case of the LH2 such a decrease in distance leads to an increase in wave function overlap and thereby to an increase in quantum-mechanic mixing between the exciton states and the CT state. In the case of Chl *a* in the organic glass, a decrease in distance leads to an increase in the dispersive interaction causing an electrochromic red-shift and/or an increase of the absolute magnitude of the electrostatic interaction, which may cause both a red- and blue-shift.

The latter aspect becomes important in proteins. As electrostatic calculations of static site energies and spectral densities of the dynamic pigment–protein coupling show, an electrochromic red-shift in general does not correlate with the Huang–Rhys factor, that is, the integral over the spectral density of the site energy fluctuations.[14,15] In principle, all scenarios are possible: anticorrelation, correlation, and no correlation. Since the electrostatic site energy shifts contain contributions of different signs, depending on the relative position of the charge density of the protein in the difference potential between excited and ground state of the chromophore, the different contributions may partially compensate each other in the static site energy. In contrast, if the charge density is varied in a correlated way (e.g., due to normal mode vibrations of the pigment–protein complex), one could well imagine that the different contributions add constructively in the dynamic modulation of the transition energy.

We, therefore, conclude that for the present system electrostatic interactions are responsible for the static and dynamic shifts of the transition energies of the low-energy exciton states.

The large scattering of the Huang–Rhys factor indicates that the respective Chls are exposed to a certain amount of variability in the interaction with their close surrounding. A measure to determine the flexibility of parts of a protein in the X-ray structure is given by the crystallographic *B*-factors. Figure 5 shows the *B*-factors of dPSIIcc. Chls 11, 48, and 49 show the largest *B*-factors in PSII (using the nomenclature of Loll et al.[56]). Among the Chls showing an increased *B*-factor is Chl29 of CP47. Chl29 seems to be responsible for the emission at 695 nm,[9,11,12,60] and Chl11 also is supposed to be red-shifted significantly.[9,12] Other studies assign Chl26 as the mostly red-shifted.[57] In the case of CP43, pigments with large red-shifts were proposed to be Chls 37, 43, and 45[9,12,61] or Chls 37 and 44.[62] There seems to be no correlation between these red-shifts and an increased *B*-factor. Irrespective of the preliminary character of these assignments, this seems to indicate that there

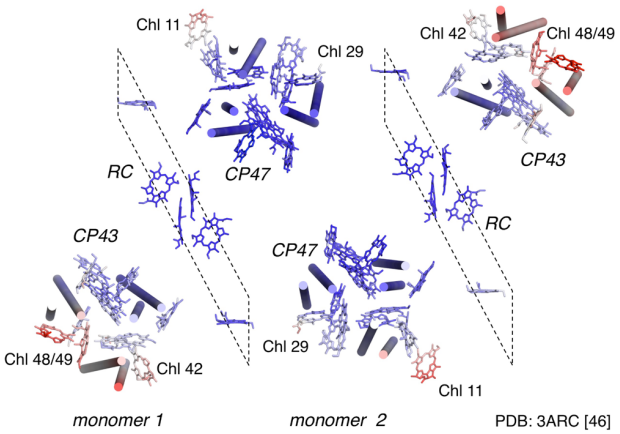

Figure 5. Distribution of the Debye–Waller factor (*B*-factor) for the Chl *a* in X-ray structure of dPSIIcc (PDB: 3ARC).[59] The averaged *B*-factors vary between 20 (colored deep blue) and 50 (deep red). Blue color indicates a small *B*-factor, and red indicates a high *B*-factor. Chl *a* molecules at the outer rim of dPSIIcc show an increased *B*-factor; one is Chl29 of CP47.

is no correlation between red-shift and Huang–Rhys factor, in agreement with our results.

Weak exciton-vibrational coupling strengths as observed here are common for photosynthetic antenna complexes.[63,64] Our SMS study gives uniquely detailed information on the exciton-vibrational coupling where it allows us to determine the Huang–Rhys factor accurately through the homogeneous broadened spectra, whereas SHB and FLN were so far interpreted by assuming a single *S*-value.[28,65,66]

It is encouraging to see that our average *S*-value for F685 ($S = 0.3$) agrees with the *S*-value inferred from SHB experiments on CP43 complexes,[27,53] where F685 is supposed to be located.[9,12] The underlying large variations of the individual *S*-values ($0.1 < S < 0.6$) for this state clearly show that the exciton-vibrational coupling of protein-bound pigments in PSII can vary substantially along the energy landscape of the protein. This result has implications also for the calculation of EET. So far, *S* was assumed to be constant, since no detailed information was available for PSII. In future calculations, it will be interesting to see how the energy transfer changes if a distribution of *S*-values is taken into account.

CONCLUSION

In summary, we have found that the electron-vibrational coupling of protein-bound pigments with low excitation energies in PSIIcc varies substantially. This conclusion can be drawn irrespectively of the accumulation of triplet states, which likely occurs under our experimental conditions and causes the mostly red-shifted emitters to be underrepresented. An implicit assumption in our analysis is that the presence of triplet states does not affect the variations of Huang–Rhys factors. Since these variations are not correlated with the emission wavelength, we conclude that electrostatic interactions are the main contributor to the electron-vibrational coupling in this system.

ASSOCIATED CONTENT

Supporting Information

Description of the algorithm to calculate *S* and the error in the evaluation of the *S*-factors are explained in detail. This material is available free of charge via the Internet at http://pubs.acs.org.

DOI: 10.1021/jp510631x
J. Phys. Chem. B XXXX, XXX, XXX–XXX

AUTHOR INFORMATION

Corresponding Author

*Phone +49-7071-29-76239; Fax +49-7071-29-5490; e-mail marc.brecht@uni-tuebingen.de (M.B.).

Notes

The authors declare no competing financial interest.

ACKNOWLEDGMENTS

This work was supported by the Heisenberg-Program of the Deutsche Forschungsgemeinschaft DFG (BR 4102/1-1 and BR 4102/2-1), by the DFG within the framework of the cluster of excellence on unifying Concepts in catalysis (UniCat), project B1, coordinated by the TU Berlin, Sfb 1078, project A5 (A.Z.), HFSP RGP0063/2013, and by the Austrian Science Fund (FWF), project P24774-N27 (T.R.).

REFERENCES

(1) van Grondelle, R.; Novoderezhkin, V. I. Energy transfer in photosynthesis: experimental insights and quantitative models. *Phys. Chem. Chem. Phys.* **2006**, *8*, 793−807.

(2) Scholes, G. D.; Fleming, G. R.; Olaya-Castro, A.; van Grondelle, R. Lessons from nature about solar light harvesting. *Nat. Chem.* **2011**, *3*, 763−774.

(3) Müh, F.; Zouni, A. Light-induced water oxidation in photosystem II. *Front. Biosci.* **2011**, *16*, 3072−3132.

(4) Müh, F.; Zouni, A. Light-induced quinone reduction in photosystem II. *Biochim. Biophys. Acta* **2012**, *1817*, 44−65.

(5) Mörschel, E.; Schatz, G. H. Correlation of photosystem II complexes with exoplasmatic freeze-fracture particles of thylakoids of the cyanobacterium *Synechococcus-sp*. *Planta* **1987**, *172*, 145−154.

(6) Folea, I. M.; Zhang, P.; Aro, E.-M.; Boekema, E. J. Domain organization of photosystem II in membranes of the cyanobacterium *Synechocystis* PCC6803 investigated by electron microscopy. *FEBS Lett.* **2008**, *582*, 1749−1754.

(7) Dekker, J. P.; Boekema, E. J. Supramolecular organization of thylakoid membrane proteins in green plants. *Biochim. Biophys. Acta* **2005**, *1706*, 12−39.

(8) Caffarri, S.; Kouril, R.; Kereiche, S.; Boekema, E. J.; Croce, R. Functional architecture of higher plant photosystem II supercomplexes. *EMBO J.* **2009**, *28*, 3052−3063.

(9) Raszewski, G.; Renger, T. Light harvesting in photosystem II core complexes is limited by the transfer to the trap: can the core complex turn into a photoprotective mode? *J. Am. Chem. Soc.* **2008**, *130*, 4431−4446.

(10) Müh, F.; Renger, T.; Zouni, A. Crystal structure of cyanobacterial photosystem II at 3.0Å resolution: a closer look at the antenna system and the small membrane-intrinsic subunits. *Plant Physiol. Biochem.* **2008**, *46*, 238−264.

(11) Renger, T.; Schlodder, E. Optical properties, excitation energy and primary charge transfer in photosystem II: theory meets experiment. *J. Photochem. Photobiol., B* **2011**, *104*, 126−141.

(12) Shibata, Y.; Nishi, S.; Kawakami, K.; Shen, J. R.; Renger, T. Photosystem II does not possess a simple excitation energy funnel: time-resolved fluorescence spectroscopy meets theory. *J. Am. Chem. Soc.* **2013**, *135*, 6903−6914.

(13) Renger, T.; Marcus, R. A. On the relation of protein dynamics and exciton relaxation in pigment-protein complexes: an estimation of the spectral density and a theory for the calculation of optical spectra. *J. Chem. Phys.* **2002**, *116*, 9997−10019.

(14) Renger, T.; Klinger, A.; Steinecker, F.; Schmidt am Busch, M.; Numata, J.; Müh, F. Normal mode analysis of the spectral density of the Fenna-Matthews-Olson light-harvesting protein: how the protein dissipates the excess energy of excitons. *J. Phys. Chem. B* **2012**, *116*, 14565−14580.

(15) Renger, T.; Müh, F. Understanding photosynthetic light-harvesting: a bottom up theoretical approach. *Phys. Chem. Chem. Phys.* **2013**, *15*, 3348−3371.

(16) Groot, M. L.; Peterman, E. J. G.; van Stokkum, I. H. M.; Dekker, J. P.; van Grondelle, R. Triplet and fluorescing states of the CP47 antenna complex of photosystem II studied as a function of temperature. *Biophys. J.* **1995**, *68*, 281−290.

(17) Groot, M. L.; Frese, R. N.; de Weerd, F. L.; Bromek, K.; Pettersson, A.; Peterman, E. J. G.; van Stokkum, I. H. M.; van Grondelle, R.; Dekker, J. P. Spectroscopic properties of the CP43 core antenna protein of photosystem II. *Biophys. J.* **1999**, *77*, 3328−3340.

(18) Krausz, E.; Hughes, J. L.; Smith, P. J.; Pace, R. J.; Arsköld, S. P. Assignment of the low-temperature fluorescence in oxygen-evolving photosystem II. *Photosynth. Res.* **2005**, *84*, 193−199.

(19) Andrizhiyevskaya, E. G.; Chojnicka, A.; Bautista, J. A.; Diner, B. A.; van Grondelle, R.; Dekker, J. P. Origin of the F685 and F695 fluorescence in photosystem II. *Photosynth. Res.* **2005**, *84*, 173−180.

(20) Brecht, M.; Skandary, S.; Hellmich, J.; Glöckner, C.; Konrad, A.; Hussels, M.; Meixner, A.; Zouni, A.; Schlodder, E. Spectroscopic properties of photosystem II core complexes from *Thermosynechococcus elongatus* revealed by single-molecule experiments. *Biochim. Biophys. Acta* **2014**, *1837*, 773−781.

(21) Neupane, B.; Dang, N. C.; Acharya, K.; Reppert, M.; Zazubovich, V.; Picorel, R.; Seibert, M.; Jankowiak, R. Insight into the electronic structure of the CP47 antenna protein complex of photosystem II: hole burning and fluorescence study. *J. Am. Chem. Soc.* **2010**, *132*, 4214−4229.

(22) Acharya, K.; Neupane, B.; Reppert, M.; Feng, X.; Jankowiak, R. On the unusual temperature-dependent emission of the CP47 antenna protein complex of photosystem II. *J. Phys. Chem. Lett.* **2010**, *1*, 2310−2315.

(23) Komura, M.; Shibata, Y.; Itoh, S. A new fluorescence band F689 in photosystem II revealed by picosecond analysis at 4−77 K: function of two terminal energy sinks F689 and F695 in PSII. *Biochim. Biophys. Acta* **2006**, *1757*, 1657−1668.

(24) van Dorssen, R.; Breton, J.; Plijter, J.; Satoh, K.; van Gorkom, H.; Amesz, J. Spectroscopic properties of the reaction center and of the 47 kDa chlorophyll protein of photosystem II. *Biochim. Biophys. Acta* **1987**, *893*, 267−274.

(25) van Dorssen, R.; Plijter, J.; Dekker, J.; den Ouden, A.; Amesz, J.; Gorkom, H. Spectroscopic properties of chloroplast grana membranes and of the core of photosystem II. *Biochim. Biophys. Acta* **1987**, *890*, 134−143.

(26) Dekker, J. P.; Hassoldt, A.; Pettersson, A.; van Roon, H.; Groot, M. L.; van Grondelle, R. On the nature of the F695 and F685 emission of photosystem II. In *Photosynthesis: From Light to Biosphere*; Mathis, P., Ed.; Kluwer Academic Publishers: Dordrecht, The Netherlands, 1995; Vol. *1*, pp 53−56.

(27) Najafi, M.; Herascu, N.; Seibert, M.; Picorel, R.; Jankowiak, R.; Zazubovich, V. Spectral hole-burning, recovery and thermocycling in chlorophyll-protein complexes: distribution of barriers on the protein energy landscape. *J. Phys. Chem. B* **2012**, *116*, 11780−11790.

(28) Rätsep, M.; Pajusalu, M.; Freiberg, A. Wavelength-dependent electron-phonon coupling in impurity glasses. *Chem. Phys. Lett.* **2009**, *479*, 140−143.

(29) Kunz, R.; Timpmann, K.; Southall, J.; Cogdell, R. J.; Freiberg, A.; Köhler, J. Exciton self trapping in photosynthetic pigment-protein complexes studied by single-molecule spectroscopy. *J. Phys. Chem. B* **2012**, *116*, 11017−11023.

(30) van Oijen, A. M.; Ketelaars, M.; Köhler, J.; Aartsma, T. J.; Schmidt, J. Unraveling the electronic structure of individual photosynthetic pigment-protein complexes. *Science* **1999**, *285*, 400−402.

(31) Tamarat, P.; Maali, A.; Lounis, B.; Orrit, M. Ten years of single-molecule spectroscopy. *J. Phys. Chem. A* **2000**, *104*, 1−16.

(32) Lu, H. P.; Xie, X. S. Single-molecule spectral fluctuations at room temperature. *Nature* **1997**, *385*, 143−146.

(33) Rutkauskas, D.; Novoderezhkin, V. I.; Cogdell, R. J.; van Grondelle, R. Fluorescence spectroscopy of conformational changes of single LH2 complexes. *Biophys. J.* **2005**, *88*, 422−435.

(34) Schleifenbaum, F.; Blum, C.; Subramaniam, V.; Meixner, A. J. Single-molecule spectral dynamics at room temperature. *Mol. Phys.* **2009**, *107*, 1923−1942.

DOI: 10.1021/jp510631x
J. Phys. Chem. B XXXX, XXX, XXX−XXX

(35) Berlin, Y.; Burin, A.; Friedrich, J.; Köhler, J. Low temperature spectroscopy of proteins. part II: experiments with single protein complexes. *Phys. Life Rev.* **2007**, *4*, 64−89.
(36) Shibata, Y.; Ishikawa, H.; Takahashi, S.; Morishima, I. Time-resolved hole-burning study on myoglobin: fluctuation of restricted water within distal pocket. *Biophys. J.* **2001**, *80*, 1013−1023.
(37) Hofmann, C.; Ketelaars, M.; Matsushita, M.; Michel, H.; Aartsma, T. J.; Köhler, J. Single-molecule study of the electronic couplings in a circular array of molecules: light-harvesting-2 complex from *Rhodospirillum molischianum*. *Phys. Rev. Lett.* **2003**, *90*, 013004.
(38) Huang, K.; Rhys, A. Theory of light absorption and non-radiative transitions in F-centres. *Proc. R. Soc. London, A* **1950**, *204*, 406−423.
(39) Pullerits, T.; Monshouwer, R.; van Mourik, F.; van Grondelle, R. Temperature-dependence of electron-vibronic spectra of photosynthetic systems-computer-simulations and comparison with experiment. *Chem. Phys.* **1995**, *194*, 395−407.
(40) Renge, I. Impurity spectroscopy in glasses and disordered crystals: inhomogeneous broadening and electron phonon coupling. *J. Lumin.* **2008**, *128*, 413−420.
(41) Rebane, K. K. *Impurity Spectra of Solids*; Plenum: New York, 1970.
(42) Personov, R. I. In *Spectroscopy and Excitation Dynamics of Condensed Molecular Systems*; Agranovich, V. M., Hochstrasser, R. M., Eds.; North Holland: Amsterdam, 1983; Chapter 10.
(43) Peterman, E. J. G.; Pullerits, T.; Grondelle, R.; Amerongen, H. Electron-phonon coupling and vibronic fine structure of light-harvesting complex II of green plants: temperature dependent absorption and high-resolution fluorescence spectroscopy. *J. Phys. Chem. B* **1997**, *101*, 4448−4457.
(44) Pieper, J.; Rätsep, M.; Irrgang, K. D.; Freiberg, A. Chromophore-chromophore and chromophore-protein interactions in monomeric light-harvesting complex II of green plants studied by spectral hole burning and fluorescence line narrowing. *J. Phys. Chem. B* **2009**, *113*, 10870−10880.
(45) Hofmann, C.; Aartsma, T. J.; Michel, H.; Köhler, J. Direct observation of tiers in the energy landscape of a chromoprotein: a single-molecule study. *Proc. Natl. Acad. Sci. U. S. A.* **2003**, *100*, 15534−15538.
(46) Brecht, M.; Hussels, M.; Schlodder, E.; Karapetyan, N. V. Red antenna states of photosystem I trimers from *Arthrospira platensis* revealed by single-molecule spectroscopy. *Biochim. Biophys. Acta* **2012**, *1817*, 445−452.
(47) Hofmann, C.; Michel, H.; van Heel, M.; Köhler, J. Multivariate analysis of single-molecule spectra: surpassing spectral diffusion. *Phys. Rev. Lett.* **2005**, *94*, 195501.
(48) Hussels, M.; Brecht, M. Effect of glycerol and PVA on the conformation of photosystem I. *Biochemistry* **2011**, *50*, 3628−3637.
(49) Kern, J.; Loll, B.; Luneberg, C.; DiFiore, D.; Biesiadka, J.; Irrgang, K. D.; Zouni, A. Purification, characterisation and crystallisation of photosystem II from *Thermosynechococcus elongatus* cultivated in a new type of photobioreactor. *Biochim. Biophys. Acta* **2005**, *1706*, 147−157.
(50) Zouni, A.; Kern, J.; Frank, J.; Hellweg, T.; Behlke, J.; Saenger, W.; Irrgang, K. Size determination of cyanobacterial and higher plant photosystem II by gel permeation chromatography, light scattering, and ultracentrifugation. *Biochemistry* **2005**, *44*, 4572−4581.
(51) Hussels, M.; Konrad, A.; Brecht, M. Confocal sample-scanning microscope for single-molecule spectroscopy and microscopy with fast sample exchange at cryogenic temperatures. *Rev. Sci. Instrum.* **2012**, *83*, 123706.
(52) Bittl, R.; Schlodder, E.; Geisenheimer, I.; Lubitz, W.; Cogdell, R. J. Transient EPR and absorption studies of carotenoid triplet formation in purple bacterial antenna complexes. *J. Phys. Chem. B* **2001**, *23*, 5525−5535.
(53) Herascu, N.; Najafi, M.; Amunts, A.; Pieper, J.; Irrgang, K.-D.; Picorel, R.; Seibert, M.; Zazubovich, V. Parameters of the protein energy landscapes of several light-harvesting complexes probed via spectra hole growth kinetics measurements. *J. Phys. Chem. B* **2011**, *115*, 2737−2747.
(54) Raszewski, G.; Diner, B. A.; Schlodder, E.; Renger, T. Spectroscopic properties of reaction center pigments in photosystem II core complexes: revision of the multimer model. *Biophys. J.* **2008**, *95*, 105−119.
(55) Brecht, M.; Studier, H.; Radics, V.; Nieder, J. B.; Bittl, R. Spectral diffusion induced by proton dynamics in pigment-protein complexes. *J. Am. Chem. Soc.* **2008**, *130*, 17487−17493.
(56) Loll, B.; Kern, J.; Saenger, W.; Zouni, A.; Biesiadka, J. Towards complete cofactor arrangement in the 3.0Å resolution structure of photosystem II. *Nature* **2005**, *438*, 1040−1044.
(57) Reppert, M.; Achary, K.; Neupane, B.; Jankowiak, R. Lowest electronic states of the CP47 antenna protein complex of photosystem II: simulation of optical spectra and revised structural assignments. *J. Phys. Chem. B* **2010**, *114*, 11884−11898.
(58) Renger, T. Theory of optical spectra involving charge transfer states: dynamic localization predicts a temperature dependent optical band shift. *Phys. Rev. Lett.* **2004**, *93*, 188101.
(59) Umena, Y.; Kawakami, K.; Shen, J. R.; Kamiya, N. Crystal structure of oxygen-evolving photosystem II at a resolution of 1.9Å. *Nature* **2011**, *473*, 55−60.
(60) de Weerd, F. L.; Palacios, M. A.; Andrizhiyevskaya, E. G.; Dekker, J. P.; van Grondelle, R. Identifying the lowest electronic states of the chlorophylls in the CP47 core antenna protein of photosystem II. *Biochemistry* **2002**, *41*, 15224−15233.
(61) Müh, F.; Madjet, M. E.; Renger, T. Structure-based simulation of linear optical spectra of the CP43 core antenna of photosystem II. *Photosynth. Res.* **2012**, *111*, 87−101.
(62) Reppert, M.; Zazubovich, V.; Dang, N. C.; Seibert, M.; Jankowiak, R. Low-energy chlorophyll states in the CP43 antenna protein complex: simulation of various optical spectra. II: simulation of optical spectra and revised structural assignments. *J. Phys. Chem. B* **2008**, *112*, 9934−9947.
(63) Reddy, N.; Lyle, P. A.; Small, G. J. Application of spectral hole burning spectroscopies to antenna and reaction center complexes. *Photosynth. Res.* **1992**, *31*, 167−194.
(64) Pieper, J.; Voigt, J.; Small, G. J. Chlorophyll *a* Franck-Condon factors and excitation energy transfer. *J. Am. Chem. Soc.* **1999**, *103*, 2319−2322.
(65) Pieper, J.; Voigt, J.; Renger, G.; Small, G. J. Analysis of phonon structure in line-narrowed optical spectra. *Chem. Phys. Lett.* **1999**, *310*, 296−302.
(66) Kikas, J. Effects of inhomogenety and site selective impurity-phonon coupling in solid solutions. *Chem. Phys. Lett.* **1987**, *57*, 511−513.

DOI: 10.1021/jp510631x
J. Phys. Chem. B XXXX, XXX, XXX−XXX

Chapter 11

Orientations between red antenna states of Photosystem I monomers from Thermosynechococcus elongatus revealed by single-molecule spectroscopy

In this chapter the spectral properties of single Photosystem I monomers from *Thermosynechococcus elongatus* are described by measuring the polarization of the fluorescence. Analyzing the fluorescence of single monomers by a polarizer as function of rotation angle in front of the spectrograph allows to distinguish two different oriented emitters. The rotator angle dependent intensity distribution of both fluorescent bands is evaluated with respect to their phase shift for several recorded monomers yielding the angle between the respective polarization vectors of the fluorescence emitted by the corresponding Chlorophylls. By a monte-carlo simulation a characteristic distribution of this experimentally accessible angle are determined for given mutual orientations between two transition dipole moments in order to compare the simulated results with the experimentally acquired angles. It can be stated that the respective emitters are almost perpendicular oriented allowing to draw concluding about the energy transfer dynamics within PSI.

This chapter is baesd on:
Skandary, S., Hussels, M., Konrad, A., Meixner, A.J., Brecht, M. "Orientations between red antenna states of photosystem I monomers from Thermosynechococcus elongatus revealed by single-molecule spectroscopy", *The Journal of Physical Chemistry B*, **2015**, *119*(43), 13888-13896

THE JOURNAL OF PHYSICAL CHEMISTRY B

Article

pubs.acs.org/JPCB

Orientations between Red Antenna States of Photosystem I Monomers from *Thermosynechococcus elongatus* Revealed by Single-Molecule Spectroscopy

Sepideh Skandary,[†] Alexander Konrad,[†] Martin Hussels,[†] Alfred J. Meixner,[†] and Marc Brecht*[,†,‡]

[†]IPTC and Lisa+ Center, University of Tübingen, D-72076 Tübingen, Germany

[‡]Zurich University of Applied Science (ZHAW), CH-8401 Winterthur, Switzerland

Supporting Information

ABSTRACT: Single-molecule spectroscopy at low temperature was used to study the spectral properties, heterogeneities, and spectral dynamics of the chlorophyll *a* (Chl *a*) molecules responsible for the fluorescence emission of photosystem I monomers (PS I-M) from the cyanobacterium *Thermosynechococcus elongatus*. The fluorescence spectra of single PS I-M are dominated by several red-shifted chlorophyll *a* molecules named C708 and C719. The emission spectra show broad spectral distributions and several zero-phonon lines (ZPLs). Compared with the spectra of the single PS I trimers, some contributions are missing due to the lower number of C719 Chl's in monomers. Polarization-dependent measurements show an almost perpendicular orientation between the emitters corresponding to C708 and C719. These contributions can be assigned to chlorophyll dimers B18B19, B31B32, and B32B33.

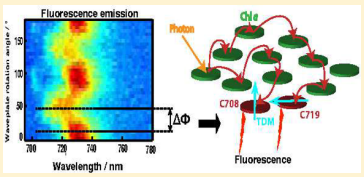

INTRODUCTION

Photosystem I (PS I) is one of two transmembrane pigment–protein complexes essential for oxygenic photosynthesis. It is located in the thylakoid membranes of cyanobacteria, algae, and plants and mediates light-induced electron transfer from plastocyanin or cytochrome C_6 on the lumenal side to ferredoxin on the stromal side.[1] The first step of the photosynthetic reaction is the absorption of a photon by the antenna system of PS I, followed by subsequent energy transfer to the reaction center. At this point, the captured excitation energy is used to induce a transmembrane charge separation starting at the chlorophyll (Chl) pair P700, which has its main absorption at 700 nm.[1,2]

The absorption spectra of PS I from green plants, algae, and cyanobacteria show the existence of Chl *a* molecules absorbing at lower energy with respect to the usual Q_y absorption at 664 nm for Chl *a* in 80% acetone,[3,4] and in particular at wavelengths larger than that of the primary donor P700.[5,6] These red-shifted Chl *a* molecules are often called the long-wavelength (also red or low-energy) Chl's (LWCs).[7] If the excitation energy is localized at these LWCs, a direct excitation of P700 is not possible any more, and the energy is trapped. Additional activation energy, e.g., thermal energy provided by the phonon bath, is necessary to oxidize P700 and start the charge separation process.[8−11] (For a detailed discussion of the properties of the red-Chl *a*, we refer the reader to ref 12.)

Detailed analysis of the absorption spectra of *Thermosynechococcus elongatus* yields the separation of the red emitting Chl's into two pools.[13−16] Their main absorption bands are at 708 and 719 nm, denoted commonly as C708 and C719, respectively. The distinction of two pools remains tentative due to a large spectral overlap of the respective bands.[13] Additionally, a red subpool (C715) was found by analysis of non-photochemical hole-burning spectra.[17] Estimations for the number of Chl *a* molecules involved in the red pool in *Th. elongatus* are based on the integrated absorbance at wavelengths longer than 700 nm. Zazubovich et al.[17] determined 7 Chl *a*'s belonging to the red pool (under the assumption that 96 Chl *a* molecules are in one PS I monomer), while Palsson et al.[13,18] estimated 9−11 Chl *a* molecules (assuming 110 Chl *a* molecules). Normalized to same number of Chl *a*'s, both estimations are in reasonable agreement.[19] Numerous studies[6,7,14] revealed that these Chl's have a crucial impact on the kinetics of energy transfer and trapping. Until now, it has been under discussion whether the energy transfer within this antenna system proceeds along well-defined pathways or utilizes variable routes.[20−22] For this purpose, it is necessary to obtain more details about the spectral distributions of these Chl *a* molecules using the advantages of various spectroscopic methods.

PS I from cyanobacteria can be isolated in monomeric and trimeric forms.[23,24] The trimer is proposed to be the native form, at least under certain physiological conditions.[25] Both the trimeric and monomeric species absorb light at room temperature and show a probability of >95% of inducing charge separation.[26] Energy exchange between monomers seems to be negligible, and as a consequence single monomer can be used to describe the optical properties of PS I. [27]

Special Issue: Wolfgang Lubitz Festschrift

Received: May 10, 2015
Revised: July 8, 2015
Published: July 30, 2015

DOI: 10.1021/acs.jpcb.5b04483
J. Phys. Chem. B 2015, 119, 13888−13896

At room temperature, the quantum efficiency of photochemistry is virtually not affected by the LWCs. However, recent studies using far-red excitation provided a deeper insight into the efficiency of charge separation by LWCs in PS I. [12] The thermal energy of the surrounding enables efficient uphill energy transfer via bulk Chl's to P700. At cryogenic temperatures, however, the fluorescence of the long-wavelength pigments increases considerably, suggesting that a significant part of the excitation energy is no longer able to reach P700. [6] Thus, at lower temperatures, the red Chl's act as traps for the excitation energy, which means the quantum efficiency of the charge separation decreases while the fluorescence intensity increases.[6,28]

The numbers of LWCs for trimeric and monomeric PS I from *Th. elongatus* are equal in C708, but they are lower in C719 for monomers.[6] The absorption spectra of the trimeric complexes at 5 K indicate a more ordered structure compared with monomers. The most remarkable difference can be observed around 720 nm, where the monomeric complexes show less absorption. In addition, the quantum yield of charge separation in monomers is higher than that in trimers at 4 K, which can be explained by the lower number of LWCs in C719.[6]

Due to the unstructured shape of the ensemble fluorescence spectra, it is difficult to obtain detailed information about the spectral characteristics of the red pools.[15] Therefore, site-selective spectroscopic techniques like spectral hole burning, fluorescence line narrowing,[29] and single-molecule spectroscopy (SMS)[30,31] are effective methods. SMS is an excellent technique to cope with inhomogeneous broadening and reveals subtle spectral details often obscured by averaging over heterogeneous ensembles.[30,32]

At room temperature, spectral diffusion and photobleaching hamper the collection of detailed spectroscopic information for most single molecules.[33−39] Lowering the temperature reduces the impact of spectral diffusion,[39−41] and the emission profile of a single emitter composed of a sharp zero-phonon line (ZPL) and so-called phonon wing (PW), which consist of vibrational sidebands, becomes observable.[42−45] The PW on the low-energy side of the ZPL is caused by the interaction of the chromophore with its surroundings, leading to the excitation of phonons (lattice vibrational modes).[46]

The first single-molecule spectra of PS I at cryogenic temperature were recorded by Jelezko et al.[47] Furthermore, assignment of red antenna states in single PS I-T from *Th. elongatus* was reported by Brecht et al.[19] In this study, we show the fluorescence of single PS I-M from *Th. elongatus* at 1.6 K for the first time. To obtain detailed information about the LWCs of PS I-M responsible for the emissions of these contributions, we performed polarization-dependent experiments on single PS I-M, allowing us to draw conclusions about the relative orientation of the respective red Chl's. The polarization-dependent measurements reveal two spectrally separated fluorescence bands at low temperature with distinguishable polarization. Analysis of our data sets indicates that the orientation between the emitters corresponding to these two contributions depends on the mutual orientation of the transition dipole moments (TDMs) of the respective emitters. Moreover, we compare our experimental results with simulations based on the projected polarization of a randomly oriented pairs of emitting dipoles with fixed angles. This comparison enables us to estimate the real angle between the TDMs of the respective emitters of C708 and C719. Finally, we discuss several candidates for red-coupled Chl dimers based on the X-ray structure of PS I. [48]

MATERIALS AND METHODS

Sample Preparation. PS I-Ms from *Th. elongatus* have been isolated as described in refs 49 and 50. The purified PS I-Ms were diluted in buffer solution (pH 7.5) containing 20 mM Tricine, 25 mM $MgCl_2$, and 0.4 mM β-DM detergent to reach a Chl *a* concentration of 20 μM. This amount of detergent is adequate for the critical solubilization of a PS I-M concentration of 0.5 μM to avoid PS I aggregation.[51] In further steps, the PSI-containing (buffer) solution was diluted (with the same buffer conditions) to a PS I-M concentration of ∼3 pM. About 1 μL of this suspension was placed between two glass coverslips. Finally, the sample was transferred directly into the cryostat and rapidly plunged into liquid helium. Experiments were carried out using a home-built confocal microscope operating at 1.6 K, as described in ref 52.

A broadband fiber laser with 40 MHz repetition rate (SuperK Extreme 40 MHz VIS, NKT Photonics) combined with an acousto-optic tunable filter set to 675 nm was used for excitation. The excitation intensity of the laser was 10 μW, measured before entering the cryostat. The highest resolution of the spectrometer (Shamrock 500 spectrograph with 400 lines/mm gratings in combination with Andor Newton back-illuminated deep-depleted CCD) is ∼0.05 nm. In a sequence of spectra, the usual exposure time for each spectrum was 2 s. For polarization measurements, a combination of a $\lambda/2$ waveplate (10RP52-2, Newport) on a motorized rotator (PRM1/MZ8, Thorlabs) and a polarizing beam displacer (BD27, Thorlabs) can be moved into the optical path in front of the spectrograph. The polarizing beam displacer splits the light into two beams with perpendicular polarizations, which can be acquired individually by the CCD camera. In combination with the rotating $\lambda/2$ waveplate, it is possible to measure spectrally resolved the fluorescence intensity as a function of rotator angle.[52]

Data Evaluation Process. For determining the phase between different contributions in fluorescence emission, an analysis based on discrete Fourier transformation was applied on two-dimensional fluorescence spectra, which are recorded as a function of waveplate rotation angle. Using our setup described above, the s- and p-polarized components of the emission are acquired simultaneously. Rotating the $\lambda/2$ waveplate, two fluorescence spectra series can be recorded, depending on the rotation angle of the waveplate with respect to the initial orientation. Both spectra series contain same information and differ only in phase. The $\lambda/2$ waveplate rotates the polarization of the incident light by double the angle between the polarization plane and toward the crystal axis. Together with the symmetry of polarization, this leads to a modulation period of 90° rotation angle of the waveplate. In addition, with the known frequency of the rotator this gives the expected modulation frequency of the spectra along the angle axis. For more information, see Supporting Information S1.

Determination of the Phase Difference between Two Arbitrarily Distributed Vectors. For a pair of emitting dipoles, representing the contributions of the polarization-dependent fluorescence data sets, their TDMs are denoted as $\vec{\mu}_1$ and $\vec{\mu}_2$, enclosing the angle α. In our case, $\vec{\mu}_1$ corresponds to the TDM of the emitter C708 and $\vec{\mu}_2$ corresponds to the TDM of the emitter C719, whereby the angle α is assumed to be constant for all single PS I-M complexes. However, the

DOI: 10.1021/acs.jpcb.5b04483
J. Phys. Chem. B 2015, 119, 13888−13896

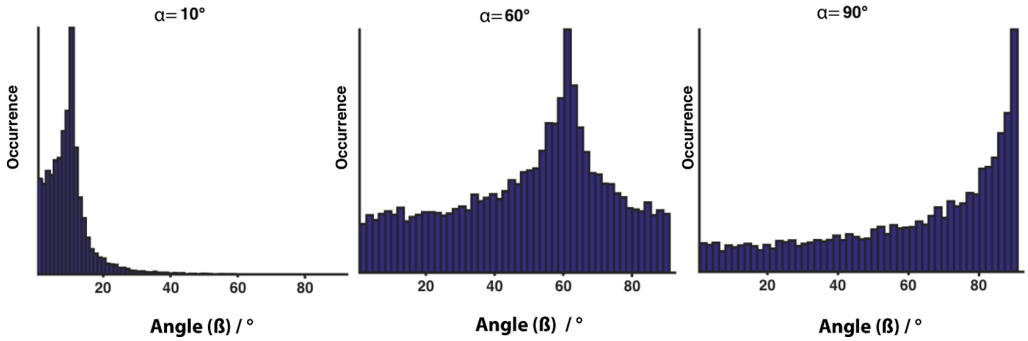

Figure 1. Angular distribution for the projection of a randomly rotated pair of vectors with fixed angles α = 10°, 60°, and 90°. The maximum of the phase difference distributions stays with the fixed angle.

orientation of each observed single PS I-M complex and also the pair of vectors corresponding to the respective emitters are arbitrarily distributed in space. By our measurement technique, we are not able to observe the three-dimensional polarization vectors but only their two-dimensional projections onto the plane of the camera, denoted as $\vec{\nu}_1$ and $\vec{\nu}_2$, which enclose the angle β. However, determining a large distribution of angles β from different polarization-dependent data sets of the single PS I-M complexes, enables us to draw conclusions on the value of α. Therefore, a simple simulation is used to illustrate the distribution of the projected angles for the randomly oriented vector-pair depending only on the angle α. Therefore, two vectors $\vec{\mu}_1$ and $\vec{\mu}_2$ with angle α are randomly rotated using Euler rotation theorem and then projected into the detection plane in order to get the projected angle β. For more details, see Supporting Information S2. Repeating this procedure for a large number of random rotations, yields a broad distribution for a given α, exhibiting its maximum occurrence around the value of α. In Figure 1, the distribution of the observable angles β is shown exemplarily for α = 10°, 60°, and 90°. It can be seen that each histogram exhibits its maximum around the given angle α. Respecting the experimental restriction, we are not able to detect fluorescence of emitters, $\vec{\mu}_1^*$ or $\vec{\mu}_2^*$, oriented perpendicular to the detection plane. We excluded the respective angles β from the distribution of one of the randomly oriented vectors related 10° or less to the optical axis because they cannot be detected due to the limitation of the objective numerical aperture. Thus, by experimentally determining a statistically significant number of angles β, each representing the evaluated phase of a polarization-dependent data sets, we are able to determine α.

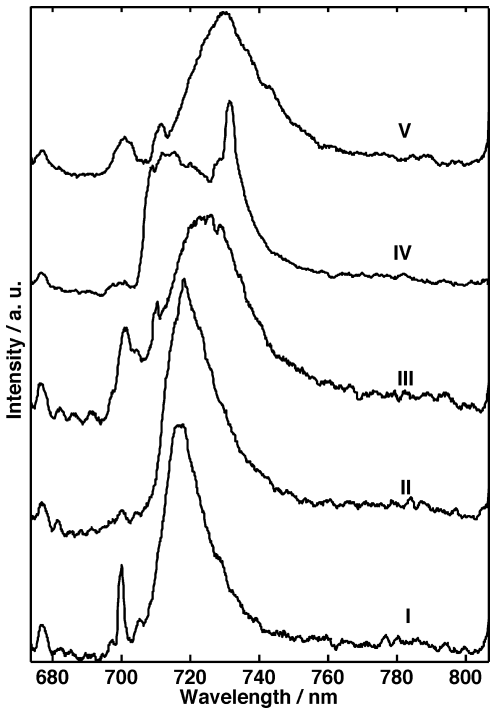

Figure 2. Single-molecule fluorescence spectra of PS I-M from *Th. elongatus*. Spectra were recorded on different individual complexes at 1.6 K. For better comparability, all spectra are scaled to a similar magnitude. The accumulation time was 72 s. Excitation wavelength was 675 nm.

RESULTS

The spectral properties of the fluorescence spectra series of 70 individual PS I-M were analyzed at low temperature (1.6 K). A selection of five fluorescence spectra (denoted *I*–*V*) of different single PS I-M is shown in Figure 2. The complete acquisition time for each data set was 72 s. For better comparability, all spectra were scaled to a similar magnitude. The emission spectra of single PS I-M are characterized by sharp ZPLs and a broad intensity distribution covering the whole emission range from 700 to 780 nm.

Despite of all differences between the dynamics of the emitters in time-dependent data sets of single PS I-M, the fluorescence range covered by the ZPLs is restricted to a defined spectral range within nanometer scale. However, the ZPLs are not prominently distributed in all spectra series but they are visible in few data sets, whereby their spectral distribution as well as their time-dependent behavior varies from complex to complex. For more detailed information, please see Supporting Information S3 and S4.

Figure 3 shows the average emission spectrum obtained for the summation of all 70 data sets of single PS I-M (red curve). The maximum intensity is located at 726.6 ± 0.5 nm, which is close to the values reported for single PS I-T from *Th. elongatus* in buffer solution (blue curve, taken from ref 53). The corresponding fwhm for single PS I-M is 29.6 ± 0.4 nm, whereas for single PS I-T, fwhm is slightly wider (31.8 ± 0.5 nm).[53] Additionally, in the average spectrum of single PS I-M (see Figure 3) some contributions are missing in intervals between 730 and 760 nm compared to the average spectrum of trimers (see Discussion).

DOI: 10.1021/acs.jpcb.5b04483
J. Phys. Chem. B 2015, 119, 13888–13896

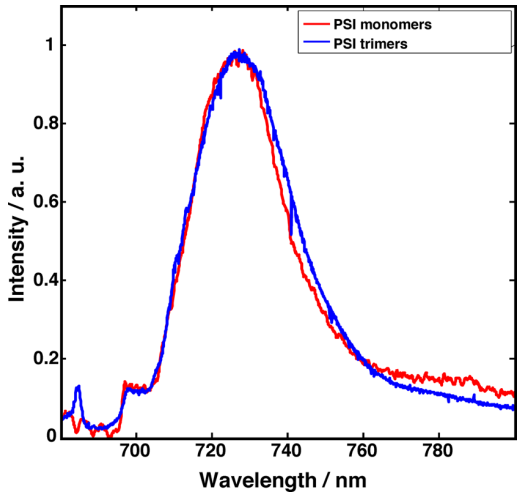

Figure 3. Average spectra obtained from the summation of 70 PS I-M (red curve) and 137 PS I-T (blue curve) data sets in buffer solution. The average spectrum of PS I-T is taken from ref 53. Both data sets are scaled to a similar amplitude for a better comparison.

The number and spectral positions of emitters responsible for the fluorescence of single PS I-M are obtained from the analysis of their polarization. Figures 4 and 5 show two fluorescence data sets of a single PS I-M as a function of the rotation angle of the waveplate in front of the spectrograph. This angle is defined with respect to an arbitrary laboratory axis and is uncorrelated to the polarization of the excitation light. In both data sets, the dependence of the emission spectra on the waveplate orientation is shown for s- and p-polarization. However, the accumulation time was increased to 10 s to enhance the S/N ratio, because the intensity of signal was attenuated in the presence of the wave plate and the polarizing beam displacer. Figure 4a shows the time-dependent data sets of single PS I-M and the respective average spectrum on top. A broad emission band can be seen in the time-dependent spectra series and in the average spectrum. Figure 4b shows the spectra of a single PS I-M complex with distinguished s- and p-polarization data sets. Here, two contributions are visible with separated spectral positions. When the contribution with peak position at 715.9 nm is intense (e.g., s-polarization data set) the other at 729.2 nm is weak. This behavior is consistent for the whole spectra series of this data set. Therefore, an almost perpendicular alignment between the projected polarization vectors of the respective contributions can be estimated. Figure 4c shows the integrated emission intensity for both contributions as a function of rotation angle over the spectral range between 706.7 and 749.3 nm. In this representation, it can be seen more clearly that the intensity of each emitter is shifted by almost 45° by the angle of the waveplate. Due to that phase shift, an almost perpendicular orientation of the projected polarization vectors can be assigned.

Figure 5a shows another time-dependent data set and the average spectrum on top. Figure 5b shows a weak contribution with spectral peak positions at 715.2 nm and an intense contribution at 730.4 nm in data sets with s- and p-polarization. The contributions show a certain overlap in time-dependent spectra series. In contrast to the data set in Figure 4b, both contributions show nearly no phase shift (see Figure 5c). Thus, a parallel alignment of the projected polarization vectors can be assumed. This difference between these two data sets can be explained simply by the different orientations of observed single PS I-M complexes. As described above, the phase between both contributions of single PS I-M were determined for each data

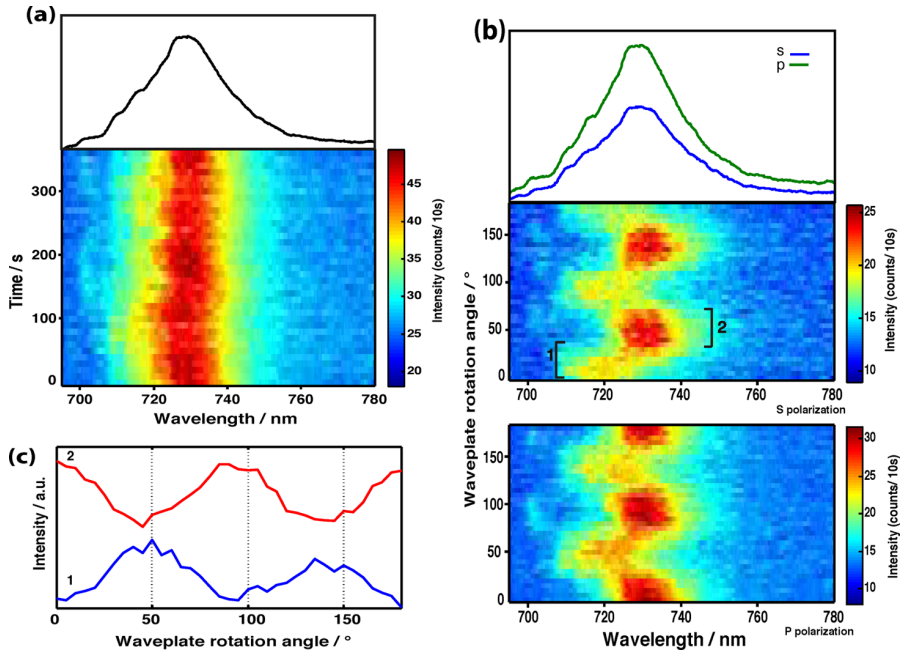

Figure 4. (a) Time-dependent data sets and the average on the top. Excitation wavelength 675 nm; temperature 1.6 K. (b) Sequence of fluorescence spectra of a single PS I-M as a function of the rotation of the waveplate in front of the spectrograph is shown. Two contributions are numbered at their spectral positions. This data set contains 37 spectra, and the acquisition time was 10 s for each spectrum. The individual spectra were recorded in steps of 5°. The waveplate rotation angle is shown on the right side. (c) Integrated fluorescence intensity versus angle of two corresponding contributions of the single PS I-M is shown. The angle between two contributions has been estimated around 90°.

DOI: 10.1021/acs.jpcb.5b04483
J. Phys. Chem. B 2015, 119, 13888−13896

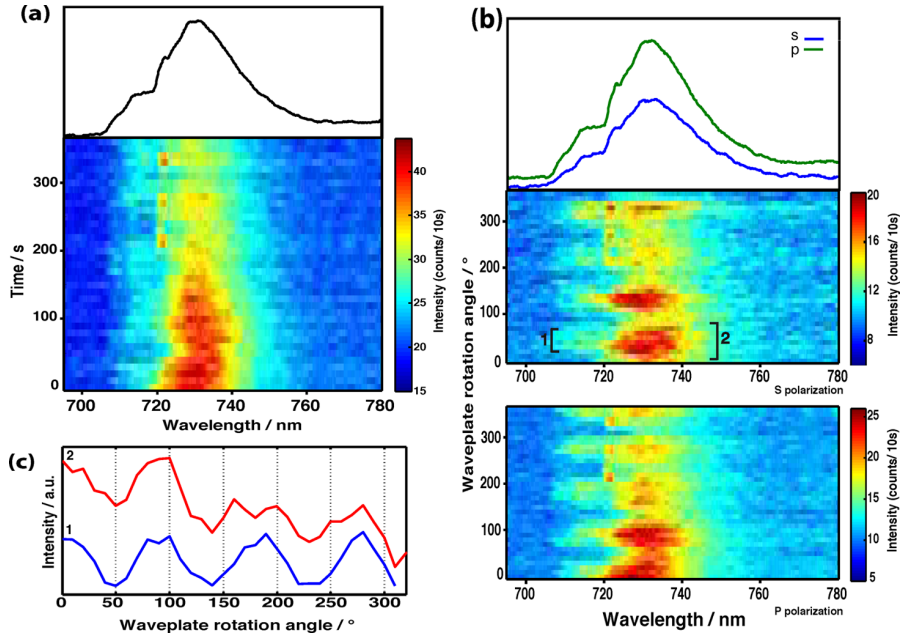

Figure 5. (a) Time-dependent data sets and the average on the top. Excitation wavelength 675 nm; temperature 1.6 K. (b) Sequence of fluorescence spectra of a single PS I-M as a function of the rotation of the waveplate in front of the spectrograph is shown. Two contributions are numbered at their spectral positions. This data set contains 37 spectra, and the acquisition time was 10 s for each spectrum. The individual spectra were recorded in steps of 10°. The waveplate rotation angle is shown on the right side. (c) Integrated fluorescence intensity versus angle of two corresponding contributions of the single PS I-M is shown. The angle between two contributions has been estimated around 0°.

set using data evaluation process explained in the Materials and Methods section (also see Supporting Information S1). Only data sets with tilted and distorted spectral shapes were not used for analysis. Therefore, by applying our evaluation method described above on 49 data sets, statistically significant distribution of angles β could be determined. In Figure 6,

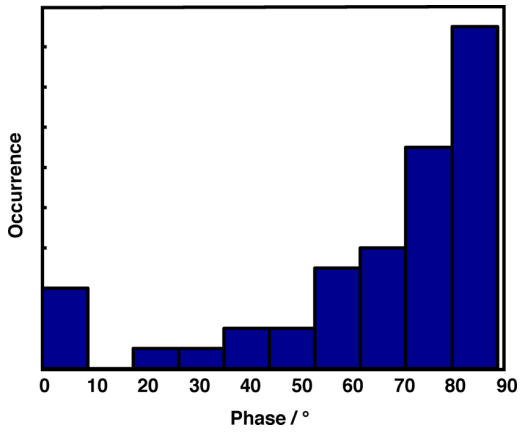

Figure 6. Distribution of angles between two contributions of single PS I-M from *Th. elongatus* for 49 fluorescence polarization-dependent data sets.

this distribution is shown and has its maximum between 80 and 90°. The histogram shows a decay profile for decreasing angles from 90 to 10°, as expected from simulations. Comparing the experimentally determined distribution (Figure 6) with the simulated histograms (Figure 1), we approximate α be within the range between 80 and 90°.

The analysis of the polarization measurements allows us to clearly distinguish overlapping emission bands in the fluorescence. In Figure 7, the distributions of the spectral

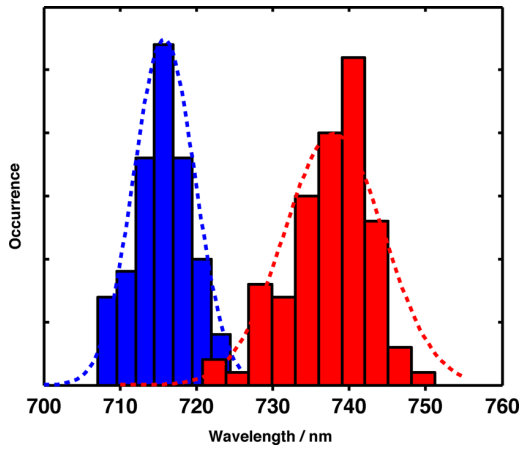

Figure 7. Histogram plots obtained from the statistical analysis of the fluorescence polarization spectra of single PSI-M. Blue histograms show the spectral distributions of C708 contributions. Red histograms show the spectral distributions of C719 contributions. Dotted lines are Gaussian fitted curves for each contribution.

peak positions of the short (blue bars) and the long (red bars) wavelength contributions of all data sets of single PS I-M are shown. The spectral distribution of each contribution has been assigned regardless whether the intense contribution is a ZPL or broad emission. Figure 7 clearly demonstrates two spectrally separated contributions in single PS I-M data sets whereas spectra without polarization-dependent analysis show only one broad emission band over the whole wavelength range.

DOI: 10.1021/acs.jpcb.5b04483
J. Phys. Chem. B 2015, 119, 13888−13896

Table 1. Angles (deg) between the TDMs of the Candidates for the Red-Emitting Chl's in PS I-M from *Th. elongatus*[a]

Coupled Chl *a*	B22B34	B31B32	B32B33	A24A35	A38A39	A33A34	A26A27	B24B25	A16A17	B37B38	A16A25	A31A32	A32B7
B18B19	**90**	**86**	**80**	78	50	66	44	45	22	52	50	61	53
B22B34		61	70	12	**80**	65	**86**	**81**	69	**87**	74	45	73
B31B32			11	73	58	69	63	60	**88**	60	58	34	34
B32B33				47	31	48	39	36	**80**	32	48	37	28
A24A35					**88**	59	**85**	**90**	58	**85**	65	54	**81**
A38A39						39	8	5	50	8	27	43	7
A33A34							35	39	50	31	16	72	45
A26A27								5	42	8	21	41	15
B24B25									49	9	26	36	10
A16A17										30	37	74	56
B37B38											20	42	14
A16A25												62	34
A31A32													28

[a]Those angles larger than 80° matching our experimentally acquired result are highlighted in bold.

DISCUSSION

The fluorescence spectra of the individual PS I-M are dominated by ZPLs and broad intensity distributions (Figure 2) at low temperatures. These contributions differ in number, intensity, and wavelength positions for each single PS I-M. In our data sets, the fluorescence spectra of single PS I-M can be separated into two wavelength regions: the region <710 nm where almost stable ZPLs are detected and the region >710 nm, where broad intensity distributions are dominating the spectra (see Supporting Information S3 and S4). Spectral diffusion is the main broadening mechanism within the time scale of the actual accumulation time (2 s).[36,54,55] The broadening mechanism is comparable for C708 and C719, the difference is the value of the electron−phonon coupling. Based on the initial shape of the single emitter, the spectral diffusion process yields a faster broadening for emitters with high Huang−Rhys factors (C719) than for those with lower Huang−Rhys factors (C708). The average spectrum of all single-complex PS I-M data sets (Figure 3) is in good agreement with the results reported for ensemble spectra of PS I-M by Schlodder et al. with oxidized P700.[50] Comparing our spectra with this reference is most reasonable, because due to the high flux of light, which is necessary to perform SMS, P700 is held out in its oxidized state.[19,50] As shown by Figure 3, the fluorescence of monomers and trimers show comparably intensities between 705 and 730 nm, while the intensity of the monomer spectrum is decreased between 730 and 760 nm. This can be explained by the different number of Chl's. The PS I-M and PS I-T complexes have the same number of red Chl's for C708, whereas PS I-M complex contains lower number of C719 Chl's;[6,50] in trimers some strongly coupled aggregates contributing to C719 are present as a result of the trimerization.[49,50]

Single-molecule spectroscopy combined with the polarization measurement provides a detailed insight into the fluorescence dynamics of the red Chl's and their interaction with other chromophores mainly mediated by excitation energy transfer (EET). Single PS I-M complexes show less spectral diversity of their fluorescence compared with PS I-T. Therefore, the analysis of the polarization-dependent data sets from single PS I-M is more feasible than for PS I-T. Using our polarization measurements we are able to separate two contributions of single monomer fluorescence into blue and red wavelength bands showing almost no spectral overlap. The blue wavelength band of single PS I-M at <720 nm is assigned to C708,[47,56,57] whereas the red wavelength band at >720 nm is most probably related to the emission of C719.[19,21] The evaluation of the angles between the projected polarization vectors corresponding to these contributions show a maximum between 80 and 90° (Figure 6). By the comparison of this distribution with simulated histograms, we are able to estimate an almost perpendicular three-dimensional orientation of the TDMs corresponding to C708 and C719.

This insight allows us to discuss the possible energy transfer pathways responsible for exciting C708 and C719. The EET between chromophors is usually described by the framework of FRET originally developed by Förster.[58] To describe an antenna pigment as a part of the energy transfer chain, it is shown that the EET depends on the distance and orientations of TDMs of the molecules by using the dipole−dipole approximation:[20,59,60]

$$V_{12} = \frac{\overrightarrow{\mu_1}\cdot\overrightarrow{\mu_2}}{r^3} - 3\frac{(\overrightarrow{\mu_1}\cdot\vec{r})(\overrightarrow{\mu_2}\cdot\vec{r})}{r^5} \quad (1)$$

Here, V_{12} is the coupling potential between two dipoles, $\vec{\mu}_1$ and $\vec{\mu}_2$ representing the TDMs of the red pools, $\vec{r}$ is the vector connecting the centers of the dipoles, and r is their separation in space. Orientation factor κ is defined by $\kappa = \hat{u}\cdot\hat{v} - 3(\hat{u}\cdot\hat{R})(\hat{v}\cdot\hat{R})$, with $\hat{u}$ and $\hat{v}$ being unit vectors of TDMs and $\hat{R}$ the unit vector of the line joining their centers.[20] According to this, if the TDMs of two dipoles are oriented almost perpendicular to each other, their κ tends toward zero ($V_{12} \simeq 0$) if their connection vector also has a perpendicular orientation to the center of TDMs. For such a weak coupling, each dipole can be considered as a separate emitter. For parallel orientation the coupling potential is maximized, which can lead to strong coupling between two Chl's behaving together as one emitter. Apparently, our polarization-dependent fluorescence data sets show two spectrally separated and mutually perpendicular arranged emitters at the wavelengths assigned to C708 and C719.

To obtain more detailed information about the emission from the coupled LWCs assigned to C708 and C719 in PS I-M complex, we calculated the orientations between coupled red Chl candidates in PS I complexes from *Th. elongatus* discussed in the literature.[8,20,48,50,61] The orientations of their respective TDMs were calculated using the spatial information on the Chl's provided by the X-ray structure of PS I from *Th. elongatus* (1JB0;[48] see Supporting Information S5). Table 1 shows the

DOI: 10.1021/acs.jpcb.5b04483
J. Phys. Chem. B 2015, 119, 13888−13896

results of these calculations whereas the candidate-pairs enclosing angles larger than 80 degree are highlighted. The suggested dimer candidates in Table 1 were taken from Byrdin et al.[20] Among the Chl's showing almost perpendicular orientation, those pairs assigned to the same Chl pool, e.g., C708 or C719, can be ruled out as potential candidates, because in our polarization-dependent data sets, we did not observe two perpendicular contributions both at the wavelengths assigned to C708 or C719. Therefore, the dimer pairs B18B19−B22B34, B22B34−A38A39, and B22B34−B37B38 should be ruled out due to their assignment to C708,[8,50,61] If there is a second emitter in the blue wavelength region we should have observed two components for the blue wavelength range. The results from reduced-minus-oxidized spectra showed that the emission from C715 is probably quenched by oxidized P700 (see Figure 4 in ref 50). Thus, the dimers assigned to C715 (A26A27, A24A35, and B24B25)[8,50] cannot be candidates for the red wavelength range.

Under these assumptions, dimers B18B19 and A16A17, assigned to C708,[50] and B31B32 and B32B33, assigned to C719,[50] with matching mutual orientations remain. However, A16A17 cannot be considered as a strongly coupled dimer, and its TDM of the low-energy exciton state is not parallel-oriented to the membrane plane;[20] therefore, A16A17−B31B32 and A16A17−B32B33 are not suitable candidates. So, the remaining candidates are B18B19−B31B32 (C708−C719) and B18B19−B32B33 (C708−C719), exhibiting strong excitonic coupling energy and a parallel orientation of their low-energy excitonic state to the membrane plane.[20,50,61] Moreover, calculating the orientation factor κ for the candidates B18B19−B31B32 (κ = 0.32) and B18B19−B32B33 (κ = 0.55) yields very low, almost negligible coupling potential. Thus, we can conclude that there is no direct energy transfer pathway between these two pools within PS I-M complexes. Both C708 and C719 have to be fed from different, energetically higher lying antenna states by two different pathways (see Figure 8). From this, we can conclude that the energy transferred from higher lying energy states to the red Chl's at low temperature is not trapped only by one final lowest energy state.[21] Their fluorescence is expected in the blue and red wavelength regions, respectively. Consequently, we can conclude that these pairs might be the most promising candidates responsible for the fluorescence of PS I-M.

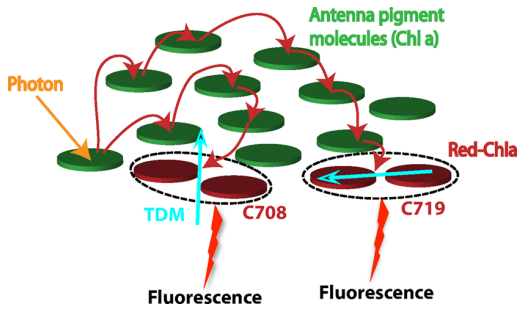

Figure 8. Schematic representation of the EET in PS I-M. The number of participating Chl *a* molecules was reduced to the minimal number sufficient for the qualitative description. Red Chl's coupled as dimers schematically show two main emitters of PS I-M, with perpendicular TDMs assigned to C708 and C719. It illustrates a direct feeding of the red pools C708 and C719 by energetically higher lying antenna states where each one emits separately due to their perpendicular TDMs.

CONCLUSION

The fluorescence of a single PS I-M from *Th. elongatus* shows the same contributions for C708 as the fluorescence of a single PS I-T; differences in the contributions are attributed to C719, mostly due to the lower number of C719 Chl's in monomers. The polarization-dependent data set of a single PS I-M complex demonstrates two spectrally separate emissions, corresponding to C708 and C719. We estimate almost perpendicular orientation between these two contributions and conclude that they are not connected with each other via energy-transfer pathways. Finally, these contributions can be assigned to Chl dimers B18B19, B31B32, and B32B33.

ASSOCIATED CONTENT

Supporting Information

The Supporting Information is available free of charge on the ACS Publications website at DOI: 10.1021/acs.jpcb.5b04483.

S1, procedure for determining the angle between dierent components in polarization-dependent data sets; S2, description of a pair of emitting dipoles with arbitrary distributions; S3, statistical analysis of kinetic information; S4, spectral positions of ZPLs; and S5, illustration of the TDM vector of a Chl *a* molecule and the coupling vectors (PDF)

AUTHOR INFORMATION

Corresponding Author

*Phone: +49-7071-29-76239. Fax: +49-7071-29-5490. E-mail: marc.brecht@uni-tuebingen.de.

Notes

The authors declare no competing financial interest.

ACKNOWLEDGMENTS

We thank Dr. Eberhard Schlodder for the PSI samples and helpful discussions. This work was supported by Heisenberg-Program of the Deutsche Forschungsgemeinschaft (DFG BR 4102/1-1 and BR 4102/2-1), along with financial support from the German Research Council (DFG ME1600/13-1).

REFERENCES

(1) Brettel, K. Electron Transfer and Arrangement of the Redox Cofactors in Photosystem I. *Biochim. Biophys. Acta, Bioenerg.* **1997**, *1318*, 322−373.

(2) Brettel, K.; Leibl, W. Electron Transfer in Photosystem I. *Biochim. Biophys. Acta, Bioenerg.* **2001**, *1507*, 100−114.

(3) Schlodder, E. Introduction to Optical Methods in Photosynthesis. *Photosynth. Res.* **2009**, *101*, 93−104.

(4) Porra, R.; Thompson, W.; Kriedemann, P. Determination of Accurate Extinction Coefficients and Simultaneous-Equations for Assaying Chlorophyll-a and Chlorophyll-b Extracted with 4 Different Solvents-Verification of the Concentration of Chlorophyll Standards by Atomic-Absorption Spectroscopy. *Biochim. Biophys. Acta, Bioenerg.* **1989**, *975*, 384−394.

(5) Gobets, B.; Ericsson, M.; Palsson, L.; Shubin, V.; Karapetyan, N.; van Grondelle, R.; Dekker, J. Site Selected Polarized Fluorescence Spectroscopy of Photosystem I Particles Isolated from the Cyanobacteria *Spirulina Platensis*. *Prog. Biophys. Mol. Biol.* **1996**, *65*, 156.

(6) Palsson, L. O.; Flemming, C.; Gobets, B.; van Grondelle, R.; Dekker, J. P.; Schlodder, E. Energy Transfer and Charge Separation in Photosystem I: P700 Oxidation Upon Selective Excitation of the Long-Wavelength Antenna Chlorophylls of *Synechococcus Elongatus*. *Biophys. J.* **1998**, *74*, 2611−2622.

DOI: 10.1021/acs.jpcb.5b04483
J. Phys. Chem. B 2015, 119, 13888−13896

(7) Gobets, B.; van Grondelle, R. Energy Transfer and Trapping in Photosystem I. *Biochim. Biophys. Acta, Bioenerg.* **2001**, *1507*, 80−99.
(8) Sener, M. K.; Lu, D. Y.; Ritz, T.; Park, S.; Fromme, P.; Schulten, K. Robustness and Optimality of Light Harvesting in Cyanobacterial Photosystem I. *J. Phys. Chem. B* **2002**, *106*, 7948−7960.
(9) Rivadossi, A.; Zucchelli, G.; Garlaschi, F. M.; Jennings, R. C. The Importance of PSI Chlorophyll Red Forms in Light-Harvesting by Leaves. *Photosynth. Res.* **1999**, *60*, 209−215.
(10) Gobets, B.; van Stokkum, I. H. M.; van Mourik, F.; Dekker, J. P.; van Grondelle, R. Excitation Wavelength Dependence of the Fluorescence Kinetics in Photosystem I Particles from *Synechocystis* PCC 6803 and *Synechococcus Elongatus*. *Biophys. J.* **2003**, *85*, 3883−3898.
(11) Bruggemann, B.; Sznee, K.; Novoderezhkin, V. I.; van Grondelle, R.; May, V. From Structure to Dynamics: Modeling Exciton Dynamics in the Photosynthetic Antenna PSI. *J. Phys. Chem. B* **2004**, *108*, 13536−13546.
(12) Schlodder, E.; Lendzian, F.; Meyer, J.; Cetin, M.; Brecht, M.; Renger, T.; Karapetyan, N. V. Long-wavelength limit of photochemical energy conversion in photosystem I. *J. Am. Chem. Soc.* **2014**, *136*, 3904−3918.
(13) Palsson, L. O.; Dekker, J. P.; Schlodder, E.; Monshouwer, R.; van Grondelle, R. Polarized Site-Selective Fluorescence Spectroscopy of the Long-Wavelength Emitting Chlorophylls in Isolated Photosystem I Particles of *Synechococcus Elongatus*. *Photosynth. Res.* **1996**, *48*, 239−246.
(14) Byrdin, M.; Rimke, I.; Schlodder, E.; Stehlik, D.; Roelofs, T. A. Decay Kinetics and Quantum Yields of Fluorescence in Photosystem I from *Synechococcus Elongatus* with P700 in the Reduced and Oxidized State: Are the Kinetics of Excited State Decay Trap-Limited or Transfer-Limited? *Biophys. J.* **2000**, *79*, 992−1007.
(15) Gobets, B.; van Amerongen, H.; Monshouwer, R.; Kruip, J.; Rögner, M.; van Grondelle, R.; Dekker, J. P. Polarized Site-Selected Fluorescence Spectroscopy of Isolated Photosystem I Particles. *Biochim. Biophys. Acta, Bioenerg.* **1994**, *1188*, 75−85.
(16) Frese, R. N.; Palacios, M. A.; Azzizi, A.; van Stokkum, I. H. M.; Kruip, J.; Rogner, M.; Karapetyan, N. V.; Schlodder, E.; van Grondelle, R.; Dekker, J. P. Electric Field Effects on Red Chlorophylls, Beta-Carotenes and P700 in Cyanobacterial Photosystem I Complexes. *Biochim. Biophys. Acta, Bioenerg.* **2002**, *1554*, 180−191.
(17) Zazubovich, V.; Matsuzaki, S.; Johnson, T. W.; Hayes, J. M.; Chitnis, P. R.; Small, G. J. Red Antenna States of Photosystem I from Cyanobacterium *Synechococcus Elongatus*: a Spectral Hole Burning Study. *Chem. Phys.* **2002**, *275*, 47−59.
(18) Palsson, L. O.; Gobets, B.; Fleming, C.; Ericsson, L. M.; van Grondelle, R.; Schlodder, E.; Dekker, J. P. Long-Wavelength Antenna Pigments in Photosystem I. *Prog. Biophys. Mol. Biol.* **1996**, *65*, 217−217.
(19) Brecht, M.; Studier, H.; Elli, A. F.; Jelezko, F.; Bittl, R. Assignment of Red Antenna States in Photosystem I from *Thermosynechoccocus Elongatus* by Single-Molecule Spectroscopy. *Biochemistry* **2007**, *46*, 799−806.
(20) Byrdin, M.; Jordan, P.; Krauss, N.; Fromme, P.; Stehlik, D.; Schlodder, E. Light Harvesting in Photosystem I: Modeling Based on the 2.5-Å Structure of Photosystem I from *Synechococcus Elongatus*. *Biophys. J.* **2002**, *83*, 433−457.
(21) Brecht, M. Spectroscopic Characterization of Photosystem I at the Single-Molecule Level. *Mol. Phys.* **2009**, *107*, 1955−1974.
(22) Konrad, A.; Trost, A.; Skandary, S.; Hussels, M.; Meixner, A.; Karapetyan, N.; Brecht, M. Manipulating the Excitation Transfer in Photosystem I by a Fabry-Perot Metal Resonator with Optical Sub-Wavelength Dimensions. *Phys. Chem. Chem. Phys.* **2014**, *16*, 6175−6181.
(23) Boekema, E.; Dekker, J.; van Heel, M.; Rögner, M.; Saenger, W.; Witt, I.; Witt, H. Evidence for a Trimeric Organization of the Photosystem I Complex from the Thermophilic Cyanobacterium *Synechococcus SP. FEBS Lett.* **1987**, *217*, 283−286.
(24) Rögner, M. U.; Mühlenhoff, X.; Boekema, E. J.; Witt, H. T. Mono-, Di- and Trimeric PSI Reaction Center Complexes Isolated from the Thermophilic Cyanobacterium *Synechococcus SP*. Size, Shape and Activity. *Biochim. Biophys. Acta, Bioenerg.* **1990**, *1015*, 415−424.
(25) Kruip, J.; Bald, D.; Boekema, E.; Rögner, M. Evidence for the Existence of Trimeric and Monomeric Photosystem I Complexes in Thylakoid Membranes from Cyanobacteria. *Photosynth. Res.* **1994**, *40*, 279−286.
(26) Turconi, S.; Kruip, J.; Schweitzer, G.; Rögner, M.; Holzwarth, A. R. A Comparative Fluorescence Kinetics Study of Photosystem I Monomers and Trimers from *Synechocystis* PCC 6803. *Photosynth. Res.* **1996**, *49*, 263−268.
(27) Abramavicius, D.; Mukamel, S. Exciton Delocalization and Transport in Photosystem I of Cyanobacteria *Synechococcus Elongates*: Simulation Study of Coherent Two-Dimensional Optical Signals. *J. Phys. Chem. B* **2009**, *113*, 6097−6108.
(28) Schlodder, E.; Cetin, M.; Byrdin, M.; Terekhova, I. V.; Karapetyan, N. V. $P700^{+}$- and $^{3}P700$- Induced Quenching of the Fluorescence at 760 nm in Trimeric Photosystem I Complexes from the Cyanobacterium *Arthrospira Platensis*. *Biochim. Biophys. Acta, Bioenerg.* **2005**, *1706*, 53−67.
(29) Purchase, R.; Bonsma, S.; Jezowski, S.; Gallus, J.; Konz, F.; Volker, S. The Power of Line-Narrowing Techniques: Applications to Photosynthetic Chromoprotein Complexes and Autofluorescent Proteins. *Opt. Spectrosc.* **2005**, *98*, 699−711.
(30) Tamarat, P.; Maali, A.; Lounis, B.; Orrit, M. Ten Years of Single-Molecule Spectroscopy. *J. Phys. Chem. A* **2000**, *104*, 1−16.
(31) Vosgröne, T.; Meixner, A. J. Surface and Resonance Enhanced Micro Raman Spectroscopy of Xanthene Dyes: From the Ensemble to Single Molecules. *ChemPhysChem* **2005**, *6*, 154−163.
(32) van Oijen, A. M.; Ketelaars, M.; Köhler, J.; Aartsma, T. J.; Schmidt, J. Unraveling the Electronic Structure of Individual Photosynthetic Pigment-Protein Complexes. *Science* **1999**, *285*, 400−402.
(33) Lu, H. P.; Xie, X. S. Single-Molecule Spectral Fluctuations at Room Temperature. *Nature* **1997**, *385*, 143−146.
(34) Stracke, F.; Blum, C.; Becker, S.; Muellen, K.; Meixner, A. Intrinsic Conformer Jumps Observed by Single Molecule Spectroscopy in Real Time. *Chem. Phys. Lett.* **2000**, *325*, 196−202.
(35) Blum, C.; Stracke, F.; Becker, S.; Muellen, K.; Meixner, A. Discrimination and Interpretation of Spectral Phenomena by Room-Temperature Single-Molecule Spectroscopy. *J. Phys. Chem. A* **2001**, *105*, 6983−6990.
(36) Piwonski, H.; Stupperich, C.; Hartschuh, A.; Sepiol, J.; Meixner, A.; Waluk, J. Imaging of Tautomerism in a Single Molecule. *J. Am. Chem. Soc.* **2005**, *127*, 5302−5303.
(37) Rutkauskas, D.; Novoderezhkin, V. I.; Cogdell, R. J.; van Grondelle, R. Fluorescence Spectroscopy of Conformational Changes of Single LH2 Complexes. *Biophys. J.* **2005**, *88*, 422−435.
(38) Schleifenbaum, F.; Blum, C.; Subramaniam, V.; Meixner, A. J. Single-Molecule Spectral Dynamics at Room Temperature. *Mol. Phys.* **2009**, *107*, 1923−1942.
(39) Berlin, Y.; Burin, A.; Friedrich, J.; Köhler, J. Low Temperature Spectroscopy of Proteins. Part II: Experiments with Single Protein Complexes. *Phys. Life Rev.* **2007**, *4*, 64−89.
(40) Shibata, Y.; Ishikawa, H.; Takahashi, S.; Morishima, I. Time-Resolved Hole-Burning Study on Myoglobin: Fluctuation of Restricted Water within Distal Pocket. *Biophys. J.* **2001**, *80*, 1013−1023.
(41) Hofmann, C.; Ketelaars, M.; Matsushita, M.; Michel, H.; Aartsma, T. J.; Köhler, J. Single-Molecule Study of the Electronic Couplings in a Circular Array of Molecules: Light-Harvesting-2 Complex from *Rhodospirillum Molischianum*. *Phys. Rev. Lett.* **2003**, *90*, 013004.
(42) Huang, K.; Rhys, A. Theory of Light Absorption and Non-Radiative Transitions in F-Centres. *Proc. R. Soc. London, Ser. A* **1950**, *204*, 406−423.
(43) Pullerits, T.; Monshouwer, R.; van Mourik, F.; van Grondelle, R. Temperature-Dependence of Electron-Vibronic Spectra of Photosynthetic Systems-Computer-Simulations and Comparison with Experiment. *Chem. Phys.* **1995**, *194*, 395−407.

DOI: 10.1021/acs.jpcb.5b04483
J. Phys. Chem. B 2015, 119, 13888−13896

(44) Renge, I. Impurity Spectroscopy in Glasses and Disordered Crystals: Inhomogeneous Broadening and Electron Phonon Coupling. *J. Lumin.* **2008**, *128*, 413−420.
(45) Rätsep, M.; Pajusalu, M.; Freiberg, A. Wavelength-Dependent Electron-Phonon Coupling in Impurity Glasses. *Chem. Phys. Lett.* **2009**, *479*, 140−143.
(46) Jankowiak, R.; Reppert, M.; Zazubovich, V.; Pieper, J.; Reinot, T. Site Selective and Single Complex Laser-Based Spectroscopies: A Window on Excited State Electronic Structure, Excitation Energy Transfer, and Electron-Phonon Coupling of Selected Photosynthetic Complexes. *Chem. Rev.* **2011**, *111*, 4546−4598.
(47) Jelezko, F.; Tietz, C.; Gerken, U.; Wrachtrup, J.; Bittl, R. Single-Molecule Spectroscopy on Photosystem I Pigment-Protein Complexes. *J. Phys. Chem. B* **2000**, *104*, 8093−8096.
(48) Jordan, P.; Fromme, P.; Witt, H. T.; Klukas, O.; Saenger, W.; Krauss, N. Three-Dimensional Structure of Cyanobacterial Photosystem I at 2.5 Å Resolution. *Nature* **2001**, *411*, 909−917.
(49) El-Mohsnawy, E.; Kopczak, M. J.; Schlodder, E.; Nowaczyk, M.; Meyer, H. E.; Warscheid, B.; Karapetyan, N. V.; Rogner, M. Structure and Function of Intact Photosystem I Monomers from the Cyanobacterium *Thermosynechococcus Elongatus*. *Biochemistry* **2010**, *49*, 4740−4751.
(50) Schlodder, E.; Hussels, M.; Cetin, M.; Karapetyan, N. V.; Brecht, M. Fluorescence of the Various Red Antenna States in Photosystem I Complexes from Cyanobacteria is Affected Differently by the Redox State of P700. *Biochim. Biophys. Acta, Bioenerg.* **2011**, *1807*, 1423−31.
(51) Müh, F.; Zouni, A. Extinction Coefficients and Critical Solubilisation Concentrations of Photosystems I and II from *Thermosynechococcus Elongatus*. *Biochim. Biophys. Acta, Bioenerg.* **2005**, *1708*, 219−228.
(52) Hussels, M.; Konrad, A.; Brecht, M. Confocal Sample-Scanning Microscope for Single-Molecule Spectroscopy and Microscopy with Fast Sample Exchange at Cryogenic Temperatures. *Rev. Sci. Instrum.* **2012**, *83*, 123706.
(53) Hussels, M.; Brecht, M. Effect of Glycerol and PVA on the Conformation of Photosystem I. *Biochemistry* **2011**, *50*, 3628−3637.
(54) Brecht, M.; Studier, H.; Radics, V.; Nieder, J. B.; Bittl, R. Spectral Diffusion Induced by Proton Dynamics in Pigment-Protein Complexes. *J. Am. Chem. Soc.* **2008**, *130*, 17487−17493.
(55) Brecht, M.; Radics, V.; Nieder, J. B.; Bittl, R. Protein Dynamics-Induced Variation of Excitation Energy Transfer Pathways. *Proc. Natl. Acad. Sci. U. S. A.* **2009**, *106*, 11857−11861.
(56) Hayes, J. M.; Matsuzaki, S.; Ratsep, M.; Small, G. J. Red Chlorophyll a Antenna States of Photosystem I of the Cyanobacterium *Synechocystis SP* PCC6803. *J. Phys. Chem. B* **2000**, *104*, 5625−5633.
(57) Rätsep, M.; Johnson, T. W.; Chitnis, P. R.; Small, G. J. The Red-Absorbing Chlorophyll a Antenna States of Photosystem I: A Hole-Burning Study of *Synechocystis SP* PCC 6803 and its Mutants. *J. Phys. Chem. B* **2000**, *104*, 836−847.
(58) Förster, T. Energiewanderung und Fluoreszenz. *Naturwissenschaften* **1946**, *33*, 166−175.
(59) Renger, T.; May, V.; Kühn, O. Ultrafast Excitation Energy Transfer Dynamics in Photosynthesis Pigment-Protein Complexes. *Phys. Rep.* **2001**, *343*, 137−254.
(60) Abramavicius, D.; Palmieri, B.; Voronine, D.; Sanda, F.; Mukamel, S. Coherent Multidimensional Optical Spectroscopy of Excitons in Molecular Aggregates; Quasiparticle versus Supermolecule Perspectives. *Chem. Rev.* **2009**, *109*, 2350−2408.
(61) Karapetyan, N. V.; Schlodder, E.; van Grondelle, R.; Dekker, J. P. The Long Wavelength Chlorophylls in Photosystem I. In *Photosystem I: The Light-Driven Plastocyanin:Ferredoxin Oxidoreductase*; Golbeck, J. H., Ed.; Advances in Photosynthesis and Respiration *24*; Springer: Berlin, 2006; pp 177−192.

DOI: 10.1021/acs.jpcb.5b04483
J. Phys. Chem. B 2015, 119, 13888−13896

Orientations Between Red Antenna States of Photosystem I Monomers from *Thermosynechococcus Elongatus* Revealed by Single-Molecule Spectroscopy

Sepideh Skandary,[†] Alexander Konrad,[†] Martin Hussels,[†] Alfred J. Meixner,[†] and Marc Brecht[*,†,‡]

University of Tübingen, IPTC and Lisa+ Center, Tübingen, Germany, and Zurich University of Applied Science Winterthur (ZHAW), Winterthur, Switzerland

E-mail: marc.brecht@uni-tuebingen.de

Phone: +49-7071-29-76239. Fax: +49-7071-29-5490

S1

The procedure for determining the angle between different components in polarization dependent data sets is based on discrete Fourier transformation (DFT). Figure 1 shows the workflow to determine the angle between two components clearly differing in polarization. Figure 1a shows the 2D data set of fluorescence spectra in dependence of the angle of the $\lambda/2$-waveplate. For analysis, DFT is applied on this data set along the angular (also time)

[*]To whom correspondence should be addressed
[†]University of Tübingen, IPTC and Lisa+ Center, Tübingen, Germany
[‡]Zurich University of Applied Science Winterthur (ZHAW), Winterthur, Switzerland

axis. In the second step, those Fourier components are selected corresponding to the expected modulation frequency caused by rotation of the $\lambda/2$-waveplate. Figure 1b and c show the amplitude and the phase of these components. In Figure 1b, two ranges of high amplitude can be identified and correlated to ranges of stable phase which is indicated by two dashed squares in Figure 1c. Then, using the phase plot (Figure 1c) their phase difference is calculated to 3.065 rad (nearly π). Due to the two-fold rotational symmetry of the polarization this gives two times the angular difference. Therefore, the angular difference of the polarization is then divided by two, which gives 1.532 rad (88 degree) for this example.

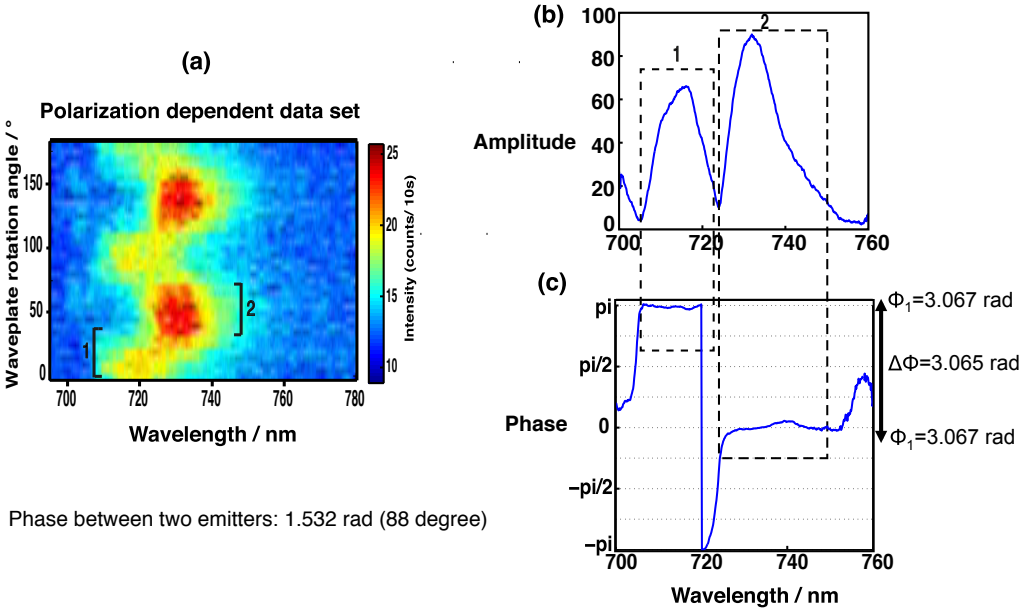

Figure 1: (a): Polarization dependent data sets with the angle nearly 90 degree between two emitters (1) and (2). (b): The amplitude modulation calculated by DFT. (c) The phase modulation calculated by DFT.

S2

For a pair of emitting dipoles with arbitary distributions, $\overrightarrow{\mu_1}$ and $\overrightarrow{\mu_2}$ are representing their TDMs responsible for fluorescence in polarization dependent data sets. The vectors $\overrightarrow{\mu_1}$ and $\overrightarrow{\mu_2}$ with angle α are shown in Figure 2 by green arrows. With respect to the arbitrary

orientation of each observed single monomer, this pair of vectors is rotated by a random angle around a random axis (calculated by the Euler rotation theorem). The new vectors, $\overrightarrow{\mu_1^*}$ and $\overrightarrow{\mu_2^*}$, shown in Figure 2 by blue arrows, represent now the emitters C708-C719 for a certain single PS I-M complex. The experimentally determined vectors $\overrightarrow{v_1}$ and $\overrightarrow{v_2}$, shown in Figure 2 by red arrows, enclosing the angle β can now be easily given by the projection onto the xy-plane, which is defined as the plane of the camera (detection plane).

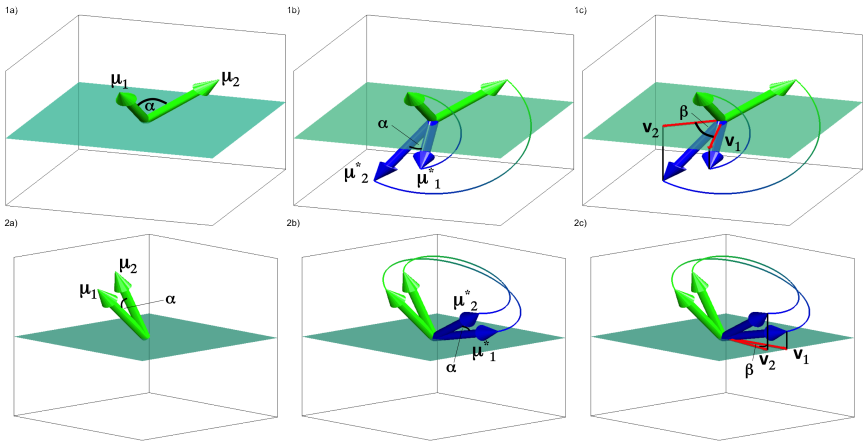

Figure 2: The TDMs of two emitters (green), the rotated vector pair (blue) and the projected vectors (red) which we detect during our polarization dependent measurements; (a): α= 60°, (b): α= 20°.

S3

To demonstrate all kinetic information of various recorded spectra of individual PS I-M data sets, a further statistical approach has been used. An algorithm (described as algorithm I in Ref.[1]) was used to determine the wavelength position of the most intense contributions in the fluorescence spectra of each individual PS I complex together with its full width at half maximum (FWHM). These parameters are determined regardless whether the intense contribution is a ZPL or a broad distribution. The result of this analysis applied on the whole data sets of single PS I-M is shown as a 2D scatter plot in Figure 3. The contributions are

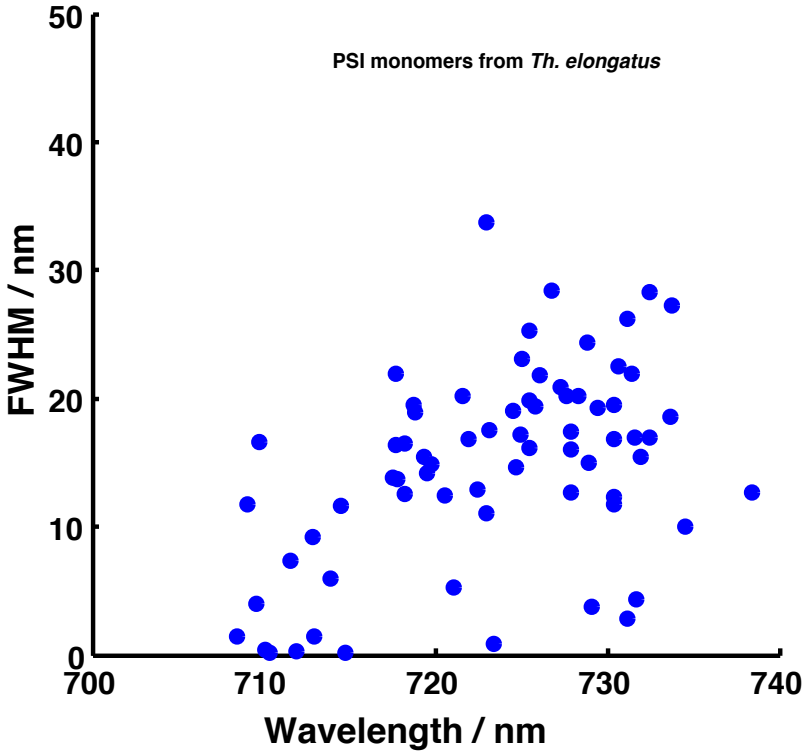

Figure 3: 2D-scatter plot obtained from the evaluation of the emission spectra of single PS I-M. Each dot represents the FWHM and wavelength position of the highest intensity peak in the spectra of individual PSI complexes.

scattered over a wide wavelength and line width range. 73% are found within a wavelength range from 717 to 735 nm and FWHM changed from 10 to 34 nm. 23% of the contributions are found within the wavelength range from 708 to 735 nm and FWHM less than 10 nm.

S4

The spectral positions of ZPLs were determined for all 70 individual data sets of monomers. Figure 4 shows the relative distributions of the spectral positions of ZPLs by counting their wavelength positions, their dynamics and occurrence along with the average spectrum of the whole data sets. For this purpose, the spectral positions of ZPLs for all single PS I-M data

sets were determined by using an algorithm explained in Ref.[1] Figure 4 shows the relative occurrence of ZPLs together with the average spectrum of the whole data sets taken from single PS I-M. The histogram shows the relative occurrence of ZPL spectral positions as a

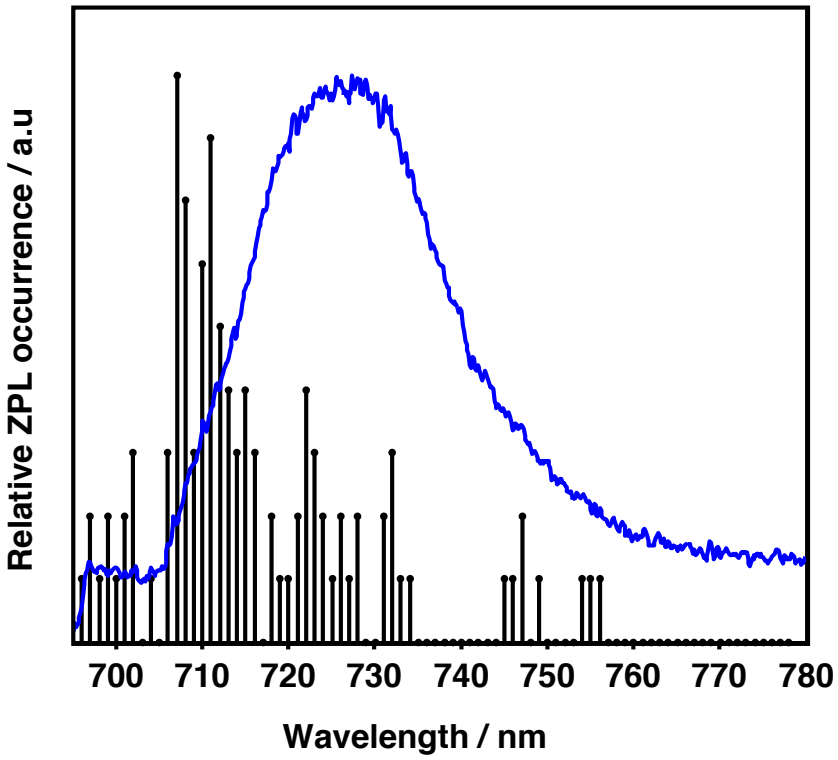

Figure 4: The ZPL distributions (histogram) and the average emission spectrum for PS I-M. The average spectrum (solid line) represents the summation of all data sets from single PS I-M at low temperature, 1.6 K. The data were scaled to similar amplitude.

function of wavelength between 695 nm to 780 nm. The ZPLs dominantly occurred in the range between 695 to 757 nm. The high relative occurrence of ZPLs are distributed in the spectral range <720 nm; The maximum are found at 707±1 nm. The peak of the average spectrum is at 726.6±0.1 nm (FWHM= 29.6±0.4 nm). The relative occurrence of ZPLs at 746 nm to 757 nm is very small. Based on their low integral intensity, these contributions are almost invisible in the average spectrum.

The major proportion of ZPLs of single PS I-M from *Th. elongatus* occurred around 710 nm

assigned to C708. Observed changes in the shape of ZPL distributions can be due to the environment of the involved chromophore assemblies.[1–4] The rate of conformational changes increases for chromophores of C715/C719 compared to C708, because less ZPLs are observed in the range >720 nm. For more detailed discussion, please see Ref.[4]

S5

For each Chl *a* molecule the TDM vectors were determined by the spatial information of the nitrogen atoms N_B and N_D given by the 1JB0. PDB-file as illustrated by Figure 5. For strong coupled Chls the determination of the resulting TDM is illustrated by Figure 6 and is based on the approximations made by Byrdin et al.[5]

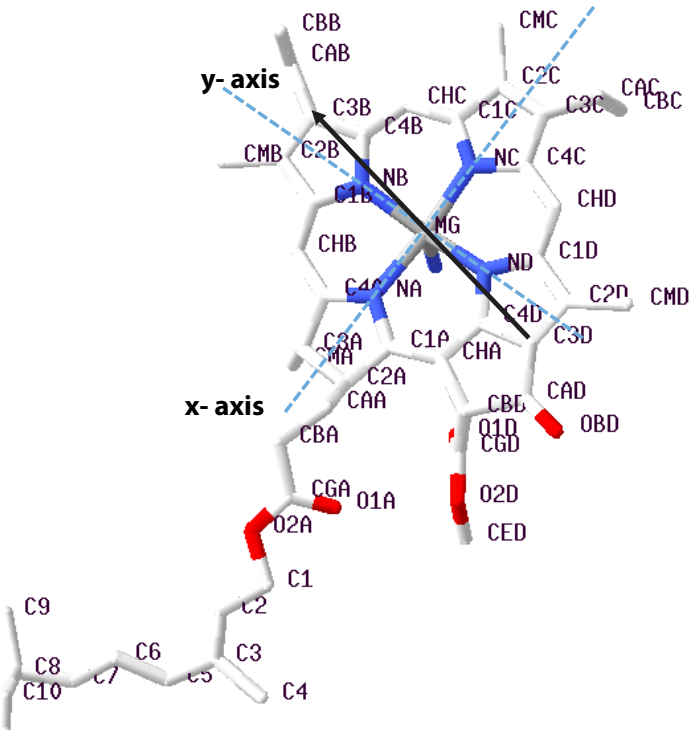

Figure 5: The black vector shows the TDM vector of each Chl *a* molecule.; from 1JB0. PDB; Jordan *et al.*[6]

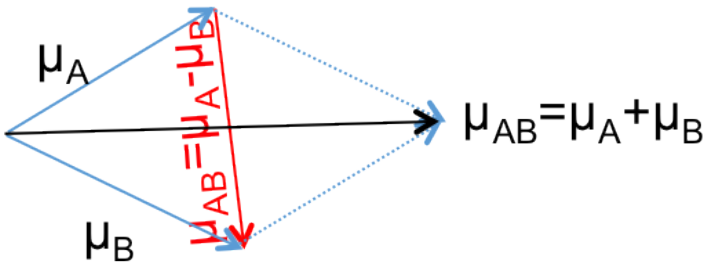

Figure 6: The coupling vectors.

Transition dipoles of coupled Chls e.g. B18B19 in table 1 in manuscript are calculated based on the approximation in table (3) of Byrdin et al.[5] (J $<$ 0 of sum bands (Σ) are energetically lower except for dimers: A16A17, A31A32 and A32B7, difference bands (Δ) are energetically lower.

References

(1) Hussels, M.; Brecht, M. Effect of Glycerol and PVA on the Conformation of Photosystem I. *Biochemistry* **2011**, *50*, 3628–3637.

(2) Brecht, M.; Hussels, M.; Schlodder, E.; Karapetyan, N. V. Red Antenna States of Photosystem I Trimers from *Arthrospira Platensis* Revealed by Single-Molecule Spectroscopy. *Biochim. Biophys. Acta* **2012**, *1817*, 445–452.

(3) Brecht, M.; Studier, H.; Elli, A. F.; Jelezko, F.; Bittl, R. Assignment of Red Antenna States in Photosystem I from *Thermosynechoccocus Elongatus* by Single-Molecule Spectroscopy. *Biochemistry* **2007**, *46*, 799–806.

(4) Brecht, M.; Studier, H.; Radics, V.; Nieder, J. B.; Bittl, R. Spectral Diffusion Induced by Proton Dynamics in Pigment–Protein Complexes. *J. Am. Chem. Soc.* **2008**, *130*, 17487 – 17493.

(5) Byrdin, M.; Jordan, P.; Krauss, N.; Fromme, P.; Stehlik, D.; Schlodder, E. Light Harvesting in Photosystem I: Modeling Based on the 2.5-Å Structure of Photosystem I from *Synechococcus Elongatus*. *Biophys. J.* **2002**, *83*, 433–457.

(6) Jordan, P.; Fromme, P.; Witt, H. T.; Klukas, O.; Saenger, W.; Krauss, N. Three-Dimensional Structure of Cyanobacterial Photosystem I at 2.5 Å Resolution. *Nature* **2001**, *411*, 909–917.

Chapter 12

Manipulating the excitation transfer in Photosystem I using a Fabry-Perot metal resonator with optical subwavelength dimensions

The energy transfer within photosynthetic complexes mainly depends on the arrangements of the participating Chlorophyll pools but also on the coupling of the protein to the surrounding matrix. At ambient conditions the energy transfer dynamics of a FRET-pair can be altered by changing the photonic mode density induced by a $\lambda/2$-micro-resonator, which leads to an enhancement or a suppression the fluorescent deactivation channel of individual chromophores within the transfer chain. The following chapter demonstrates how the energy transfer dynamics of PSI from *Arthrospira platensis* can be altered even at cryogenic temperatures (1.6 K) by a fixed $\lambda/2$-micro-resonator with embedded complexes and various cavity lengths. For several spatially separated locations representing different on-axis cavity wavelengths measured by white light transmission spectra the respective fluorescence spectra were recorded. Describing the free space fluorescence spectrum of PSI at 1.6 K by six Gaussian bands and calculating the impact of the Purcell factor affecting these fluorescent bands for each mirror separation allows to reproduce the measured spectra without respect to the energy transfer dynamics. To spectrally determine the alterations in the energy transfer chain induced by altered radiative decay rates of emitting Chlorophyll pools the simulations assuming no coupling between the contributors of the spectral bands were compared to the measured fluorescence spectra that include this coupling. The difference spectra show, which spectral band and respective Chlorophyll pool become more populated or depopulated by the altered transfer dynamics compared to free space.

This chapter is baesd on:
Konrad, A., Trost, AL., Skandary, S., Hussels, M., Meixner, A.J., Karapetyan, N.V., Brecht, M. "Manipulating the excitation transfer in Photosystem I using a Fabry-Perot metal resonator with optical subwavelength dimensions" *Physical Chemistry Chemistry Physics*, **2014**, *16*,6175-6181.

PCCP

PAPER

View Article Online
View Journal | View Issue

Cite this: *Phys. Chem. Chem. Phys.*, 2014, **16**, 6175

Manipulating the excitation transfer in Photosystem I using a Fabry–Perot metal resonator with optical subwavelength dimensions†

Alexander Konrad,[a] Anna-Lisa Trost,[a] Sepideh Skandary,[a] Martin Hussels,[a] Alfred J. Meixner,[a] Navasard V. Karapetyan[b] and Marc Brecht*[ac]

Received 9th December 2013,
Accepted 5th February 2014

DOI: 10.1039/c3cp55195d

www.rsc.org/pccp

We demonstrate controlled modification of the fluorescence and energy transfer properties of Photosystem I (PSI) – one of the most important light harvesting systems – by using a newly developed approach to produce optical subwavelength microcavities for cryogenic temperature issues. The experiments were carried out on PSI from the cyanobacterium *Arthrospira platensis* as it shows a broad and structured fluorescence emission. By changing the distance between the cavity forming mirrors, the electromagnetic field mode structure around PSI is varied affecting the emission and energy transfer properties, which allows us to selectively enhance signals of resonant emitters and suppress off-resonant emission. By comparing the experimental data with simulations, we are able to show how excitation transfer within PSI is affected by the microcavity. The ability to control the energy transfer within such efficient energy converters as photosynthetic proteins can establish the opportunity for enhancing the efficiencies of bio-solar applications. The defined control of the resonance conditions by microcavities makes them a preferable tool to study the effects of additional electromagnetic modes on the energy transfer in any coupled multi-chromophore system. The resonator geometry excludes the direct contact of the proteins with any surface. Possible quenching or denaturation of the complexes close to metal surfaces is still an insuperable obstacle for studies with proteins and nanostructures, which can be avoided by resonators.

1 Introduction

Optical microcavities are efficient tools to tailor the fluorescence of embedded emitters to a narrow spectral range.[1] Placing an emitter within a confined geometry of a resonator modifies its emission properties,[2] in particular, the spectral, spatial and temporal distributions. According to Fermi's golden rule, the spontaneous emission lifetime of a dipole emitter depends on both the transition dipole moment and the density of modes of the electromagnetic field.[3] Inside cavities, the density of modes coupling to the dipole emitter is changed with respect to free space and hence the emission rate of the emitter. This effect – first described by Purcell[2] – can be used to enhance and shape the fluorescence emission down to the single particle/molecule level.[4–7] One type of such cavities is realized by Fabry–Perot like microresonators, which are emerging devices for manipulating optical properties of fluorophores.[6] In the last few years, experimental studies on cavity-controlled photo-luminescence have been carried out on model systems such as single quantum dots,[8] molecules,[4] atoms,[9] nitrogen-vacancy centers in diamonds[10] and simple energy transfer systems.[11,12] In this article, we demonstrate first optical experiments of a prominent and complex energy transfer coupled protein system confined in an optical resonator at cryogenic temperatures (1.6 K). We selectively tune the fluorescence of emitting pools in Photosystem I (PSI) by a subwavelength microcavity and describe the consequent modifications in the exciton transfer dynamics.

PSI is one of the key proteins of the photosynthetic apparatus and a promising candidate for bio-solar applications.[13–15] Especially, interactions with electric fields created by plasmonic nanostructures have attracted a lot of attention during the last few years.[13,14,16–22] The attractiveness of PSI relies partially on its simple function, which is capturing and converting solar energy into electric energy. For this purpose around 100 chlorophyll

[a] *Institut für Physikalische und Theoretische Chemie, Universität Tübingen, Auf der Morgenstelle 18, 72076 Tübingen, Germany. E-mail: marc.brecht@uni-tuebingen.de; Fax: +49-7071-29-5490; Tel: +49-7071-29-76239*

[b] *A.N. Bakh Institute of Biochemistry, Russian Academy of Sciences, Leninsky Prospect, 33, 119071 Moscow, Russia*

[c] *Zürcher Hochschule für Angewandte Wissenschaften, Institut für Angewandte Mathematik und Physik, Technikumstrasse 13, 8401 Winterthur, Switzerland*

† Electronic supplementary information (ESI) available. See DOI: 10.1039/c3cp55195d

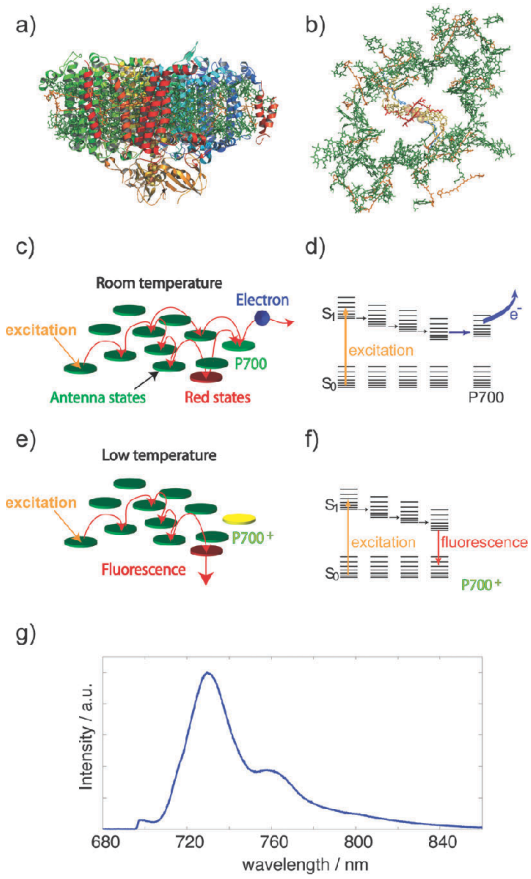

Fig. 1 Photosystem I from oxygenic photosynthesis. (a) Side view of PSI from cyanobacteria (protein data bank (PDB) entry: 1JB0).[24] (b) Top view of PSI without the protein backbone. In each monomer about 100 chlorophyll molecules (green) absorb excitation energy and transfer it to a chlorophyll dimer (red) in the reaction center[23] which absorbs at 700 nm (P700). (c and d) Illustration of excitation-energy transfer pathways at ambient temperatures and an energy-level scheme. Upon excitation of P700 a charge-separated state across the membrane is formed.[23] Interestingly, red chlorophyll states (red) with lower excitation energies than P700 are also involved in energy transfer. (e and f) At low temperatures the transfer from the red chlorophylls towards P700 is partially blocked, as a consequence these chlorophylls become fluorescent. (g) The low temperature fluorescence emission of PSI trimers (blue) is composed of several contributions having different wavelength positions, width and intensity (for further details, see ref. 25 and 26).

molecules per monomer are involved in efficient light-harvesting and excitation energy transfer leading to light induced charge separation in the reaction center and a subsequent transfer of an electron (Fig. 1a–d).[23] An intriguing feature of the PSI core antenna of cyanobacteria is the presence of several chlorophyll (Chl) molecules absorbing at lower energy than the reaction center at 700 nm (P700). These Chls have a pronounced effect on the excitation energy transfer within the whole antenna system (Fig. 1c–f).[27] These red-shifted Chls are often referred to as "red-most" Chls or long-wavelength Chls (for details see ref. 25 and 28). At low temperatures, these long-wavelength Chls act as traps for excitons, partially releasing this excitation energy as fluorescence (Fig. 1e–f).[23] The fluorescence emission of PSI is a composition of several spectroscopically discernible contributions from different long-wavelength Chls.[25] The high quality of the protein preparations, the large absorption cross section, the red-shifted emission and its prominence makes PSI a perfect system to analyze the influence of external fields on the optical properties and excitation energy transfer dynamics of coupled multi-chromophoric systems.[16–18,22,29]

The modifications of the excitation energy transfer in PSI embedded in a subwavelength microcavity result in altered fluorescence spectra which are observed using a confocal microscope. Revealing these altered exciton transfer dynamics is achieved by comparing the experimental spectra with simulated spectra of uncoupled chromophores. The resonance wavelength and with that the cavity length can be measured and modified by scanning the position of the focal spot (confocal volume) over the microcavity as shown in Fig. 2. This approach enables the collection of transmission and fluorescence spectra of PSI complexes exposed to different electromagnetic field mode structures. Production and application of the microresonators at cryogenic temperatures are described in the ESI.† Altering transfer efficiencies in transfer coupled systems embedded in resonators by modifying their optical properties has already been shown by Andrew *et al.*[12] or Schleifenbaum *et al.*[11] who used model systems at room temperature. It has been shown for such coupled systems that microcavities enable the enhancement and characterization of luminescence bands which are suppressed in free space. Addressing individual fluorescent pools in PSI is hampered by large lifetime variations,[30,31] overlapping of spectral bands,

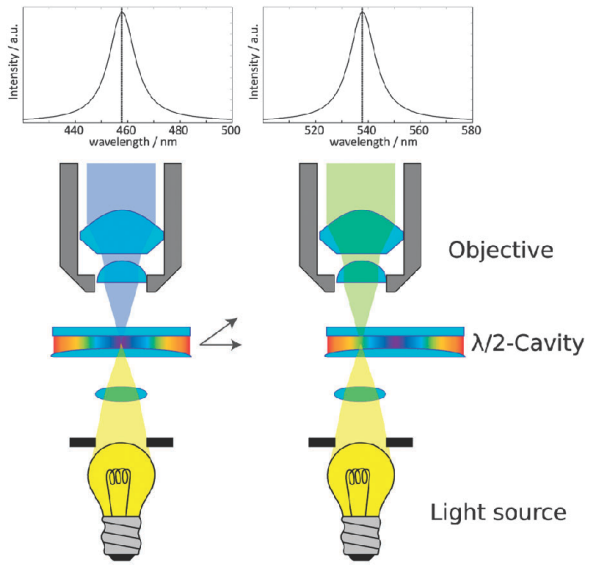

Fig. 2 Simplified scheme showing the scanning of the focal spot over a $\lambda/2$ microcavity. The curved shape of one of the mirrors results in a continuous change of the resonance conditions as indicated by the rainbow colors inside the cavity. The cavity is illuminated by a white light source to determine the cavity properties at the focal spot; only the components fulfilling the resonance conditions pass the cavity. This light is collected by an objective yielding the transmission spectrum (on top). The resonance wavelength of the resonator is changed simply, by changing the position of the focal spot in relation to the cavity (right). For detailed information concerning the setup and manufacturing of the cavities, see also the ESI.†

potentially hidden quenched pools and spectral diffusion even at cryogenic temperatures. In this article we report on the selective control of the energy transfer in a complex and one of the most important protein systems in nature for the first time. We can also confirm previously reported[22,25,32] approaches addressing fluorescent Chl pools by measurements and the used model for interpretation. With our new approach for low temperature Fabry–Perot resonators any biological sample can be prepared and frozen in standard solutions like water–glycerol-mixtures. Contrary to experiments with nanostructures, we can also exclude any chemical interaction of the proteins at metal surfaces due to a large cavity mode volume and a glass spacing layer on the silver mirrors. Conformational changes or denaturation induced by nearby metal surfaces is a severe problem for observing native protein states. The defined control of light-harvesting and energy-transfer coupled system is one prerequisite for developing or improving bio-solar devices.

2 Results and discussion

In the first order of interference of the cavity ($\lambda/2$ region), several positions with different resonance conditions were selected as illustrated in Fig. 2. At these positions, the white light transmission spectrum of the cavity and the fluorescence emission of PSI were recorded one after the other. For each position, the cavity length was determined from the white light transmission spectrum (as shown in the ESI†). The $\lambda/2$ region contains only one matching order of resonator modes in the wavelength range of the absorption and emission of PSI. This gives the opportunity to control the mode density with high precision over a large spectral range. The excited photosystems in the resonator are forced to enhanced decoherence resulting in changed lifetimes and restricted energy distribution.

Several fluorescence spectral series with tuned resonance frequencies of the resonator covering the whole wavelength range of the fluorescence emission of PSI were collected. Fig. 3a shows four emission spectra (blue curves) out of one series together with the corresponding Lorentzian fits of the white light transmission spectra (black curves). For comparison, the spectrum on top shows the free space emission spectrum of PSI trimers from *A. platensis* (blue curve). The same spectrum is also displayed in Fig. 3b described by a multiple Gaussian fit (see also Table 1). The four measured spectra at selected resonance wavelengths differ extremely from the free-space spectrum but also from each other. Mostly emission around the white light transmission maximum is enhanced and emission on the long wavelength side inhibited. On the short wavelength

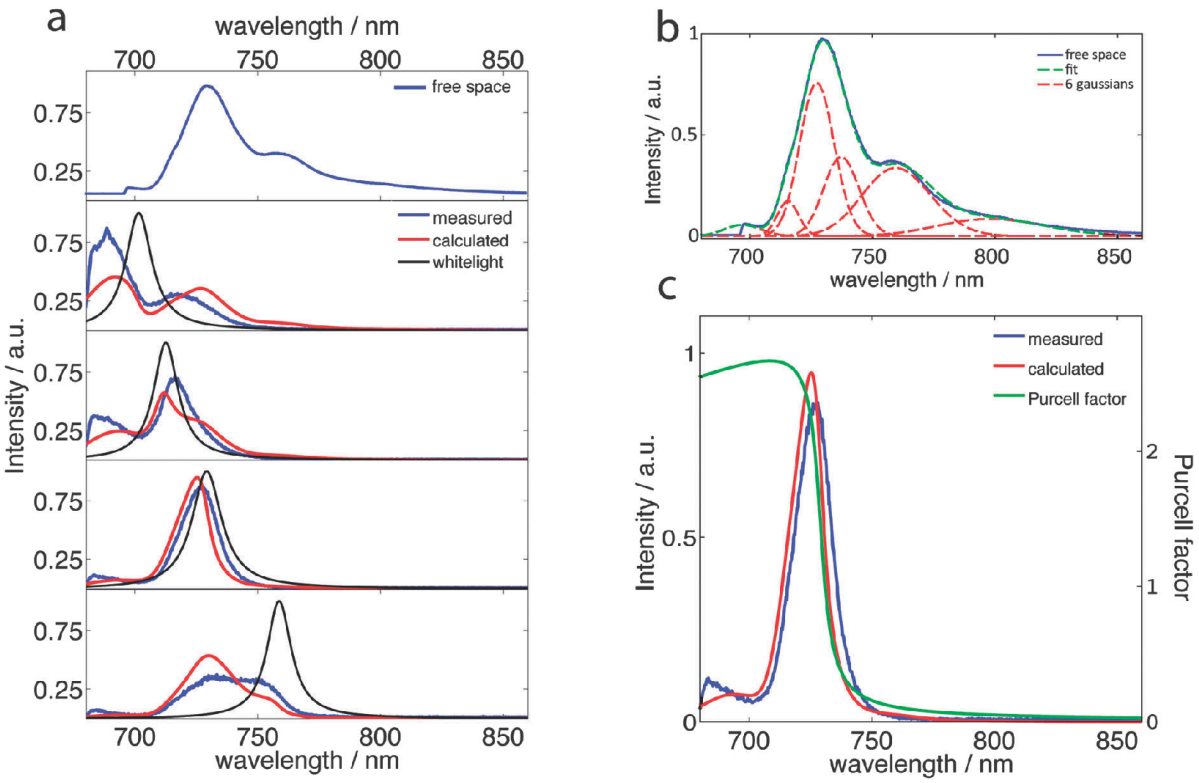

Fig. 3 (a) Four measured (blue curves) and calculated (red curves) fluorescence spectra of PSI placed inside the microresonator at different cavity lengths. The white light transmission (black curves) shows their resonance wavelengths at 702, 712, 730, and 759 nm. On top, the free-space fluorescence spectrum of PSI trimers from *A. platensis* is given (the drop down of the intensity at <695 nm is due to the longpass filter used). (b) The free space spectrum of PSI from *A. platensis* (blue curve) together with a fit (green dotted curve) based on six individual Gaussian functions (red dotted curves), the details are given in the text and in Table 1. (c) One selected set of measured (blue curves) and calculated spectrum (red curves) in combination with the Purcell factor (green curve) as given in ref. 33 and the ESI.†

Table 1 Comparison of parameters resulting from a fit of the free-space emission spectrum of PSI trimers from *A. platensis* with wavelength positions of fluorescent pools reported in the literature

Gaussian	Wavelength/nm	Width/nm	Pool
1	697	21	F699[32]
2	715	12	F714[26]
3	727	20	F726[25,26]
4	737	20	F731[25]
5	759	39	F760[26]
6	798	62	—

side angular distribution modes are still able to couple with emitters to enhance their radiative rate, visible in Fig. 3c by the shown Purcell factor distribution.[33] We claim that the influences on PSI resulting in the shown spectra are on the one hand determined by the spectral shaping of the Purcell factor and on the other hand by altered transfer dynamics, depending on changed population/depopulation rates.

To highlight the pure contribution caused by modifications within the transfer dynamics we simulated the emission spectrum of PSI inside the cavity without assuming any coupling between the emitting pools and compared these simulations with the experiment. The method for simulating the cavity influenced spectra is based on ref. 7. The main concept is grounded on the assumption that the spectral band and its overall intensity are proportional to the fluorescence quantum yield and the population probability of its corresponding emitter. In a cavity, the radiative rate is altered leading to a changed intensity of the band. Also the shape of the spectral band is changed due to the spectral shape of the cavity mode distribution. Therefore, the characteristic spectral distribution of the Purcell factor enables enhancing or suppressing and addressing of single emitting bands inside a composite spectrum. For this purpose the single spectral bands of the free-space PSI spectrum are characterized by Gaussian fits (see Fig. 3b). Five Gaussian contributions, centered at 697, 715, 727, 737 and 760 nm, are used with wavelength positions and widths in agreement with the recently reported positions of the red-emitting states, for details, see ref. 25, 26 and 32. A sixth contribution at 798 nm is not reported for PSI in the literature up to now, but the contribution is necessary to reconstruct the emission profile properly. The spectral position and the width of all six contributions together with the assigned red Chls are summarized in Table 1.

Each Gaussian is overlapped with the corresponding Purcell factor distribution for each corresponding resonance wavelengths. The spectral distribution of the Purcell factors was calculated by using ref. 33. Finally the six single shaped Gaussians were summed up again and scaled to same integral intensity as the corresponding measured spectrum to make their comparison feasible. A more detailed description is given in the ESI.†

Fig. 3a and c show experimental (blue) and simulated spectra (red) at various resonance wavelengths. Each experimental spectrum differs from its corresponding simulation with various degrees within various spectral regions, indicating the additional effect of disturbed transfer pathways inside PSI. Fig. 4a and b show the complete fluorescence spectral series of experimental (a) and calculated (b) spectra for resonance wavelengths between 697 and 850 nm (white circles). Comparing (a) and (b) it can be seen that the simulations of the uncoupled system differ slightly for specific wavelength ranges from the experiment. To highlight these specific differences between coupled and uncoupled systems the simulated series was subtracted from the experimental series, whose result is shown in Fig. 4c. This series now shows the fluorescence enhancement/inhibition (violet/red), depending on wavelengths and cavity lengths, of the coupled system compared to the uncoupled system. Red colors show less fluorescence to the simulation, meaning a lowered population of these emitting pools, while violet and blue show more fluorescence, meaning an increased population of these emitting pools. Positive values

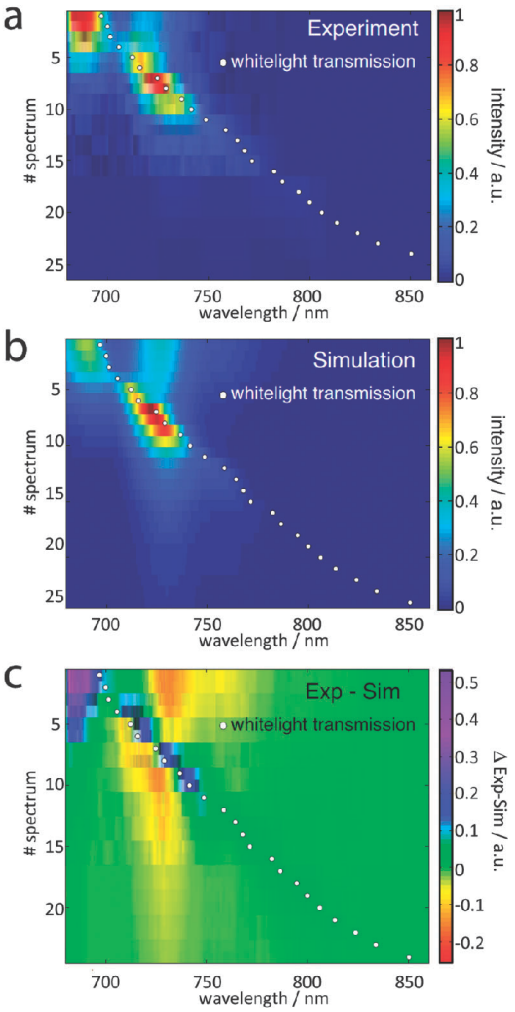

Fig. 4 (a) Contour plot of a fluorescence spectral series of experimental data taken from a scan of the resonance wavelength of the resonator over the emission profile of PSI from *A. platensis*. The resonance wavelength of the resonator is given by white dots; it varies between 697 nm and 850 nm. (b) Contour plot of a fluorescence spectral series of the calculated spectra based on the conditions given in (a) and without respect to coupling between the emitters. (c) Contour plot showing the difference between the plots given in (a) and (b) revealing the cavity induced modifications in the energy transfer dynamics. Violet means more emission, red less emission of the coupled to the uncoupled system.

can be observed for the first five spectra in the region at ~690 nm and for spectra with number 3–10 close to their resonance wavelengths. Negative values are observed for almost all spectra in the wavelength range close to the emission maximum of PSI.

The specific effects of alterations of the process rates in PSI can be seen in Fig. 4 and are schematically visualized in Fig. 5. Spectra with resonances <720 nm show increased intensity at wavelengths around 690 nm. This enhanced fluorescence indicates a deactivation of states, which show virtually no fluorescence emission in the absence of the resonator. This can be explained by an increased residence time of excitons at these emitters and therefore an inhibited transfer to chromophores with lower energies. Also the off-resonant (longer wavelengths than transmission maximum) emitters are inhibited in their radiative deactivation leading to increased saturation than to free space. The spectra with resonances >750 nm show lowered intensity for all emitting pools, mostly for Chls emitting at around 730 nm. This can be explained by the enhanced deactivation of all fluorescent Chls because of the flattened flank of the Purcell factor to short wavelengths. Therefore a lowered excitonic population probability of these emitters induced by the resonator compared with the simulations can be assumed.

The most striking effects are found in the wavelength areas of the pools F699, F726 and F731 (see Table 1). In Fig. 5 this behavior is sketched for three different mirror spacings. On the left the modified spectra are shown (red) with the corresponding transmission spectra (gray) below the free-space spectrum on top. On the right the arrangement of the Chl, the emitting pools (see Table 1) and their deactivation rates are sketched by red arrows.

The specific arrangement and coupling of the chromophores in PSI is optimized for efficient excitation transfer to the reaction center.[34] The energy transfer efficiency between chromophores depends on the spectral overlap, distance, and orientation,[34,35] the individual relaxation properties and saturation effects of long-living states. This means, each Chl within the transfer chain features a characteristic time and probability of accepting, containing and transferring an exciton. By changing one or more Chl relaxation rates within PSI all other relaxation properties are influenced. Such cavity enhanced transfer efficiency changes have been shown already for two simple systems under ambient conditions: a two-chromophore model system[12] and the fluorescent protein DsRed.[6,11]

As a consequence, the field in the microresonator can change the specific and controllable exciton distribution within PSI by involving additional chromophores in excitation energy transfer[19,22,29] or by changing the evolution inside the energy transfer pathways by enhanced/inhibited population/depopulation of excited states. Fig. 4 also supports the assignment of the fluorescent pools according to Table 1. Obvious deviations between experiment and simulation are only found in wavelength regions corresponding to reported Chl pools.

Comparable effects on the fluorescence emission of different photosynthetic complexes were recently observed in the vicinity of plasmonic nanostructures.[20,22,29] Such effects on optical

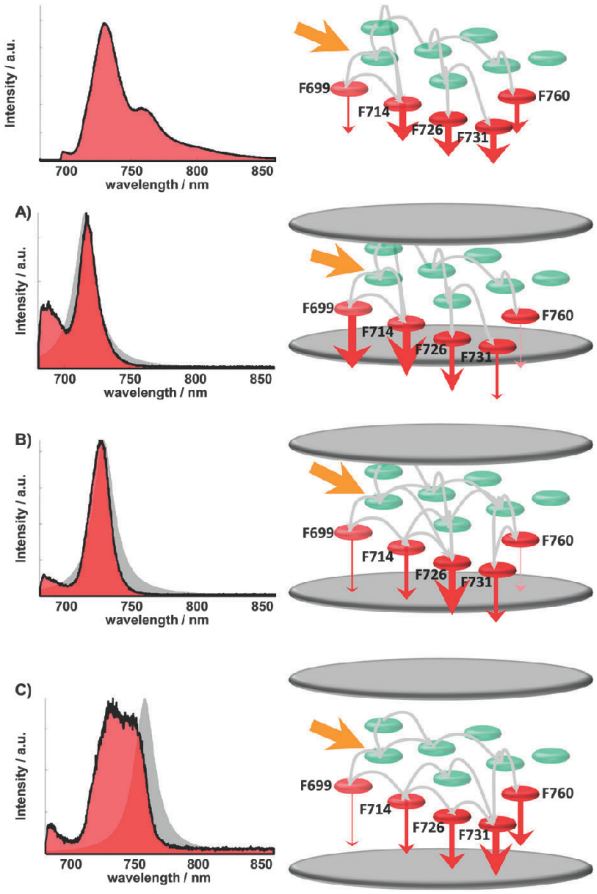

Fig. 5 Visualization of altered excitation energy transfer pathways in Photosystem I (exaggerated and simplified). From (A) to (C) the cavity length increases, noticeable by the spectral position of the white light transmission (grey area). The set of radiative transition rates and the population of the red states are modified by the additional mode density depending on mirror spacing. Changing the radiative rate (to free space) as a depopulation channel of a certain luminescent chlorophyll containing pool also alters the population dynamics of its corresponding transferring and receiving pools. The observed spectrum is a superposition of every single pool emission (see Table 1), depending on its population amount, the wavelength dependent resonator emission pattern and the radiative rate enhancement/inhibition. The altered spectrum enables therefore statements on the relative population probability of every luminescent pool. The altered occupations, indicated by Fig. 4, are visualized exemplarily on the right side by the thickness of the red arrows illustrating the emission intensity, together with the corresponding spectra (left, red area).

properties of chromophores are induced by the optical near-field of the nanostructures.[36,37] The interaction between pigments and the electric near-field of plasmonic nanostructures shows a strong distance- and orientation-dependence.[36,37] A fluorophore coupled to an Au nanosphere of 100 nm diameter shows within 13 nm a change from quenching to maximum enhancement,[36] this value is even smaller than the diameter of a PSI trimer (~20 nm). As a consequence, the effect of a plasmonic near field on the different Chls in one single protein complex can vary between quenching and maximal enhancement.[20,22,29] If one aims to control the optical properties of a protein complex by plasmonic nanostructures a precise positioning in the sub-nanometer regime is required and in

addition, the relative orientations must be controlled. As a consequence, studies to investigate the interaction of the electromagnetic fields produced by plasmonic nanostructures are hindered by these constraints. Optical microcavities, however, exhibit several advantages. The field distribution within a Fabry–Perot resonator is well defined by the distance between the mirrors and it changes only slightly over the dimension of a single protein ($\lambda/2$ *vs.* 20 nm for PSI); therefore the mode structure of the electric field at the position of the proteins can be determined directly from the transmission spectrum. This approach simplifies theoretical modeling of the decoherence induced by the mode structure and provides further insights into coherent or incoherent parts of the transfer. Another advantage compared to metallic nanostructures lies in the possibility to exclude chemical interactions with the protein complexes. The protein structure can be altered or even denaturized upon direct contact with metal surfaces.[38,39] Thus, in experiments with proteins close to metal surfaces or structures one can never be sure to gather information on native states. The volume of the microcavity is comparably large and a spacing layer of SiO_2 covering the silver surfaces prevents interactions completely. Therefore, chemical interactions by the field enhancing geometry on luminescent proteins can be excluded in the reported experiments. In principle, all pigment–proteins can be investigated by the resonator production and sample transfer[40] method presented here.

3 Experimental section

A schematic along with a detailed description of the manufacturing process of low temperature cavities and the confocal microscope used for efficient excitation and detection of the emission of PSI in the microresonator are given in the ESI.†

In short, the microcavity consists of two silver mirrors one being planar and one being slightly curved such that the gap between the mirrors slowly increases with increasing distance from the center, shown in Fig. 2. The cavity mirrors were fabricated by coating quartz substrates with several layers. The first layer is made of 1 nm chromium, followed by a silver layer (60 nm bottom and 30 nm top mirror), a 1 nm gold layer that is finally covered by a 30 nm SiO_2 layer, which acts as a spacer between the proteins and the silver surface. Their reflectivity was determined by transmission spectroscopy to be 0.95 (bottom) and 0.90 (top) @ 700 nm.

On one of the coated glass substrates less than 1 μL of the PSI containing sample solution was placed and then covered by a second coated glass substrate. This sandwich was transferred to the sample holder designed for our low temperature setup (for details see ref. 40). The sample holder is fixed on a stage for squeezing the mirrors together yielding a Fabry–Perot resonator showing concentric Newton rings in transmission indicating variable mirror distances and resonance conditions. The whole squeezer (including the sample holder and the sample) is then transferred into a Dewar flask filled with liquid nitrogen. The frozen sample solution acts as a glue holding the squeezed mirrors in position. A home-built sample transfer system[40] enables us to transfer the squeezed resonator into the cold cryostat (4.2 K) without temperature increase during handling and transfer. After mounting the sample inside the cryostat, the temperature is lowered to 1.6 K.

The wavelength of the cavity mode perpendicular to the mirror surfaces was determined from the white light transmission spectrum (see Fig. S2 and S4 in the ESI†). The design of our low temperature microresonator results in a quality factor of ~60 (fwhm ~ 15 nm in the transmission spectrum at 1.6 K), which is several times smaller than the full width at half maximum of the emission spectrum of PSI trimers from *A. platensis*. All fluorescence measurements were done with cw-excitation at 665 nm.

4 Conclusion

In conclusion, our experiments show an altered fluorescence emission of PSI in an optical microresonator with subwavelength dimensions. Comparing the experimental data with simulations assuming uncoupled emitters provides the intensity changes caused by altered energy transfer pathways. Particularly chlorophyll molecules with site-energies close to that of the reaction center undergo much stronger deactivation through fluorescence emission as the uncoupled model, indicating an increased presence probability of excitons. We suppose that altered responses can generally be expected for multichromophore coupled systems in any resonate optical structure. The mode density can be changed by microcavities in a defined manner in a very simple way. Any structural distortion or denaturation of the proteins by the metallic surfaces in our experiments can be ruled out. Therefore, optical microresonators are superior to plasmonic nanostructures for studying the influence of optical fields on any kind of luminescent particles.

Acknowledgements

Financial support from the German Research Council (DFG) for ME1600/13-1 and Heisenberg-Programm (BR 4102/1-1 and BR 4102/2-1), the Russian Academy of Sciences, program MCB and RFBR (Grant 14-04-00148a, to N.V.K.) is gratefully acknowledged.

References

1 K. J. Vahala, *Nature*, 2003, **424**, 839–846.
2 E. M. Purcell, *Phys. Rev.*, 1946, **69**, 681.
3 E. Fermi, *Rev. Mod. Phys.*, 1932, **4**, 88–132.
4 M. Steiner, F. Schleifenbaum, C. Stupperich, A. V. Failla, A. Hartschuh and A. J. Meixner, *J. Lumin.*, 2006, **119**, 167–172.
5 M. Steiner, A. V. Failla, A. Hartschuh, F. Schleifenbaum, C. Stupperich and A. J. Meixner, *New J. Phys.*, 2008, **10**, 123017.
6 S. Bar, A. Chizhik, R. Gutbrod, F. Schleifenbaum, A. Chizhik and A. J. Meixner, *Anal. Bioanal. Chem.*, 2010, **396**, 3–14.
7 A. I. Chizhik, A. M. Chizhik, A. M. Kern, T. Schmidt, K. Potrick, F. Huisken and A. J. Meixner, *Phys. Rev. Lett.*, 2012, **109**, 223902.

8 D. Englund, D. Fattal, E. Waks, G. Solomon, B. Zhang, T. Nakaoka, Y. Arakawa, Y. Yamamoto and J. Vuckovic, *Phys. Rev. Lett.*, 2005, **95**, 013904.
9 T. Aoki, B. Dayan, E. Wilcut, W. P. Bowen, A. S. Parkins, T. J. Kippenberg, K. J. Vahala and H. J. Kimble, *Nature*, 2006, **443**, 671–674.
10 S. Schietinger, T. Schroder and O. Benson, *Nano Lett.*, 2008, **8**, 3911–3915.
11 F. Schleifenbaum, K. Elgass, M. Steiner, J. Enderlein, S. Peter and A. Meixner, *Proc. SPIE*, 2009, **7185**, 718504.
12 P. Andrew and W. L. Barnes, *Science*, 2000, **290**, 785–788.
13 R. A. Grimme, C. E. Lubner, D. A. Bryant and J. H. Golbeck, *J. Am. Chem. Soc.*, 2008, **130**, 6308–6309.
14 C. E. Lubner, R. Grimme, D. A. Bryant and J. H. Golbeck, *Biochemistry*, 2010, **49**, 404–414.
15 A. Mershin, K. Matsumoto, L. Kaiser, D. Yu, M. Vaughn, M. K. Nazeeruddin, B. D. Bruce, M. Graetzel and S. Zhang, *Sci. Rep.*, 2012, **2**, 234.
16 L. Frolov, Y. Rosenwaks, C. Carmeli and I. Carmeli, *Adv. Mater.*, 2005, **17**, 2434–2437.
17 A. O. Govorov and I. Carmeli, *Nano Lett.*, 2007, **7**, 620–625.
18 I. Carmeli, I. Lieberman, L. Kraversky, Z. Fan, A. O. Govorov, G. Markovich and S. Richter, *Nano Lett.*, 2010, **10**, 2069–2074.
19 J. B. Nieder, PhD thesis, Freie Universitaet Berlin, Germany, 2011.
20 S. R. Beyer, S. Ullrich, S. Kudera, A. T. Gardiner, R. J. Cogdell and J. Koehler, *Nano Lett.*, 2011, **11**, 4897–4901.
21 H. Toporik, I. Carmeli, I. Volotsenko, M. Molotskii, Y. Rosenwaks, C. Carmeli and N. Nelson, *Adv. Mater.*, 2012, **24**, 2988–2991.
22 M. Brecht, M. Hussels, J. B. Nieder, H. Fang and C. Elsässer, *Chem. Phys.*, 2012, **406**, 15–20.
23 B. Gobets and R. van Grondelle, *Biochim. Biophys. Acta*, 2001, **1507**, 80–99.
24 P. Fromme, P. Jordan and N. Krauss, *Biochim. Biophys. Acta, Bioenerg.*, 2001, **1507**, 5–31.
25 E. Schlodder, M. Hussels, M. Cetin, N. V. Karapetyan and M. Brecht, *Biochim. Biophys. Acta*, 2011, **1807**, 1423–1431.
26 M. Brecht, M. Hussels, E. Schlodder and N. V. Karapetyan, *Biochim. Biophys. Acta, Bioenerg.*, 2012, **1817**, 445–452.
27 A. N. Melkozernov, *Photosynth. Res.*, 2001, **70**, 129–153.
28 N. V. Karapetyan, E. Schlodder, R. van Grondelle and J. P. Dekker, *Photosystem I: The Light-Driven Plastocyanin: Ferredoxin Oxidoreductase*, Advances in Photosynthesis and Respiration, Springer, 2006, vol. 24.
29 J. B. Nieder, R. Bittl and M. Brecht, *Angew. Chem., Int. Ed.*, 2010, **49**, 10217–10220.
30 B. Gobets, I. H. M. van Stokkum, M. Rogner, J. Kruip, E. Schlodder, N. V. Karapetyan, J. P. Dekker and R. van Grondelle, *Biophys. J.*, 2001, **81**, 407–424.
31 B. Gobets, I. H. M. van Stokkum, F. van Mourik, J. P. Dekker and R. van Grondelle, *Biophys. J.*, 2003, **85**, 3883–3898.
32 M. Brecht, V. Radics, J. B. Nieder, H. Studier and R. Bittl, *Biochemistry*, 2008, **47**, 5536–5543.
33 G. Bjork, *IEEE J. Quantum Electron.*, 1994, **30**, 2314–2318.
34 M. Byrdin, P. Jordan, N. Krauss, P. Fromme, D. Stehlik and E. Schlodder, *Biophys. J.*, 2002, **83**, 433–457.
35 M. Yang, A. Damjanovic, H. M. Vaswani and G. R. Fleming, *Biophys. J.*, 2003, **85**, 140–158.
36 P. Anger, P. Bharadwaj and L. Novotny, *Phys. Rev. Lett.*, 2006, **96**, 113002.
37 A. M. Kern, A. J. Meixner and O. J. F. Martin, *ACS Nano*, 2012, **6**, 9828–9836.
38 L. Shang, Y. Z. Wang, J. G. Jiang and S. J. Dong, *Langmuir*, 2007, **23**, 2714–2721.
39 S. Chah, M. R. Hammond and R. N. Zare, *Chem. Biol.*, 2005, **12**, 323–328.
40 M. Hussels, A. Konrad and M. Brecht, *Rev. Sci. Instrum.*, 2012, **83**, 123706.

Manipulating the excitation transfer in Photosystem I by a Fabry-Perot metal resonator with optical subwavelength dimensions

Alexander Konrad,[a] Anna-Lisa Trost,[a] Sepideh Skandary,[a] Martin Hussels,[a] Alfred J. Meixner,[a] Navasard V. Karapetyan,[b] and Marc Brecht*[a,c]

[a] *Universität Tübingen, Institut für Physikalische und Theoretische Chemie, Auf der Morgenstelle 18, 72076 Tübingen, Germany. Fax: +49-7071-29-5490 ; Tel: +49-7071-29-76239; E-mail: marc.brecht@uni-tuebingen.de*
[b] *A.N. Bakh Institute of Biochemistry, Russian Academy of Sciences, Leninsky Prospect, 33, 119071 Moscow, Russia.*
[c] *Zürcher Hochschule für Angewandte Wissenschaften, Institute of Applied Mathematics and Physics, Technikumstrasse 13, 8401 Winterthur, Switzerland.*

1 Supplementary Materials

1.1 Cavity preparation

The mirrors of the resonator are composed of multiple layers deposited on 4 × 4 mm (thickness 200 μm) quartz substrate. The order of the layers is: 1 nm Cr, 30 nm (upper mirror)/60 nm Ag (lower mirror), 1 nm Au, and finally 30 nm SiO_2 (Figure 1). The final SiO_2 layer is used to exclude conformational changes

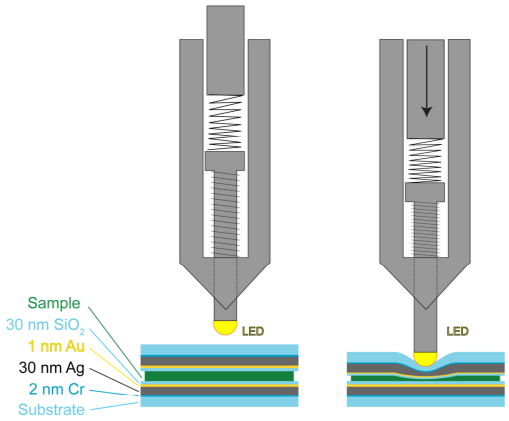

Figure 1 Scheme showing the squeezing mechanism. The cavities are formed by a sandwich of two mirrors coated with a multi-layer mirror. The squeezing is induced by a LED that is lowered (right). Note: For clarity the deformation of the upper mirror is overstated. A spring ensures that the force on the mirrors is only slightly increased.

or degradation of Photosystem I induced by contact with the metal mirrors. The layers were prepared by vapor deposition onto the quartz substrate using an electron-beam source (EB3, Edwards) under high-vacuum conditions (≈10^{-6} mbar). The film thickness was monitored during vapor deposition using an oscillating quartz unit (FTM7, Edwards) and verified by atomic force microscopy (AFM) measurements. On top of one of the mirrors less than 1μL of the sample solution (see below) was placed and then covered by the second mirror (Figure 1). This sandwich was then transfered to the sample holder designed for our low temperature transfer system (for details see Ref.[1]). This holder is fixed on the base plate of a squeezer used to produce λ/2-cavities. As shown in Figure 1, the LED is lowered to squeeze the upper mirror onto the lower mirror. The squeezing mechanism contains a spring that ensures only a slight increase of the force on the mirror during squeezing. Using a LED for squeezing features special advantages, because the curvature of the LED head can be varied to meet the requirement of the cavities and in addition, the LED serves as light source to control the formation of the Newton rings in transmission.

Figure 2a shows the side view of the squeezer constructed for the experiments. In Figure 2b, the top view of the squeezer is shown; the formation of the Newton ring pattern can be directly observed in the middle of the squeezer. Figure 2c shows a magnified image of the formed Newton ring pattern. When the inner Netwon rings belong to the first order (optical mirror distance λ/2) the squeezing process is stopped, the LED is turned off and the whole setup is plunged into a vessel filled with liquid nitrogen. The assignment of the interference orders can be done by white light transmission spectra of the resonator under a confocal microscope to determine the interference order depending on the free spectral range.

By freezing, the sample solution acts as glue holding the mirrors in the squeezed position together. The advantage of the described process is that optical glues can be avoided. This is of special advantage for biological samples, because standard sample solutions like buffer/glycerol mixtures for low temperature optical experiments can be used and the proteins are not exposed to optical glues that might damaged or at least modify the proteins. Using a home built sample transfer system enables (for details see Ref.[2]) us to transfer the squeezed sample into the cold cryostat (4.2 K) without temperature changes during handling. After mounting the sample inside the cryostat the temperature is lowered to 1.6 K.

The optical length of the cavity was determined by the white light transmission spectra as shown in Figure 3. The design

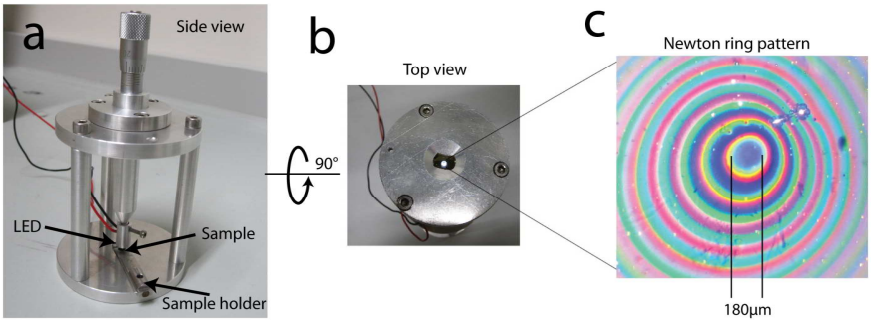

Figure 2 Squeezer for squeezing optical microcavities. (a) Side view of the squeezer. The sample holder is fixed by a screw on the base plate of the squeezer. By turning the micrometer screw, the head of the LED is lowered and squeezes the cavity. (b) Top view on the squeezer, by turning the LED on, the white light transmission through the cavity can be seen. Due to the good visibility of the Newton ring patter, the first order can be very easily adjusted with this setup. (c) Magnification of the Newton ring pattern. The inner transmission ring shows the first order of interference; here the diameter of the first order is ≈180 μm.

of our low temperature microresonator results in a mean cavity quality factor of Q ∼60 at 1.6 K, compared to Q factors of ∼30 at ambient conditions.

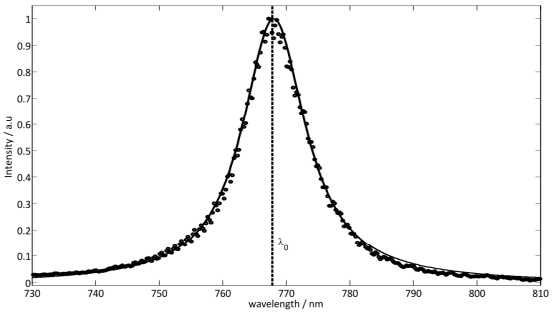

Figure 3 Microcavity white light transmission spectrum (○) fitted by a Lorentzian function (–). Resonance frequency λ_0 = 768 nm, line width 12 nm, Q = 63.

1.2 Purcell effect

According to Fermi's golden rule, the spontaneous emission rate of a two-level system depends on both, the transition dipole moment between the states and the density of modes of the electromagnetic field inside the cavity[3].

$$\Gamma_{spE} = \frac{1}{\tau_{spE}} = \frac{2\pi}{h^2} \left| \langle | \hat{\mu} \cdot \hat{E}^{+}_{cav} | \rangle \right|^2 \rho_{cav}(\omega) \qquad (1)$$

Where τ_{spE} is the lifetime of the spontaneous emission, $\hat{\mu}$ is the dipole moment of the emitter, $\hat{E}_{cav}$ is the unit-vector of the electric field of the mode with frequency ω and ρ_{cav} is the local photonic mode density of the electromagnetic field.
Dipole-like emitters undergo according to the present mode structure an enhanced or inhibited radiative relaxation. The mode structure and the subsequent modified radiative rate can be calculated according to Bjork[4]:

$$P(\lambda,L) = \Gamma_{sp}(\lambda,L)/\Gamma_{sp0} = \frac{3}{4}\int_0^{\pi/2} d\theta sin(\theta) \times \frac{(1-R)[1+R-2\sqrt{R}cos(kLcos(\theta))][1+cos^2(\theta)]}{(1-R)^2+4Rsin^2(kLcos(\theta))}. \qquad (2)$$

Here, R are the reflectivities of the resonator mirrors, Γ_{sp0} the free space radiative rate, θ is the angle of the emission due to the perpendicular axis of the plane mirrors, L is the length of the cavity in the simplified resonance condition $L = m\lambda/2$ and $k = 2\pi/\lambda$ with λ as the transmitted wavelength and m as the number of the interference order. The enhancement/inhibition factor (Purcell factor) of Γ_{sp} mirroring the wavelength depending mode distribution for a distinct cavity length.
For simulating the spectrum of an emitter *i* inside a given mode structure with Purcell factor $P(\lambda,L)$, the spectral band is here approximated to a Gaussian curve $\mathscr{G}_i(\lambda)$ with height A_i, peak position λ_0 and peak width w. Figure4a shows six Gaussians describing the free space spectrum of PSI from *A. platensis*, Figure4b the Purcell factor as green line for a transmission maximum of ∼740 nm. It can be seen, that on the short-wavelength side also off-axis modes with increasing θ contribute. The used objective lens (NA = 0.85) collects a variety of angular distributed resonator modes showing also off-axis emission components in the blue spectral range. For the modified spectrum $\mathscr{G}'_i(\lambda)$ the changed height $A^*_i(L)$ can be calcu-

lated by:

$$A_i^*(L) = A_i \int \mathscr{G}_i(\lambda) P(\lambda, L). \quad (3)$$

The new Gaussian $\mathscr{G}'_i$ is therefore given by:

$$\mathscr{G}'_i(\lambda, L) = A_i^*(L) e^{-(\frac{\lambda-\lambda_{0_i}}{0.5w})^2}. \quad (4)$$

Finally, the asymmetry of the Purcell factor has to be considered and all j Gaussians have to be summed up. The resulting spectrum is therefore:

$$\mathscr{G}^*(\lambda, L) - \sum_j A_i^*(L) \frac{\mathscr{G}'_i(\lambda, L) P(\lambda, L)}{\int \mathscr{G}'_i(\lambda, L) P(\lambda, L) d\lambda}. \quad (5)$$

One example spectrum is given in Figure 4b as red line. The blue line shows the measured spectrum including modifications by altered transfer dynamics inside PSI.

1.3 Confocal spectroscopy and imaging setup

Figure 5 shows the setup of our home-built confocal microscope. The microscope is mounted on a damped optical table (Opta). During measurement the sample and the microscope objective (Mikrothek 60× NA= 0.85) are immersed in liquid Helium inside a bath-cryostat (SVT-200, Janis). Temperatures below 4.2 K are generated by pumping the Helium gas with a Edwards TwoStage E2M80 combined with a Edwards EH250 booster pump. The temperature is measured close to the sample by a LakeShore Model 336 temperature controller equipped with a Cernox sensor (CX-1030-SD-HT 0.3L).
For excitation we use a fibre-coupled 665 nm *cw* diode-laser (iBEAM-660-3V2, TOPTICA Photonics). The laser is coupled into the setup using a dichroic mirror (ZQ670RDC, AHF Analysentechnik). The excitation light is then aligned along the optical axis of the microscope objective to get an optimal focus. The emitted light passes the dichroic mirror, a 30 μm pinhole, and a longpass filter (HQ 695 LP, AHF Analysentechnik) and then it can be detected by an APD (COUNT-100C, Laser Components) or a CCD-Camera (DU920P-PR-DD, Andor) mounted on a spectrograph (Shamrock 500, Andor) with 200 lines/mm and 400 lines/mm gratings. The different detectors for the emission light are selected by computer-controlled flip-mirrors. For data acquisition of the APD signals a National Instruments NI6601 counter board and a Becker & Hickl TCSPC-module (SPC-130) are used. The white light illumination is done by a white light LED. The head of the LED has a diameter of 3 mm, the radiation angle is 15°. The light of the LED is focussed on the cavity inside the cryostat by a 2″ lens with f = 60 mm as shown on the left of Figure 5.
The whole setup is controlled by a self-developed LabVIEW software. The software controls all components described above. The special aim of the software is to simplify the acquisition of high resolution spectroscopic data in fluorescence emission and white light transmission mode.

1.4 Photosystem I preparation

Trimeric Photosystem I complexes have been isolated from the cyanobacterium *A. platensis* according to Ref.[5]. Purified complexes at a concentration of about 200 μM Chl were stored in 50 mM Tris-HCl buffer (pH 8.0) and 0.08 mM (0.04% w/v) detergent n-dodecyl β-D-maltoside (Sigma) at -80 °C. For fluorescence measurements, the sample was diluted in buffer solution containing 20 mM Tricine, 25 mM $MgCl_2$ and 0.4 mM (0.02% w/v) detergent n-dodecyl β-D-maltoside (Sigma) and 5 mM sodium ascorbate for prereduction of P700 to a concentration of about 20 μM Chl. In further steps the sample was further diluted in buffer solution. In a last step glycerol was added (66% glycerol w/w). Sample preparation was carried out under indirect daylight. Several seconds before plunging the sample in liquid nitrogen, the LED used for squeezing was switched off. Due to preparation, the low temperature and the used excitation intensity, PSI is most of the time in the oxidized P700 state; for further details see Refs.[6,7]

References

[1] M. Hussels, A. Konrad and M. Brecht, *Review of Scientific Instruments*, 2012, **83**, 123706.

[2] M. Hussels, J. B. Nieder, C. Elssser and M. Brecht, *Acta Physica Polonica A*, 2012, **122**, 269–274.

[3] E. Fermi, *Rev. Mod. Phys.*, 1932, **4**, 88–132.

[4] G. Bjork, *IEEE Journal of Quantum Electronics*, 1994, **30**, 2314–2318.

[5] E. Schlodder, M. Cetin, M. Byrdin, I. V. Terekhova and N. V. Karapetyan, *Biochimica et Biophysica Acta*, 2005, **1706**, 53–67.

[6] E. Schlodder, M. Hussels, M. Cetin, N. V. Karapetyan and M. Brecht, *Biochimica et biophysica Acta*, 2011, **1807**, 1423–31.

[7] M. Brecht, M. Hussels, J. B. Nieder, H. Fang and C. Elsässer, *Chem. Phys.*, 2012, **406**, 15 – 20.

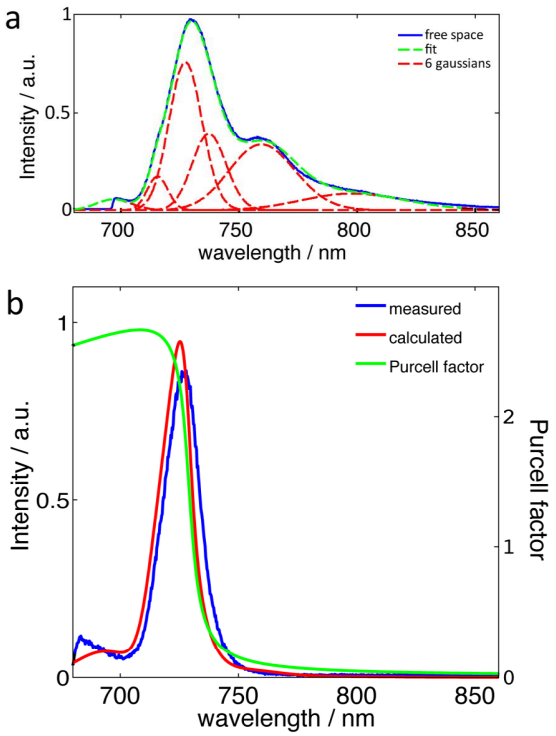

Figure 4 a) Free space spectrum of PSI from *A. platensis* (blue curve) together with a fit (green dotted curve) based on six individual Gaussian functions (red dotted curves). b) Calculated Purcell factor (green) by Eq.2 for transmission maximum of 740 nm. Also shown in red the calculated spectrum for the six Gaussians a) by Eq.3-4 and in blue the corresponding measured spectrum.

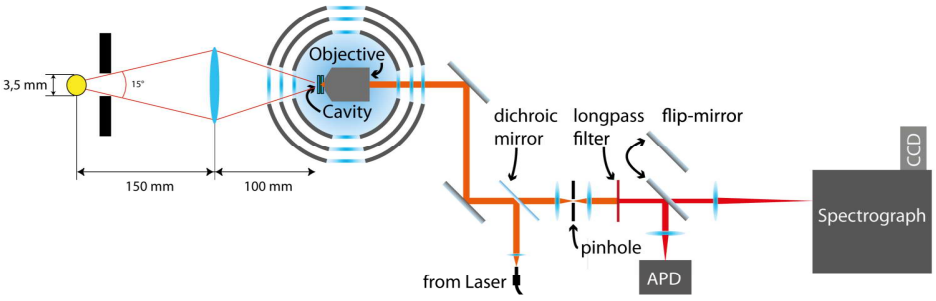

Figure 5 Scheme of the setup used for low temperature confocal spectroscopy and imaging. The details of the setup are given in the text. On the left side of the cryostat a white light LED is mounted. The light of the LED is focussed onto the cavity/sample by a 2″lens. In this arrangement the fluorescence and the white light transmission spectra can be recored by the same optical path.

Chapter 13

Temperature Dependent Luminescence and Dephasing of Gold Nanorods

In this chapter the long-wavelength one-photon luminescence band of single gold nanorods recorded in the temperature range from 1.6 to 295 K by confocal microscopy is examined. The long-wavelength band of these gold rods is associated to the long-wavelength band of white light scattering spectra, which both are suggested to correspond to the long-axis plasmon mode. Due to the assumption that a plasmon can be described by a Lorentzian oscillation the homogeneous linewidth of a spectral band of a radiative decaying plasmon directly corresponds to its dephasing time. Additionally, assuming that the luminescence of the long-wavelength band is originated directly by a plasmon the dephasing times can be simulated as a function of temperature by a Debye model for solid metals. The main contributions to the dephasing mechanisms are hence electron-phonon scattering, electron-electron scattering, electron-surface scattering and radiative damping. It can be seen that the spectral linewidths of the luminescence bands increase with temperature according to the simulation based on the Debye model.

This chapter is based on:
Konrad, A., Wackenhut, F., Hussels, M., Meixner, A.J., Brecht, M. "Temperature Dependent Luminescence and Dephasing of Gold Nanorods" *The Journal of Physical Chemistry C*, **2013**, *117*, 21476-21482.

THE JOURNAL OF PHYSICAL CHEMISTRY C

Article

pubs.acs.org/JPCC

Temperature Dependent Luminescence and Dephasing of Gold Nanorods

Alexander Konrad, Frank Wackenhut, Martin Hussels, Alfred J. Meixner,* and Marc Brecht*

University of Tübingen, IPTC, Auf der Morgenstelle 18, 72076 Tübingen, Germany

ABSTRACT: In this study we demonstrate the impact of temperature on the luminescence emission of plasmonic nanoparticles. We examine the optical properties of single gold nanorods (GNRs) in the temperature range 1.6−295 K by confocal microscopy. Decreasing temperature leads to a reduction of the full width at half-maximum (fwhm) of the luminescence spectra, thus we can conclude that the damping of the plasmonic oscillation is strongly reduced. The main contribution to the dephasing mechanism is electron−phonon scattering and we are able to determine its contribution to the dephasing using quantitative simulations, which can describe the temperature dependent dephasing of plasmonic nanoparticles.

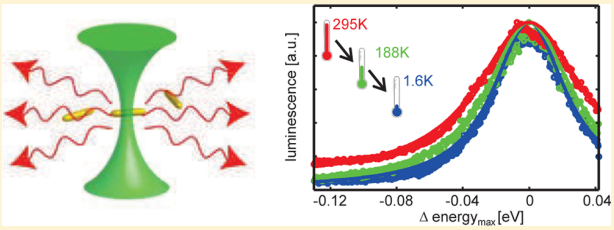

INTRODUCTION

Noble metal nanoparticles, e.g., of gold, are used in a variety of aspects: for example, as markers in cells[1] or as antennas for enhancing or exciting luminescence of other particles or molecules like proteins[2] (for reviews, see refs 3,4). The optical properties of these particles are dominated by so-called particle plasmons, i.e., a collective oscillation of the conduction band electrons. Such plasmonic particles exhibit a strong interaction with light when excited close to the plasmon resonance, leading to large scattering cross sections.[4] They are thus easily observable and many experiments deal with their scattering properties[5,6] which can be described and understood theoretically by models like the Mie-Gans Theory.[7]

The plasmonic properties also give rise to the so-called antenna effect which leads to highly enhanced local electric fields close to the surface of the particle.[8,9] Another effect of plasmonic structures and particles is the occurrence of luminescence after absorption of light.[10] The mechanism of their photoluminescence is a field of numerous studies because this effect gives deep insight into the physics of plasmonic particles and the interaction with their environment, but is not yet completely understood.[11]

Since the first observation of this phenomenon by Mooradian in 1969,[10] there have been several theoretical and experimental attempts to describe the photoluminescence of gold nanoparticles. For a general overview, the favored models are an energy transfer[5,12,13] and a field enhancement model.[14−16]

According to the most discussed models in literature, the origin of the one-photon luminescence signal is either a decaying plasmon itself or based on a recombination of electron−hole pairs,[12] which is triggered by a plasmon. Currently, it is supposed,[17] for rod shaped particles with two resonances, that the excited plasmon of the short axis generates an electron−hole pair, which creates a second plasmon, decaying radiatively. Such a mechanism would explain why scattering and luminescence spectra are very similar in energy and shape, because both phenomena have the same origin.

The knowledge of how photons are generated and the evolution time of a decaying plasmon are required for tailoring and optimizing systems with interactions on other particles. Measurements of this time evolution, which would give additional information about the origin of the luminescence, are difficult because of the short lifetime of plasmons, which is in the range of a few femtoseconds.[18] The underlying mechanisms and processes of the plasmon decay and damping are thus not completely assigned yet.[19] The total dephasing rate, however, can be measured by the full width of half-maximum (fwhm) of the scattering or the luminescence signals, assuming a simple damped harmonic oscillator model leading to homogeneous broadening, combined with macroscopic and nanoscopic solid state physics.[20] For now, there are several theoretical and experimental attempts to determine the underlying mechanisms and processes of a decaying plasmon quantitatively for scattering spectra[21,22] by changing decay mechanism dependent parameters like temperature or geometry, but not yet for luminescence spectra which may show certain differences and similarities between both phenomena and might explain the origin of the luminescence.

Many studies on luminescent nanoparticles were done by using nanorods, because rod-shaped particles of a few nanometers in length and width show an observable amount of luminescence and quantum yield that is larger than in other noble nanoparticles.[11,17] Gold nanorods (GNRs) are often used for determining luminescence properties independent of shape and size. By now, the correlation between the plasmon energy and the geometry of the particle is well understood from studies of the of scattering and luminescence spectra.[23,24] In

Received: July 19, 2013
Revised: September 4, 2013
Published: September 10, 2013

this article, we present the first measurements of the one-photon luminescence signal of plasmonic particles as a function of temperature. This was done by exciting the long axis plasmon of single GNRs and observing the response by confocal microscopy and spectroscopy at various temperatures ranging from 1.6 to 295 K. By taking spectra and determining the particle plasmon resonance frequencies and widths of their luminescence signals, the temperature dependent dephasing mechanisms can be assigned using theoretical models. The temperature dependency of the determined dephasing rates can give insight into the physical processes leading to the luminescence signal and provides for further experiments the theoretical knowledge by simulations to determine intrinsic optical parameters of the nanoparticles. Therefore, we provide a complete set for simulating the fwhm of homogeneous broadened luminescence spectra for variable particle geometries and temperatures.

EXPERIMENTAL AND THEORETICAL METHODS

Sample Preparation and Experimental Setup. According to the manufacturer, the GNRs (Nanopartz) have the following properties: LSPR = 780 nm; width = 10 nm; length = 38 nm; aspect ratio = 3.8; concentration = 2×10^{11} particles/mL. A droplet of suspension was deposited on a cleaned glass coverslip and the rods became attached and immobilized on the glass surface. After four minutes the droplet was removed by spin coating and only GNRs deposited on the glass surface remained,[25] mainly oriented parallel to the surface. This method allows us to prepare samples where the long axis of the GNRs is oriented parallel to the glass substrate. For room temperature measurements a droplet of water was put on the coverslip (22×22 mm^2) for increasing the refractive index. To ensure comparable conditions for the low temperature measurements a droplet of water was put on the prepared coverslip (4×4 mm^2). The optical measurements at room temperature were performed on a home-built confocal microscope with an objective (NA of 0.8; Edmund optics, 60× magnifications JIS) and a three axis scanning table (Physik Instrumente P-517.3CL, $100 \times 100 \times 20$ μm^3) for sample scanning measurements. For low temperature measurements, the sample was inserted into a He-bath cryostat (Janis) equipped with a home-built confocal microscope with an objective (NA of 0.8) and a multiaxis scanning stage (attocube). The samples were excited with a 1.86 eV (665 nm) cw diode laser (TOPTICA Photonics AG, iBeam-660) with a linear polarized Gaussian beam, and an excitation power of ∼10 μW. For further details about the low temperature microscope and the signal detection, the setup was described recently by Hussels et al.[26]

Theoretical Models. The assumption of the plasmonic origin of the one-photon luminescence signal of GNRs leads to the implication that the total decay rate of a plasmon can be determined, assuming a model of a damped harmonic oscillator for the electrons involved in the plasmon oscillation, by measuring the fwhm of the observed luminescence spectrum. The usage of this model requires the condition that only homogeneously broadened signals with a Lorentzian line shape and their fwhm are permitted for evaluation. The measured fwhm of the luminescence signals Γ_{tot} are assigned to the decay rate of the plasmon, which values Γ are given in eV. The total dephasing time τ can be calculated by the following equation: $T_2^{-1} = \Gamma_{tot} = 2\hbar/\tau$.

According to the literature, the main dephasing mechanisms with their amounting rates Γ_{mech} are due to scattering of the electrons at phonons (Γ_{e-ph}: electron−phonon scattering), the particle surface (Γ_{surf}: electron-surface scattering), with themselves (Γ_{e-e}: electron−electron scattering) and by radiative damping of the collective electron oscillation (Γ_{rad}).[27] The aim of this work is to divide the single contributions into their temperature dependent ($\Gamma_{temp}(T)$) and independent (Γ_0) parts and to compare them quantitatively with experimental data.

$$\Gamma_{tot} = \Gamma_{temp}(T) + \Gamma_0$$
$$\Gamma_{tot} = \Gamma_{e-ph}(T) + \Gamma_{surf} + \Gamma_{rad} + \Gamma_{e-e} \quad (1)$$

In the following we will discuss in detail the influence of the different factors on the total decay rate.

Electron−Phonon Scattering. The electrons in the conduction band, which cause the plasmon oscillation, can interact with occupied phonon modes of the particle and the matrix, causing the dephasing of the plasmon. Distortions of the particle structure by phonon emission causing significant changes in the particle geometry are only relevant for particles smaller than 1 nm.[28,29] The GNRs used here are rather large (length of 38 nm, aspect ratio 3.8 according to the manufacturer), thus only the macroscopic bulk contribution of the phonon coupling needs to be considered, which can be described using two macroscopic solid state models. We used these two models, which are presented in the following, to describe the temperature dependence of the electron−phonon coupling for temperatures below and above the Debye temperature of the material. The first model is a solid-state Debye model, which considers the partial occupation of phonon modes and is therefore used to determine $\Gamma_{e-ph}(T)$ for $T < \Theta_{Debye}$:[30]

$$\Gamma_{e-ph}(T) = \frac{\hbar}{\tau_0}\left[\frac{2}{5} + 4\left(\frac{T}{\Theta_{Debye}}\right)^5 \int_0^{\Theta_{Debye}/T} \frac{z^4}{e^z - 1}\,dz\right] \quad (2)$$

with $\tau_0 = 30$ fs,[22] $\Theta_{Debye} = 170$ K,[31] and $T < \Theta_{Debye}$, where τ_0 is a constant for the metal, consisting of the atomic density, the ion mass, the Debye temperature, the Fermi energy, the Fermi velocity, and the effective electron mass. Θ_{Debye} is the Debye temperature and T is the temperature; z mainly represents all possible phonon wave vectors smaller than the maximum wave vector. Therefore, the integral on the right side accounts for the temperature dependent occupation of phonon modes. The temperature independent part ($2\hbar/5\tau_0$) arises from spontaneous emission of phonons, which at 0 K is stimulated by zero-point fluctuations of the lattice.

Assuming a reasonable low surface roughness, the value of the Debye temperature can be regarded to be constant even when going to the nanoparticle scale.[32] Eq 2 is also only valid if the excitation and plasmon energies are above the thermal energy but below the Fermi energy of the material, because otherwise, interband transitions can occur, which would change the occupation of phonons and electrons. With this model the electron−phonon coupling reaches a constant minimum value of 8.8 meV for $T \leq 50$ K for gold.

For $T > \Theta_{Debye}$, the phonon coupling increases linearly with temperature because all phonon modes are occupied. With a

dx.doi.org/10.1021/jp407178u | J. Phys. Chem. C 2013, 117, 21476−21482

simple solid-state model for metals[31] a temperature dependent rate can be derived

$$\Gamma_{e-ph}(T) = \lambda\pi\frac{k_B T}{\hbar} \quad (3)$$

with the metal dependent constant λ, and the Boltzmann constant k_B. In the following the first ($T < \Theta_{Debye}$) is denoted as the low-temperature model and the second ($T > \Theta_{Debye}$) as the high-temperature model.

Electron−Surface Scattering. The scattering of plasmon electrons at the interface between the particle and the surrounding medium is a particle size and shape dependent dephasing mechanism,[33] which simply means that scattering at the particle surface becomes more probable for increasing surface area. Furthermore, the resonance frequency of plasmonic particles depends on their size and shape. Hence, the observable correlation between fwhm and spectral position of the emission maxima[18] of measured spectra can be explained by the surface scattering Γ_{surf}. The scattering rate in eV can be given by

$$\Gamma_{e-surf} = A\frac{\nu_F}{L_{eff}} \quad (4)$$

To calculate the effective path length L_{eff} we used the model of Coronado et al.:[6] $L_{eff} = 4V/S$ with V as the particle volume and S as the surface area. Parameter A is a phenomenological factor related to the geometry of the particle and ν_F is the metal dependent Fermi velocity ($\nu_F = 1.39 \times 10^{15}$ (nm/fs) for gold[6]). The A-factor differs with size and shape of the particles and is an important parameter regarding the field enhancement effect near plasmonic particles.

Electron−Electron Scattering. Another damping mechanism is the scattering of electrons on other electrons. The probability of electron−electron collisions is mainly depending on the distance between the electron energy and the Fermi level and therefore also on the distribution of electrons near the Fermi level.[34] The contribution of this mechanism was theoretically and experimentally studied by Parkins et.al.,[35] who assumed a simple Drude model to describe the electron−electron scattering depending on the squared photon energy:

$$\Gamma_{ee} = \frac{\pi^3\Sigma\Delta}{12\hbar E_F}\left[(k_B T)^2 + \left(\frac{\hbar\omega}{2\pi}\right)^2\right] \quad (5)$$

where Σ is the Fermi-surface average, Δ is the fractional umklapp scattering, and E_F is the Fermi energy. The term $k_B T$ represents the thermal energy which is overwhelmed by the photon energy $\hbar\omega/(2\pi)$; thus, the e−e scattering can be regarded to be temperature independent. This leads to the simplification

$$\Gamma_{ee} = \beta(\hbar\omega)^2 \quad (6)$$

Parkins et al.[35] calculated the β-value for gold to be 0.76×10^{13} s^{-1} eV^{-2}.

Radiative Damping. Another contribution to the total dephasing process is radiative damping, which also depends on size and shape of the particle. This mechanism was studied by several groups[18,36] and the corresponding decay rate can be given by

$$\Gamma_{rad} = \kappa V \quad (7)$$

with $\kappa = 4 \times 10^{-7}$ fs^{-1} nm^{-3},[18] where κ is an experimentally determined factor and V is the volume of the GNR.

Plasmon Energies. Electron-surface-scattering (eq 4), radiative damping (eq 7), and electron−electron scattering (eq 6, implicit by the resonance energy) describe the dependency of the decay rate (fwhm) on size and shape of nanoparticles. Thus the plasmon resonance frequency strongly depends on geometrical parameters, e.g., the aspect ratio of a distinct GNR. Nevertheless, the plasmon resonance can also vary for one particular GNR as it is strongly dependent on the surrounding medium, because the plasmon resonance occurs if $\mathrm{Re}(\varepsilon(\omega)) = -2\varepsilon_m$ (for spheres), with $\varepsilon(\omega)$ as the permittivity of the metal and ε_m the permittivity of the surrounding medium.[27] Thus a change of the refractive index of the surrounding medium (e.g., water to ice) will shift the spectral position of the plasmon resonance. There are several models[7,37] given in the literature to determine the plasmon resonance depending on geometry and dielectric environment, leading to the possibility to determine the refractive index as a local sensor by measuring the resonance wavelength.[38] The local refractive index around the GNRs depends on the embedded medium and the capping material, covering the GNRs.

In summary, the different contributions to the dephasing of the plasmon can be separated into temperature-dependent and -independent parts. The electron-surface scattering, the electron−electron scattering, and the radiative damping can be regarded to be independent of temperature as variations of the shape and the size of the particles can be neglected within the investigated temperature range.[32] Moreover, by using eqs 4, 6, and 7 we can determine the contribution of the temperature-independent factors to the total dephasing, and as the temperature dependence of electron−electron scattering can be neglected, the only temperature dependent mechanism is electron−phonon scattering, which can be described by the models presented in the Electron−Phonon Scattering section .

RESULTS

In order to experimentally determine the different contributions to the dephasing times of GNRs, we recorded a number of luminescence spectra in the temperature range of 1.6−295 K (135 spectra at 1.6 K; 58 spectra at 93 K; 82 spectra at 153 K; 141 spectra at 188 K; 159 spectra at 295 K). Figure 1 shows spectra of three different single GNRs, together with their

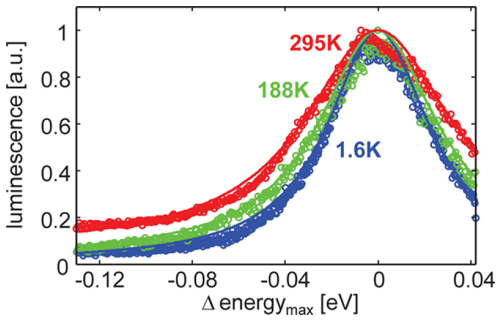

Figure 1. Three spectra of different GNRs at 1.6 K (blue), 188 K (green), and 295 K (red) together with their Lorentzian line fits. The recorded luminescence maxima show their peak maximum at comparable energies (~1.74 eV). For clarity the spectra are aligned with respect to their maximum, indicated by the x-axis showing the relative energy difference to the maximum emission energy ($\Delta\mathrm{energy}_{max}$ in eV). The excitation source has an energy shift of ~0.12 eV to the shown spectra. An increase of the fwhm from 53 to 80 meV with rising temperature can be seen.

dx.doi.org/10.1021/jp407178u | J. Phys. Chem. C 2013, 117, 21476−21482

corresponding Lorentzian fits[21] with comparable peak energies at different temperatures (1.6, 188, 295 K). The fwhm's for these three particles show an increase with rising temperature from 53 meV (1.6 K) to 63 meV (188 K) to 80 meV (295 K). For further evaluation, spectra were only used if they exhibited a symmetric and Lorentzian peak shape, which gives an indication that a single particle was being observed. Spectra with asymmetrical and non-Lorentzian shapes were discarded from the analysis to exclude clustered and inhomogeneously broadened particles. Determining the fwhm of the Lorentzian fits provides the total dephasing times ($\tau = 2\hbar/\Gamma$) of the decaying plasmon.

In Figure 2, all determined spectral peak positions are plotted against their corresponding fwhm for 1.6 and 295 K (center).

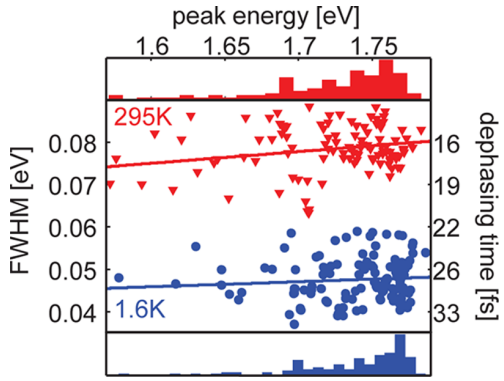

Figure 2. Fwhm of single GNR luminescence bands vs peak energy [eV] for 1.6 K (blue circles) and 295 K (red triangles) with linear fits. The histograms on top and bottom reflect the occurrence of the peak energies with maxima at 1.76 eV for 295 K and 1.77 eV for 1.6 K. The mean widths for these resonance energies are 76.5 meV (295 K) and 46.5 meV (1.6 K). The cutoff from the long-pass filter around 1.79 eV can be seen.

The histograms for the peak positions are shown at the top/bottom. Due to the presence of different aspect ratios, there exists a broad distribution of the spectral peak positions and the fwhm's at both temperatures. At low temperature (1.6 K) the fwhm varies between 37 and 59 meV. We can observe a broadening of the luminescence peaks for room temperature (295 K), and the fwhm ranges here between 63 and 88 meV. The histograms of the peak maxima exhibit their maximum at 1.77 ± 0.02 eV (1.6 K) and at 1.76 ± 0.05 eV (295 K), respectively, indicating the plasmon resonance of GNRs with the most frequent aspect ratio. Therefore, the most frequent peak energy is assigned to the known aspect ratio of 3.8. For the corresponding mean values of the fwhm for these peak energies, we obtained 46.5 ± 2.5 meV (1.6 K) and 76.5 ± 2.8 meV (295 K). For the observed GNRs, the dephasing time varies between 22 and 35 fs at 1.6 K and between 15 and 21 fs at 295 K. Moreover, Figure 2 shows two linear fits between the spectral peak position and the fwhm. According to the size-dependent contributions to the plasmon dephasing[18] a linear behavior between resonance energy and fwhm in the shown energy interval can be assumed. For a larger energy range the behavior is to be regarded quadratic according to eq 6.

Figure 3 shows the spectral peak positions plotted against their fwhm for 1.6, 93, 153, 188, and 295 K with their corresponding histograms for the peak energies on the top and the fwhm on the left. To guide to the eye, the linear fits for 1.6 and 295 K from Figure 2 are shown. It can be seen that the spreading of the spectral positions is comparable and that the most frequent peak energy is at ∼1.77 eV for all temperatures, with an exception made for the measurement at 295 K (∼1.76 eV) with water instead of ice as the surrounding medium. With increasing temperature, the fwhm values increase, which can be clearly seen in the histograms of the fwhm in Figure 3. The data for all measured temperatures are summarized in Table 1, where the peak energies for the most frequent spectral peak position and their corresponding mean fwhm are reported. The last column shows the simulated fwhm. For the case of 188 and 295 K, two values show the different results for the low- and high-temperature model (in brackets). The assignment of the most frequent peak maximum to the mean aspect ratio of 3.8 is valid in regard to the dropping of peak occurrence for higher energies, so it is unlikely that the maximum peak occurrence is cut off by the sharp edge filter.

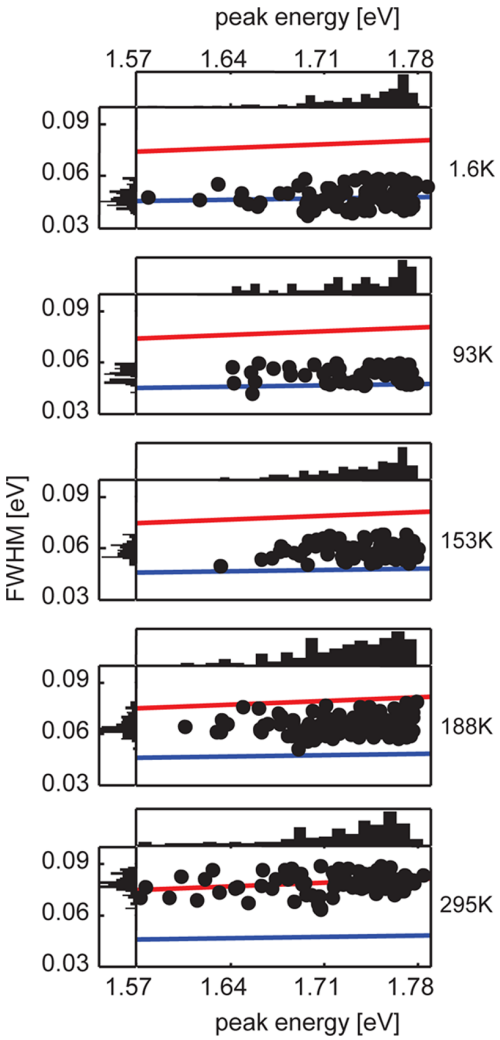

Figure 3. Peak maximum vs fwhm in eV for all measured temperatures (1.6, 93, 153, 188, 295 K). On top of each scatter plot the histogram of the peak maxima and on the left the histogram of the fwhm are shown. The main occurring peak energies are ∼1.77 eV (1.6−188 K) and 1.76 eV (295 K). The distribution of the widths on the other hand shifts to larger values for increasing temperature. The linear fits from Figure 2 in blue (1.6 K) and red (295 K) are shown as guides for the reader's eye.

dx.doi.org/10.1021/jp407178u | J. Phys. Chem. C 2013, 117, 21476−21482

Table 1. Experimental Results for the Determined fwhm for the Most Frequent Peak Energies of the Fitted Spectra[a]

temperature [K]	most frequent peak energy [eV]	corresponding fwhm [meV]	simulated [meV]
1.6	1.77 ± 0.01	46.5 ± 2.5	46.8
93	1.77 ± 0.05	52.8 ± 2.1	52.2
153	1.77 ± 0.05	58.6 ± 2.3	59.1
188	1.77 ± 0.03	64.7 ± 2.7	63.4 (62.8)
295	1.76 ± 0.01	76.5 ± 2.8	76.8 (76.8)

[a]For 188 and 295 K two simulated values are depicted and are based on the two models used. The left value represents the low-temperature model while the right value in brackets represents the high-temperature model.

The experimental results can be used to determine the pure contributions of the main dephasing rate, assuming

$$\Gamma_{tot}(T) = \Gamma_{temp}(T) + \Gamma_0 \quad (8)$$

with $\Gamma_{temp}(T) = \Gamma_{e-ph}(T)$ and $\Gamma_0 = \Gamma_{e-surf} + \Gamma_{e-e} + \Gamma_{rad}$. The decay rate Γ_{e-ph} reaches a minimum value of 8.8 meV at 50 K (see eq 2) and thus this value can also be used at 1.6 K. This enables us to calculate the temperature independent contribution Γ_0 by

$$\Gamma_0 = \Gamma_{tot}(1.6\ \mathrm{K}) - \Gamma_{e-ph}(1.6\ \mathrm{K})$$

$$= 46.5\ \mathrm{meV} - 8.8\ \mathrm{meV} = 37.7\ \mathrm{meV}.$$

With this value for Γ_0 the electron−phonon scattering rate Γ_{e-ph} at 295 K can be determined

$$\Gamma_{e-ph}(295\ \mathrm{K}) = \Gamma_{tot}(295\ \mathrm{K}) - \Gamma_0$$

$$= 76.5\ \mathrm{meV} - 37.7\ \mathrm{meV} = 38.8\ \mathrm{meV}$$

The determined fwhm values enable the fitting of the remaining parameters A (for electron-surface scattering, see eq 4) to be 0.2 and λ (for electron−phonon scattering, see eq 3) to be 3.15×10^{-16} eV s.

For the electron−surface scattering we determined a contribution of 20.7 meV, for the electron−electron scattering 15.8 meV, and for the radiative damping 1.6 meV. The electron−phonon scattering ranges from 8.8 meV (1.6 K) to 38.8 meV (295 K).

Figure 4 shows the results of the experimental data and the simulations for the temperature dependent fwhm and dephasing rates. The black solid curve represents the total dephasing rate calculated with the low-temperature model, while the dashed curve marks the total dephasing rate for the high-temperature model. The circles describe the experimental values of the fwhm at the most frequent peak maximum for each temperature; the bars indicate their corresponding errors.

DISCUSSION

The determined fwhm values (see Figure 4, Table 1) show a temperature dependence which can be assigned to the temperature-dependent electron−phonon scattering rate. In order to make a quantitative statement about the single dephasing contributions and to determine the unknown parameters, i.e., the λ-parameters (eq 3) and the shape factor A (eq 4) in the theoretical models (see section 2.2), we fitted the luminescence spectra and thus obtained the fwhm and spectral position of the luminescence maxima at various temperatures. In the following we discuss the results and compare them with the literature.

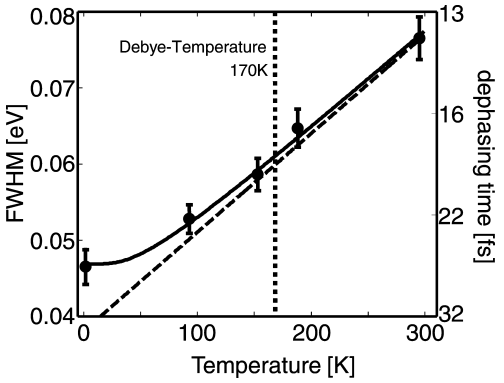

Figure 4. Measured and calculated (solid: LT-model, dashed: HT-model) fwhm of GNRs with an aspect ratio 3.8 and a rod diameter of 10 nm for different temperatures. The circles show the mean fwhm value for the most frequent peak energy position for each temperature, displayed with the corresponding error bars (see Table 1). The black solid line indicates the sum of the single simulated contributions based on the low-temperature model for the phonon coupling (eq 2) with the fitted parameter $A = 0.2$ (see eq 4) and the Debye temperature of 170 K. The dashed line displays the sum of the simulated contributions calculated from the high-temperature model for the phonon coupling (eq 3) with $\lambda = 3.15 \times 10^{-16}$ eV s. The vertical dashed line indicates the Debye temperature of gold of 170 K.

In Figure 4, it can be seen that the temperature behavior of the fwhm is described very well by our simulations. The curve of the low-temperature model is converging the curve of the high-temperature model for increasing temperatures, as expected.

The low-temperature model is in good agreement with all measured values, while the high-temperature model is only suitable for temperatures above 153 K. This supports the assumption that the electron−phonon scattering is the only effectively temperature-dependent dephasing mechanism, and the λ-value, as the slope of the high-temperature models, was fitted well to the experimental data. This result shows that this model can only be utilized to describe the dephasing of GNRs plasmon above the Debye temperature. The offset of the simulations, consisting of the electron−surface scattering, the electron−electron scattering, and the radiative damping, could be approximated in good agreement with the experimental results.

The surface scattering and the A-factor is dependent on the shape and the geometry of the GNR. For cylindric particles it was assumed to be 0.3[33] and for pyramids 0.1,[22] respectively. By fitting the data we determined A to be 0.2, which is reasonable because the GNRs differ from the cylindrical shape by their rounded edges, which can be seen on TEM pictures delivered by the manufacturer (Nanopartz). The shape factor is an important property of GNRs with regard to their function as antennas[39] and the field enhancement effect.

The simulation of the electron−electron scattering mainly depends on the β-value (see eq 6). When β is set to the experimentally determined value[35] of $\sim 2.3 \times 10^{13}$ s^{-1} eV^{-2}, the contribution rises to a value of ∼47 meV for resonance energies of ∼1.77 eV, which exceeds the measured total fwhm at 1.6 K of 46.5 meV. This indicates that the measurements of Parkins et al.[35] did not provide the pure electron−electron scattering rate. On the other hand, the simulated value of 0.76×10^{13} s^{-1} eV^{-2} does indeed, combined with the other dephasing mechanisms, fit well to our results.

dx.doi.org/10.1021/jp407178u | J. Phys. Chem. C 2013, 117, 21476−21482

The significantly lower rate determined by our experiments can be justified by our measurements on single particles compared to previous bulk measurements[22,35] which are not completely able to exclude inhomogeneous broadening.

Heating effects of the examined GNRs can be mainly excluded due to the low amount of absorbed energy which can be estimated by the focal area of $\sim 4 \times 10^{-9}$ cm^2, the absorption cross section[40] of $\sim 1.5 \times 10^{-13}$ cm^2 and the excitation power of ~ 20 μW yielding an absorption rate of lower than 1 nJ/s. According to the studies by Richardson et al.[41] a rise in temperature should not exceed 1−2 K.

The agreement between the simulated total fwhm's and the measured fwhm's, especially their temperature behavior, indicates that the models used are suitable to describe the decay of plasmons in GNRs within the observed temperature and energy range. This would mean that there is a direct relation between decay of the plasmon and the one-photon luminescence signal.

When we compare our results with temperature-dependent scattering spectra of pyramids examined by Liu et.al.[22] and the experiments with GNRs by Yorulmaz et.al.,[11] it is obvious that the luminescence and scattering spectra exhibit similar dephasing times. Therefore, it should be possible to describe both processes with the same models. Referring to Yorulmaz et al.[11] and the simulations made by Link et al.[7] and Huang et al.,[37] the peak position of the luminescence emission coincidences also with the scattering and the absorbance spectra. The agreement of the simulations also indicate that the observed spectral broadening is not caused by luminescent electron−hole pair recombinations or is negligibly low. However, this does not exclude any interplay between electron−hole pairs and a radiatively or nonradiatively decaying plasmon because the energy of the excitation source (1.86 eV) is high enough to cause possible interband transitions.[21]

CONCLUSION

The luminescence spectra of individual GNRs were collected from cryogenic to room temperatures. We adapted solid state models for the single plasmon decay mechanisms, which fit well to the experimental data. With experiments in the temperature range from 1.6 to 295 K, essential parameters for the understanding of plasmonic nanoparticles can be deduced. Using this approach, we were able to fit the shape factor A of the surface-scattering contribution for the used GNRs to a value ~0.2. The presented method can be used to determine various and important parameters for other nanoparticles and structures. The assumption of the direct plasmonic origin of the luminescence signal could be fortified by simulations of plasmon dephasing mechanisms, especially the temperature dependent electron−phonon scattering rate.

AUTHOR INFORMATION

Corresponding Authors

*E-mail: alfred.meixner@uni-tuebingen.de. Phone: +49 7071-29-76903. Fax: +49 7071-29-5490.

*E-mail: marc.brecht@uni-tuebingen.de. Phone: +49 7071-29-76239. Fax: +49 7071-29-5490.

Notes

The authors declare no competing financial interest.

ACKNOWLEDGMENTS

We thank Virgillio Failla and Andreas Kern for helpful discussions. The financial funding by the DFG (BR4102/1-1, BR4102/2-1, and ME1600/16-1) and the BW Netz Funktionelle Nanostrukturen is gratefully acknowledged.

REFERENCES

(1) Nan, X. L.; Sims, P. A.; Xie, X. S. Organelle Tracking in a Living Cell with Microsecond Time Resolution and Nanometer Spatial Precision. *ChemPhysChem* **2008**, *9*, 707−712.

(2) Nieder, J. B.; Bittl, R.; Brecht, M. Fluorescence Studies into the Effect of Plasmonic Interactions on Protein Function. *Angew. Chem., Int. Ed.* **2010**, *49*, 10217−10220.

(3) Hartland, G. V. Optical Studies of Dynamics in Noble Metal Nanostructures. *Chem. Rev.* **2011**, *111*, 3858−3887.

(4) Zijlstra, P.; Orrit, M. Single Metal Nanoparticles: Optical Detection, Spectroscopy and Applications. *Rep. Prog. Phys.* **2011**, *74*, 106401.

(5) Bouhelier, A.; Bachelot, R.; Lerondel, G.; Kostcheev, S.; Royer, P.; Wiederrecht, G. P. Surface Plasmon Characteristics of Tunable Photoluminescence in Single Gold Nanorods. *Phys. Rev. Lett.* **2005**, *95*, 267405.

(6) Coronado, E. A.; Schatz, G. C. Surface Plasmon Broadening for Arbitrary Shape Nanoparticles: A Geometrical Probability Approach. *J. Chem. Phys.* **2003**, *119*, 3926−3934.

(7) Link, S.; Mohamed, M. B.; El-Sayed, M. A. Simulation of the Optical Absorption Spectra of Gold Nanorods as a Function of their Aspect Ratio and the Effect of the Medium Dielectric Constant. *J. Phys. Chem. B* **1999**, *103*, 3073−3077.

(8) Muhlschlegel, P.; Eisler, H. J.; Martin, O. J. F.; Hecht, B.; Pohl, D. W. Resonant Optical Antennas. *Science* **2005**, *308*, 1607−1609.

(9) Kern, A. M.; Meixner, A. J.; Martin, O. J. F. Molecule-Dependent Plasmonic Enhancement of Fluorescence and Raman Scattering near Realistic Nanostructures. *ACS Nano* **2012**, *6*, 9828−9836.

(10) Mooradian, A. Photoluminescence of Metals. *Phys. Rev. Lett.* **1969**, *22*, 185−187.

(11) Yorulmaz, M.; Khatua, S.; Zijlstra, P.; Gaiduk, A.; Orrit, M. Luminescence Quantum Yield of Single Gold Nanorods. *Nano Lett.* **2012**, *12*, 4385−4391.

(12) Dulkeith, E.; Niedereichholz, T.; Klar, T. A.; Feldmann, J.; von Plessen, G.; Gittins, D. I.; Mayya, K. S.; Caruso, F. Plasmon Emission in Photoexcited Gold Nanoparticles. *Phys. Rev. B* **2004**, *70*, 205424.

(13) Tcherniak, A.; Ha, J. W.; Dominguez-Medina, S.; Slaughter, L. S.; Link, S. Probing a Century Old Prediction One Plasmonic Particle at a Time. *Nano Lett.* **2010**, *10*, 1398−1404.

(14) Beversluis, M. R.; Bouhelier, A.; Novotny, L. Continuum Generation From Single Gold Nanostructures Through Near-Field Mediated Intraband Transitions. *Phys. Rev. B* **2003**, *68*, 115433.

(15) Mohamed, M. B.; Volkov, V.; Link, S.; El-Sayed, M. A. The 'Lightning' Gold Nanorods: Fluorescence Enhancement of over a Million Compared to the Gold Metal. *Chem. Phys. Lett.* **2000**, *317*, 517−523.

(16) Imura, K.; Nagahara, T.; Okamoto, H. Plasmon Mode Imaging of Single Gold Nanorods. *J. Am. Chem. Soc.* **2004**, *126*, 12730−12731.

(17) Fang, Y.; Chang, W. S.; Willingham, B.; Swanglap, P.; Dominguez-Medina, S.; Link, S. Plasmon Emission Quantum Yield of Single Gold Nanorods as a Function of Aspect Ratio. *ACS Nano* **2012**, *6*, 7177−7184.

(18) Sonnichsen, C.; Franzl, T.; Wilk, T.; von Plessen, G.; Feldmann, J.; Wilson, O.; Mulvaney, P. Drastic Reduction of Plasmon Damping in Gold Nanorods. *Phys. Rev. Lett.* **2002**, *88*, 077402.

(19) Klar, T.; Perner, M.; Grosse, S.; von Plessen, G.; Spirkl, W.; Feldmann, J. Surface-Plasmon Resonances in Single Metallic Nanoparticles. *Phys. Rev. Lett.* **1998**, *80*, 4249−4252.

(20) Berciaud, S.; Cognet, L.; Tamarat, P.; Lounis, B. Observation of Intrinsic Size Effects in the Optical Response of Individual Gold Nanoparticles. *Nano Lett.* **2005**, *5*, 515−518.

(21) Sonnichsen, C.; Franzl, T.; Wilk, T.; von Plessen, G.; Feldmann, J. Plasmon Resonances in Large Noble-Metal Clusters. *New J. Phys.* **2002**, *4*, 93.
(22) Liu, M. Z.; Pelton, M.; Guyot-Sionnest, P. Reduced Damping of Surface Plasmons at Low Temperatures. *Phys. Rev. B* **2009**, *79*, 035418.
(23) Link, S.; El-Sayed, M. A. Shape and Size Dependence of Radiative, Non-Radiative and Photothermal Properties of Gold Nanocrystals. *Int. Rev. Phys. Chem.* **2000**, *19*, 409−453.
(24) Wackenhut, F.; Failla, A. V.; Zuchner, T.; Steiner, M.; Meixner, A. J. Three-Dimensional Photoluminescence Mapping and Emission Anisotropy of Single Gold Nanorods. *Appl. Phys. Lett.* **2012**, *100*, 263102.
(25) Züchner, T.; Wackenhut, F.; Failla, A. V.; Meixner, A. J. Nanoscale Characterization of Single Au Nanorods by Confocal Microscopy. *Appl. Surf. Sci.* **2009**, *255*, 5391−5395.
(26) Hussels, M.; Konrad, A.; Brecht, M. Confocal Sample-Scanning Microscope for Single-Molecule Spectroscopy and Microscopy With Fast Sample Exchange at Cryogenic Temperatures. *Rev. Sci. Instrum.* **2012**, *83*, 123706.
(27) Kreibig, U.; Vollmer, M. *Optical Properties of Metal Clusters*; Springer: Berlin, 1995.
(28) Hodak, J. H.; Henglein, A.; Hartland, G. V. Electron-Phonon Coupling Dynamics in very Small (Between 2 and 8 nm Diameter) Au Nanoparticles. *J. Chem. Phys.* **2000**, *112*, 5942−5947.
(29) Hodak, J. H.; Henglein, A.; Hartland, G. V. Photophysics of Nanometer Sized Metal Particles: Electron-Phonon Coupling and Coherent Excitation of Breathing Vibrational Modes. *J. Phys. Chem. B* **2000**, *104*, 9954−9965.
(30) McKay, J. A.; Rayne, J. A. Temperature Dependence of the Infrared Absorptivity of the Noble Metals. *Phys. Rev. B* **1976**, *13*, 673−685.
(31) Kittel, *Introduction to Solid State Physics*; Wiley, 1986.
(32) Sadaiyandi, K. Size Dependent Debye Temperature and Mean Square Displacements of Nanocrystalline Au, Ag and Al. *Mater. Chem. Phys.* **2009**, *115*, 703−706.
(33) Novo, C.; Gomez, D.; Perez-Juste, J.; Zhang, Z. Y.; Petrova, H.; Reismann, M.; Mulvaney, P.; Hartland, G. V. Contributions from Radiation Damping and Surface Scattering to the Linewidth of the Longitudinal Plasmon Band of Gold Nanorods: a Single Particle Study. *Phys. Chem. Chem. Phys.* **2006**, *8*, 3540−3546.
(34) Coleman, R. *Solid State Physics*; Elsevier Science, 1974.
(35) Parkins, G.; Lawrence, W.; Christy, R. Interband Optical Conductivity Sigma(Omega,Tau) of CU, AG, and AU - Contribution from Electron-Electron Scattering. *Phys. Rev. B* **1981**, *23*, 6408−6416.
(36) Wokaun, A.; Gordon, J. P.; Liao, P. F. Radiation Damping in Surface-Enhanced Raman Scattering. *Phys. Rev. Lett.* **1982**, *48*, 957−960.
(37) Huang, C. P.; Yin, X. G.; Huang, H.; Zhu, Y. Y. Study of Plasmon Resonance in a Gold Nanorod with an LC Circuit Model. *Opt. Express* **2009**, *17*, 6407−6413.
(38) McFarland, A. D.; Van Duyne, R. P. Single Silver Nanoparticles as Real-Time Optical Sensors with Zeptomole Sensitivity. *Nano Lett.* **2003**, *3*, 1057−1062.
(39) Eustis, S.; El-Sayed, M. Aspect Ratio Dependence of the Enhanced Fluorescence Intensity of Gold Nanorods: Experimental and Simulation Study. *J. Phys. Chem. B* **2005**, *109*, 16350−16356.
(40) He, G. S.; Zhu, J.; Yong, K. T.; Baev, A.; Cai, H. X.; Hu, R.; Cui, Y. P.; Zhang, X. H.; Prasad, P. N. Scattering and Absorption Cross-Section Spectral Measurements of Gold Nanorods in Water. *J. Phys. Chem. C* **2010**, *114*, 2853−2860.
(41) Richardson, H. H.; Hickman, Z. N.; Govorov, A. O.; Thomas, A. C.; Zhang, W.; Kordesch, M. E. Thermooptical Properties of Gold Nanoparticles Embedded in Ice: Characterization of Heat Generation and Melting. *Nano Lett.* **2006**, *6*, 783−788.

Chapter 14

Strong and Coherent Coupling of a Plasmonic Nanoparticle to a Subwavelength Fabry-Pérot Resonator

In this chapter the coupling between a plasmonic gold nanorod and the cavity modes of a tunable $\lambda/2$-micro-resonator is spectrally examined by confocal microscopy. For several detected particles the luminescence of the long-wavelength band associated with the long-axis plasmon of these rods are recorded as a function of on-axis transmission wavelength. The behavior of the luminescence of the coupled systems indicates strong coupling between the plasmon and the cavity modes, which is revealed by luminescence on the long-wavelength side with respect to the transmission maximum, spectral shifts indicating anti-crossing and a non-linear dephasing behavior of the coupled system. By a model of two classical coupled oscillators both, the spectral shifts and the spectral linewidths of the luminescence of the coupled system can be described as a function of resonator wavelength showing strong coupling. Due to the angular distributed mode spectrum induced by the Fabry-Pérot-geometry of the cavity the plasmon can couple to the on-axis mode but also to one or more off-axis modes depending on the orientation of the gold nanorod with respect to the mirror surface.

This chapter is based on:
Konrad, A., Kern, A.M., Meixner, A.J., Brecht, M. "Strong and Coherent Coupling of a Plasmonic Nanoparticle to a Subwavelength Fabry-Pérot Resonator", *Nano Letters*, **2015**, 15(7):4423-4428.

NANO LETTERS

Letter

pubs.acs.org/NanoLett

Strong and Coherent Coupling of a Plasmonic Nanoparticle to a Subwavelength Fabry–Pérot Resonator

Alexander Konrad,*[,†] Andreas M. Kern,[†] Marc Brecht,[‡] and Alfred J. Meixner*[,†]

[†]Institut für Physikalische und Theoretische Chemie, Universität Tübingen, Auf der Morgenstelle 18., 72076 Tübingen, Germany

[‡]Institute of Applied Mathematics and Physics, Technikumstrasse 13, 8401 Winterthur, Switzerland

Supporting Information

ABSTRACT: A major aim in experimental nano- and quantum optics is observing and controlling the interaction between light and matter on a microscopic scale. Coupling molecules or atoms to optical microresonators is a prominent method to alter their optical properties such as luminescence spectra or lifetimes. Until today strong coupling of optical resonators to such objects has only been observed with atom-like systems in high quality resonators. We demonstrate first experiments revealing strong coupling between individual plasmonic gold nanorods (GNR) and a tunable low quality resonator by observing cavity-length-dependent nonlinear dephasing and spectral shifts indicating spectral anticrossing of the luminescent coupled system. These phenomena and experimental results can be described by a model of two coupled oscillators representing the plasmon resonance of the GNR and the optical fields of the resonator. The presented reproducible and accurately tunable resonator allows us to precisely control the optical properties of individual particles.

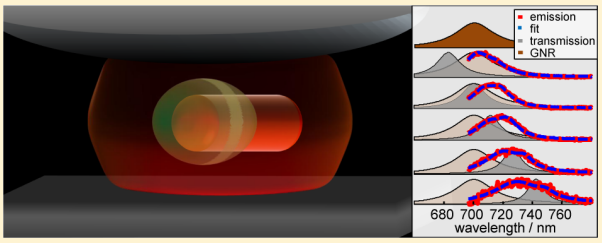

KEYWORDS: *Plasmonics, photonics, LDOS, microresonator, strong coupling*

Two coupled oscillators with similar resonance frequencies and damping constants can exchange energy back and forth in a coherent manner behaving as a single system.[1,2] This phenomenon, known as strong coupling, has, until now, only been observed in the optical regime with quantum systems in high-Q-resonators[1,3−9] and between, e.g., two or more spatially separated plasmonic particles or structures.[10−12] This coupling regime is characterized by energy-level anticrossing, energy shifts, and altered damping rates of the coupled system. Here, we experimentally demonstrate and theoretically analyze strong coupling between the long-axis plasmon oscillation of a single gold nanorod (GNR), dephasing within ∼10−15 fs, and a tunable $\lambda/2$-resonator,[13] displayed in Figure 1a, with a Q-factor of ∼30−40 ($T_2 \approx 30$ fs) consisting of silver mirrors that are separated by half a wavelength in the visible regime.

The GNRs (longitudinal axis 38 nm, transversal axis 10 nm) with a longitudinal plasmon mode of 690 ± 25 nm (1.8 ± 0.3 eV) and a transversal mode of 520 nm (2.38 eV)[15] are positioned halfway between the mirrors on a SiO_2 layer about 60 nm above the planar mirror ensuring no direct coupling to the silver.[16] The longitudinal plasmon can continuously be excited close to resonance by 665 nm cw radiation. The tunable resonator, shown in Figure 1a, is mounted on a translation stage in a confocal microscope allowing to record confocal images showing individual GNRs, select single ones in the excitation focus, and tune the mirror separation. For every GNR and resonator configuration first a white light spectrum was recorded to determine the longitudinal cavity resonance (λ_0) as a function of mirror spacing as indicated in Figure 1b (blue data points) and in Figure 1c (1−9: fitted gray Lorentzian shapes) for particular mirror separations. The white light transmission spectra are probing the on-axis resonance wavelengths of the resonator exactly at the position of a GNR for the respective mirror separation as sketched by the blue arrows in Figure 1c. After introducing a long-pass filter in front of the spectrograph, transmitting at 680 nm the luminescence spectrum (red lines) for the respective cavity length is recorded by laser illumination as shown in Figure 1b (red data point). Now, one mirror is moved by the piezoelectric stacks to change the resonator configuration, and again, a white light transmission and luminescence spectrum is recorded. For linearly decreasing mirror separations the cavity on-axis wavelengths λ_0 show a linear blue shift (Figure 1b). The luminescence spectra of the GNR show also a blue shift for decreasing mirror separations (Figure 1b, spectra 1−9) along with a significant spectral narrowing and an intensity increase. However, in contrast to the resonator wavelengths, the luminescence maxima approach asymptotically the value of ∼700 nm, i.e., the longitudinal plasmon resonance of the GNR, with further decreasing mirror spacings. This spectral behavior must be analyzed on the basis of the resonance conditions of a $\lambda/2$ Fabry–Pérot resonator and the longitudinal plasmon resonance of the GNR. As sketched in Figure 1c such a resonator can support a longitudinal mode (blue Lorentzian curve in Figure 1c) with the resonance condition: $L = \lambda_0/2$ where L is the effective optical cavity length and λ_0 is the

Received: February 25, 2015
Revised: May 22, 2015

DOI: 10.1021/acs.nanolett.5b00766
Nano Lett. XXXX, XXX, XXX−XXX

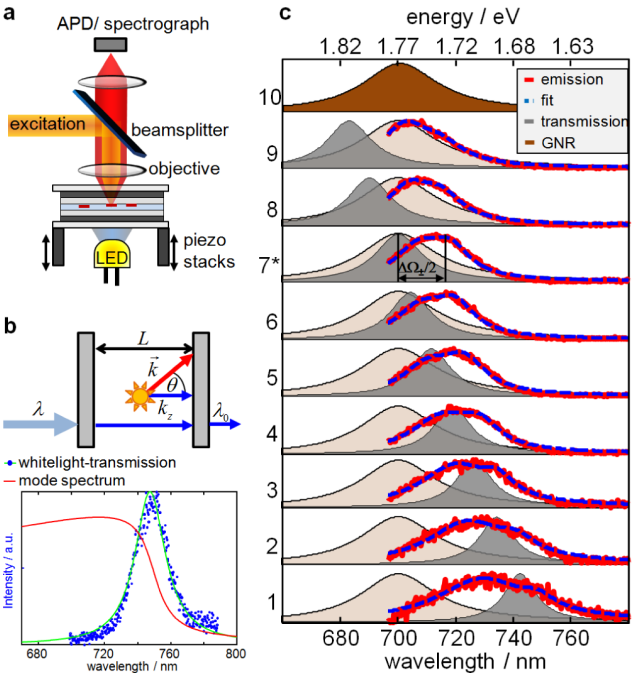

Figure 1. (a) Excitation (665 nm cw laser) is focused by an objective (NA = 0.8) on the embedded GNRs in the resonator, which was scanned in *xy*-direction to localize single particles. The luminescence and white light transmission of the resonator was analyzed by a spectrograph with CCD camera. The cavity length is tuned by piezoelectric stacks altering the *z*-position of the lower mirror. (b) Idealized resonance condition for the Fabry−Pérot geometry in the weak coupling regime. For a propagation vector $\vec{k}$ of a photon by a broadband emitter k_z has to match the condition $L = \lambda_0/2$ (with $|\vec{k}| = 2\pi/\lambda$ and $|\vec{k}| = k_z \cos(\theta)$). This is fulfilled for $\lambda \leq \lambda_{res}$ leading to a mode spectrum $S(\omega)$[14] (red curve) according to a given white light transmission spectrum (blue dots, measured; green curve, Lorentzian fit). (c) Luminescence spectra (red curves) of a single GNR coupled to a tunable $\lambda/2$ resonator. (1−9) For each mirror separation, white light transmission spectra (gray areas) were recorded probing the on-axis resonator wavelength showing a blue shift with decreasing mirror separations. The luminescence spectra (red lines) of the coupled system taken at the same lateral position for the respective mirror distances show also a blue shift along with spectral narrowing for decreasing cavity lengths. The spectrum on top (10) shows a modeled Lorentzian curve representing the long-axis plasmon of the GNR in free space appearing in the lower panels (1−9) as light red area. In spectrum 7* displaying the situation of resonance of the coupled system ($\omega_R = \omega_G$) the intensity maximum shows the red shift $\Delta\Omega/2 \approx$ 15 nm with respect to the resonance wavelength. The fitted curves (blue curves) correspond to the model described in the main communication and Supporting Information yielding, e.g., the parameters for the uncoupled luminescence spectrum in 10.

transmitted optical wavelength in the medium. A $\lambda/2$ resonator can also support a distribution of off-axis modes (red trace in Figure 1c) with smaller wavelengths.[14] Their occurrence is a consequence of $L \approx \lambda_0$ and the resonance condition $L \geq \lambda_0/2$, which is illustrated in Figure 1c. A photon with *k*-vector $|\vec{k}| = 2\pi/\lambda$ and its *z*-component $k_z = |\vec{k}| \cos(\theta)$ is only fitting between the mirrors if $k_z = \pi/L$. Thus, such off-axis modes can efficiently be excited by an angular distribution of *k*-vectors generated by, e.g., a broad band dipole emitter embedded in the resonator.[17] Hence, the spectral behavior in Figure 1b can not be explained by an optical filtering effect of the cavity mode distribution since the luminescence of a weakly coupled emitter such as a single fluorescent molecule or quantum dot must fulfill the resonance condition of the Fabry−Pérot geometry and cannot emit radiation at $\lambda \leq \lambda_0$. Instead, the luminescence spectra of GNR in the resonator are increasingly red-shifted with respect to the white light transmission spectra as the mirror distance is reduced. Such a behavior of spectral anticrossing is a typical sign of strong coupling. The observed spectral behavior can easily be explained and fitted (blue curve) by a model assuming strong coupling between two harmonic oscillators:[2,18] the cavity field[19] (measured gray Lorentzian line shape functions for the on-axis cavity mode) and the longitudinal plasmon mode of the GNR[20] represented by the brown Lorentzian curve with the fixed spectral maximum and spectral width as fitting parameters.

Both can be regarded as damped Lorentzian oscillators $\mathcal{L}_i$ with intrinsic eigenfrequency ω_i and damping constant γ_i where $i = R,G$ symbolizing the resonator (R) and the GNR (G). The respective differential equations (see Supporting Information) for such coupled systems can be solved for the coupled resonance frequencies $\omega_\pm$ by introducing a complex eigenfrequency for i:

$$\tilde{\omega}_i^2 = \omega_i^2 - i\omega_i\gamma_i \tag{1}$$

with solutions[2,18]

$$\tilde{\omega}_\pm^2 = \frac{1}{2}\left[\tilde{\omega}_R^2 + \tilde{\omega}_G^2 \pm \sqrt{(\tilde{\omega}_R^2 - \tilde{\omega}_G^2)^2 + 4g^2}\right] \tag{2}$$

where the coupling g is given in terms of the coupling frequencies[21] Ω_i by

$$g = \Omega_G\Omega_R \tag{3}$$

which are only equal for identical oscillators. As can be seen from eq 2 the coupled system shows a high frequency $\mathcal{L}^+$ and a low frequency mode $\mathcal{L}^-$ with resonance frequencies $\omega_\pm$ = Re($\tilde{\omega}_\pm$) and respective damping rate constants $\gamma_\pm = 2$ Im($\tilde{\omega}_\pm$) enabling to determine the dephasing times $T_2 = 2\hbar/\gamma_\pm$.[22] The modes $\mathcal{L}^\pm$ corresponding to the antisymmetric and symmetric modes of two coupled oscillators have a frequency separation $\Delta\Omega_\pm$ reaching a minimum of $\Delta\Omega_\pm = 2g$ when the intrinsic eigenfrequencies are identical ($\tilde{\omega}_R = \tilde{\omega}_G$).

In our experiment the resonance frequency of the uncoupled longitudinal plasmon oscillation ω_G is fixed, whereas the frequency of the cavity modes $\omega_{R,0} = c/\lambda_0(L)$ can be tuned. Thus, all properties concerning the resonator $\mathcal{L}_R$ are given as a function of the transmission maximum wavelength λ_0. Our GNRs exhibit typical longitudinal resonances of 1.8 ± 0.3 eV (690 ± 25 nm), which can be observed in free space as luminescence bands with spectral widths corresponding to dephasing times of 15 ± 5 fs.[22−25] The frequency-dependent properties of the $\lambda/2$ resonator $\omega_R(\lambda_0)$ and $\gamma_R(\lambda_0)$ can be experimentally determined by Lorentzian linefits to white light transmission spectra[26−29] as shown in Figure 1b, while the optical properties of the observed plasmon in its uncoupled condition (ω_G,γ_G) have to be determined by a fitting method.

In Figure 2 we illustrate the effect on the luminescence of coupling a GNR to a $\lambda/2$ resonator for a certain mirror spacing L. The longitudinal plasmon resonance of the GNR in free space without resonator is modeled by a Lorentzian line shape function (dark red curve) as shown in Figure 2a. The Lorentzian in Figure 2b (blue full line) represents the modeled white light transmission spectrum of the resonator $\mathcal{L}_{R,0}$ with its maximum at 690 nm. The spectral distribution of the off-axis

DOI: 10.1021/acs.nanolett.5b00766
Nano Lett. XXXX, XXX, XXX−XXX

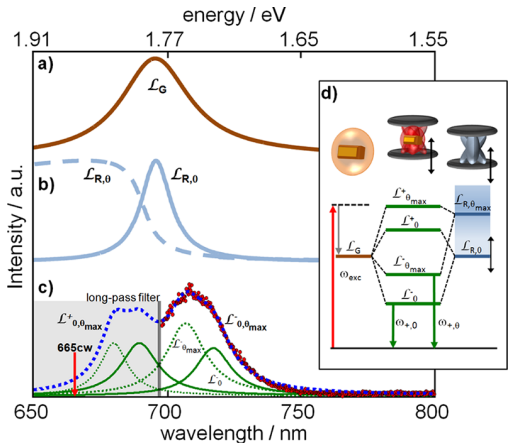

Figure 2. (a) Modeled Lorentzian line shape (dark red curve) representing the band of the one-photon luminescence of a single GNR ($\mathcal{L}_G$) with spectral maximum at ω_G and fwhm of γ_G, reflecting the longitudinal plasmon mode of the GNR. The respective parameters were determined by a global fitting procedure applied on the respective spectra series in Figure 3a. (b) The solid light blue curve represents a cavity transmission spectrum (Lorentzian fit) of a $\lambda/2$ resonator under white light illumination ($\mathcal{L}_{R,0}$) with spectral maximum at $\omega_{R,0}$ and fwhm $\gamma_{R,0}$. The dashed light-blue curve represents the modeled mode spectrum $S(\omega)$ for this resonator setting according to ref 14 including the full angular distribution of modes $\mathcal{L}_{R,\theta}$, which can be excited by a white light source centered in the resonator. (c) Luminescence spectrum (red dots) recorded from a $\lambda/2$ resonator with an embedded GNR excited by 665 nm radiation (red arrow) taken from the spectra series displayed in Figure 3a. The spectral parameters determined for the GNR and the resonator are the same as for the spectra *a* and *b*. The green solid curve represents the modes $\mathcal{L}_0^{\pm}$ originating from coupling the on-axis cavity mode with the longitudinal plasmon oscillation of the GNR and the dashed curve represents the modes $\mathcal{L}_{\theta_{max}}^{\pm}$ originating from coupling the angular mode with $\omega_{R,\theta_{max}}$ to the longitudinal plasmon oscillation of the same GNR. The red wavelength side of the blue curve representing the sum of both green curves fits the experimental data. (d) Illustration of the energy splitting by coupling the longitudinal plasmon to the on-axis and one off-axis cavity mode. Due to the presence of high energy modes, excited by the initial coupling, the continuous excitation is able to excite modes with energies close to the laser.

modes $\mathcal{L}_{R,\theta}$ shown in Figure 2b (blue dashed curve) with the frequencies $\omega_{R,\theta}(\lambda_0)$ and damping constants $\gamma_{R,\theta}(\lambda_0)$ for the respective on-axis wavelength can be calculated[14] by integrating over θ:

$$S(\omega, \lambda_0) = \int_0^{\pi/2} \mathcal{L}_{R,\theta}(\theta, \omega, \lambda_0)\, d\theta \quad (4)$$

A broad band plasmon oscillation of the GNR $\mathcal{L}_G$ can now couple to the longitudinal mode $\mathcal{L}_{R,0}$ of the resonator and also to one or more off-axis modes $\mathcal{L}_{R,\theta}$ depending on the orientation of the GNR with respect to the mirror surfaces. The mode overlapping best with the plasmon mode and therefore exhibiting the most effective coupling is denoted as $\mathcal{L}_{R,\theta_{max}}$. For GNRs orientated parallel to the mirror surfaces this mode has the frequency of the spectral maximum of $S(\omega,\lambda_0)$. Figure 2c shows the superposition (blue dashed curve) of the four coupled oscillation modes: $\mathcal{L}_{R,0}^{\pm}$ (green solid curve) and $\mathcal{L}_{R,\theta_{max}}^{\pm}$ (green dashed curve) calculated according to eq 2 with those parameters determining the spectra in *a*,*b* and adapted to the intensity of the measured spectrum (red dots). The measured luminescence spectrum in *c* is taken from series *a* in Figure 3. The high energy modes $\mathcal{L}_{R,0}^{+}$ and $\mathcal{L}_{R,\theta_{max}}^{+}$ are hidden by a long-pass filter (gray area), suppressing the laser, and are not visible in the experimental spectrum. However, their expected spectral positions are indicated by the green curves behind the gray area and are part of the solutions of eq 2. A schematic term scheme in Figure 2d illustrates the coupling between the oscillators and the resulting modes. Such as in Figure 2c the scheme illustrates that the excitation source is able to excite continuously the high energy modes enhancing the observability of the strong coupling behavior in contrast to the excitation of the low energy on-axis cavity mode by white light. To determine the spectral parameters for the respective GNR and the coupling properties (plasmon frequency ω_G, damping constant γ_G, which directly corresponds to the plasmon frequency ω_G,[25] coupling frequencies Ω_G,Ω_R, and spectral separation $\Delta\omega_{0,\theta_{max}} = \omega_{R,0} - \omega_{R,\theta_{max}}$) a global fitting procedure was applied (see Supporting Information) for each spectra series representing each a different GNR.

Measured series of luminescence spectra for three GNRs at different lateral positions in the resonator as a function of on-axis transmission wavelength are shown in Figure 3. For each mirror spacing the resonance wavelengths of the longitudinal cavity mode $\omega_{R,0}$ were measured by white-light transmission spectra and are indicated by the blue dots. They are shifting to shorter wavelengths for decreasing mirror separation. The main luminescence intensities of the coupled system are also shifting to shorter wavelengths as the mirror spacing decreases (with increasing displacement of the moveable mirror). In all three series we see a similar qualitative behavior, i.e., the blue shift of the luminescence is smaller than the blue shift of the on-axis transmission of the resonator as it approaches the plasmon resonance of the GNR (see also Figure 1b). Applying the fitting method (see Supporting Information) to each spectral series yields the eigenfrequencies $\omega_{\pm,0}(\omega_{R,0})$ of the coupled oscillations as a function of transmission wavelength (blue solid lines for $\omega_{-,0}$, dashed lines for $\omega_{+,0}$), the set of parameters for the respective GNR, and the damping constants $\gamma_{\pm,0}(\omega_{R,0})$. The parameters are summarized in Table 1 with the coupling frequency of the on-axis cavity mode $\Omega_{R,0}$ given for resonance between plasmon and resonator. For clarity the oscillation modes by off-axis coupling $\mathcal{L}_{\theta_{max}}^{\pm}$ and their respective eigenfrequencies are not displayed in Figure 3a,b since they are very close to the results of the on-axis mode. The plasmon resonances determined by the fitting method for the three GNRs are drawn as orange lines. In Figure 3c we observe an additional blue-shifted contribution with respect to the main intensity, which can be explained by deviating orientation of the individual GNR with respect to the mirror surface or by two very close particles with similar plasmon resonances where one is oriented perfectly parallel to the mirror surface and one is oriented with a small deviation with respect to the *xy*-plane, e.g., induced by a slight roughness of the SiO_2 spacing layer. However, the off-axis cavity mode $\mathcal{L}_{R,\theta_{max}}$ with $\omega_{R,\theta_{max}}$ (white dashed line) coupling most effectively to a plasmon thus has to have a decreased wavelength due to an increased θ. The corresponding resonance wavelengths of the low energy modes $\mathcal{L}_{0,\theta_{max}}^{-}$ are displayed as solid blue ($\omega_{-,0}$) and white lines (ω_{-},θ_{max}) and of the high energy modes $\mathcal{L}_{0,\theta_{max}}^{+}$ as dashed blue

DOI: 10.1021/acs.nanolett.5b00766
Nano Lett. XXXX, XXX, XXX−XXX

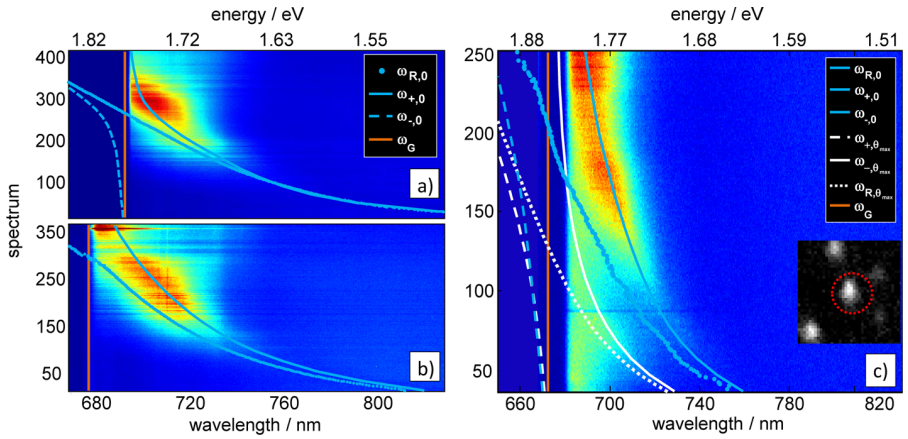

Figure 3. (a–c) Luminescence spectra series of three different GNRs inside a microresonator, excited with 665 nm radiation, as a function of on-axis transmission wavelength. The gray lines represent the spectral maxima of the measured white light transmission $\omega_{R,0}$ (blue dots) for respective mirror distances. The fitted eigenfrequencies of the coupled system $\omega_{\pm,0}$ (blue solid line, $\omega_{-,0}$; blue dashed line, $\omega_{+,0}$) match the observed main luminescence intensities. In a and b only the eigenfrequencies of the coupled system consisting of the longitudinal cavity mode and the plasmon are shown. While series a and b are completely dominated by coupling of the plasmon to the longitudinal cavity mode, series c shows a significant contribution resulting from coupling between the plasmon and an off-axis mode with $\omega_{R,\theta_{max}}$ (white dashed line). The respective eigenfrequencies are displayed as white solid ($\omega_{-,\theta_{max}}$) and dashed line ($\omega_{+,\theta_{max}}$). The fitted eigenfrequencies ω_G of the long-axis plasmons of the GNRs are represented as orange lines. The inset on the right shows a confocal scan image (dimensions: 5 μm × 5 μm) of the GNR in c.

Table 1. Determined Set of Parameters for the Luminescence Spectra Series Shown in Figure 3[a]

series	g_0 [eV^2]	ω_G [eV]	$\Omega_{R,0}(\Delta\omega_{RG})$ [eV]	Ω_G [eV]
a	0.12	1.78	0.683	0.169
b	0.21	1.83	1.074	0.200
c	0.20	1.81	1.020	0.200

[a]The coupling frequency of the resonator is given for the resonant case $\Delta\omega = 0$ and g_0 for coupling with the on-axis cavity mode as indicated by the subscript 0.

($\omega_{+,0}$) and white lines ($\omega_{+,\theta_{max}}$) determined by the outlined fitting procedure. The long-pass filter at 680 nm blocks a main part of the $\mathcal{L}^{+}_{0,\theta}$ contribution, except a shoulder in the first 50 spectra indicating the spectral anticrossing.

In Figure 4 the damping constants and corresponding dephasing times (colored circles) representing the three spectral series are displayed together with the imaginary solutions of eq 2 (colored curves) with the respective parameters of Table 1 as a function of detuning $\Delta\omega_{RG} = \omega_R - \omega_G$. They were determined by the fwhm of Lorentzian linefits of the $\mathcal{L}^{-}_{R,0}$ contribution. For $\omega_R \ll \omega_G$ the damping rates of the three data sets have values around 0.04 eV corresponding to the damping of the uncoupled $\lambda/2$ resonator (see Supporting Information). For $\omega_R \gg \omega_G$ the damping rates reach values between 0.06 and 0.08 eV, corresponding to the damping rates of uncoupled longitudinal plasmon modes.[25] The same behavior can be seen for the eigenfrequencies $\omega_{-,0}$ (Figure 3) tending for large $|\Delta\omega_{RG}|$ to the intrinsic values of the corresponding uncoupled oscillator. In case of resonance ($\Delta\omega_{RG} \approx 0$) the damping constants and the eigenfrequencies cannot be assigned any more to one specific isolated oscillator but reflect the coupled system.

Also the coupling parameters g can be determined from the fitting model and are clearly larger than the resonator and plasmon damping constants, which is a prerequisite for strong coupling between the plasmon and the resonator modes. In

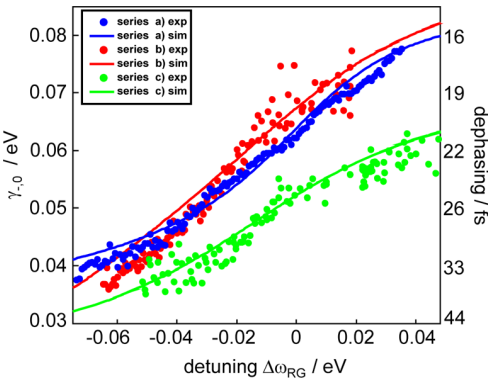

Figure 4. Experimentally determined fwhm values (colored circles for the three GNRs from Figure 3), $\gamma_{-,0}$, of the coupled mode between the cavity on-axis wavelengths and the fitted plasmon frequencies ($\mathcal{L}^{-}_{0}$) representing the dephasing times ($T_2 = 2\hbar/\gamma$) of the system are shown as a function of detuning ($\Delta\omega = \omega_R - \omega_G$). The values are obtained from the Lorentzian $\mathcal{L}^{-}_{0}$-like presented in Figure 2. The full lines represent the dephasing rates of the coupled mode calculated by the model and eq 2 with the same parameters as the simulations of the eigenfrequencies in Figure 3.

general, the strong coupling regime occurs when $g \gg \gamma_i$,[6] which can be claimed for the examined system.

The observed behavior is quite different from the luminescence of weakly coupled quantum systems (i.e., fluorophores) to resonator modes. For such systems[28,30,31] the luminescence can be described by the overlap of the spectral mode distribution $S(\omega,\lambda_0)$ (see Figure 2b) of the resonator and the free space fluorescence spectrum and can hence occur exclusively on the high energy side with respect to the on-axis resonance in Fabry–Pérot resonators. In the weak coupling regime the resonator affects the spontaneous emission rate of an emitter by an altered mode density[1] with respect to free space. This so-called Purcell effect[32] leads to a maximum enhanced emission rate in the case of resonance between

DOI: 10.1021/acs.nanolett.5b00766
Nano Lett. XXXX, XXX, XXX–XXX

emitter and resonator and an inhibition toward zero in the case of detuning.[14,26]

The fitted plasmon related parameters, resonance frequency, and damping constant agree perfectly with the values obtained for the same GNRs measured without resonator.[15,25] Also it was shown recently, that the red wavelength luminescence band of these particles is directly generated by a decaying plasmon.[25,33] Also, the difference between the exchange frequencies is expected. The energy of an excited cavity mode is stored in the electric field within a cavity mode with $L \approx 250 \pm 50$ nm (whose length is tunable), while a comparable amount of energy of an oscillating plasmon is stored in the coherent oscillation of the conduction electrons over an effective path lengths of ~20 nm.[34] Variations of the coupling are thus due to intrinsic properties of the resonator and the GNR.[25]

In a nontunable resonator Mitra et al. observed a shift of the resonance wavelengths of the microcavity at the focal locations of present gold nanoparticles. This shift between different positions with and without a present particle can be explained by a local perturbation in the dielectric constant of the intracavity material.[35] In our measurements we observe a difference between the cavity transmission and the spectral shift of the plasmon decay for one and the same particle as a function of mirror separation. However, the cavity perturbation scheme, which is based on the local average refractive index, cannot explain the observed spectral behavior.

The insights and techniques described by this study lead to several advantages and new opportunities. Strong coupling between optical resonators and plasmonic particles implies that the energy of an excited plasmon is coherently transferred to at least one resonant cavity mode, which, in turn, re-excites the plasmon oscillation allowing to tune the resonance frequency of a plasmon without annihilating its coherence in a precise and controllable fashion. This possibility can be useful, i.e., for the controlled excitation of nearby systems by the so-called antenna-effect of plasmonic particles.[33,36] The developed resonator based on the design described in refs 26 and 27 including broadband reflective silver mirrors and sensor-equipped piezo stacks, allows us also to mechanically control the resonance frequencies of the resonator in a reproducible way. The advantage of our low-Q resonators is that the tuning occurs by changing the cavity length directly in contrast to most high-Q resonators with fixed geometries. Tuning such high-Q resonators may affect the optical properties like emission wavelengths or lifetimes of embedded emitters induced by a temperature change or a dielectric material variation,[25,37,38] which must carefully be taken into account.

In summary, we present a resonator construction for changing the mirror distances up to the $\lambda/2$ region with a high amount of accuracy and reproducibility. It is possible to detect the luminescence of single GNRs embedded in a tunable microresonator as a function of its on-axis wavelengths. The emission of the GNR shows strong coupling to the resonator such as the indicated spectral shift leading to nonlinear dephasing and emission on the long-wavelength side of the cavity transmission implying a coherent energy transfer between plasmon and cavity mode.

Methods. Details are given in the Supporting Information. In short, the resonator consists of a planar and a curved silver mirror, with reflectivities of 0.90 and 0.95, respectively, the latter being mounted on piezoelectric stacks equipped with position sensors for reproducibly adjusting the mirror separation. GNRs, 38 nm long and 10 nm wide, were purchased from Nanopartz and deposited in low concentration, suitable for single particle detection, on a 60 nm SiO_2 layer with a roughness of ±5 nm above the planar mirror and about half way between the mirror surfaces. The low roughness ensures that the GNRs are parallel with respect to the mirror surface (see Supporting Information and refs 39 and 40). Tridest water was used as a flexible medium allowing to tune the mirror separation with a low refractive index deviation to glass. The resonator was mounted on a feed-back controlled sample-scanning stage (PI-instruments) of a home-built confocal microscope equipped with as spectrograph and a cooled CCD-detector for recording single-particle spectra.[41] A white-light LED was used for recording transmission spectra of the resonator as a function of mirror spacing. Confocal luminescence images and spectra were taken by exciting the system with a 665 nm, 20 μW cw laser diode via a NA = 0.8 objective lens. The luminescence was collected by the same objective lens and guided through an edge filter and a pinhole onto the detector: either an APD or the spectrograph. In the tuning series, the laser wavelength is mostly off-resonant to the cavity leading to an effective power of around 1 μW at the location of the GNR and an absorption rate lower than 0.05 nJ/s.[23] It was shown that such low excitation powers should not cause a rise of temperature by more than 1 K.[25,42,43]

■ ASSOCIATED CONTENT

Supporting Information

Detailed description of the resonator, the confocal microscope, and the theoretical framework. The Supporting Information is available free of charge on the ACS Publications website at DOI: 10.1021/acs.nanolett.5b00766.

■ AUTHOR INFORMATION

Corresponding Authors

*Phone: +49 (0)7071-29-76903. Fax: +49 (0)7071-29-5490. E-mail: alexander.konrad@uni-tuebingen.de.

*E-mail: alfred.meixner@uni-tuebingen.de.

Notes

The authors declare no competing financial interest.

■ ACKNOWLEDGMENTS

Financial support from the German Research Council (DFG) for ME1600/13-1 and Heisenberg-Programm (BR 4102/1-1 and BR 4102/2-1) is gratefully acknowledged.

■ REFERENCES

(1) Vahala, K. J. *Nature* **2003**, *424*, 839−846.

(2) Novotny, L. *Am. J. Phys.* **2010**, *78*, 1199−1202.

(3) Kimble, H. J. *Phys. Scr.* **1998**, *T76*, 127−137.

(4) Yoshie, T.; Scherer, A.; Hendrickson, J.; Khitrova, G.; Gibbs, H. M.; Rupper, G.; Ell, C.; Shchekin, O. B.; Deppe, D. G. *Nature* **2004**, *432*, 200−203.

(5) Reithmaier, J. P.; Sek, G.; Loffler, A.; Hofmann, C.; Kuhn, S.; Reitzenstein, S.; Keldysh, L. V.; Kulakovskii, V. D.; Reinecke, T. L.; Forchel, A. *Nature* **2004**, *432*, 197−200.

(6) Aoki, T.; Dayan, B.; Wilcut, E.; Bowen, W. P.; Parkins, A. S.; Kippenberg, T. J.; Vahala, K. J.; Kimble, H. J. *Nature* **2006**, *443*, 671−674.

(7) Wallraff, A.; Schuster, D. I.; Blais, A.; Frunzio, L.; Huang, R. S.; Majer, J.; Kumar, S.; Girvin, S. M.; Schoelkopf, R. J. *Nature* **2004**, *431*, 162−167.

(8) Hennessy, K.; Badolato, A.; Winger, M.; Gerace, D.; Atature, M.; Gulde, S.; Falt, S.; Hu, E. L.; Imamoglu, A. *Nature* **2007**, *445*, 896−899.

DOI: 10.1021/acs.nanolett.5b00766
Nano Lett. XXXX, XXX, XXX−XXX

(9) Niemczyk, T.; Deppe, F.; Huebl, H.; Menzel, E. P.; Hocke, F.; Schwarz, M. J.; Garcia-Ripoll, J. J.; Zueco, D.; Hummer, T.; Solano, E.; Marx, A.; Gross, R. *Nat. Phys.* **2010**, *6*, 772−776.
(10) Su, K. H.; Wei, Q. H.; Zhang, X.; Mock, J. J.; Smith, D. R.; Schultz, S. *Nano Lett.* **2003**, *3*, 1087−1090.
(11) Huang, C. P.; Yin, X. G.; Kong, L. B.; Zhu, Y. Y. *J. Phys. Chem. C* **2010**, *114*, 21123−21131.
(12) Vakevainen, A. I.; Moerland, R. J.; Rekola, H. T.; Eskelinen, A. P.; Martikainen, J. P.; Kim, D. H.; Torma, P. *Nano Lett.* **2014**, *14*, 1721−1727.
(13) Kern, A. M.; Zhang, D.; Brecht, M.; Chizhik, A. I.; Failla, A. V.; Wackenhut, F.; Meixner, A. J. *Chem. Soc. Rev.* **2014**, *43*, 1263−1286.
(14) Bjork, G. *IEEE J. Quantum Electron.* **1994**, *30*, 2314−2318.
(15) Wackenhut, F.; Failla, A. V.; Meixner, A. J. *J. Phys. Chem. C* **2013**, *117*, 17870−17877.
(16) Chen, H.; Ming, T.; Zhang, S.; Jin, Z.; Yang, B.; Wang, J. *ACS Nano* **2011**, *5*, 4865−4877.
(17) Steiner, M.; Failla, A. V.; Hartschuh, A.; Schleifenbaum, F.; Stupperich, C.; Meixner, A. J. *New J. Phys.* **2008**, *10*, 123017.
(18) de Magalhaes, A. R. B.; Fonseca, C. H. D.; Nemes, M. C. *Phys. Scr.* **2006**, *74*, 472−480.
(19) Lipson, S.; Lipson, H. *Optical Physics*; Cambridge University Press: Cambridge, U.K., 1995.
(20) Maier, S. *Plasmonic: Fundamentals and Applications*; Springer: New York, 2007.
(21) Garg, S.; Ghosh, C. K.; Gupta, S. *Oscillations and Waves*; Raj Press: New Delhi, India, 2009.
(22) Sonnichsen, C.; Franzl, T.; Wilk, T.; von Plessen, G.; Feldmann, J. *New J. Phys.* **2002**, *4*, 93.
(23) He, G. S.; Zhu, J.; Yong, K. T.; Baev, A.; Cai, H. X.; Hu, R.; Cui, Y. P.; Zhang, X. H.; Prasad, P. N. *J. Phys. Chem. C* **2010**, *114*, 2853−2860.
(24) Yorulmaz, M.; Khatua, S.; Zijlstra, P.; Gaiduk, A.; Orrit, M. *Nano Lett.* **2012**, *12*, 4385−4391.
(25) Konrad, A.; Wackenhut, F.; Hussels, M.; Meixner, A. J.; Brecht, M. *J. Phys. Chem. C* **2013**, *117*, 21476−21482.
(26) Steiner, M.; Schleifenbaum, F.; Stupperich, C.; Failla, A. V.; Hartschuh, A.; Meixner, A. J. *ChemPhysChem* **2005**, *6*, 2190−2196.
(27) Chizhik, A.; Schleifenbaum, F.; Gutbrod, R.; Chizhik, A.; Khoptyar, D.; Meixner, A. J.; Enderlein, J. *Phys. Rev. Lett.* **2009**, *102*, 073002.
(28) Bar, S.; Chizhik, A.; Gutbrod, R.; Schleifenbaum, F.; Chizhik, A.; Meixner, A. J. *Anal. Bioanal. Chem.* **2010**, *396*, 3−14.
(29) Chizhik, A. I.; Chizhik, A. M.; Kern, A. M.; Schmidt, T.; Potrick, K.; Huisken, F.; Meixner, A. J. *Phys. Rev. Lett.* **2012**, *109*, 223902.
(30) Konrad, A.; Trost, A. L.; Skandary, S.; Hussels, M.; Meixner, A. J.; Karapetyan, N. V.; Brecht, M. *Phys. Chem. Chem. Phys.* **2014**, *16*, 6175−6181.
(31) Konrad, A.; Metzger, M.; Kern, A. M.; Brecht, M.; Meixner, A. J. *Nanoscale* **2015**, *7*, 10204−10209.
(32) Purcell, E. *Phys. Rev.* **1946**, *69*, 674−674.
(33) Zijlstra, P.; Orrit, M. *Rep. Prog. Phys.* **2011**, *74*, 106401.
(34) Coronado, E. A.; Schatz, G. C. *J. Chem. Phys.* **2003**, *119*, 3926−3934.
(35) Mitra, A.; Harutyunyan, H.; Palomba, S.; Novotny, L. *Opt. Lett.* **2010**, *35*, 953−955.
(36) Nieder, J. B.; Bittl, R.; Brecht, M. *Angew. Chem., Int. Ed.* **2010**, *49*, 10217−10220.
(37) Shang, L.; Wang, Y. Z.; Jiang, J. G.; Dong, S. J. *Langmuir* **2007**, *23*, 2714−2721.
(38) Chah, S.; Hammond, M. R.; Zare, R. N. *Chem. Biol.* **2005**, *12*, 323−328.
(39) Failla, A. V.; Qian, H.; Qian, H.; Hartschuh, A.; Meixner, A. J. *Nano Lett.* **2006**, *6*, 1374−1378.
(40) Zuchner, T.; Wackenhut, F.; Failla, A. V.; Meixner, A. J. *Appl. Surf. Sci.* **2009**, *255*, 5391−5395.
(41) Hussels, M.; Konrad, A.; Brecht, M. *Rev. Sci. Instrum.* **2012**, *83*, 123706.
(42) Link, S.; El-Sayed, M. A. *Int. Rev. Phys. Chem.* **2000**, *19*, 409−453.
(43) Richardson, H. H.; Hickman, Z. N.; Govorov, A. O.; Thomas, A. C.; Zhang, W.; Kordesch, M. E. *Nano Lett.* **2006**, *6*, 783−788.

DOI: 10.1021/acs.nanolett.5b00766
Nano Lett. XXXX, XXX, XXX−XXX

Supplementary material: Strong and coherent coupling of a plasmonic nanoparticle to a sub-wavelength Fabry-Perot resonator

Alexander Konrad, Andreas M. Kern, Marc Brecht, and Alfred J.Meixner*
IPTC, University of Tuebingen, Auf der Morgenstelle 18,
72076 Tuebingen, Germany

I. THEORETICAL

A. Coupled oscillators

Assuming that the plasmon oscillation and the cavity field can be described both by Lorentzian oscillators, the eigenfrequencies of the coupled system can be derived in analogy to mechanical oscillators. Their time depending amplitudes $x_i(t)$ $(i = 1, 2)$ can be described by two coupled differential equations:

$$\ddot{x}_1(t)+2\frac{d_1}{m_1}\dot{x}_1(t)+\frac{k_1}{m_1}x_1(t)+\frac{\kappa}{m_1}(x_1(t)-x_2(t)) = 0, \quad (1)$$

$$\ddot{x}_2(t)+2\frac{d_2}{m_2}\dot{x}_2(t)+\frac{k_2}{m_2}x_2(t)+\frac{\kappa}{m_2}(x_2(t)-x_1(t)) = 0. \quad (2)$$

Here, $m_{1,2}$ denote the masses, $d_{1,2}$ the friction constants, $k_{1,2}$ the spring constants and κ the coupling spring constant. First, we can replace the spring constants by the eigenfrequencies ω_i of the uncoupled oscillators and the frequencies of the coupling Ω_i by:

$$\omega_i = \sqrt{\frac{k_i}{m_i}}; \Omega_i = \sqrt{\frac{\kappa}{m_i}}. \quad (3)$$

Similarly, we can replace the friction term d_i/m_i by the damping rate constant γ_i:

$$\gamma_i = \frac{d_i}{m_i}. \quad (4)$$

The new differential equations can now be easily solved by introducing the approximation for the eigenfrequencies with included damping:

$$\widetilde{\omega}_i^2 = \omega_i^2 - i\omega_i\gamma_i, \quad (5)$$

which is valid for $\omega_i >> \gamma_i$ and leads to complex eigenfrequencies with damping as imaginary solution. The long-axis plasmon of our GNRs exhibit resonance frequencies ω_G of around 1.8±0.6 eV with damping rates γ_G of 0.08±0.02 eV. The eigenfrequencies of the tunable on-axis cavity mode $\omega_{R,0}(\lambda_0)$ in this experiment were tuned from 1.6 eV to 1.8 eV with damping rates $\gamma_{R,0}(\lambda_0)$ between 0.02 eV and 0.04 eV depending on the experimentally determinable spectral maximum of the white light transmission spectrum λ_0.
The generalized equations can either be solved for the frequency depending amplitudes or for the new eigenfrequencies of the coupled system. Using the steady state ansatz $x_i(t) = x_i^0 exp[-i\omega_\pm t]$ yields the eigenfrequencies for the coupled system[1]:

$$\widetilde{\omega}_\pm^2 = \frac{1}{2}[\widetilde{\omega}_1^2 + \widetilde{\omega}_2^2 \pm \sqrt{(\widetilde{\omega}_1^2 - \widetilde{\omega}_2^2)^2 + 4g^2}] \quad (6)$$

with:

$$g = \Omega_1\Omega_2, \quad (7)$$

indicating the coupling rate. For identical oscillators $(\widetilde{\omega}_1 = \widetilde{\omega}_2)$ the frequency separation $\Delta\omega_{1,2}$ between the high and low energy modes can be calculated by:

$$\Delta\Omega_{1,2} = 2g. \quad (8)$$

B. Resonator-modes

The differential equations can also be solved for the amplitudes $x_{1,2}$ representing the luminescence intensities shown in Figure 1 for series c) from the main article.

The spectral mode distribution is calculated according to ref.[2] with following assumptions: loss-less, planar, parallel and infinitly extended mirrors. Also, the dielectric material between the mirrors and the phase change of waves at boundary surfaces are neglected. In this approach the electric field is described by two traveling waves with opposed propagation directions E_+ and E_- which add between the two mirrors and interfere constructively or destructively. Their amplitudes are given by:

$$E_- = \frac{\sqrt{1-R_2}exp[ik(L-z_0)cos(\theta)]}{1-\sqrt{R_1R2}exp[i2kLcos(\theta)]}E_0, \quad (9)$$

$$E_+ = \frac{\sqrt{R_1(1-R_2)}exp[i(k(L+z_0)cos(\theta)+\pi)]}{1-\sqrt{R_1R_2}exp[i2kLcos(\theta)]}E_0. \quad (10)$$

Here, R_i are the (real valued) reflectivities of the mirrors, depending on the angle of incidence/transmission θ and the wavelength λ, k is the wave-vector with:

$$|k| = 2\pi/\lambda, \quad (11)$$

* alfred.meixner@ipc.uni-tuebingen.de

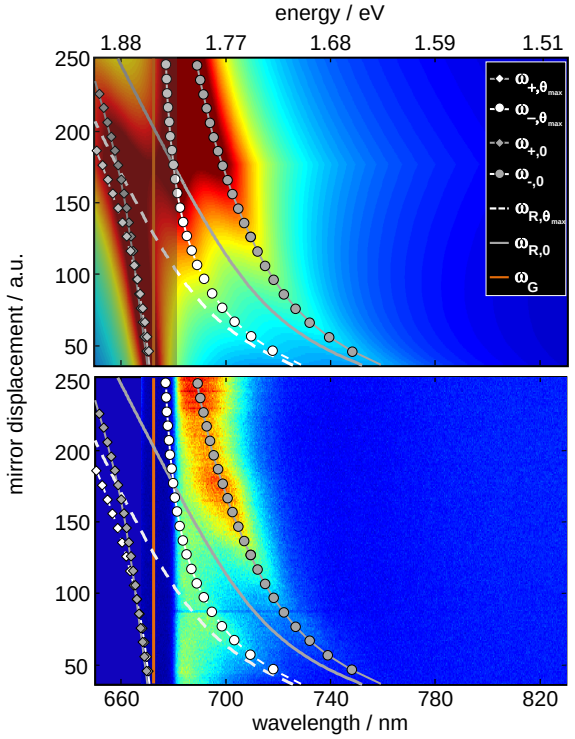

FIG. 1. *Comparison of simulated (upper) and measured (lower) luminescence spectra of a GNR inside a mircoresonator for decreasing mirror separation in a two-dimensional false color plot. The simulation was done for solving the differential equations 1 and 2 for two coupled systems (GNR-longitudinal mode and GNR-angular mode) like shown in Figure 2 of the main article without respect to the experimental intensities. Also shown are the solutions of Equation 6 for the eigenfrequencies as dots and rhombi perfectly matching to the intensity maxima of the measured luminescence spectra. In gray the line represents the spectral maxima course of the longitudinal cavity modes $\omega_{R,0}$ the dots and rhombi are the solutions of $\omega_{-,0}$ and $\omega_{+,0}$. In white the line represents the spectral maxima course of the θ_{max}-mode $\omega_{R,\theta_{max}}$ the dots and rhombi are the solutions of $\omega_{-,\theta_{max}}$ and $\omega_{+,\theta_{max}}$.*

where L is the effective cavity length, z_0 is the position on the light source inside the cavity and E_0 is the initial field amplitude. To respect phase changes of waves at boundary surfaces Equations 9,10 can be corrected by a phase term between real and imaginary parts of the complex reflectivity coefficients. For calculating the spectral mode distribution, the field-amplitudes of the superposition of $E_{-,+}$ have to be integrated over θ (see Figure 2) with respect to the polarization of the traveling waves. The idealized resonance condition for Fabry-Perot resonator is illustrated in Figure 2A. For perpendicular white light illumination only the on-axis cavity modes can be occupied and only those waves can enter the cavity if $L = \lambda/2$. A broadband emitter in the center of the cavity can emit also into angular distributed modes if the z-komponentes of the emission k-vector is fulfilling the resonance condition by the relations in Equation 11 and:

$$|\vec{k}| = \sqrt{k_x^2 + k_y^2 + k_z^2}, \tag{12}$$

$$k_z = |\vec{k}| \cdot cos(\theta), \tag{13}$$

Thus, for arbitrary angles θ the resonance condition is by $k_z = \pi/L$:

$$L \geq \lambda_\theta/2. \tag{14}$$

The real mirror distances can be approximated by extending the resonance condition according to Steiner et.al.[3]:

$$L = \left(m - (2\pi)^{-1} \sum_i \Delta\phi_i(d_i, \vartheta, \lambda_{trans}) \right) \lambda_0/2ncos\vartheta. \tag{15}$$

Here ϕ_i represents the phase change at mirror i depending on the mirror thickness d_i, the angle of the incident light ϑ, the transmitted wavelength λ_{trans}, the refractive index n of the intra-cavity medium and m as the order of interference. The polar plot in Figure 2B shows the calculated angular distribution of the k-vector originating in the cavity center at $z_0 = L/2$ with a specific wavelength (750 nm) and two mirror separations (left: 375 nm, right: 390 nm). Blue shifted wavelengths with respect to on-axis wavelength are emitted with an angle θ which detection is limited in practice by the numerical aperture of the objective lens. The plot in Figure 2C shows both the on-axis transmission spectrum (blue dots) for white light illumination and the spectral mode distribution (red line). The FWHM of the Lorentzian shaped transmission signal is a measure for the time a photon stays inside the cavity and given by: $T_2 = 2\hbar/\Gamma_i$ with T_2 as the decay time and Γ as the FWHM of a Lorentzian. Treating a plasmon oscillation of a gold nanorod as a resonator, the dephasing times of the plasmon can be determined analogously[4]. The quality of a resonator is given by the so called quality factor: $Q = \lambda_0/FWHM$ with λ_0 as the spectral maximum of the transmission peak. The Q factor varies as a function of the resonance frequencies in transmission as the reflection coefficients are dependent on the wavelength. The reflectivities for silver layers of certain thicknesses are based on the dielectric function[5] and can be determined by the transfer matrix method (TMM). The decrease of the silver reflectivity to shorter wavelengths leads to a reduction of the quality factor for decreasing wavelengths. Hence, the experiment was carried out with gold nanorods that have a longitudinal plasmon resonance around 700 nm.

II. EVALUATION

To determine the spectral parameters for the respective GNR and the coupling properties a global fitting procedure was applied for each spectra series representing each a different GNR. The respective parameters

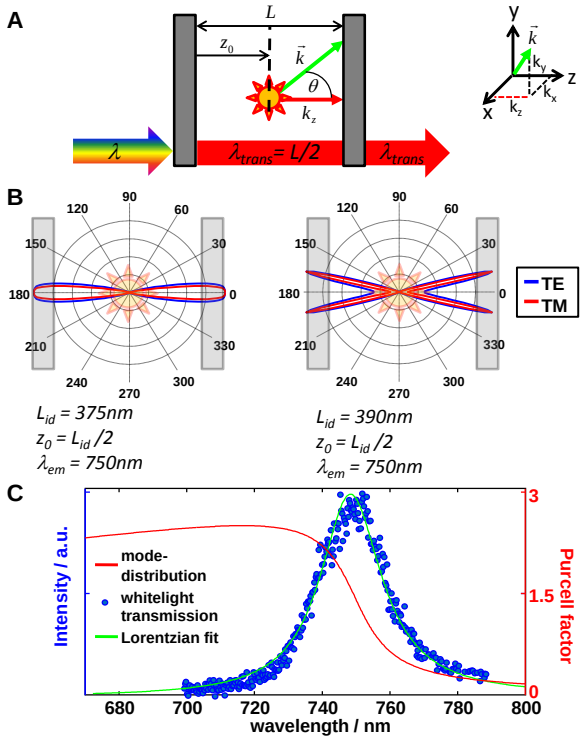

FIG. 2. *A: Illustration of the resonance condition for white light illumination and an broad band emitter in the cavity center. B: Angular distribution of a single mode with TE/TM-polarization and one wavelength (750 nm) at different mirror spacings (left: 375 nm; right: 390 nm). Only modes with* $\theta < \alpha$ *(*$NA = n \cdot \sin\alpha$*) are detectable by a collecting objective (with numerical aperture:* $NA = 0.8$ *and the refractive index* $n = 1.33$*). B: Calculation of the spectral mode distribution (red line) taking into account the on-axis mode and the off-axis modes and a mesaured white light transmission spectrum (blue dots) which can be perfectly fitted by a Lorentzian line shape function (green line). In the weak coupling regime, the mode distribution determines the altered fluorescence lifetime.*

are: plasmon frequency ω_G, damping constant γ_G which directly corresponds to the plasmon frequency ω_G[6], coupling frequencies Ω_G,Ω_R and the spectral separation $\Delta\omega_{0,\theta_{max}} = \omega_{R,0} - \omega_{R,\theta_{max}}$. For one GNR and the corresponding five parameters a start vector was defined. By this start vector each single luminescence spectrum of one series was now fitted by four Lorentzians which spectral properties are described by the unknown parameters, the measured on-axis cavity resonance ($\omega_{R,0}(\lambda_0)$), damping rate ($\gamma_{R,0}(\lambda_0)$ and the relations given by equations in the main article with the band intensities as a free parameter. Afterwards, the start vector was modified by the algorithm to improve the fits of the single spectra in order to finally optimize the five parameters within narrow intervals for each complete series (with more than 200 spectra for each GNR). The error between simulation and experiment was minimized by the method of least squares such that in the whole spectra series the parameters ω_G,γ_G,Ω_G and Ω_R have the same values.

III. EXPERIMENTAL

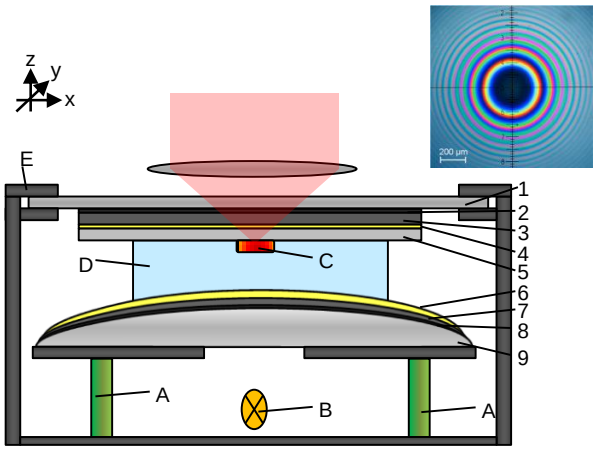

FIG. 3. *Scheme of the resonator construction with following layers: 1) Glas cover slip (22x22 mm) 2) Chromium 1 nm 3) Silver 30 nm 4) Gold 1 nm 5)* SiO_2 *60 nm; 6) Gold 1 nm 7) Silver 60 nm 8) Chromium 1 nm 9) Glass lens (F=150). A) Piezoelectric Stacks B) Polychromatic LED C) GNR D) water E) Aluminium housing on piezoelectric scanning table. On the upper side the excitation source and the objective lense are indicated. The z-axis is denoted as the path of light. By increasing the voltage on A the stacks expand resulting in a decreasing distance between bottom and top mirror. The inset on the upper right shows the Newton-Ring pattern visible with white light illumination.*

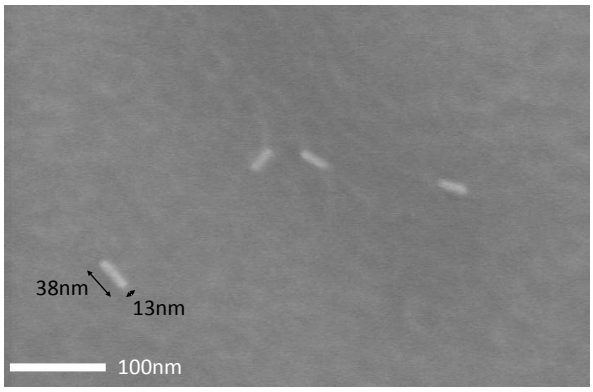

FIG. 4. *SEM-Image of GNRs attached to the plane mirror. The layers of the mirror are: 1 nm chromium, 30 nm silver, 1 nm gold, 60 nm* SiO_2 *according to the layer sequence in Figure 3. The roughness of the surface is low enough to guarantee a parallel orientation of the GNRs with respect to the mirror surface.*

The tunable $\lambda/2$-Fabry-Perot resonator sketched in Figure 3 consists of two silver mirrors with piezoelectric

stacks. The resonator design is based on the construction developed by Steiner et.al.[7–9]. The mirrors consist of a silver coated glass cover slip and a silver coated F=150 lens from Thorlabs. The mirror reflectivities were chosen to be ∼0.9 for the top mirror (for excitation and detection) and ∼0.95 for the bottom mirror both at 700 nm wavelength. On the cover slip an additional spacing layer of 60 nm SiO_2 was coated to hold the GNRs (Nanopartz. Length: 38 nm, width: 10 nm; see also ref[10]) about halway between the mirrors with tridest water serving also as intra cavity medium that allowed to vary the mirror spacing. The resonator, was mounted on a feed-back controlled xyz-piezoelectric scanning stage of a home-built confocal microscope with spectrograph for recording single particle spectra, as recently described in Ref[11]. A white light LED was installed under the curved mirror to illuminate the resonator with a parallel beam to record on-axis transmission spectra.
The transmitted LED spectra were corrected with the free space LED spectrum and fitted by a Lorentzian line shape function to determine the spectral maximum and FWHM of the resonator as a function of the mirror spacing. Confocal images and emission spectra were taken by exciting the system with a 665nm cw laser diode and guiding the luminescence through a pinhole onto an APD or spectrograph with CCD-camera.
The individual GNRs differ slightly in size and geometry leading to a distribution of the resonance frequencies and dephasing rates[6]. Here, the GNRs have a fixed distance to the top mirror (60 nm), but different distances to the second mirror as the resonator is tuned. For GNRs with higher resonance frequencies the mirror separation has to be more decreased for resonance between cavity and plasmon which means, that these GNRs are closer to the center of the cavity in case of resonance. This is explaining higher coupling rates for plasmons with higher eigenfrequencies. Also, for higher frequencies the reflectivity of silver decreases, leading to an increased matching of the damping rates of plasmon and resonator.

[1] L. Novotny, American Journal of Physics **78**, 1199 (2010).
[2] G. Bjork, Ieee Journal of Quantum Electronics **30**, 2314 (1994).
[3] M. Steiner, F. Schleifenbaum, C. Stupperich, A. V. Failla, A. Hartschuh, and A. J. Meixner, Journal of Luminescence **119**, 167 (2006).
[4] C. Sonnichsen, T. Franzl, T. Wilk, G. von Plessen, and J. Feldmann, New Journal of Physics **4**, 93 (2002).
[5] P. B. Johnson and R. W. Christy, R, Physical Review B **6**, 4370 (1972).
[6] A. Konrad, F. Wackenhut, M. Hussels, A. J. Meixner, and M. Brecht, The Journal of Physical Chemistry C **117**, 21476 (2013).
[7] M. Steiner, F. Schleifenbaum, C. Stupperich, A. V. Failla, A. Hartschuh, and A. J. Meixner, Chemphyschem **6**, 2190 (2005).
[8] S. Bar, A. Chizhik, R. Gutbrod, F. Schleifenbaum, A. Chizhik, and A. J. Meixner, Analytical and Bioanalytical Chemistry **396**, 3 (2010).
[9] A. Chizhik, F. Schleifenbaum, R. Gutbrod, A. Chizhik, D. Khoptyar, A. J. Meixner, and J. Enderlein, Physical Review Letters **102**, 073002 (2009).
[10] T. Zuchner, F. Wackenhut, A. V. Failla, and A. J. Meixner, Applied Surface Science **255**, 5391 (2009).
[11] M. Hussels, A. Konrad, and M. Brecht, Review of Scientific Instruments **83**, 123706 (2012).

Abbreviations

A. platensis	Arthrospira platensis
APD	Avalanche photodiode
CCD	Charge-coupled device
FRET	Förster resonance energy transfer
FWHM	Full width at half maximum
HOMO	Highest occupied molecule orbital
IC	Internal conversion
IRF	Instrument response function
ISC	Inter system crossing
LDOS	Local density of optical states
LUMO	Lowest unoccupied molecule orbital
NA	Numerical aperture
PSF	Point spread function
P	Parallel polarized
PSI	Photosystem I
PSII	Photosystem II
PW	Phonon Wing
S	Perpendicular (*senkrecht*) polarized
TCSPC	Time correlated single photon counting
ZPL	Zero-phonon-line

Acknowledgment

I would like to express my gratitude to:

- my supervisor Prof. Dr. Alfred J. Meixner for giving me the opportunity to participate in his nano-optics group and supporting me in any scientific issue. Each discussion with him was an honor and he taught me to open my mind for different points of view.
- my supervisor PD Dr. Marc Brecht for introducing me into the world of science, transferring his own enthusiasm on me and his ability to combine a strong sense of purpose with great amity. He always encouraged me to improve myself as a scientist and a human being and taught me to pursue reasonable serenity for each appropriate situation.
- my wife Ludmila Prokopieva for her invaluable emotional support and comfort during the years. She always had a sympathetic ear and found the right words to empower me.
- my father Hugo Konrad especially for his financial support enabling my first Staatsexamen in the first place.
- my elder brothers Michael and Andreas for representing inspiring role models as by their style of lives.
- my former colleague Dr. Martin Hussels for representing a shining example of the complete scientist I tried to emulate.
- my colleague Michael Metzger for his outrageous technical skills and the cheerful and casual working atmosphere.
- Dr. Andreas Kern for helping me to understand the world of theory and his amazing electronic and programming skills.
- the members of the Meixner and Brecht group for a nice and productive atmosphere, helpful suggestions and interesting discussions.

- Loki and Mary for being such lovely living things.
- all namely not mentioned friends for their unconditional support.